ASSESSMENT OF MICRO AND NANOPLASTIC TOXICITY

AND THEIR PROTEIN CORONA USING IN VITRO AND IN SILICO NEW APPROACH METHODOLOGIES

HUGO BROUWER

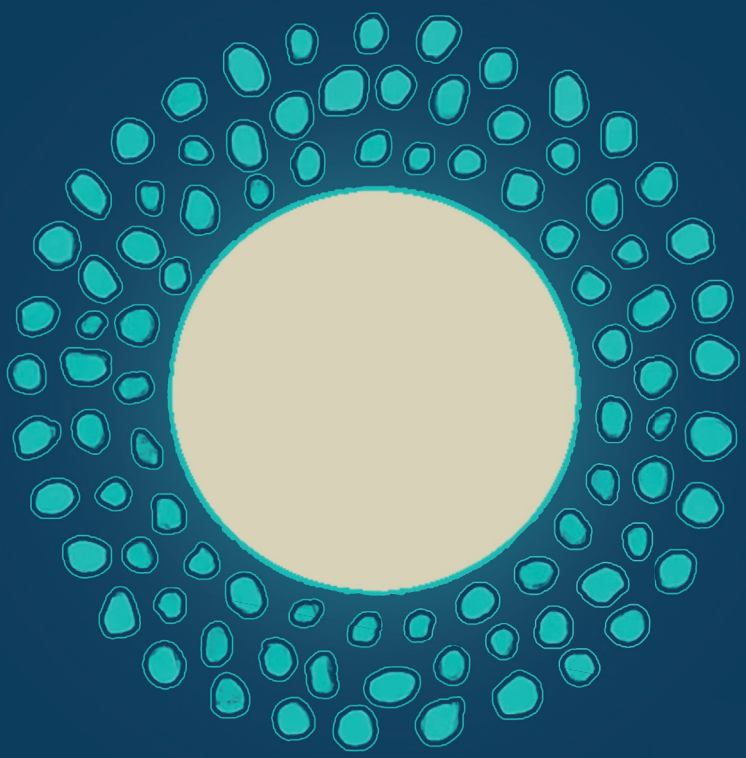

Propositions

1. Current dosing schemes for micro- and nanoplastic toxicity studies do not provide relevant data for human risk assessment.
   (This thesis)
2. Leaching of molecular labels from micro- and nanoplastics compromises measured tissue concentrations.
   (This thesis)
3. Recency of scientific literature is a poor criterion for its value.
4. The complexity of scientific models is not correlated with their usefulness.
5. Originality and inspiration are methodological, not spontaneous.
6. Music is the best medium to understand different cultures.
7. The benefits of generative AI models do not weigh up to their environmental and societal costs.

Propositions belonging to thesis entitled
Assessment of micro and nanoplastic toxicity and their protein corona using in vitro and in silico new approach methodologies

Hugo Brouwer
Wageningen, 22nd of January

Assessment of micro and nanoplastic toxicity and their protein corona using in vitro and in silico new approach methodologies

Hugo Brouwer

Thesis committee:

Promotors
Prof Dr H. Bouwmeester
Professor in Toxicology
Wageningen University & research

Co-promotors
Dr M. Busch
Researcher, Toxicology Group
Wageningen University & research

Other members
Prof. Dr M. van Duursen, Vrije Universiteit Amsterdam
Prof. Dr *ir.* J. Legler, Utrecht University
Prof. Dr *ir.* A.A.B. Koelmans, Wageningen University & Research
Prof. Dr *ir.* A.G.A. Oomen, Universiteit van Amsterdam & National Institute for Public Health and the Environment (RIVM)

This research was conducted under the auspices of the VLAG Graduate School (Biobased, Biomolecular, Chemical, Food and Nutrition Sciences)

Assessment of micro and nanoplastic toxicity and their protein corona using in vitro and in silico new approach methodologies

Hugo Brouwer

Thesis

submitted in fulfilment of the requirements for the degree of doctor
at Wageningen University
by the authority of the Rector Magnificus,
Prof Dr C. Kroeze,
in the presence of the
Thesis Committee appointed by the Academic Board
to be defended in public
on Thursday 22 January 2026
at 3.30 p.m. in the Omnia Auditorium

Dedication:

This thesis is dedicated to past and current victims of cancer, including Lenie and Willem who are dearly missed.

"A comfort zone is a beautiful place – but nothing ever grows there." John Assaraf

Hugo Brouwer
Assessment of micro and nanoplastic toxicity and their protein corona using in vitro and in silico new approach methodologies.
292 pages.

PhD thesis, Wageningen University, Wageningen, the Netherlands (2026)

With references, with summary in English.

ISBN: 978-94-6534-077-7
DOI: 10.18174/681575

Table of Contents

CHAPTER 1

General introduction

Hugo Brouwer

1.1 Historical perspective on micro- and nanoplastics

Throughout its history, mankind has continually sought novel materials to meet the ever-increasing demands of society. Until the mid-19th century, industry relied on natural materials including steel, wood and leather which were heavy, rigid and sensitive to degradation (1). The increasing demand for luxury products during the industrial revolution caused an excessive need for animal-derived polymers such as ivory, turtle shell and shellac, which could no longer be met by the mid-1800s (2). In order to stave off mass animal extinction, synthetic plastics were invented in 1863, which endowed man with a material that is readily available, long lasting, and pliable. The maturation of polymer chemistry in the 1930s, combined with high material demands during the second world war, kickstarted the plastic boom as we know it today (2, 3). Currently, over 460 million tons of plastics are produced on an annual basis with a recycling rate of less than 9% (4). Although plastics have been a great boon to human innovation, the once desirable ease of production and long-persistence has now made plastics one of the most abundant environmental pollutants (5).

Macroscopic waste in the environment is continually exposed to environmental forces including abrasion by wind and waves, ultraviolet (UV) light and biological fouling. Through these processes, plastic waste can slowly be degraded into plastic fragments smaller than 5 mm called microplastics and nanoplastics (MNPs). The small size of MNPs facilitates their spread throughout earth's ecosystems by the tidal circulation and atmospheric airstreams (6, 7). As a result, MNPs and microplastics have been detected in all locations in the known ecosphere including remote locations devoid of anthropogenic activity like the Mariana trench (8, 9), mount Everest (10) and the north pole (11).

Micro- and nanoparticles below 10 µm, like small MNPs or metallic particles, are called colloids and are subject to both physical forces like sedimentation and thermodynamic forces that commonly act on a molecular scale. Colloidal MNPs are undetectable by the naked eye, can traverse biological barriers and can accumulate in biological tissues otherwise inaccessible to larger plastic objects (12, 13). Human exposure to MNPs has been confirmed by the recent detection in various human tissues (14-18), which raises concerns about the effect of MNPs on human health. In view of this, MNPs have recently been designated as a contaminant of emerging concern (19-21) and have received increasing scientific attention by the European Food Safety Authority (EFSA), the World Health Organization (WHO) and the environmental protection agency (EPA) (22-24). To warrant human health throughout a lifelong exposure to MNPs, there is an urgent need to understand human exposure to microplastics, the fate of MNPs in the human body and the potential toxicity of MNPs to humans.

1.2 Generation of micro- and nanoplastics

MNPs can either be formed due to natural processes leading to weathering of macroscopic plastic or by intentional synthesis at a microscopic size. MNPs which have been synthesized intentionally are called primary MNPs and have historically been used as abrasive agents in cosmetics or building materials(25) and are still commonly used in laboratory settings. While there are multiple ways of generating primary MNPs, the most common method of synthesis is by solvent displacement and emulsion polymerization (26, 27). Here, monomers are initially dispersed in a solvent which is then subsequently added to a non-miscible aqueous liquid. As a result, microscopic droplets form in the aqueous phase containing plastic monomers the size of which can be controlled with solvents or mechanical stimulation(26, 27), and polymerization can be initiated within the solvent droplets(28). This method allows for accurate control of MNP size and various additives like fluorophores can be added to the solvent phase to allow internal labelling of MNPs (29, 30). Importantly, solvent displacement methods require the use of monomers which are highly soluble in an organic solvent, but poorly soluble in the non-miscible liquid(31). Of all polymers with high production volume, polystyrene (PS) is the most suitable for solvent displacement methods and the size of the resulting MNPs can be controlled even for small nanoparticles(28). Contrastingly, the other polymers with high production volume have a higher water solubility which makes it more difficult to be efficiently synthesized at colloidal sizes(28). Consequently few primary MNPs are available for non-PS MNPs.

The other main group of MNPs are the secondary MNPs which are either generated due to environmental weathering of macroscopic plastic waste, or by intentional artificial weathering of larger plastics products or particles. As mentioned earlier, environmental weathering occurs mainly through abrasion by waves, UV light causing internal breaks in the plastic structure and biological degradation by plastic degrading bacteria (32). Environmental weathering has both physical and chemical consequences to the MNPs. Chemically, UV radiation and oxidation causes exchange of methyl/carbon groups with carbonyl and hydroxyl groups, and alteration of the crystalline structure of MNPs and accumulation of oxidated end-products leading to discolouration (32-34). Physically speaking, the main consequences of weathering are the formation of cracks and pores in MNPs by degradation of the polymer backbone and repeated thermal expansion and contraction. Both cracking and pore forming increase the total surface area of MNPs which in turn increase their ability to adsorb environmental toxicants (35). Thermal weathering and physical weathering of plastics occurs frequently in both environmental MNPs and food-contact materials. Thermal weathering typically occurs at temperatures above 200°C, although combined action of UV radiation and oxidation can accelerate this process. Thermal degradation results in the formation of free radicals which, under the influence of oxygen, result in similar alterations as oxidative weathering (36, 37).

Physical weathering, unlike UV, oxidative and thermal-induced weathering, mainly affects the physical structures of MNPs with minimal alterations to the chemical structure. It is not practical to collect weathered plastics from the environment as there is a lack of suitable separation techniques to obtain relatively homogenous MNP mixtures from environmental samples. Instead, environmentally weathering is typically mimicked by accelerated top-down degradation of plastic products. The five main accelerated weathering methodologies are cryogenic grinding (38), thermal degradation (39), laser ablation (40) , UV-induced fragmentation (41, 42) and advanced oxidative degradation (43). It is poorly understood how similar the chemical and physical MNP modifications of these accelerated weathering methodologies are to natural weathering, but likely cryogenic grinding, will only mimic physical alterations while the remaining methods will introduce both physical and chemical modifications to the material. Regardless of environmental or artificial weathering, secondary MNP formation generates homogenous mixtures of MNP sizes and shapes with little possibility to control resulting MNP properties. As such, the variety and complexity of secondary MNPs tends to be higher than primary MNPs. As a result, laboratory studies with MNPs have largely been carried out with primary MNPs despite the fact that secondary MNPs are more common in nature.

1.3 Physicochemical properties of micro- and nanoplastics

The physicochemical properties of MNPs can influence their behaviour in the environment and their interactions with humans. The most important physicochemical properties are particle size, shape and polymer type, and these properties are frequently used for MNP grouping. As highlighted earlier, small size is the main determining factor of MNPs. While the term microplastic was coined over 20 years ago, there is an ongoing discussion on the exact size definition of MNPs (44). In general, microplastics are considered any plastic particle ranging from 1 µm - 5mm, while nanoplastics are defined to range from 1 - 100 nm and the particles ranging from 100 nm - 1 µm are ambiguously referred to as nanoplastics or microplastics. For the remainder of the thesis, particles ranging from 100 nm - 1000 nm are considered microplastics, as this definition is in line with the definitions set by the international organization for standardization (ISO), EFSA and the OECD (45).

Another key property of MNPs is the polymer composition, which determines the chemical reactivity, density and rigidity (32). The polymer composition of secondary MNPs mimics the polymer composition of macroscopic plastic material, while primary MNPs are mostly made of PS. In Europe, 91% of all produced plastics are comprised of polyethylene (PE), polypropylene (PP), polyvinyl chloride (PVC), polyethylene terephthalate (PET), polyurethane (PUR) and polystyrene (PS) (46-53) and the remaining 9% are classified as other

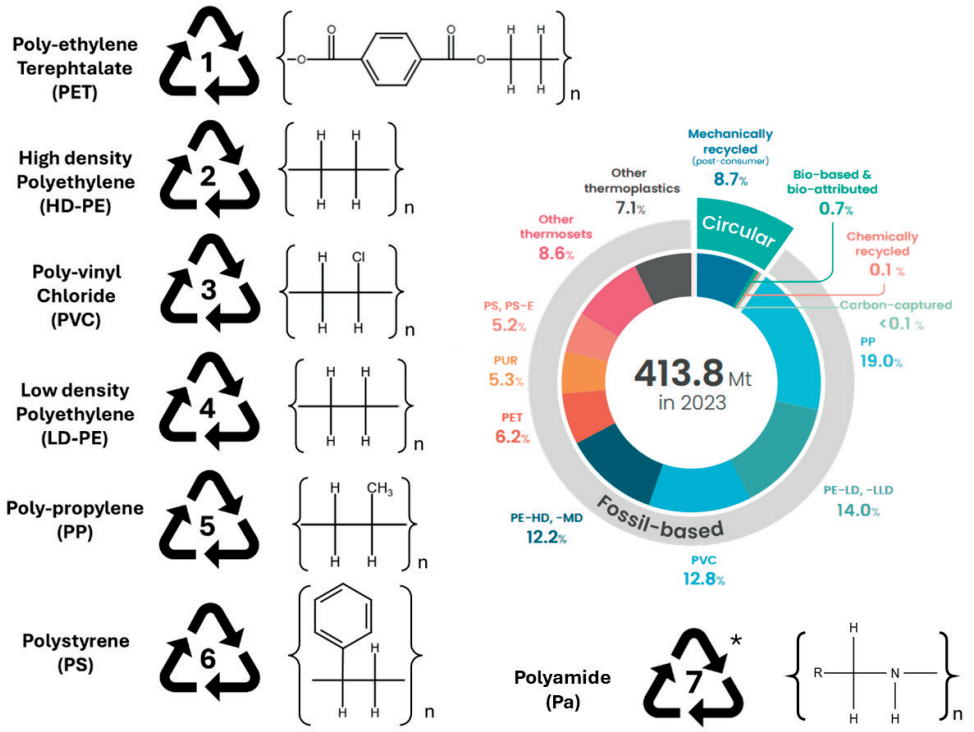

Fig 1. Overview of polymer types and global plastic production

The symbols on the left-hand side show the chemical backbone of the most produced polymer types and their associated resin recycling code as classified by society of the plastic industry (SPI). *Resin recycling code 7 applies to all plastics other than PET, HD-PE, PVC, LD-PE, PP or PS. The pie chart on the right shows the percentual contribution of each polymer type to global plastic pollution taken from PlasticsEurope (4).

The polymer composition also impacts the crystallinity, roughness and chemical reactivity of the material, however it is poorly understood how this impacts the interaction with humans. In laboratory settings, the MNP polymer is often modified by addition of carboxyl or amine groups to the surface of the MNP polymer, imparting a negative and positive surface charge respectively. The surface charge of MNPs largely impacts their interaction with humans, as human cell and mitochondrial membranes are negatively charged and can be disrupted by a positive charge of colloids (54).

Finally, the shape of MNPs largely determines their behaviour. Microplastics can exist as spheres, sheets, rods, fibres, foams or fragments of heterogenic aspect ratios (55, 56). Spherical microplastics are the most frequently tested in laboratory settings, but only comprise a minor part of environmental MNPs where fibres, fragments and films are most common (55, 56). The shape of MNPs is inherently linked to their total surface area which

impacts both their reactivity and binding capacity. Additionally, the shape of MNPs impacts their aerodynamic and hydrodynamic properties, which alter their environmental deposition and biodistribution in the body (discussed in detail in section 1.6) (57-59). Specific shapes also impart unique mechanisms of toxicity such as frustrated phagocytosis which causes inflammation through the inability for phagocytes to engulf long fibres (60, 61).

Overall, the importance of physicochemical properties of MNPs on their toxicity is known, but vaguely understood.

1.4 Additives and fillers

Besides differences in physicochemical properties, another main distinguishing feature of MNPs is the presence of additives and fillers. Additives shape the functional properties of plastics, and all plastic products contain additives to some degree. In the European union, plastic additives are categorized as functional additives, colorants, fillers and reinforcements (62). A table of the most common additives and their typical weight fraction in percentage is included in table 1.

Table 1: Typical additives used in plastics

Category	Weight fraction	Notable Examples
Plasticizer	10-70%	Chlorinated paraffins BPA, DEHP, BBP
Flame retardant	0.7-25%	Halogenated phenols, aluminium oxide, halogenated hydrocarbons
Stabilizers	0.05-3%	Cadmium, lead, stannum, barium, zinc, phenolic antioxidants
Biocides	0.001-1%	Arsenic compounds, organic tin, triclosan
Organic colorants	0.001-5%	Azocolorants
Inorganic pigments	0.01-10%	Cadmium, chromium, lead
Fillers	<50%	Calcium carbonate, Talc, Clay, ZnO, glass, plant-derived polymers, TiO_2 etc.
Reinforcements	15-30%	Glass fiber, carbon fiber, aramide fiber, plastic nanomaterials, metal nanomaterials, ceramic nanomaterials

Table is recreated from the table presented in (63) and contains information from (64) and (65).

Functional additives include flame-retardants, antioxidants, plasticizers, heat/light stabilizers, biocides among others (63). The most abundant additives in terms of weight/weight fraction are plasticizers, flame retardants, fillers and reinforcements. Many of the functional additives like phenolic compounds and halogenated flame retardants have suspected endocrine disrupting potential, while heavy metals used as pigments may induce neurotoxicity (25, 66-74). For macroscopic plastic products, the leaching of these materials is typically assessed by *in silico* prediction of leaching (62), however it may be possible that leaching from MNPs is higher than macroscopic plastics. Furthermore, MNPs show higher bioavailability than macroscopic plastics and may act as a vector to shuttle these compounds to otherwise inaccessible locations, which is called the trojan-horse effect (63, 75). As such, there is large scientific and regulatory interest in establishing the role of functional additives and pigments on MNP toxicity. Filler materials and reinforcements are typically included in plastic materials at high weight fractions to alter physicochemical properties of the plastic, reduce the cost, or improve degradability (76, 77). Typical filler materials do not have well established roles in toxicity, and the role of fillers and reinforcements has been largely ignored from a toxicological perspective. However, when plastics are degraded, these fillers are also miniaturized, potentially imparting novel toxicity. Furthermore, degradation of plastic leads to release of the filler material (78) which can lead to secondary exposure to inorganic or organic filler nanoparticles. No studies could be identified which investigated the role of fillers in MNP toxicity, which represents an important knowledge gap. Besides these additives mentioned above, plastics typically also contain unreacted monomers and oligomers, which are often cytotoxic and carcinogenic and may contribute to overall effects of MNPs (63, 79). As evident from their physicochemical properties and common additives, there is a near limitless combination of possible MNPs a highly diverse suite of contaminants, the complexity of which is not subservient to the complexity of small molecules.

1.5 Human exposure to micro- and nanoplastics

Humans cannot visually or physically detect MNPs (present in food and air) and consequently may unintentionally be exposed to up to hundred thousands of MNP fragments per year (80). There are four possible exposure routes to MNPs: ingestion, inhalation, dermal absorption and intravenous release. Barring uptake through open wounds, dermal absorption of MNPs is virtually absent, making the dermal route of exposure largely negligible. Intravenous exposure is mostly due to release of MNPs from tubing intended for intravenous application or released from prosthetic implants (81-84). While intravenous exposure is highly relevant for specific patient populations and the elderly, it has a negligible contribution to the general population.

While not the focus of this thesis, one of the two main routes of human MNP exposure is inhalation of contaminated air. MNPs comprise a significant part of particulate matter in air and numerous studies have confirmed their presence in both indoor and outdoor air. Currently there is a consensus that exposure to indoor air represents the major route of inhalatory MNP exposure, both due to higher reported concentrations (85) and because humans spend around 70-90% of their time indoors (86). Inhalatory exposure is limited to spherical particles with a hydrodynamic diameter smaller than 10 µm due to deposition of larger MNPs in the upper airways followed by exhalation or clearance, while fibres longer than 10 µm can still be internalized (87). Fibres have been shown to translocate to the pulmonary region more efficiently than particles (88) and can have pronounced local toxicity through frustrated phagocytosis (60), but translocation to the bloodstream is highly unlikely. A study on indoor air demonstrated microplastic concentrations of 0.4 to 56.5 particles per cubic meter (89), while occupational exposures can be many times higher than regular indoor exposure. The majority of inhaled particles get trapped in mucous or macrophages lining the lung epithelia. These particles are subsequently cleared from the lung by a process called the mucociliary escalator, after which they are swallowed (90). The exact degree of mucociliary clearance is unknown, but various studies have shown clearance of ~ 50-85% of inhaled particles of size 220 nm - 4.2 µm within 24 h (91-93). Additional contribution of airborne particles to the total oral MNP burden occurs through settling of airborne dust on the ground and on plates (94-96). The daily inhalation of microplastic fibres was estimated to be between 26 - 130 fibres of 50 - 500 µm (85) or around 272 fibres of approximately 250 µm in size per day (97).

The consumption of contaminated foodstuffs represents the largest vector of human MNP exposure. There is an increasing tendency to package food in plastic containing food-contact materials, which upon opening, microwaving, heating, or passively over time can generate MNPs (98-101). Additionally, foodstuffs themselves can get contaminated through consumption of MNPs by animals or livestock through grazing of contaminated plants, ingestion of MNPs in surface water and the consumption of other animals leading to trophic transfer (102-105). MNPs have been detected in virtually all food commodities, including meat (13, 106), milk, fruit and vegetables (107), honey (108), salt (109), shellfish (110), fish (111), beer (112) and drinking water (113), carbonated drinks, coffee (114). Based on MNP concentrations in these sources, there are multiple estimates of human oral exposure. In terms of numbers of particles, an estimate of total human food consumption predicted oral exposure to 114000 and 94000 MNPs per year for males and females, respectively (115), while consumption of tea was estimated to lead to exposure to $2.93*10^{10}$ particles per year, although this also included non-MNP particulates (116). In addition to number-based estimates based on particle counting, two mass-based estimates exist which range between 4.1 µg/week (80) and 0.1-5 g/week (117).

The above exposure estimations range over six orders of magnitude, which highlights the difficulty of plastic exposure assessment as recently discussed by the European Food Safety Authority (EFSA) and the U.S. Food and Drug Administration (FDA) (13, 114). Current analytical methods have difficulty detecting microplastics <1 µm in complex samples and as a result the concentrations of nanoplastics in food have to be estimated from the presence of larger microplastics. Plastic abundance in nature generally follows a power law relation with smaller particles being exponentially more present (80, 118). Additionally, nanoplastics are more bioavailable and have a higher capacity for toxicity (13). It is therefore commonly believed that nanoplastics pose a larger risk than microplastics for humans, but the lack of analytical techniques precludes accurate nanoplastic exposure assessment.

1.6 Biodistribution of MNPs

After ingestion of MNPs, their biodistribution within the body is determined by their absorption from the gastrointestinal tract to the central circulation, their distribution from the central circulation to organs and their elimination from organs into urine or feces.

Oral ingestion of MNPs has no clear size cutoff and all swallowed MNPs eventually traverse the entire gastrointestinal tract, consisting of the esophagus, stomach, small intestine and large intestine. Throughout the gastrointestinal tract, MNPs are subjected to large fluctuations in pH, osmotic strength and various digestive (e.g. enzymes) and non-digestive proteins (e.g. mucins) which line the inside of the gastrointestinal organs. Due to their high recalcitrance to chemical modifications, no substantial MNP metabolism occurs in humans and MNPs can pass the stomach with minimal alterations (119-121). After passing the stomach, MNPs enter the small intestine, where the majority of absorption occurs. The small intestine consists of a luminal compartment containing the digesta, an epithelial layer which forms both a barrier to foreign agents as well as the main site of nutrient absorption, and a submucosal layer containing various immune cells as well as lymphatic and capillary vessels.

The epithelial layer consists of finger like protrusions called villi, invaginations in between the villi called crypts and scattered lymphoid structures called Peyer's patches. The villi serve to increase the surface area of the small intestine increasing the capacity to absorb nutrients and chemicals. Villi are comprised of two main cell types, enterocytes and goblet cells of which goblet cells represent approximately 10% of all cells (122). Goblet cells secrete a negatively charged mucous into the luminal compartment which covers the entirety of the small intestine epithelium. The mucous layer strongly restricts transport of particles with a size of >2 µm (123-125), as well as charged particles (126, 127). The

mucous layer is fully renewed every 1-3 h leading to fecal excretion of the old mucous with all entrapped particles (128, 129).

After passage through the mucous layer, MNPs between 50 and 500 nm can be taken up directly by enterocytes through endocytosis (particles <150 nm) or macropinocytosis (particles <500 nm). Larger particles can be internalized by phagocytosis(130), but the phagocytotic capacity of enterocytes is limited. The crypts house intestinal stem cells, which, through stimuli by Paneth cells, differentiate into new intestinal cell types which migrate upwards from the base of the crypt to the tip of the villi. Dead cells are shedded from the villi tips, leaving transient gaps in the villi membrane. It has been proposed that gaps at the tips of the villi through enterocyte shedding might allow MNPs up to a size of 150 µm to enter the basolateral tissue (131, 132), through a process called persorption but this mechanism is still highly debated (133). A final route how MNPs can pass the intestinal epithelium is via specialized lymphoid regions, the Peyer's patches (also called the gastric lymphoid associated tissue (GALT)). The intestine contains approximately 100-300 Peyer's patches sparsely spread throughout the small intestine which are responsible for a large part of the intestinal microparticle absorption (134, 135). Unlike the remainder of the small intestinal epithelium, Peyer's patches have a minimal mucous layer (136, 137) and are home to specialized enterocytes called microfold cells (M-cells). M-cells display a much increased phagocytic capacity compared to enterocytes and have been shown to internalize particles up to 10 µm, with optimal internalization of 1 µm particles (138). The degree of intestinal absorption of MNPs in humans is unknown, but mouse studies show an absorption of ranging typically between 0.1 - 2% (13, 139, 140).

After intestinal absorption, MNPs get deposited in the *lamina propria* or the submucosal area of Peyer's patches. Particles below 5 µm can distribute to the rest of the body through the villous capillaries and lymphatic vessels called lacteals (141), while particles >5 µm typically remain in the intestine. The intestinal capillaries are porous, allowing the entry of particles below 12 nm like proteins and small molecules (142). The majority of MNPs cannot directly pass into the intestinal capillaries and are instead transported by the lacteals to collecting lymph nodes, from where they can enter the bloodstream by deposition in the subclavian vein.

After entry into the bloodstream the distribution of MNPs is governed mostly through capture by phagocytotic cells and the porosity of blood vessels. The majority of MNPs are rapidly sequestered in the liver and spleen, due to the high phagocytic activity of resident macrophages, and because of large fenestrations in liver capillaries and open-ended capillaries in the spleen (142, 143). Distribution to other organs has been confirmed *in vivo*, but biodistribution studies indicate that this fraction is small compared to concentrations in the intestine, spleen and liver (139, 144, 145).

MNPs are eventually removed from the body by urinary or biliary excretion. The kidneys have capillary fenestrations up to 70 nm and bloodborne MNPs <10 nm are rapidly excreted into the urine (146). Urinary excretion of larger fluorescently labelled MNPs has also been shown *in vivo*, but as of yet there is no theoretical justification how this is possible and may be an artifact due to leaching of fluorophores from the plastic surface. Biliary excretion of MNPs occurs by the transfer of MNPs from the liver into proximal bile channels with a diameter of 2 µm called canaliculi, which are subsequently released back into the intestine through the sphincter of Oddi. The presence of microplastics up to 3 µm has been confirmed in bile ducts (147), however as the particles exceeded the size of canaliculi, the mechanism of biliary excretion is unknown. While biliary excretion is thought to be the main excretion pathway for MNPs, the excretion of MNPs appears slow (hours to months) (148) and no exact rates or size cutoffs for biliary excretion are known.

1.7 Protein corona

Colloidal MNPs very efficiently adsorb surrounding molecules due to their high surface area and hydrophobic nature, which leads to the formation of a layer of biomolecules on MNPs as they traverse the body. This layer of molecules is called the corona and can significantly impact nanoparticle toxicity through modulation of biological interactions(149-152).

While any lipophilic or amphiphilic molecule (like proteins, saccharides and lipids) can be part of the MNP corona, the protein component of the corona, referred to as the protein corona, has received the most scientific attention and is the best comprehended aspect of the micro- and nanoparticle corona (151, 153). The body consists of various matrices including blood, tissue, lymph and digesta, each with their specific protein compositions. As a result, the protein corona develops dynamically as MNPs transit through different biological compartments. The development of the protein corona within the body can be divided in two phases, formation of the hard protein corona and the soft protein corona. First, proteins with a high abundance but low affinity attach to the MNP, forming the weakly interacting soft protein corona within seconds to minutes. Within the timespan of several minutes to hours, weakly interacting proteins are exchanged for high-affinity proteins forming the hard protein corona, which is rapidly covered by proteins of the soft-protein corona through protein-protein binding (154). The timeframes of these processes cause the soft protein corona to change rapidly during bodily transit while the hard protein corona partially endures and shows fewer alterations at a biologically relevant timeframe. The mutability of the soft-protein corona complicates *in vitro* studies, as any manipulation steps leads to significant alterations. Instead, research has largely

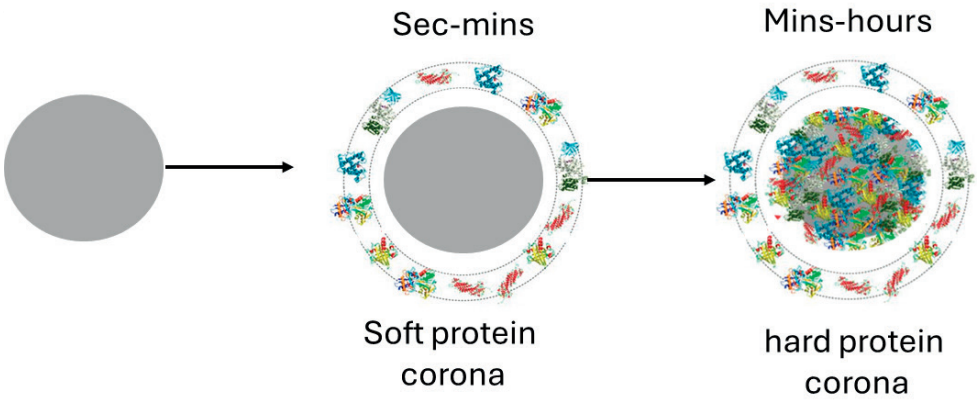

Fig. 3: overview of protein corona formation.
Adapted from (155)

The protein corona covers the entire surface of MNPs which shields cells from potential cell membrane destabilization due to the reactive MNP surface and the presence or absence affects cell membrane attachment of micro- and nanoparticles (156-158). Importantly, the composition of the protein corona can affect both cellular uptake of MNPs and toxicity. Many proteins are targets for cell surface receptors, and misfolded proteins within the protein corona can be recognized by scavenger receptors leading to phagocytosis and immune stimulation. Additionally, the binding of specific proteins, like digestive proteins, can interfere with their physiological functions leading for example to reduced lipid metabolism (159). Oral ingestion of MNPs appears the main vector of human exposure, making the protein corona formed during digestion most relevant to human toxicity, however little is known on the composition of the digestion-associated protein corona.

It has been recognized that the protein corona is more predictive of nanoparticle toxicity than the physiological properties of particles themselves, highlighting it's importance for the potential toxicity of MNPs (152, 160-164).

1.8 Toxicity of MNPs

1.8.1 Toxicity in animals

Given the population-wide exposure to MNPs, there is a large interest in establishing the risk MNPs pose to human health. Macroscopic plastic materials are generally designed to be biologically inert and many of the polymers used today including PU, PS, PVC, PP have been used for medical applications (165). However, as particles decrease in radius,

the total surface area increases linearly, and the particle number scales to the third power which can impart new material properties. For example, a single 1 mm microplastic has the potential to degrade into a trillion nanoplastics of 100 nm with a total surface of $3.15*10^4$ mm^2. It is well recognized that cellular interaction is largely driven by surface processes and the increase in surface area associated with miniaturization of materials bestows novel mechanisms of toxicity (166-170).

The toxic potential of MNPs was first established in aquatic animals due to their high environmental exposure and most MNP research to date focused on aquatic animals (171, 172). *In vivo* exposure of fish, crustaceans and mollusks to microplastics show that MNPs can induce neurotoxicity, metabolic disruption, immunotoxicity, reproductive toxicity, oxidative toxicity and genotoxicity (173-180). Similar results to those found in aquatic animals are reported in rodents, as several mouse studies have shown that oral exposure to high doses of polystyrene can lead to metabolic disorders, reproductive toxicity (181), behavioural alterations, gut microbiota dysbiosis (159, 182-184), hemotoxicity (185, 186), hepatotoxicity (187, 188). Most of these effects appear to be mediated through ROS formation and inflammation (189, 190). Additionally studies have reported that oral MNP exposure may lead to alterations of mucus secretion, loss of barrier integrity, and inflammation of the gastrointestinal tissues, as well as alterations in the gut microbiome composition (191). However, the concentrations used in rodent studies tend to be high and are often criticised for having unrealistic exposure settings and assessing endpoints with questionable human relevance. Rodent studies frequently have reported contradicting findings, showing no effect on gut microbiota (192), inflammation (193), behaviour (184, 194), hemotoxicity (186) and multiple studies with PS MNPs have reported no observed adverse effects (139, 195). The inconsistency of reported effects and absence of consensus on realistic MNP concentrations hinder the translation of *in vivo* rodent studies to humans.

1.8.2 Toxicity in humans

While the presence of MNPs has been reported in most human tissues including saliva (196), blood (14), breast milk (18), liver (197), kidney (197), placenta (17, 18, 198), lung (199), spleen (197) and brain (16), little is known on human toxicity of MNPs. Epidemiological studies showing a relation between pulmonary diseases and exposure to inhalable plastic particles by factory workers have been available for over 20 years, however it is uncertain if this relation holds true for the general population (200, 201). Recent studies have shown that the abundance of microplastics in stool correlated to inflammatory bowel disease (202) and that MNPs are present in cirrhotic liver tissue (197) and arterial thrombi isolated after acute embolism (203). While these findings indicate a potential role for MNPs in the etiology of inflammatory diseases and tissue damage, MNPs appear

to have a low acute toxicity and there is too little in *in vivo* data to conclude whether MNPs are toxic to humans.

In an attempt to fill these data-gaps using human relevant data, there has been a rapid rise in *in vitro* toxicity testing using human cell lines. Overt cytotoxicity of MNPs is low, although exposure to very high concentrations of MNPs may induce minor levels of cell death in lung cells (204), hepatocytes (205), intestinal enterocytes (206), fibroblasts (207) and hematopoietic cells (208). Knowledge on nanomaterial toxicity and *in vitro* studies on MNP toxicity, indicate that MNP toxicity likely is driven by two main processes: the stimulation of inflammatory responses and the generation of ROS.

Immune cells are susceptible to MNP toxicity as MNPs are actively phagocytosed by various immune cells including neutrophils, dendritic cells, macrophages and monocytes. Under normal physiology, immune cells maintain a balance of pro-inflammatory and anti-inflammatory states which promotes the elimination of xenobiotic entities, without inducing inflammatory tissue damage. Phagocytosis of charged MNPs appear have shown to influence the polarization of macrophages and dendritic cells either towards the pro-inflammatory M1 or anti-inflammatory M2 cells (209) and exposure to MNPs can induce the secretion of pro-inflammatory cytokines IL-1β IL-6, IL-8, TNF-α in both immune (210, 211) and epithelial cells (204, 212, 213). Together, the induction of inflammatory cytokines and alteration of cellular polarization may tilt the balance of pro-inflammatory and anti-inflammatory stimuli towards inflammation, which may contribute to tissue damage such as lung and liver fibrosis (197, 214, 215), loss of barrier integrity (216, 217) and chronic inflammatory.

The second toxicity pathway with a well-known role in the toxicity of nanoparticles is the generation of ROS. Non-polymeric nanoparticles can spontaneously generate oxygen radicals through chemical reactions at the surface. While microplastics themselves do not spontaneously form oxygen radicals, metal fillers or aggregation of metals on the MNP surface can lead to ROS generation (218). MNPs can additionally generate ROS through their interaction with cells and organelles. Multiple studies have shown that MNPs can bind and destabilize the mitochondrial membrane leading to dysregulation of cellular lipid and energy metabolism and the release of ROS-producing redox proteins (219, 220). Additionally, the aforementioned recognition and phagocytosis by macrophages stimulates the production of hydrogen peroxide radicals which can lead to oxidative damage. The generation of ROS and inflammation are both linked to the etiology of tissue damage, cell death and barrier permeability (221) and may synergistically contribute towards these endpoints.

In addition to the well-established effects of nanoparticles, an increasing number of studies have shown that MNPs may induce genotoxicity or reproductive toxicity (222). Some studies have shown internalization of MNPs in the nucleus of the cell and theorize a direct interaction between microplastics and the DNA. Indirect genetic damage through ROS, inflammation and genotoxicity may in theory cause MNPs to stimulate the formation of neoplasms (85). Although the genotoxicity of MNPs warrants attention, *in vitro* results are inconclusive and no epidemiological correlation between MNPs and carcinogenesis has been established (222, 223).

Overall, the *in vitro* and *in vivo* data show low to negligible toxicity at concentrations of <20 µg/ml and a potential role for MNPs in tissue damage, the onset of neoplasms, reproductive toxicity and inflammation, at concentrations of 50 - 1000 µg/ml.

1.9 New approach methodologies for MNP toxicity testing

As outlined above there is a near limitless diversity in MNP types which may differ in uptake and toxicity profiles. The sheer multitude of MNPs is too vast to allow for exhaustive *in vivo* toxicity testing (114), precluding conventional risk assessment. *In vitro* and *in silico* models show advantages over animal models in terms of ethical acceptance, throughput and mechanistic insight obtained. *In vitro* and *in silico* methods are collectively referred to as new approach methodologies (NAMs) and aim to predict human toxicity in an animal-free manner (224). The following sections outline NAMs which are frequently used for MNP research.

1.9.1 In vitro NAMs

The intestine is the portal to the bloodstream, and multiple *in vitro* models of the small intestine are available. The most commonly used *in vitro* models are based on the adenocarcinoma-derived Caco-2 cells. Caco-2 cells differentiate into cells with colon- and enterocyte- like features (225), which can be cultured on semi-permeable membranes to assess MNP transport through the intestinal layer. Caco-2 cells are frequently co-cultured with other intestinal cell lines or immune cell lines to increase physiological relevance. Caco-2 cells show a minimal secretion of mucus, and goblet-like HT29-MTX cells are often included in a 1:10 ratio, as HT29-MTX cells secrete a mucus layer on top of the cells. While there are no cell lines available for M-cells, it was found that the inclusion of Raji-B lymphocytes at the basolateral side causes Caco-2 cells to display an M-cell like phenotype with increased particle phagocytosis, the lack of microvilli and expression of M-cell markers (226). In addition to intestinal cell lines, immune cell lines are frequently utilized to assess the immunogenicity of particles. THP-1 cells are acute-leukemia derived monocytes which can be differentiated into macrophages through the addition of

phorbol 12-myristate 13-acetate (PMA). THP-1 cells have been utilized as monocultures to assess cytokine secretion, macrophage polarization and rate of phagocytosis upon MNP exposure. Co-cultures of Caco-2 and THP-1 have been established to model intestinal inflammatory processes, and the THP-1 derived macrophages can be driven towards a pro or anti-inflammatory state to mimic healthy or inflamed gut. Inverted versions of the models outlined above have also been generated to model transport and toxicity of buoyant MNPs like PE and PP.

While studies using cell line models greatly increased our understanding of MNP toxicity, their cancerous origin causes limitations when assessing MNP toxicity. Cancers typically show aberrant upregulation of glycolysis which is called the Warburg effect (227, 228). Cancerous cells also display an upregulation of cellular survival and reduced expression of toll-like receptors (TLR) required for immune activation. The lack of TLR expression, aberrant use of glycolysis and lack of responsiveness to inflammation have also been confirmed in cell lines like Caco-2 (229-232). The majority of MNP toxicity is inflammation and ROS mediated, thus the reduced applicability of cell lines for these endpoints casts doubts on the relevance of results.

As an alternative to cell line models, primary cells can directly be isolated from patient derived material and show optimal physiological relevance. Primary blood derived monocytes (PBMCs) are frequently used for the study of MNP toxicity and some studies have assessed the effects of MNPs on other primary cells like keratinocytes and astrocytes (233-235). Primary cells of intestinal cells cannot be kept in culture for long and the isolation of separate cell types often involves complicated isolation procedures which can be time-intensive and require consistent availability of patient material.

Instead, stem cell-derived intestinal cultures can be generated either from isolated adult intestinal stem cells or from commercially available induced-pluripotent stem cells (iPSCs). Stem cell-derived intestinal epithelial models typically contain more varied cell-types than cell-culture models and show a better expression of receptors involved in active transport and immune stimulation leading to an increased sensitivity for inflammation and better correlation of intestinal permeability with human data (236-240). While stem cell-derived intestinal models are rapidly being adopted for the prediction of transport and toxicity of chemicals, few studies have attempted to assess MNP toxicity. A detailed overview of the potential advantages and disadvantages of stem cell-derived models is given in chapter 2.

1.9.2 PBK models

In vitro data can be generated rapidly and can give insight in potential toxicity pathways, but it is non-trivial to link the dose used *in vitro* to the exposure *in vivo*. The prediction

of the exposure required to reach *in vitro* concentrations is called quantitative *in vitro* to *in vivo* extrapolation (QIVIVE) and typically requires physiologically based kinetic (PBK) models(241, 242). PBK models are mathematical representations of the human body, which rely on a set of species-specific physiological parameters and chemical-specific parameters to predict absorption, distribution, metabolism and elimination processes. Species-specific physiological parameters are well documented and can be used to guide interspecies extrapolation of *in vivo* concentrations in animals to humans. The chemical-specific parameters for small molecules are typically derived using quantitative structure activity relationships (QSARs)(241), however these are not available for MNPs. Instead, animal derived tissue concentrations are used as guidance to fit the MNP specific parameters so that it matches the data(243).

PBK models for nanomaterials have been developed for both oral and intravenous routes and recently, the first oral MNP PBK models were published (244, 245), demonstrating general applicability of PBK models for MNP distribution. Interspecies scaling has been demonstrated for gold nanoparticles (246, 247), but has not yet been demonstrated for MNPs. However, the reliance on empirical fitting to the *in vivo* data does not offer a mechanistic explanation of MNP transport in the body. The lack of mechanistic information makes it complicated to predict how particles with different properties distribute in the body and also complicate extrapolation to data-poor species like humans.

Despite an urgent need to validate the relevance of obtained *in vitro* results, currently, the lack of mechanistic processes in MNP PBK models hinders model extrapolations and QIVIVE for MNPs.

1.10 Outline of thesis

The field of MNP toxicity testing is rapidly evolving, but there are notable limitations to current testing strategies. Specifically, the focus on primary MNPs, the limited understanding of the protein corona and the lack of suitability of *in vitro* and *in silico* methods causes large data-gaps.

The aim of this thesis was to improve in vitro and in silico NAMs for MNP toxicity assessment and to improve understanding of the formation and effects of the protein corona on MNPs. To accomplish this, the studies presented here were designed to answer four research questions.

1. To assess the suitability of iPSC-derived intestinal models for *in vitro* MNP toxicity testing.
2. To delineate the role of the protein corona on MNPs to their cellular interaction.
3. To determine whether primary MNPs are representative of MNP toxicity as a whole.
4. To develop a mechanistic PBK model for predicting bioaccumulation after oral MNP exposure

In **Chapter 1** an introduction giving an overview of MNPs, important concepts in nanotoxicology and a list of in vitro and in silico methods is explained and discussed.

Chapter 2 presents a review of the literature that extends the discussion on *in vitro* models from chapter 1 by highlighting current intestinal models used in nanotoxicology testing and discussing the potential use of stem cell-derived *in vitro* models for MNP toxicity testing.

Chapter 3 describes the utilization and characterization of an iPSC-derived model of the intestinal epithelia. The presence of three major intestinal cell types; enterocytes, goblet cells and Paneth cells was confirmed based on immunostaining and RNA expression The intestinal epithelium was exposed to bacterial toxins and the inflammatory response and barrier disruption was compared to the Caco-2 model.

Chapter 4 describes the exposure of the iPSC-derived intestinal epithelia to secondary microplastics derived from plastic products. The barrier disruption, cytokine secretion and intracellular ROS of the IEC in response to product-derived PET-TiO_2, PP-Talc, PLA, PVC and PA microplastics was compared to the response to model PS microplastics. The serum-protein corona on all microplastics was characterized and correlated to the effects seen *in vitro*.

In **Chapter 5,** an *in vitro* digestion method was optimized for the use with MNPs and THP-1-derived macrophages, which were exposed to *in vitro* digested PS MNPs between 0.05 - 1 µm. The protein corona formed during *in vitro* intestinal digestion was characterized using mass spectrometry-based proteomics and compared to the protein corona in serum. Finally, the influence of the protein corona on PS uptake into macrophages was assessed using flow cytometry.

Chapter 6 describes the development of a size- and polymer-agnostic PBK model to predict organ concentrations in humans and mice after oral exposure to MNPs. The mechanistic PBK model was used to predict tissue concentrations in mice and humans spanning single exposure to lifelong exposure. The performance of the mechanistic PBK model was compared to an empirically fit PBK model in their ability to predict tissue concentrations after oral exposure to MNPs.

In **chapter 7**, a synthesis of all result obtained during the thesis is presented, including the main findings, their implications and recommendations for future studies.

CHAPTER 2

2

Investigating nanoplastics toxicity using advanced stem cell-based intestinal and lung in vitro models

Mathias Busch, Hugo Brouwer, Germaine Aalderink, Gerrit Bredeck, Angela A.M. Kämpfer, Roel P. F. Schins, Hans Bouwmeester

Based on Busch M, Brouwer H, Aalderink G, Bredeck G, Kämpfer AAM, Schins RPF, Bouwmeester H. Investigating nanoplastics toxicity using advanced stem cell-based intestinal and lung *in vitro* models. Front Toxicol. 2023

doi:10.3389/ftox.2023.1112212.

2.1 Abstract

Plastic particles in the nanometer range – called nanoplastics – are environmental contaminants with growing public health concern.. As plastic particles are present in water, soil, air and food, human exposure via intestine and lung is unavoidable, but possible health effects are still to be elucidated. To better understand the Mode of Action of plastic particles, it is key to use experimental models that best reflect human physiology. Novel assessment methods like advanced cell models and several alternative approaches are currently used and developed in the scientific community. So far, the use of cancer cell line-based models is the standard approach regarding *in vitro* nanotoxicology. However, among the many advantages of the use of cancer cell lines, there are also disadvantages that might favor other approaches. In this review, we compare cell line-based models with stem cell-based *in vitro* models of the human intestine and lung. In the context of nanoplastics research, we highlight the advantages that come with the use of stem cells. Further, the specific challenges of testing nanoplastics *in vitro* are discussed. Although the use of stem cell-based models can be demanding, we conclude that, depending on the research question, stem cells in combination with advanced exposure strategies might be a more suitable approach than cancer cell lines when it comes to toxicological investigation of nanoplastics.

2.2 Nanoplastics: Unknown health risks

Plastic polymers have become indispensable in our everyday life due to their favorable physicochemical properties and relatively low production costs. Annual plastics production has risen to 368 million tons in 2019 (https://plasticseurope.org) and 71% of the subsequent plastic waste ends up in aquatic or terrestrial environments (53, 248). This plastic waste is continually exposed to physical stress through abrasion or UV light and will inevitably fragment into microplastics (<5mm) and eventually nanoplastics (<100nm) (249). In addition to environment-derived micro- and nanoplastic particles, microplastics have also intentionally been included in consumer products and can subsequently fragment to the nanoscale size (250). Other direct sources of micro- and nanoplastics include the release of fibers from synthetic textiles (251) or abrasion of car tires (252).

Nanoplastics cannot easily be measured directly due to a lack of suitable analytical techniques (253), but are assumed to be present in household dust (254), particulate matter in outside air (255) and foodstuffs including salt (109), bivalves (256, 257), fish (258), honey (259) and water (109, 260). Humans are therefore exposed to nanoplastics by ingestion and inhalation and subsequent health outcomes are poorly understood. Studies on human exposure to microplastic particles show that annual intake may exceed hundred thousands of particles (80, 115), while data on nanoplastic exposure is not available yet. Societal concerns on the potential health effects of micro and nanoplastic exposure have been increasing, underpinning the need for risk assessment (261, 262).

Nanoplastics are not a homogeneous contaminant but represent a mixture of sheets, fragments and fibers of various sizes comprised mainly of polyethylene (PE), polypropylene (PP), polyethylene terephtalate (PET) and polyvinyl chloride (PVC) (https://plasticseurope.org, Karbalaei et al., 2018). This heterogeneity complicates risk assessment as past research has mostly focused on polystyrene (PS) nanospheres, which do not accurately represent the multitude of nanoplastics to which humans are exposed. Only few studies have considered alternative polymer types (40, 263-265) and even fewer studies have focused on non-spherical (211) or weathered particles (266, 267). Despite the lack of data on prototypical environmental nanoplastics, considerable effort has been made to implement read-across methodologies based on the particles' intrinsic properties, Mode of Action (MoA) or associated (bio)molecules, but these algorithms are not yet applicable to nanoplastics risk assessment (161-163).

There is limited information available on nanoplastics toxicity *in vivo* and much of our current knowledge stems from rodent studies using microplastics. These studies need to be interpreted with caution, as some of these studies have been scrutinized because of issues related to particle characterization, (overload) exposure, detection of particles

in tissues (mass balance) and methodological issues related to histopathology (262, 269). Rodent studies using high concentrations of PS nanoplastics report bioavailability after ingestion or inhalation and particle translocation to lymph nodes, liver, spleen, and kidneys (270, 271). More data on plastic particle toxicity is available in the context of occupational exposure with polymers (272-274). However, this information holds limited applicability to environmental nanoplastics exposure, as these studies were conducted to simulate high lung exposure concentrations in plastic industry workers (275-277), which is hardly comparable to the current levels of airborne plastic particles in a non-occupational environment.

Besides the direct toxicity of nanoplastics, the potential toxicity of associated chemicals and components of the eco-corona should also be considered. Nanoplastics frequently contain additives, e.g. phthalates, which may comprise up to 50% of the total mass of plastics (278, 279) and often contain known toxicants like dioxins, polycyclic aromatic hydrocarbons, halogenated flame retardants and heavy metals (63, 75, 280), which could be released from the polymers after uptake (281). Furthermore, the surface of particles spontaneously adsorbs surrounding chemicals and biomolecules, leading to an eco-corona, or bio-corona, respectively (282, 283).

The plethora of possible polymers, shapes, sizes and exposure scenarios make exhaustive testing of nanoplastics a daunting task that is ethically, financially and temporally unfeasible using animal models. The acceptance of data generated in *in vitro* models for regulatory purposes is being spurred by the ban on animal testing in the cosmetics industry (284) and nanotoxicity testing will also have to rely on data generated *in vitro* (285). Initiated by "toxicology of the 21st century" (286), and to better explain MoAs, models that emulate human physiology best, should be put forward. This is boosting the development of *in vitro* models ultimately replacing animal based testing (287). Currently, the main models used for *in vitro* oral or inhalation nanotoxicity testing are based on immortalized cell lines derived from cancer tissue, including Caco-2 for the intestine or A549 for the lung (285, 288-290). In addition to these conventional models, novel models including stem cell-based approaches have recently started being used in nanotoxicity testing. These novel methods offer advantages over cancer cell lines by having an unaltered genotype, allowing the presence of more physiologically relevant cell types and may help estimate interindividual variation. In this review we discuss novel stem cell-based *in vitro* models of the primarily exposed organs, intestine and lung, as a new approach methodology for nanoplastics toxicity testing and how the resulting data can be used to guide future risk assessment.

2.3 Selection of *in vitro* models to study the toxicity of nanoplastics

Based on the knowledge on microplastics and engineered nanomaterials, nanoplastics mainly enter the human body through ingestion or inhalation. Therefore, these barriers are initially most at risk and studying potential toxic effects *in vitro* requires physiologically relevant models of the intestine and lung, respectively. While cell line-based models have been extensively used in toxicological research, these models lack essential features, as discussed below.

Establishing advanced barrier models requires an actively dividing and tissue-specific cell source, for example fully differentiated primary cells or somatic stem cells that can be directly isolated from the human body, often obtained from biopsies. However, the replicating ability of differentiated primary cells is limited, as differentiation generally occurs after exiting the cell cycle (291). Recently, commercially available constructs based on primary human tissue of the intestine or lung, have become available and applied for toxicological studies (292, 293). These constructs are generated from human donors and are directly provided to the user for one-time experimental application. Although these primary models are highly relevant in terms of physiology, the user is dependent on donor availability and unobstructed delivery, as these models cannot be permanently established in a laboratory independently from the commercial provider.

In contrast to already differentiated primary tissue and cells, somatic stem cells are undifferentiated cells that divide to replenish dying cells under physiological conditions (294). These somatic stem cells, also called adult stem cells (ASCs), remain dormant until surrounding factors activate them to divide and terminally differentiate into functional cells (295). ASCs are multipotent, meaning that they can develop into more than one cell type, but they cannot produce all cell types of the body, as is the case for pluripotent cell types (296, 297). Despite improvements in long-term culture expansion of ASCs, their lifespan appears limited and inversely correlated to the donors age and highly affected by the extraction site (298, 299). Overall, the limited availability of biopsy material in combination with the finite dividing capacity of both primary cells and ASCs make them less suited to be used in toxicological studies. However, their use has greatly advanced the field of patient-specific disease modeling, i.e. cancer research and drug screening (300, 301).

Embryonic stem cells (ESCs) and induced pluripotent stem cells (iPSC), on the other hand, have gained increasing interest as a source of stem cells due to their ability to differentiate into all cell types of the organism and their high proliferative capacity (302). Human ESCs are pluripotent stem cells generally derived from the inner cell mass of blastocysts (303). The required number of embryos used to generate the resulting ESC lines have

only been reported in a small number of cases (304), hinting at a low success rate, which in combination with the destructive process on the blastocyst have led to an extensive ethical debate on the use of human material (305, 306). Conversely, iPSCs do not rely on the use of embryos or invasive biopsies, forming a more ethical source of pluripotent cells. iPSCs are somatic cells (e.g. fibroblasts) reprogrammed into a pluripotent state through the forced overexpression of the four transcription factors *OCT4*, *SOX2*, *KLF4* and *MYC* (307). From their pluripotent state, iPSCs have been successfully differentiated to obtain tissue-specific morphology and gene expression for various organs, including the intestine (308) and lung (309). Embryonic-like cells derived from iPSC differentiation can be used to study a wide variety of organs and exposure scenarios, due to their proliferative capacity and the wide spectrum of available differentiation protocols (310). The differentiation of iPSCs into mature models of human organs usually requires multiple sequential steps in which cells are exposed to different growth factors mimicking the *in vivo* cell environment during mammalian embryonic development (311, 312). As a result, the differentiation of iPSCs leads to models with a better representation of different tissue-specific cell types encountered *in vivo* (313), in contrast to cancer lines which only represent one dominant cell type.

Particle toxicity is often evaluated based on the range of reversible and irreversible cellular damage in addition to the cells' ability to overcome these effects, as well as signaling cascades involved in processes like proliferation and inflammation. As cancer cell lines underwent genetic changes to ensure continuous proliferation in a tumor microenvironment despite challenging metabolic conditions (314, 315), this could potentially lead to a skewed view on the toxicity-induced effects of nanoplastics on tissue. By contrast, stem cell-derived tissue-like cells maintain physiological proliferative behavior to provide a more representative view for toxicity-induced injury compared to cancer cell lines, while simultaneously providing multiple cell types in the same *in vitro* model. Thus, we view iPSC as a promising approach for quantitative nanoplastics toxicity testing with high physiological relevance in the primarily exposed organs intestine and lung.

2.4 Intestinal models

The intestine is a major part of the human digestive system, responsible for the peristalsis of chyme and the uptake of nutrients from ingested food. Accordingly, the intestinal epithelium is constantly exposed to contaminants taken up with food and water, making it an important target organ for toxicities and diseases. Therefore, research in the fields of medicine, pharmacology and toxicology has been focused on the development of suitable models to study effects on the intestine outside of animals.

To date, several studies report intestinal effects of ingested micro- and nanoplastics in a variety of *in vitro* models based on cancer cell lines. Among the available cell lines, the colorectal cancer cell line Caco-2 is by far the most utilized one (316-318), as it spontaneously differentiates into an enterocyte-like phenotype (319), representing the most abundant cell type in the human intestine. However, several attempts have been made to increase the complexity of Caco-2 based *in vitro* models by implementing additional cell lines when investigating plastic particles (see Table 1). For example, an advanced intestinal model included HT29-MTX-E12 as goblet cells and PMA-differentiated THP-1 cells as macrophages to expand the model by the presence of mucus and an immunocompetent cell type (212). Furthermore, a Caco-2/HT29 model supplemented with Raji-B cells to induce the differentiation into microfold cells (M-cells), a cell type specialized in transport across the epithelial barrier (320), was used to investigate the effects of PS nanoplastics (321). Establishing even higher levels of complexity, a quadruple culture model was used to study plastic particle effects by complementing a Caco-2/HT29-MTX co-culture with macrophages and dendritic cells derived from human blood monocytes (322). However, the co-culturing of different cancer cell lines and/or primary cells requires extensive fine-tuning of optimal culture conditions, e.g. in terms of medium composition, whereas different cell populations in cultures derived from stem cells originate from the same single cell source.

A breakthrough toward human cell-based models with advanced physiological relevance was seen through the establishment of crypt-based intestinal organoids, enabling the long-term culture of primary intestinal cells in absence of mesenchymal tissue (323, 324). Since then, research interest in stem cells has increased dramatically, resulting in the generation of numerous culture and differentiation protocols (312, 325-330), establishing two principal approaches for the generation of self-organized intestinal spheroids: (1) isolation of intestinal crypts and (2) use of ESCs or iPSCs.

Uniquely, these spheroids represent all major epithelial cell lineages within the organoid (324), and allow to skew them towards specific cell types and rare lineages like tuft cells (331-333). Even the most sophisticated non-stem cell models still fail to replicate the lineage complexity to this extent (322, 334, 335). For the purpose of hazard testing of nanoplastics, both overall effects on the tissue as well as effects in specific individual cell types may be relevant. Using organoids, cell type-specific uptake efficiencies were demonstrated for nanoplastics (336). The authors generated intestinal organoids from an iPSC line and reported the presence of enterocytes, Paneth cells, goblet cells and endocrine cells using immunofluorescence. Uptake of 50 nm PS nanoplastics was found to be cell type-dependent, which may have been overlooked or drastically underestimated in standard culture systems, as the authors report uptake primarily in goblet, Paneth and

endocrine cells. Furthermore, some cell types may be more sensitive towards stressors or noxae (337), and might, therefore, represent important targets for exposure studies.

Also their (patho)physiological identity renders intestinal stem cell models a highly versatile tool. The cultures can replicate the complexity of various regions of the intestinal tract – from duodenum to colon – as well as healthy or diseased tissue depending on the biopsy origin or growth/differentiation protocol (324, 338, 339). In contrast, standard cell models mostly rely on cancer-derived cell lines in mono- or co-culture that often require extensive differentiation times and further manipulation to obtain rather mature cell types (340, 341) and disease-like phenotypes (342, 343). Inherently diseased, these cell lines may be of limited physiological relevance for specific research questions due to biochemical and genetic differences compared to healthy intestinal tissue, e.g. the absence or limited presence of phosphoprotein p53 (344) and cytochrome (CYP) P450 isoforms (345). While typically considered in the context of drug metabolization (346), CYP enzymes also play a role in the effects of xenobiotics, e.g. organic pollutants (347, 348), which may be critical contaminants to consider in plastic particle hazard assessment (349, 350).

It is important to also realize potential differences between stem cell-based intestinal organoids and the *in vivo* situation, for example the limited presence of mucus, although refined protocols are being developed (351, 352). Whereas human organoids express physiologically relevant types of mucins – especially mucin 2 (324) – the overall luminal coverage and thickness of the mucus remains low (353). In the context of particle hazard assessment, mucus is a crucial determinant for the dose of nanoparticles that can interact with the epithelium (338).

However, stem cell-derived intestinal cultures remain scarcely used for nanoplastics hazard assessment (354, 355) with only three studies on plastic particles to date (336, 356, 357), of which two studies failed to report the differentiation procedure and/or sufficiently characterize the organoids. Even with sufficient characterization, treatment of organoids with particles is a challenge, as the organoids' morphology – the inward-facing apical side creating a lumen – and their maintenance in semi-solid media (e.g. Matrigel) impede particle exposures. Exposures would typically occur from the apical side, which is not accessible without manipulation, while diffusion of particles is obstructed in matrices like Matrigel. Various adaptions might resolve these challenges, including luminal microinjection or application of flow-through after puncturing the organoid (358, 359), reversed cell polarization (i.e. "apical-out" organoids) (360) or breaking the organoids' 3D structure down to a 2D structure. Especially the latter is applied frequently, either using the whole organoid (361-365) or selected cell types (366, 367). While the structural change from 3D to 2D did not substantially modify the expression of intestinal markers

or functional genes (368), these organoid-derived cell layers can develop a high transepithelial electrical resistance (TEER>1500 Ω•cm^2) (369), which might indicate restricted passive transport across the cell layer and may limit the transport of nanoplastics. In contrast to manipulating mature organoids back into 2D layers, other protocols are designed to differentiate iPSCs directly into intestinal epithelial monolayers, without the detour of spheroid generation (370, 371), resulting in more realistic TEER values of ~250 Ω•cm^2 (372). Besides 2D culturing, adaptions creating accessible luminal space or using perfusion in tubular intestinal structures are becoming increasingly sophisticated (373-375) and offer promising alternative test systems.

Table 1. Human intestinal in vitro models used for plastic particle toxicity assessment

Model type		Represented tissue or cell types	Reference
Cell lines, monoculture	Caco-2	**Intestinal epithelium (undifferentiated Caco-2) or Enterocytes (differentiated Caco-2)**	Liu, Wu (120), Abdelkhaliq, van der Zande (149), Stock, Bohmert (206), Cortés, Domenech (316), Domenech, Cortés (317), Stock, Laurisch (318), Schimpel, Teubl (376), Walczak, Kramer (377), Inkielewicz-Stepniak, Tajber (378), Wu, Wu (379), Wu, Wu (380), Huang, Yin (381), Jeon, Lee (382), Xu, Feng (383), Ma, Koh (384), Steckiewicz, Adamska (385)
	HT29	**Intestinal epithelium**	Inkielewicz-Stepniak, Tajber (378), Xu, Feng (383), Steckiewicz, Adamska (385), Visalli, Facciolà (386)
	LS174T	**Intestinal epithelium**	Inkielewicz-Stepniak, Tajber (378)
	CCD 841 CoN	**Intestinal epithelium**	Steckiewicz, Adamska (385)
	NCM 460	**Intestinal epithelium**	Ma, Koh (384)
	RKO	**Intestinal epithelium**	Xu, Feng (383)
	HIEC-6	**Intestinal epithelium**	Xu, Feng (383)
	HCT-116	**Intestinal epithelium**	Xu, Feng (383)
Cell lines, co-culture	Caco-2+HT29(MTX)	**Enterocytes and goblet cells**	Walczak, Kramer (150), Domenech, Hernandez (321), Schimpel, Teubl (376), Walczak, Kramer (377), Mahler, Esch (387), Fournier, Leveque (388)
	Caco-2+Raji-B (M-cell model)	**Enterocytes and microfold cells**	Schimpel, Teubl (376)
Cell lines, triple culture	Caco-2+HT29-MTX-E12+THP-1	**Enterocytes, goblet cells and macrophages**	Busch, Bredeck (212), Busch, Kämpfer (263)
	Caco-2+HT29+Raji-B (M-cell model)	**Enterocytes, goblet cells and microfold cells**	Domenech, Hernandez (321), Schimpel, Teubl (376), Walczak, Kramer (377), Mahler, Esch (387)
Cell lines, quadruple culture	Caco-2+HT29-MTX+MDDC[1]+MDM[2]	**Enterocytes, goblet cells, dendiric cells and macrophages**	Lehner, Wohlleben (322)

Table 1. continued

Model type		Represented tissue or cell types	Reference
Organoid based	Human iPSC-derived intestinal organoids	**Enterocytes, Paneth cells, enteroendocrine cells and goblet cells**	Hou, Meng (336)
	Human iPSC-derived colon organoids	**Not reported**	Park, Jung (356)
	Murine primary tissue-derived intestinal organoids	**Not reported**	Xie, Zhang (357)

[1] MDDC: monocyte-derived dendritic cells [2] MDM: monocyte-derived macrophages

2.5 Lung models

For inhaled particles, the lung epithelium forms an initial barrier and target site of interaction. Accordingly, *in vitro* testing of particulates for lung toxicity has long used cancer or immortalized epithelial cell lines (389). While being less robust and reproducible, particles have also been tested on primary epithelial cells or tissue explant cultures from lungs of rodent or human origin (390-393). The introduction of stem cell-based *in vitro* models and further advancement of associated tissue engineering methodologies in pulmonary research has contributed to an improved understanding of mechanisms of lung development, damage repair and tissue regeneration processes (394, 395). However, the use of stem cell-based models for lung toxicity testing is still in its infancy compared to, for example, developmental neurotoxicity testing (396, 397).

In sharp contrast, the specific field of particle toxicology has witnessed crucial progress through the development of improved *in vitro* assays that employ lung epithelial cell models in air liquid interface (ALI) culture conditions (398-400). Combined with aerosol generating devices, this allows for a more realistic interaction between the test particles and the surfactant-containing apical side of the epithelial cells, in contrast to models in which cells are exposed to particle suspensions under submerged conditions (401). Another innovative *in vitro* approach involves the growing of lung epithelial cells on mechanically stretchable membranes to enable testing of particles under breathing movement mimicking conditions (402).

To date, the pulmonary toxicity of micro- or nano-sized plastics has been tested in various *in vitro* models and aforementioned specific experimental approaches. Most investigators have either used the A549 human alveolar type II-like epithelial cell line or the BEAS-2B human bronchial epithelial cell line under conventional submerged testing conditions (See Table 2). The toxicity of PS nanoplastics has been investigated in suspension on BEAS-2B cells as well as HPAEpiC human pulmonary alveolar epithelial cells, comprised of type I and type II cells (403). A microfluidic-chip test model with BEAS-2B cells was employed by Gupta, Vallabani (404) to study uptake of silica particles and PS. Furthermore, A549 cells were exposed on a membrane under cyclic stretch conditions to PS nanoparticles in order to mimic the effect of breathing movements (405). Airway and alveolar epithelial toxicity has also been explored in ALI exposure settings. For example, the uptake and inflammatory properties of various PS particles were investigated in A549 cells, as well as in the Calu-3 human upper airway cell line under ALI exposure conditions (406). To account for the potential contribution of alveolar macrophages, the authors also included a co-culture model of A549 and THP-1 cells (406). To the best of our knowledge, to date only one study investigating plastics has been performed using a lung organoid-based testing approach. The toxicity of polyester fibers sampled from cloth dryers was investigated in human airway organoids that were generated from tissue resident ASCs obtained from

three donors (407). Using immunofluorescence and qRT-PCR based markers, basal cells, ciliated cells, goblet cells, club cells, and even type I cells were identified. Interestingly, the authors exposed the organoid spheres after fragmentation to allow exposure to the fibers from the outside as well as the more relevant "inner cavities" of the organoids. While the outcomes of this study may be of limited relevance in view of the dimensions of the tested materials (average length: 700 ± 400 µm and average width 10 ± 5 µm), the work provides strong proof of principle for the use of lung organoids for hazard assessment of airborne nanoplastics.

Similar to the intestine, a further introduction and application of stem cell-based models for pulmonary toxicity testing of nanoplastics seems promising. Herein, however, the principal advantage of exposing such models under ALI-conditions is to be emphasized in terms of dose and kinetics. Construction of complex organoid (e.g. scaffold) models, in such a way they that can be coupled to ALI exposure systems in a realistic, physiologically relevant manner, is a major challenge. If achieved, however, it will greatly contribute to improved safety evaluation of airborne nanoplastics.

Table 2. Human lung in vitro models used for plastic particle toxicity assessment

	Airway model	Represented tissue or cell types		Alveolar model	Represented tissue or cell types	
Cell lines, submerged	BEAS-2B	**Bronchial epithelium**	Yang, Cheng (403), Gupta, Vallabani (404), Lim, Ng (408), Dong, Chen (409), Lin, Zhang (410), Zhang, Yang (411)	A549	**Alveolar type II epithelial cells**	Brown, Wilson (412), Jeon, Clavadetscher (413), Xu, Halimu (414), Zhu, Jia (415), Goodman, Hare (416), Shi, Tang (417), Bengalli, Zerboni (418), Florance, Chandrasekaran (419), Gautam, Jo (420), Halimu, Zhang (421), Shi, Wang (422), Zhang, Zhang (423), Zhang, Wang (424), da Silva Brito, Singer (425)
				HPAEpiC	**Alveolar type I and II epithelial cells**	Yang, Cheng (403), Zhang, Yang (411)
Cell lines, submerged advanced	BEAS-2B in microfluidic-chip	**Bronchial epithelium**	Gupta, Vallabani (404)	A549 on membrane under cyclic stretches	**Alveolar type II epithelial cells**	Roshanzadeh, Park (405)
Cell lines, ALI exposed	Calu-3	**Bronchial epithelium**	Meindl, Öhlinger (406)	A549	**Alveolar type II epithelial cells**	Meindl, Öhlinger (406), Binder, Cao (426)
				A549+THP-1	**Alveolar type II epithelial cells and macrophages**	Meindl, Öhlinger (406)
Organoid based	Human ASC-derived airway organoid	**Basal cells, ciliated cells, goblet cells, alveolar type I cells and club cells**	Winkler, Cherubini (407)			

2.6 Challenges and considerations when testing plastic particles *in vitro*

When studying the MoA of nanoplastics in an *in vitro* model, certain points should be carefully considered when designing the experiment, choosing relevant endpoints, or interpreting the data in regard to plastics hazard assessment:

Low density of polymers. Industrially produced plastics cover a whole spectrum of different densities, spanning from less than 1 g/cm^3 (PP, PE), to around 1 g/cm^3 (PS), to heavier polymers (PVC, polyamide (PA), PET). The density of cell culture medium is approximately 1 g/cm^3, meaning that nanoplastics will either float or sediment during *in vitro* experiments, depending on their polymer composition. Polymers with a density lower than 1 g/cm^3 will become buoyant when applied in a traditional cell culture system and will not establish contact with cells growing on the bottom of a well plate. So far, several approaches have been used to tackle this issue: one common approach is the inversion of the cell model, e.g. by seeding cells on cover slips that are subsequently inverted and exposed to buoyant particles from below (427), or by sealing a well plate with silicone gaskets and then inverting the entire plate (428). Furthermore, it has been reported that inverted *in vitro* models can be established by seeding cells on the basolateral side of transwell inserts (318), which also enables the application of more complex co-culture models (263). Another approach to expose cells to buoyant plastic particles could be the use of ALI systems (429). The absence of medium on the apical side of cells allows exposure to particles via particle-containing aerosols that sediment on the cell layers, regardless of the particles' density. Although this approach has been used in an advanced *in vitro* model of the intestine (322), exposure via aerosols is obviously more relevant for *in vitro* models representing the lung. A very specific approach to solve the buoyancy problem was introduced by Green, Fisher (430). The authors embedded buoyant PE particles in the surface layer of agarose and seeded primary macrophages on top. However, due to the immobility of particles, this approach is only useful for phagocytizing cell models and not applicable for models of the intestinal or lung epithelium. A completely different approach to test buoyant polymers *in vitro* is the modification of the material to become denser. For example, mineral talc is a commonly used filler for PP to increase the materials' performance (431), which also increases the density of PP.

Differences in applied dose and effective dose. Apart from buoyant polymers, the low density of non-buoyant plastic particles needs to be considered as well. Polymers like PS are only marginally denser than cell culture medium and therefore exhibit very slow sedimentation rates. The amount of particles interacting with the cells (effective or delivered dose) is often small compared to the total amount of particles added to the *in vitro* system (applied dose). This may be further aggravated by particle agglomeration in the cell culture medium, which further decreases the density of the agglomerate (432).

Therefore, considerations of sedimentation kinetics for *in vitro* nanotoxicology research is important to avoid misinterpretation of concentration-dependent cellular response and uptake data (433). *In silico* dosimetry models have been developed to predict the delivered dose based on the physicochemical properties of the particles and the setup of the *in vitro* exposure scenario. Currently, three main tools are used to estimate the delivered dose during *in vitro* experiments; the *In vitro* Sedimentation, Diffusion and Dosimetry model (ISDD), the *In vitro* Sedimentation, Diffusion, Dissolution and Dosimetry model (ISD3) and the Distorted Grid model (DG) (432, 434, 435). In most cases, the ISDD model is sufficient for predicting nanoplastics dosimetry. However, ISD3 and SG are better suited for modelling buoyant particles such as PE or PP, as well as polydisperse or degradable materials (428). As an example for a severe discrepancy between the applied dose and the effective dose that interacts with cells, ISDD sedimentation modelling of 50 nm PS nanoparticles showed only 17 % deposition after 24 h at relevant *in vitro* conditions (212). Contrastingly, heavier, metal-based engineered nanomaterials like silver nanoparticles of comparable size can sediment completely within 4 h under certain conditions (436). Cell culture models grown under dynamic flow conditions to improve differentiation (437) or implemented in microfluidic chips (438, 439) might improve the distribution of nanoplastics, increasing the correspondence between the applied and delivered dose. However, *in silico* dosimetry models are not yet equipped to predict nanoparticle sedimentation under dynamic flow conditions.

Adherence of macromolecules. Particles suspended in biological media like cell culture medium will acquire a biomolecular corona, i.e. proteins, lipids or carbohydrates, that adhere to the particles' surface (440). As the adherence of these macromolecules will change the surface properties of the particles and therefore their interaction with biological systems (441, 442), the possible role of the corona has to be considered during *in vitro* testing (443). For example, Abdelkhaliq, van der Zande (149) analyzed the protein corona on different PS nanoplastics via LC-MS/MS and reported differences based on the surface modification of the particles, which in turn impacted the uptake rates of the nanoplastics.

A physiologically relevant exposure should include the history of the particles, for example a simulated gastrointestinal digestion, or incubation in lung fluids. During *in vitro* experiments, nanoplastics are commonly applied in cell culture medium containing fetal calf serum (FCS), leading to adherence of serum proteins to the nanoplastic surface (149). Contrastingly, the corona of ingested nanoplastics will more likely consist of macromolecules from the food matrix and digestive fluids, while inhaled nanoplastics will exhibit a corona that may be acquired from exogenous environmental matrices (e.g. microbial components, semivolatile organic compounds) and the obvious endogenous molecules present in lung surfactant (444, 445).

Interference with test assays and readouts. Besides changing and defining the surface identity, the adsorption of macromolecules, in particular target proteins of interest, to the surface of plastic particles, might distort the outcome of applied *in vitro* assays. Binding of extracellular lactate dehydrogenase (LDH), a common marker of membrane damage, might reduce the enzymes activity during the LDH assay, as it was reported for silver nanoparticles (446, 447). Moreover, interference of amine-modified PS with the interleukin (IL)-8 ELISA was observed in the form of exaggerated IL-8 concentrations (211). Therefore, assessing potential interferences of the tested materials with the used assays is necessary prior to toxicological investigations (448-450).

Use of fluorescently labeled nanoplastics. Often, it is important to know to what degree particles are internalized by target cells. In contrast to metal-based nanoparticles, where techniques like ICP-MS can be used to measure the cellular uptake of unlabeled particles (451), no equivalent techniques are currently available for polymeric particles. Instead, fluorescently labeled nanoplastics are commonly used to monitor the potency of cellular uptake, which can be quantified using confocal microscopy or flow cytometry. The use of fluorescent labels, while seemingly simple, require great care to avoid artifacts during the measurements. For instance, it is reported that fluorophores may leach out of the plastic particles, causing higher fluorescent signals in cells, or fluorescence in cell compartments not commonly available to nanoplastics (452, 453). Additionally, fluorophores might be pH-sensitive, leading to alterations in signal strength in subcellular compartments like lysosomes (454), complicating interpretation of data. Another issue of using fluorescent particles is the inability to distinguish between internalization and surface adhesion of particles. Flow cytometry is commonly used to assess particle internalization, as it offers higher throughput than confocal microscopy and is more easily quantifiable. However, flow cytometry is unable to distinguish between fluorescence originating from within cells or from cell surfaces, necessitating further experiments to confirm actual internalization. This can be achieved by using dyes that are specifically quenched at the cell surface (455, 456), by validating and correcting flow cytometry with confocal microscopy data (457), or by using a modified setup such as imaging flow cytometry (458, 459). Issues surrounding the use of fluorescence to determine nanoparticle internalization have received increased scientific interest and have been discussed in great detail in a recent review (460).

Size limitations depending on the exposed organ. Unlike engineered nanomaterials, environmental plastic particles do not have a clear size cutoff, covering a whole size spectrum from sub-nano size to several millimeters. In the case of ingested particles, size limitations only play a minor role, as even centimeter-sized plastics can be swallowed and are able to pass the human gastrointestinal tract. Therefore, the intestinal epithelium can, in theory, be exposed to particles of enormous size, justifying the testing of larger particles.

For example, Lehner, Wohlleben (322) applied microplastics up to 500 µm in an intestinal *in vitro* model. In contrast, however, the size of inhaled particles is strictly limited in the context of lung anatomy and physiology. Particles with an aerodynamic diameter of less than 10 µm are able to deposit in the tracheobronchial region, while only particles less than approximately 2.5 µm are small enough to reach the alveoli (461, 462). Therefore, when testing plastic particles in an *in vitro* model of the human respiratory system, the size of the test material has to be chosen accordingly.

Relevance of available model particles. When looking at available scientific literature regarding toxicological investigations of plastic particles, the majority of studies is carried out using spherical PS particles of a defined size. However, there is a strong discrepancy between available data and environmental occurrence: PS makes up only 6.1 % of globally produced polymers (www.plasticseurope.org) and shapes of micro- and nanoplastics have been described to be primarily fibers, fragments, and sheets (463). Furthermore, plastic particles in the environment cover a whole size spectrum that might exhibit synergistic effects during co-exposure of differently sized particles (464). While PS spheres are widely commercially available, particles of other polymers or shapes are very limited. Currently, research groups mostly rely on producing their own model plastics via methods like laser ablation, cryocutting or milling (40, 211, 465), which result in much more relevant polymer types, shapes and size distributions, but might limit the comparability between different studies. The urgent need for standardized, widely available reference particles of relevant polymers, sizes and shapes has already been repeatedly expressed in recent reviews (349, 466, 467).

Chemicals in nanoplastic samples. Commercial nanoplastic suspensions are often used as model particles for the hazard assessment of plastic particles in toxicological studies. These suspensions might contain additives like preservatives, antimicrobials or surfactants, which may cause artifacts in toxicity tests. For example, the preservative sodium azide that was present in a commercial PS suspension was found to be the cause of acute toxicity towards *Daphnia magna*, instead of the PS particles themselves (468). Furthermore, nanoplastics produced from bulk plastic and/or plastic products might contain additives and unpolymerized monomers, like bisphenol A, heavy metals or styrene (469-471). These chemicals might be released from the nanoplastics during incubation in the *in vitro* culture medium or in the cells that have taken up the plastic particles (281). To prevent incorrect interpretation of nanoplastics *in vitro* data and to distinguish between actual particle effects and effects stemming from associated chemicals, it is recommended to include a filtrate control in experiments (472).

2.7 Conclusions and future outlook

Currently developed (advanced) *in vitro* models, due to their increased physiological relevance for human hazard assessment and suitability for in-depth MoA studies, are well positioned for contributing to solve the complex issues surrounding nanotoxicity. Different *in vitro* models are suited to tackle different challenges and depending on the research question, stem cell-based models might be a suitable approach for the investigation of nanoplastics uptake and effects in the primarily exposed organs intestine and lung, as they offer specific advantages over traditional immortalized cell lines.

Common knowledge derived from *in vitro* models includes the prediction of absorption rates, the derivation of MoAs and the estimation of potency by relating *in vitro* endpoints to *in vivo* endpoints (473). The derivation of MoAs highly depends on the physiological relevance of the model and partly on the cell types present. Conventional cell models benefit from a high relative robustness compared to stem cell models and are comparatively easy to culture, which may lead to a higher interlaboratory comparability and more accurate estimation of the benchmark dose (474) when comparing different nanoparticles. This is especially true when comparing results found in different stem cell-based models, where a lack of consistency could imaginably complicate risk assessment. However, in the case of cellular processes altered due to the disease status of cancer cell lines, including genotoxicity, proliferation and cytokine production/response (475), iPSCs may be more relevant to study the real world situation. Similarly, when considering omics-based MoA screening approaches, the multitude of mutations commonly seen in cancer cell lines (476) can alter RNA or protein expression and can mask the true effect of many small molecule compounds (477) and potentially also nanoplastics. Especially when using approaches such as systems toxicology (478), small alterations in e.g. transcriptomics might help identifying important early signaling events at low exposure concentrations that might only lead to detectable toxicity at prolonged or repeated exposure. Furthermore, while the lack of robustness of stem cell-based models can be seen as a demerit, these models do allow for the estimation of relative sensitivity of subpopulations of cells or individuals with a particular genetic background. Such information can be especially relevant for risk assessment as this reduces the need for potentially inaccurate scaling factors. While *in vivo* studies are commonly used to derive the lower confidence limit of the benchmark dose (BMDL) and organ concentrations, special care must be taken when interpreting these results. The saying "mice are not men" (479) especially holds true regarding nanoparticles where differences in physical barriers including the amount of Peyers patches and M-cells, as well as the structure of the mucus layer in intestine and lung can cause further discrepancies between the human and animal situation (480-482).

While the methodologies to scale *in vitro* nanoparticle toxicokinetics to *in vivo* kinetics are in the explorative phase, they are the only conceivable, consistent source of human toxicokinetic data. When considering *in vitro* models for the possibility of extrapolation from *in vitro* to *in vivo* (i.e. quantitative *in vitro* to *in vivo* extrapolations or QIVIVE), stem cell-based models seem to be favored as these consist of non-diseased tissue made up of the relevant cell types found *in vivo*. In view of replacing animal experiments, efforts have already been made to apply physiologically based kinetic (PBK) models to nanomaterials in order to extrapolate *in vitro* uptake data to the *in vivo* situation (483). Although the acceptance of PBK model data in a regulatory context is still limited (484), using input data from physiologically relevant stem cell-based *in vitro* models might facilitate the development in this direction.

The identification of key events leading to adverse health outcomes and subsequent implementation in an adverse-outcome-pathway (AOP) frame is currently explored for nanomaterials. These AOPs, and associated key events, might aid in selecting relevant *in vitro* assays. It is expected that commonly used *in vitro* assays can be used, however some emphasis to typical "nano"-related endpoints are foreseen, such as cellular uptake, membrane damage, ROS generation or release of pro-inflammatory cytokines (485). However, the molecular initiating events (MIE) of nanoparticles leading to toxicity are often unspecific, in direct contrast to the MIE of a chemical that binds to a receptor or target molecule (486). Therefore, translation of *in vitro* effects to the *in vivo* situation in the case of nanomaterials including nanoplastics still requires extensive development, but will greatly benefit from *in vitro* models that closely mimic the *in vivo* situation, such as the stem cell-based models discussed in this review.

Despite the unique features that qualify stem cell-based models as a promising approach for future nanotoxicity studies, there are some limitations that can make the use of these models challenging. The cultivation and differentiation of stem cells into a mature model usually covers time spans of two weeks or more for a single experiment (372, 374), and is quite expensive in terms of consumption of medium and the multitude of growth factors required for differentiation. The handling of stem cells requires highly trained operators, since wrong handling can easily lead to death or spontaneous differentiation of stem cells, e.g. by suboptimal cell confluence or inappropriate passaging (487-489), which drastically impairs the robustness of the model itself. This issue of robustness is further supported by the lack of standardized protocols for stem cell-based models in the current literature.

Another current limitation of both cell line and stem cell-based models is the lack of immunocompetent cells, as immune cells like macrophages or neutrophils are derived from hematopoietic stem cells in the bone marrow, instead of tissue-resident stem cells,

and transported via the blood (490, 491). Organ models based on stem cells exclusively consist of the cell types that stem from the respective tissue-resident stem cells. Yet, pro-inflammatory effects appear to be one of the main mechanisms of nanoplastics toxicity, as they have been described in several *in vivo* studies (265, 492-494). Similarly, nanoplastics have been shown to interact with components of the nervous system (495), which stem cell-based models of intestine and lung are currently lacking. However, the generation of immune and neural cells from iPSCs has been reported (496-498) and the co-culture of mature stem cell-based models with additional cells is possible, e.g. intestinal organoids with an enteric nervous system (499-503). However this has, to the best of our knowledge, not been applied in the field of particle toxicology yet.

The limitations of stem cell-based models, such as the reduced robustness and the lack of standardized protocols might eventually be overcome, as the field develops rapidly and new insights are gained frequently. Similarly, the implementation of other relevant cell types into these models will be the next step towards highly versatile alternatives to animal testing, as it will be possible to investigate immune- or nervous system-related effects of nanoplastics in a physiologically relevant *in vitro* environment.

Lastly, recreating dynamic conditions as present in the intestine and lung by creating *in vitro* models in microfluidic devices (i.e. organ-on-a-chip) might also help to tackle some specific particle-related challenges such as the buoyancy issue. Initial work using a microfluidic-chip model has been performed by exposing human bronchial BEAS-2B cells to PS (404). By generating scaffold-like (504) or tubular structures (374) inside of microfluidic devices that are exposed to a dynamic flow of particle suspension, the sedimentation behavior of buoyant particles will no longer be an obstacle when testing polymers like PP or PE, allowing more accurate dosimetry estimates in intestinal or non-ALI lung models. The adaption of protocols and settings of the microfluidic devices for the purpose of particle testing will require extensive optimization, such as flow rates, exposure time and exact dosimetry calculations. However, the successful integration of such advanced models into the portfolio of validated methods of *in vitro* nanotoxicology will greatly enhance the field.

2.8 Conflict of Interest

The authors declare that the research was conducted in the absence of any commercial or financial relationships that could be construed as a potential conflict of interest.

2.9 Author Contributions

All authors listed have made a substantial, direct and intellectual contribution to the work, and approved it for publication.

2.10 Funding

This study was supported by the Netherlands Organization for Health Research and Development (ZonMw), within the MOMENTUM (Microplastics and Human Health Consortium) project (grant no. 458001101) and has received funding from the Plasticheal project under European Union's Horizon 2020 research and innovation programme (grant no. 965196). This publication is also part of the LymphChip project (number NWA-ORC 2019 1292.19.019) of the NWA research program 'Research on Routes by Consortia (ORC)', which is funded by the Netherlands Organization for Scientific Research (NWO). The work was also supported by the Leibniz Research Alliance Advanced Materials Safety.

CHAPTER 3

3

Pro-inflammatory response of human iPSC-derived intestinal epithelial monolayers towards microbial toxins LPS and nigericin

Germaine Aalderink[#], Hugo Brouwer[#], Jingxuan Wang, Aafke W.F. Janssen, Meike van der Zande, Coen Govers, Tamara Hoppenbrouwers, Hans Bouwmeester, Mathias Busch

# These authors contributed equally to this work.

Based on Germaine Aalderink, Hugo Brouwer, Jingxuan Wang, Aafke W.F. Janssen, Meike van der Zande, Coen Govers, Tamara Hoppenbrouwers, Hans Bouwmeester, Mathias Busch. Pro-inflammatory response of human iPSC-derived intestinal epithelial monolayers towards microbial toxins LPS and nigericin. Arch Toxicol. 2025 Oct 8.

doi: 10.1007/s00204-025-04215-9.

3.1 Abstract

The intestinal epithelium forms a selective barrier between the intestinal lumen and the subepithelial layer. Intestinal epithelium plays a critical role in initiating inflammatory tissue responses *in vivo,* which remains challenging to emulate *in vitro*. Caco-2 cells are commonly used models of the intestinal epithelium, but lack crucial receptors and pathways associated with pro-inflammatory reactions. Human induced pluripotent stem cell (iPSC)-based *in vitro* models are assumed to provide a system that better emulates *in vivo* responses. This study evaluated the inflammatory response of iPSC-derived intestinal epithelial cells (IEC) and Caco-2-derived intestinal epithelial cells to the microbial toxins lipopolysaccharide (LPS) and nigericin. Here, iPSCs were differentiated towards enterocyte, goblet- and Paneth-like cells without using three-dimensional culture techniques. The formed monolayer barriers were exposed to a combination of 0-100 µM nigericin and 100 ng/mL LPS on either the apical or basolateral side. The treatment-induced expression of cytokine genes and cytokine secretion were compared between the iPSC-derived cell model and differentiated Caco-2 cell layers. Nigericin exposure in combination with LPS significantly reduced transepithelial electrical resistance in the iPSC-derived model, and resulted in a 10-fold increased secretion of the pro-inflammatory cytokines interleukin (IL)-6, IL-8, and tumor necrosis factor-alpha compared to the negative control. A similar increase was observed for the mRNA expression of these cytokines. No significant effect on TEER, cytokine secretion or mRNA expression was observed in the Caco-2 model. Overall, this study shows that iPSC-IECs are a more sensitive model compared to Caco-2 to emulate inflammatory perturbations of the human intestinal epithelium.

3.2 Introduction

The human intestinal epithelium consists of a single-cell layer that separates the lumen containing the food-chyme and intestinal microbiome from the underlying submucosal tissues. The intestinal barrier protects the host from potentially harmful microbial and fungal species while being a selective barrier to nutrients and food-borne chemicals (505). Importantly, the intestinal epithelium dynamically interacts with intestinal microbiome metabolites and submucosal cells via paracrine signalling and selective paracellular, and/or transcellular transport of the metabolites (506). Proper barrier integrity and a physiological balance in epithelial cell pro-inflammatory and anti-inflammatory responses are key to maintaining a healthy gut physiology (507, 508).

The intestinal epithelial cell (IEC) layer comprises various specialized cell types such as enterocytes, goblet cells, Paneth cells, M cells and enteroendocrine cells. IECs are replenished approximately every 3 to 5 days (509, 510) through the proliferation, migration and differentiation of LGR5+ intestinal stem cells that reside in the intestinal crypt (511). Each type of IEC has a specific function that is essential for maintaining intestinal homeostasis. Enterocytes comprise 70 % of the epithelial lining and are primarily responsible for absorbing nutrients and food-borne chemicals from digested foods (512). Enterocytes, together with the other IEC types in the gut epithelium, are connected via a network of epithelial tight junction proteins that coordinate the paracellular permeability between IECs(513). Goblet cells are the second most abundant cell type and secrete mucin glycoproteins, such as Mucin 2 (MUC2), to form a highly viscous, yet porous, mucus layer on top of the IEC layer (514). The mucus layer serves as a lubricant for the transport of chyme and protects the epithelial layer from luminal contents (515). It has been shown that impaired mucus secretion due to *Muc2* deficiency results in elevated levels of pro-inflammatory cytokines secreted by IECs, underpinning the importance of an appropriate mucus layer in immunotolerance (515, 516). Paneth cells reside in the crypts of the epithelial lining and secrete antimicrobial peptides in the mucus layer, which prevents the undesired infiltration of bacteria (323, 517, 518). Paneth cells, along with goblet cells and enterocytes, form a major component of the innate immune system of the small intestine and help regulate intestinal inflammation (518). In addition, enteroendocrine cells detect the metabolites of commensal bacteria and release peptide hormones and cytokines to recruit immune cells and modulate their response (519). The so-called M-cells selectively endocytose mainly particulates like bacteria to present them to macrophages and lymphocytes in the *lamina propria* on the basolateral side of the IEC layers (520). When the intestine is in homeostasis, host-borne microbial agents from the lumen of the gastrointestinal tract induce an anti-inflammatory state, which promotes immune tolerance in the intestinal tissue (521, 522).

Imbalances in gut microbiota can alter the epithelial immune response towards an inflamed state (522). For example, luminal overgrowth of pathogenic bacteria can lead to an increased presence of a variety of endotoxins, including bacterial lipopolysaccharides (LPS), which can negatively affect the intestinal epithelial barrier (523). LPS interacts with the toll-like receptor 4 (TLR4) on IECs (524), resulting in the secretion of pro-inflammatory cytokines and increased susceptibility to inflammatory diseases(525). Pro-inflammatory cytokines induce downregulation of tight junctions, most notably zonula occludens-1 (ZO-1), resulting in a subsequent decline in barrier integrity (526). Loss of intestinal barrier integrity and long-term stimulation of pro-inflammatory pathways can result in chronic inflammation, leading to the development of inflammatory bowel diseases (IBD), such as Crohn's disease (527, 528) and ulcerative colitis (507, 529). Emulating the response of epithelial cells to intestinal pathogens and their metabolites aids our understanding of intestinal homeostasis and disease development and progression (530). To study the mechanisms of intestinal pathogens, it is essential to evaluate the inflammatory signalling capacity of appropriate intestinal epithelial models *in vitro*.

Several *in vitro* models of the intestinal epithelium have been used to replicate the complexity of intestinal inflammation to elucidate the pathogenesis of IBD (530). The immortalized Caco-2 cell line is most often chosen as the preferred cell line due to its ability to spontaneously differentiate to an enterocyte-like phenotype after reaching confluency (531). Caco-2 cells are epithelial cells derived from colon tissue of a colorectal adenocarcinoma, and their differentiation is marked by the transition of colonocyte markers to enterocyte markers between days 3-18 post-confluence (532), resembling the gene expression pattern of small intestinal enterocytes (533). However, differentiated Caco-2 cells lack important receptors involved in crucial pro-inflammatory pathways, such as TLR4 and IL1R (534), and the cellular diversity required to model the interaction with immune cells in the intestinal epithelial layer *in vivo*. Several *in vitro* models are described to complement Caco-2 cells with additional immunocompetent cell lines, such as macrophage-like THP-1 (343), dendritic cell-like MUTZ-3 (342) or primary monocyte-derived macrophages and dendritic cells, to be able to detect inflammation-related responses (322). However, the intestinal epithelium itself is a key player in pro-inflammatory responses and might even have opposite roles of typical immune cells in pathways that are involved in intestinal inflammation (211). To investigate the mechanisms underlying intestinal inflammation, such as that induced by pathogens, *in vitro*, it is essential to assess the inflammatory signalling capacity of appropriate intestinal epithelial models.

Primary microtissues would provide a relevant cell model, but their applicability is limited due to their restricted expansion, limited availability and low expression of transporters compared to *in vivo* tissue (530, 535, 536). Adult stem cells, isolated from primary intestinal material, can be grown for extended periods when cultured in an extracellular matrix

to form self-organizing three-dimensional intestinal organoids (329). The cellular composition within these organoids is modulated by a combination of growth factors (537, 538). However, intestinal organoids, derived from either adult stem cells or induced-pluripotent stem cells (iPSCs), are spherical structures with an inwards-facing apical membrane and therefore not ideally suited for exposure studies that require exposure on the apical side in a barrier model configuration. Apical-out intestinal organoids can be achieved (539), however, this would in turn complicate basolateral exposure and sampling. Moreover, the disassembly of organoids into monolayers causes the loss of self-organized cell patterns (540). Unlike the primary tissue and adult stem cells, iPSC lines are commercially available and can be grown indefinitely. iPSC differentiation can be directed into two-dimensional IEC monolayers (371), which were recently optimized to study the effects of per- and polyfluoroalkyl substances (PFAS) and heat-killed bacteria (237, 541). The diverse cell population and consistent barrier integrity of the two-dimensional iPSC-derived IECs make it an interesting model to study inflammation-related perturbations of the human intestinal epithelium.

In the present study, the inflammatory responsiveness of intestinal epithelial cell layers of iPSC-derived IECs and differentiated Caco-2 cells in response to nigericin and LPS co-exposure was evaluated and compared. Inflammatory responses were assessed by measuring cytotoxicity, barrier integrity, mRNA expression and secretion of relevant cytokines upon exposure.

3.3 Methods

3.3.1 Culture of hiPSC

Human iPSCs (CS83iCTR-33nxx) were obtained from Cedars-Sinai Medical Center's David and Janet Polak Foundation Stem Cell Core Laboratory (CA, United States) and cultured in a standard gas atmosphere with 95 % humidity and 5 % CO_2 at 37 °C under feeder-free conditions using Matrigel hESC-Qualified Matrix-coated 6 well plates (Corning, NY, USA). The cells were routinely passaged using Gentle Cell Dissociation Reagent (GCDR; Stem Cell Technologies, Saint-Egrève, France) for 6 minutes (min) at room temperature. mTeSR™ Plus medium (Stem Cell Technologies, Saint-Egrève, France) was changed every 2-3 days.

3.3.2 hiPSC differentiation into intestinal epithelial cells

Intestinal epithelial cell induction was adapted from Janssen et al. (237, 541). hiPSCs were dissociated into single cells with Accutase (Fisher Scientific, Landsmeer, Netherlands) for 6 min at 37 °C and 63,000 cells/cm^2 were seeded in Matrigel hESC-Qualified Matrix-coated 24-well plates and subsequently incubated in mTeSR™ Plus medium with 10 µM Y-27632 (Stem Cell Technologies, Saint-Egrève, France) for 24 hours. Definitive endoderm

differentiation was subsequently induced using RPMI-1640 medium (Merck, Amsterdam, Netherlands) supplemented with 1 % penicillin-streptomycin (10,000 U/mL) (Pen/Strep), 2 mM L-glutamine (Fisher Scientific, Landsmeer, Netherlands), 1 % non-essential amino acids (NEAA), 2 % B27 supplement minus vitamin A (Fisher Scientific, Landsmeer, Netherlands), 100 ng/mL Activin A (Cell guidance systems, Cambridge, United Kingdom), and 50 ng/mL bone morphogenetic protein 4 (BMP4, R&D Systems, Dublin, Ireland). On the second day, BMP4 was removed, and the medium was changed every day for two consecutive days. Intestinal stem cell induction was performed between days 3 to 7 in Dubecco's modified Eagle's medium (DMEM) / nutrient mixture F-12 (F-12) medium (Fisher Scientific, Landsmeer, Netherlands) supplemented with 2 % defined fetal bovine serum (dFBS; Cytiva, MA, United States), 1 % Glutamax (Fisher Scientific, Landsmeer, Netherlands), and 250 ng/mL fibroblast growth factor 2 (FGF2, R&D Systems, Dublin, Ireland). On day 7, the cells were dissociated using Accutase for 6 min at 37 °C. Millicell 24-well inserts with pore size of 3.0 µm were pre-coated with Matrigel Growth Factor Reduced Basement Membrane Matrix (Corning, NY, United States) and 225,000 cells/cm^2 were seeded on the apical side of the Matrigel-coated insert in intestinal cell differentiation medium (Advanced DMEM (Fisher Scientific, Landsmeer, Netherlands) supplemented with 2 % dFBS, 2 % B27 supplement minus vitamin A, 2 % HepExtend supplement, 1 % N2 supplement, 1 % NEAA, 1 % Pen/Strep, 2 mM L-glutamine, 20 ng/mL epidermal growth factor (EGF; R&D Systems, Dublin, Ireland), and 3 µM Forskolin (Stem Cell Technologies, Saint-Egrève, France). 10 µM Y-27632 was added during the first 3 days. The choice for Millicell inserts was based on the distributor's availability and its compatibility with organ-on-chip devices. The plates were then shaken at 60 rpm on a SH-200D-O Mini Orbit Shaker (Cole-Parmer, Wertheim, Germany) with medium changes every 2-3 days. Intestinal cell differentiation medium was supplemented from day 14 onwards with the small molecules 5 µM 5-aza-2'-deoxycitidine (Fisher Scientific, Landsmeer, Netherlands), 20 µM PD98059 (Stem Cell Technologies, Saint-Egrève, France) and 0.5 µM A-83-01 (Stem Cell Technologies, Saint-Egrève, France) until 26-28 days of differentiation. Cell culture was performed at 37 °C with 5 % CO_2 for all differentiation steps.

3.3.3 Gene expression analysis

Total RNA was extracted using the RNeasy Micro kit (Qiagen, Venlo, Netherlands), according to the manufacturer's instructions. RNA concentration was determined using a NanoDrop OneC Microvolume UV-Vis Spectrophotometer (Fisher Scientific, Landsmeer, Netherlands) and adjusted to 30 ng/µL in DEPC-treated ultrapure water. Reverse transcription was performed using the Quantitect Reverse Transcriptase kit (Qiagen, Venlo, Netherlands) and an iCycler (Bio-Rad, Veenendaal, Netherlands) according to the manufacturer's instructions. Real-time quantitative polymerase chain reaction (RT-qPCR) experiments were carried out on a Rotor-Gene Q (Qiagen, Venlo, Netherlands) using the Rotor-Gene SYBR green PCR kit (Qiagen, Venlo, Netherlands). CT values above 35 were

excluded from the results. The primers used are listed in *Table S2*. The efficiency of the primers was checked prior to sample measurement. Values were quantified using the comparative threshold cycle method. Target gene mRNA expression was normalised to the average of *ACTIN* and *GAPDH* expression per sample and the negative control per exposure group. Fold changes were calculated based on day 0 for Fig. 1 and the negative control for Fig. 3.

3.3.4 Immunocytochemistry

The cells were fixed with 3.7 % paraformaldehyde (Merck, Amsterdam, Netherlands) in phosphate-buffered saline (PBS; Fisher Scientific, Landsmeer, Netherlands) at room temperature for 15 min, washed twice, and stored in MilliQ water at 4 °C. Cells were permeabilizated with 0.3 % Triton® X-100 (Merck, Amsterdam, Netherlands) for 10 min and blocked with 2 % fetal bovine serum (FBS), 2 % bovine serum albumin (BSA) and 0.1 % Tween20 (Merck, Amsterdam, Netherlands) in PBS for 30 min. The membranes from the Millicell inserts were subsequently removed with a scalpel and incubated with primary antibodies for 2 h at RT. Thereafter, the cells were incubated with secondary antibodies and Hoechst 33342 (Fisher Scientific, Landsmeer, Netherlands) for 30 min. The antibodies, along with all other materials used, are listed in *Table S1*. The inserts were placed on a microscopic slide with cells facing upwards and covered with a drop of Prolong Gold antifade mountant (Fisher Scientific, Landsmeer, Netherlands) and a cover slip. Images were captured with a re-scan confocal microscope (Confocal.nl, Amsterdam, Netherlands) using a 60x magnification objective and Z-stack acquisition.

3.3.5 Culture of Caco-2

Caco-2 cells (HTB-37) were obtained from ATCC (VA, United States) and passage 15-30 were used. Caco-2 cells were cultured in Dulbecco's modified Eagle's medium (DMEM) with high glucose, L-glutamine, and sodium pyruvate (Capricorn Scientific, Eborfergrund, Germany), supplemented with 20 % FBS (Fisher Scientific, Landsmeer, Netherlands), 1 % NEAA (LifeTech, 11140050), 1 % Pen/Strep and 1 % GlutaMAX (Fisher Scientific, Landsmeer, Netherlands). Caco-2 cells were trypsinized with 0.5 % trypsin-EDTA (Fisher Scientific, Landsmeer, Netherlands) for 6 min and 200,000 cells/cm^2 were seeded on the apical side of Millicell 24-well inserts (Merck Millipore, Darmstadt, Germany). The cells were incubated for 21 days at 37 °C with 5 % CO_2 to differentiate into enterocyte-like epithelial cells. The medium was changed every 2-3 days.

3.3.6 Exposure to microbial toxins

After cultivating the hiPSC cells for 26-28 days and the Caco-2 cells for 21 days, the apical or basolateral medium was removed and replaced with fresh medium containing 100 ng/ml LPS from *Escherichia coli* O111:B4 (Merck, Amsterdam, Netherlands) together with 0-100 µM of nigericin sodium salt (Merck, Amsterdam, Netherlands) on either the apical

or basolateral side for 24 h. The supernatant was collected from the apical and basolateral compartments and stored separately at -20 °C.

3.3.7 Trans-epithelial electrical resistance measurements

Transepithelial electrical resistance (TEER) was measured using the EVOM3 Manual Epithelial Volt Ohm Meter (World Precision Instruments, Friedberg, Germany) and STX4 EVOM™ Electrode (World Precision Instruments, Friedberg, Germany). TEER was measured according to the manufacturer's instructions. The samples were measured before medium changes (every 2-3 days) and kept on a heated flask during measurements. Cell-free Matrigel-coated inserts were used as blank values. TEER values were normalized by subtracting the blank and multiplying by the insert surface area of 0.6 cm^2. Monolayers of differentiated Caco-2 cells and iPSC-derived IECs were considered of acceptable quality for the exposure experiments if the normalized TEER values were higher than 150 Ω*cm2 and 400 Ω*cm2, respectively.

3.3.8 Lactate dehydrogenase (LDH) assay

LDH reaction solution (homebrew) was prepared in advance by combining 50 µl lithium L-lactate (204 mM), 46 µl nicotinamide adenine dinucleotide sodium salt (5 mM), 2 µl iodonitrotetrazolium chloride (65 mM) and 2 µl phenazine methosulfate from Merck (29 mM) (Amsterdam, Netherlands) with 50 µl Tris buffer (200 mM, pH 8) (Trizma hydrochloride; Merck, Amsterdam, Netherlands, Trizma base; Merck, Amsterdam, Netherlands). After 24 h of LPS and nigericin exposure, 50 µl of apical and basolateral supernatant of each insert was transferred to a 96-well plate. 150 µl of LDH reaction solution was added to the supernatants and incubated at 37 °C and 5 % CO_2 for 5-15 min. The reaction was stopped by adding 50 µl of 1 M H_2SO_4 (Honeywell International Inc., Charlotte, NC, United States). Absorbance was measured using a SpectraMax iD3 plate reader and SoftMax Pro 7.1 (Molecular Devices, SJ, United States) at 490 and 680 nm. Data is presented as A_{490nm}-A_{680nm} as fold change of the untreated control. Cells subjected to 0.5 % Triton for 15 min were used as a positive control for cell death.

3.3.9 Enzyme-linked immunosorbent assay (ELISA)

The release of pro-inflammatory cytokines in the apical medium following exposure to bacterial toxins was analysed using ELISA kits (R&D Systems, Dublin, Ireland) for human Interleukin (IL)-6, IL-8, and tumor necrosis factor-alpha (TNF-α) as described elsewhere (212). The supernatants were diluted if necessary.

3.3.10 Alcian Blue/PAS staining

Cells on Millicell inserts were fixed as described in the Immunocytochemistry section. Cells were pre-treated with 3 % acetic acid (Merck, Amsterdam, Netherlands) for 3 min, followed by 1 % Alcian Blue (Merck, Amsterdam, Netherlands) in 3 % acetic acid for

30 min. Cells were subsequently washed thrice with MilliQ water and pre-treated with 1 % periodic acid solution (Merck, Amsterdam, Netherlands) for 10 min. After washing three times with MilliQ, Schiff's reagent (Merck, Amsterdam, Netherlands) was added to each sample for 15 min, followed by three times sulphite water for 2 min and two times MilliQ wash. The insert was removed and mounted on a microscopic slide as described in the Immunocytochemistry section.

3.3.11 Statistics and Data analysis

Data sets were analysed using GraphPad Prism software version 10 (GraphPad Software, CA, USA). Unless stated otherwise, values are expressed as the mean ± standard deviation (SD) of four independent experiments (N = 4) and three technical replicates in each experiment. Normal distribution in the data was tested with the Shapiro-Wilk test. Statistical analysis was performed using the Kruskal-Wallis test with Dunn's multiple comparison test for the gene expression of differentiation makers in Fig. 1B and one-way analysis of variance (ANOVA), followed by Dunnett's multiple comparisons test for TEER, LDH and gene expression data in Figures 2B-D and 3. Differences with $p < 0.05$ were considered significant (* $p < 0.05$, ** $p < 0.01$, *** $p < 0.001$, **** $p < 0.0001$). In Fig. 3, differences between the cytokine expression of the negative controls were tested with a unpaired t-test and considered significant if $p < 0.05$ (# $p < 0.05$, ## $p < 0.01$, ### $p < 0.001$, #### $p < 0.0001$).

3.4 Results

3.4.1 Intestinal epithelial-like cell layer differentiation

iPSCs were differentiated into IECs using a three-step differentiation protocol (Fig. 1A). In the current protocol, intestinal stem cells were replated onto Matrigel-coated Millicell inserts to obtain a barrier model separating the apical and basolateral compartments. To confirm the path of cell differentiation, expression of cell-specific genes was analysed at critical time points during differentiation (Fig. 1B). In accordance with our expectations, mRNA expression of the stem cell pluripotency marker *POU5F1* significantly decreased (as seen on days 14, 21 and 28) compared to expression levels detected in undifferentiated iPSCs on day 0 (Fig. 1B). Exposure of iPSCs to Activin A and BMP4 from day 1 onwards significantly increased the mRNA expression of *SOX17* on day 3 and 7 (Fig. 1B), which is a marker indicating differentiation towards an endodermal cell fate. Differentiation towards intestinal stem cells was marked by its peak *LGR5* expression on day 7 (Fig. 1B). The increased mRNA expression of *Villin 1* (*VIL1*) (Fig. 1B) between days 7 and 28 and the resulting *VIL1* protein expression at day 28 (Fig. 1C) suggests the differentiation into enterocyte-like cells. The presence of MUC2-positive cells was confirmed by the increasing mRNA expression of *MUC2* and immunocytochemistry at the later time

points (Fig. 1B, D). Histochemical analysis revealed an increasing intensity of blue and magenta Alcian Blue/PAS-positive cell clusters on top of the IEC cell monolayers, further indicating the presence of acidic and neutral mucus in the cell layers (Fig. S1). In addition, increasing *Lysozyme* (*LYZ*) mRNA expression throughout differentiation was indicative of the presence of Paneth cells (Fig. 1B), which was confirmed by immunocytochemistry (Fig. 1E). No evidence was found of iPSC differentiation towards enteroendocrine cells, as the immunostaining for the commonly used endocrine marker chromogranin A (CHGA) did not show positive cells (data not shown), and gene expression for *CHGA* in IECs significantly decreased relative to iPSCs at day 0 from day 14 onwards (Fig. 1B).

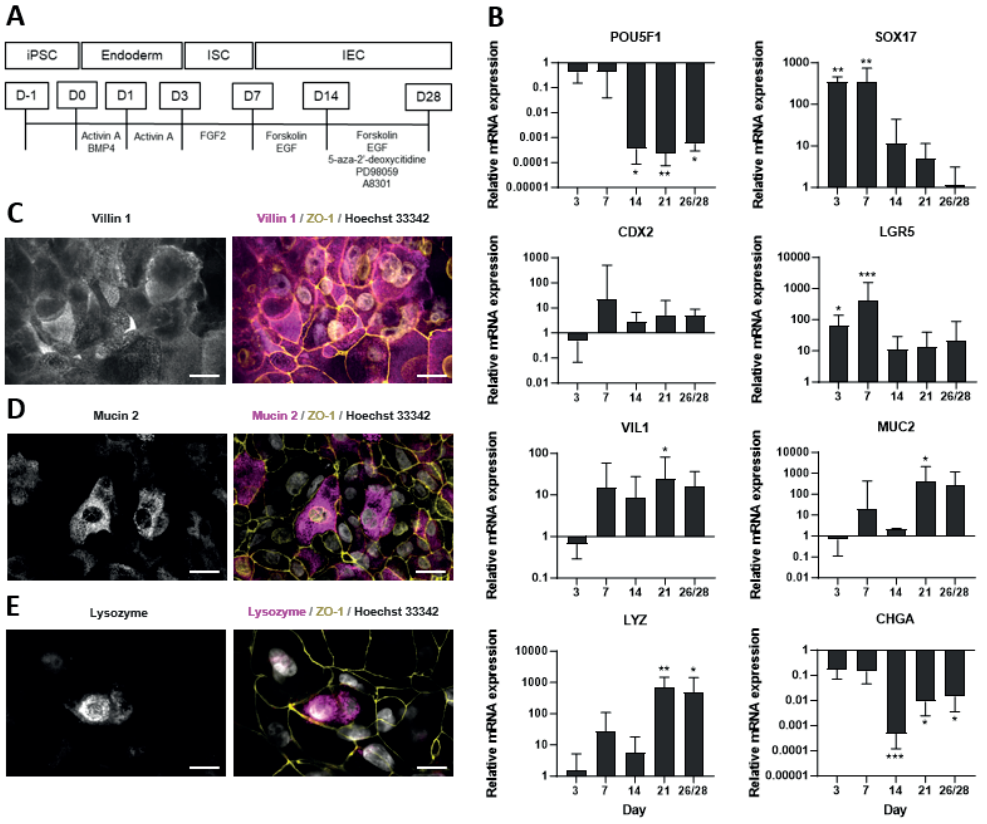

Fig. 1 - Differentiation and characterisation of two-dimensional iPSC-derived IEC layers.

(A) Schematic outline of the differentiation process of iPSCs towards IEC layers via treatment with the indicated compounds. (B) mRNA expression levels of POU5F1, SOX17, CDX2, LGR5, VIL1, MUC2, LYZ and CHGA were assessed via RT-qPCR on days 3, 7, 14, 21 and 26/28 (one of the four replicates was differentiated until day 26 instead of 28). Samples were normalised to ACTIN and GAPDH expression and presented as a fold change of the expression on day 0. Expression levels are presented as the mean ± SD (N=4) and compared to day 0 using the Kruskal-Wallis test followed by Dunn's multiple comparisons test. Differences with $p < 0.05$ were considered significant (* = $p < 0.05$, ** = $p < 0.01$,

*** = $p < 0.001$, **** = $p < 0.0001$). (C-E) Immunofluorescent staining of iPSC-derived IEC layers on day 28 for the proteins Villin 1, Mucin 2 and Lysozyme. Nuclei were stained with Hoechst 33342, and tight junction networks with anti-ZO-1 antibodies to visualise the overall morphology of the cell layers. Images were taken at 60x magnification, scalebar represents 20 µm.

3.4.2 Intestinal epithelial cell layer barrier integrity

The barrier integrity of iPSC-derived IEC layers and Caco-2 cell layers was assessed during differentiation using intermittent TEER measurements every 2-3 days. TEER remained within acceptable boundaries from day 4 for Caco-2 and day 14 for iPSC-derived IECs, respectively, averaging ~300 $\Omega*cm^2$ and ~1000 $\Omega*cm^2$ (Fig. 2A). Although differences in TEER values between the two models were observed, three technical replicates within each independent experiment displayed comparable TEER values (Fig. 2A).

Before analysis of the inflammatory responsiveness of the two cell models, LPS and nigericin were added to assess their potency to induce cytotoxicity and barrier disruption. Cytotoxicity was measured using the LDH assay on supernatants from both the apical (Fig. 2B) and basolateral side (Fig. S2) after apical or basolateral exposure for 24 h. The highest concentration of nigericin (100 µM) in combination with 100 ng/ml LPS induced significantly increased LDH release from iPSC-derived IEC layers into the apical compartment, but not from differentiated Caco-2 cell layers, irrespective of apical or basolateral exposure (Fig. 2B). The TEER values of iPSC-derived IEC layers decreased in a concentration-dependent manner, which reached statistical significance upon exposure to 10 µM nigericin in combination with 100 ng/ml LPS when exposed either to the apical or basolateral side. No effects on TEER were observed in the cell layers of differentiated Caco-2 cells (Fig. 2D). We noticed a slight decrease in baseline TEER post-exposure (~1000 $Ohm*cm^2$ to ~800 $Ohm*cm^2$ in iPSCs and ~300 $Ohm*cm^2$ to ~200 $Ohm*cm^2$ in Caco-2, see Figure A, C and D), which is likely an effect of measuring TEER 24 hours after medium change in the exposure experiment, as opposed to measuring 48 to 72 hours after medium change during the differentiation period.

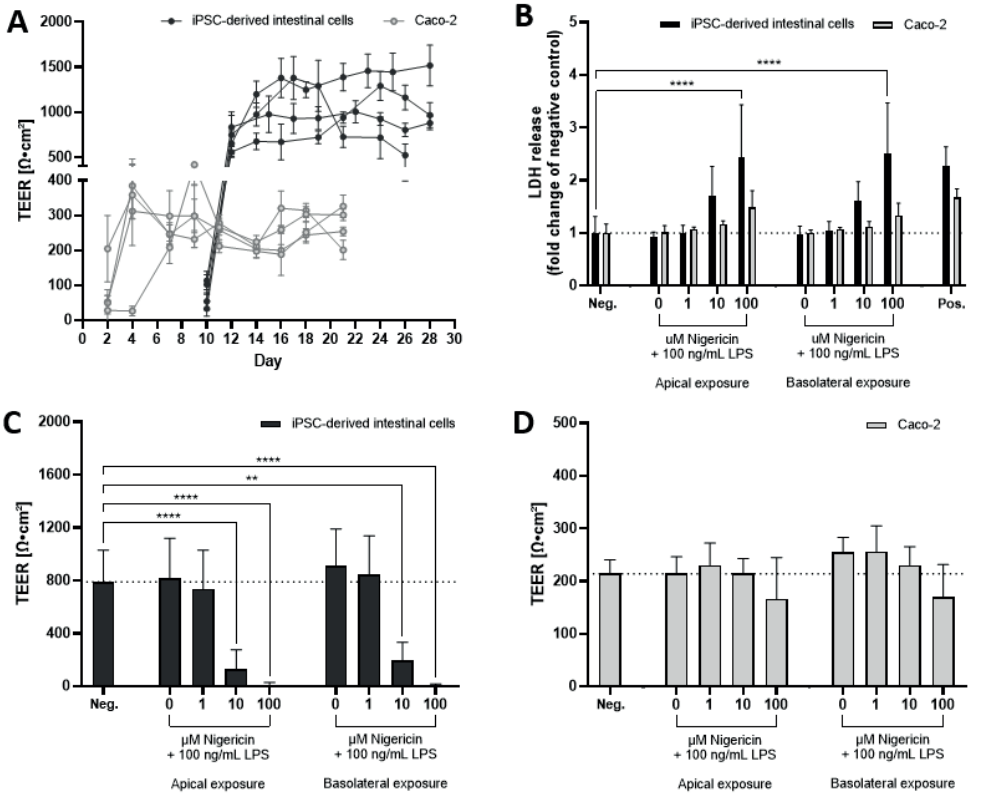

Fig. 2 - Barrier integrity and cytotoxicity in two-dimensional iPSC-derived IEC- and Caco-2 cell layers.

(A) TEER measurements in the cell layers of iPSC-derived IECs (black) and Caco-2 cells (grey). iPSC-derived IECs were first differentiated in 24-well plates and subsequently reseeded on Matrigel-coated Millicell inserts on day 7. Caco-2 cells were seeded directly onto inserts and differentiated for 21 days. Each line represents a single independent experiment (N=4), with each data point on the line representing the average of all technical replicates within the experiment. (B) LDH levels in the apical supernatant of iPSC-derived intestinal cells (black bars) and Caco-2 cells (grey bars) after 24 h exposure to LPS plus 0-100 µM nigericin on the apical or basolateral side. Data are expressed as the fold change compared to the negative control (medium only; dotted line) as the mean ± SD (N=4) and compared to the negative control using a one-way ANOVA followed by Dunnett's multiple comparisons test. (C-D) TEER after 24 h exposure to LPS plus 0-100 µM nigericin on the apical or basolateral side. The dotted line indicates the average TEER value for the negative control of both iPSC-derived IECs and Caco-2 cells, depicted as mean ± SD (N=4). Differences with $p < 0.05$ were considered significant (** = $p < 0.01$, *** = $p < 0.001$, **** = $p < 0.0001$).

3.4.3 LPS and nigericin-induced pro-inflammatory cytokine mRNA expression and secretion

Upon 24 h of co-exposure to 100 ng/ml LPS with 0-100 µM nigericin, the secretion of pro-inflammatory cytokines IL-6, IL-8, and TNF-α by iPSC-derived IECs and Caco-2 cells was determined. Cell model-dependent differences were observed in the secretion of pro-inflammatory cytokines. Exposure of iPSC-derived IEC monolayers to increasing concentrations of nigericin in the presence of 100 ng/ml LPS showed a trend of increased release of IL-6, IL-8, and TNF-α (Fig. 3A, C, E), whereas basolateral exposure to the highest concentration of nigericin caused a statistically significant effect. No significant differences in the secretion of IL-6, IL-8, and TNF-α in the differentiated Caco-2 cells were observed compared to the negative control (Fig. 3B, D, F). Of note, the basal secretion of IL-6 and IL-8 was significantly higher in the iPSC-derived IECs compared to the secretion by differentiated Caco-2 cells (Fig. 3A, C).

To determine whether transcription of *IL-6*, *IL-8*, and *TNF-α* genes in iPSC-derived IECs was upregulated upon LPS and nigericin exposure, the mRNA expression was determined using RT-qPCR. None of the cytokine mRNA expression levels were affected by LPS exposure alone, while significantly increased *IL-6*, *IL-8* and *TNF-α* mRNA expression was observed when cells were co-exposed to LPS and nigericin at 10 µM apically or 100 µM basolaterally (Fig. 3B, D, F).

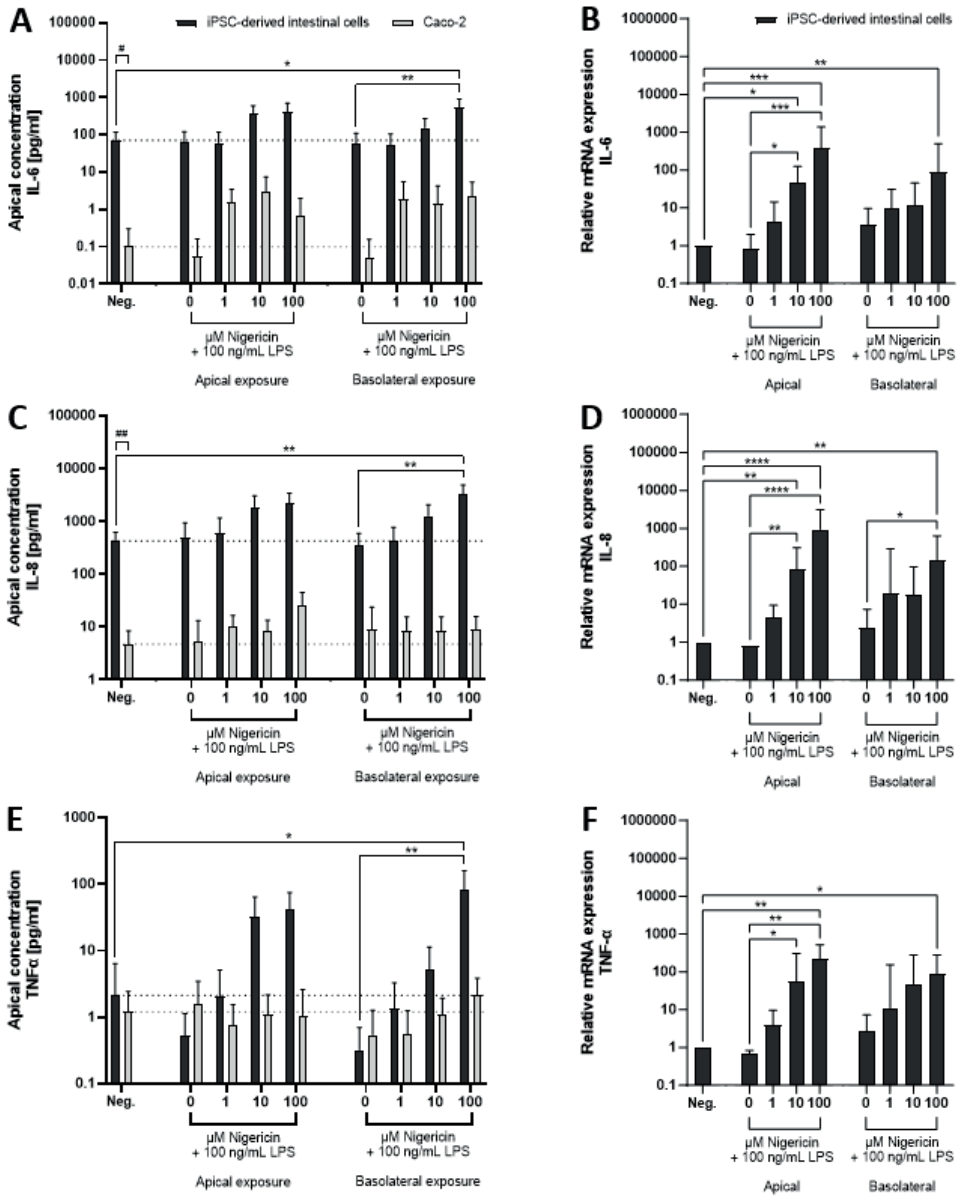

Fig. 3 – Pro-inflammatory response after exposure to LPS and nigericin in iPSC-derived IECs and Caco-2 models.

(A, C, E) Apical secretion of IL-6, IL-8 and TNF-α from iPSC-derived intestinal cells (black bars) and differentiated Caco-2 cells (gray bars) after 24h of exposure to 100 ng/ml LPS with 0-100 µM nigericin. The dotted line indicates the average cytokine concentration in the negative control of both iPSC-derived IECs and Caco-2 cells. (B, D, F) Relative mRNA expression levels of IL-6, IL-8 and TNF-α in IPSC-derived IECs after 24h of exposure to 100 ng/ml LPS with 0-100 µM nigericin. Expression levels were determined by RT-qPCR and normalised to GAPDH and ACTIN and expressed as fold

change of the negative control (Neg.) per cytokine. Expression levels are presented as the mean ± SD (N=4) and compared to the negative control using a one-way ANOVA followed by Dunnett's multiple comparisons test. Differences with $p < 0.05$ after multiple testing corrections were considered statistically significant (* $p < 0.05$, ** $p < 0.01$, *** $p < 0.001$, **** $p < 0.0001$). Differences between the cytokine concentration of the negative controls of Caco-2 and iPSC-derived IECs were tested with a student's t-test. Differences with $p < 0.05$ were considered statistically significant (# $p < 0.05$, ## $p < 0.01$).

3.5 Discussion

The current study compared the capacity of two different intestinal *in vitro* models to emulate the human intestinal inflammatory responsiveness and subsequent effects on barrier integrity. iPSC-derived IECs were found to be more responsive to LPS and nigericin exposure than differentiated Caco-2 cells. This makes the iPSC-derived IECs a more suitable model to study inflammation-related perturbations of the human intestinal epithelium *in vitro* than Caco-2 cells.

Previous studies have shown that iPSCs can differentiate into IECs (371, 541). The protocols used in the aforementioned studies make use of forskolin for IEC differentiation. Yet this might limit the applicability of the derived IECs, as forskolin has been shown to inhibit the integral pathways in the inflammation pathway (542-544). Therefore, the forskolin concentration used for IEC differentiation in the current study was reduced from 30 to 3 µM to have a negligible effect on inflammation pathways (544). In addition, iPSC-derived cells typically have an immature or fetal-like phenotype (545), while cells exposed to continuous flow and shear stress were found to be more mature (546). Thus, orbital shaking was used to induce shear stress on both the apical and basolateral sides to promote cellular maturation. Indeed, subtle modifications in the cocktail of small molecules used during differentiation can alter the ratios between intestinal epithelial cell type populations *in vitro* (537, 547). The expression of hallmark differentiation markers was confirmed to assess the progression of each differentiation stage during differentiation and expansion. Furthermore, cell type-specific immunostaining markers indicated the presence of enterocytes, goblet cells and Paneth cells on day 28 of culture. A time-dependent decrease of *POU5F1* expression indicates loss of pluripotency (548), while *LGR5* is still expressed at the end of the differentiation procedure, confirming the presence of non-terminally differentiated intestinal stem cells in the cell population (549). The upregulation of *SOX17* on day 3 and 7 indicates Activin A-mediated differentiation towards definitive endoderm as an intermediate step, while endodermal identity is lost again at the end of differentiation (day 28), as seen by a downregulation of *SOX17* (550). Further, the presence of enterocytes, goblet cells and Paneth cells was confirmed using gene expression of *VIL1*, *MUC2* and *LYZ*, respectively, and immunostaining of the associated proteins. The expression of

CHGA, a marker of enteroendocrine cells that are occasionally observed in iPSC-derived intestinal models (236), was not observed. Overall, these gene expression patterns are in line with previous characterization studies of iPSC-derived IECs (237, 541).

Exposure of iPSC-derived IECs to LPS in combination with nigericin significantly reduced TEER upon increasing nigericin concentrations, irrespective of apical or basolateral exposure to these compounds. An increase in the release of LDH by the iPSC-derived IECs was also observed at the highest compound concentrations tested, indicating major necrotic cell death through membrane damage. Nigericin is a natural antibiotic produced by *Streptomyces hygroscopicus*, which has been used as a costimulatory inducer of intestinal inflammation (551-553). Nigericin acts as an ionophore, allowing in- and efflux of several types of ions, including H^+ and K^+, leading to changes in pH gradients and mitochondrial membrane potential (554). Furthermore, nigericin is a potent activator of inflammasomes, which, once activated, lead to the release of pro-inflammatory cytokines and possibly pyroptosis, an inflammatory form of lytic cell death. Cell death upon nigericin treatment has been reported in several cell models (555-557). In Caco-2 cells, LPS and nigericin only induced very minor, non-significant effects on TEER and LDH release, hinting either towards higher robustness of these cells or the previously reported lack of crucial receptors/pathways that are involved in the response towards nigericin (558).

Although LPS is commonly reported as a potent activator of multiple pro-inflammatory pathways in other *in vitro* models (559), 100 ng/ml LPS alone did not induce any pro-inflammatory effect in the iPSC-derived IECs. Interestingly, a combination with at least 10 µM nigericin seems to be sufficient to result in detectable changes in markers indicative of intestinal inflammation, such as an impaired barrier, cell death, and release of the pro-inflammatory cytokines IL-6, IL-8 and TNF-α. IL-6 has been described to be essential in bacterial-epithelial cross-talk in the gastrointestinal tract (560). IL-8 is a chemoattractant largely produced by intestinal epithelial cells to recruit immune cells in response to bacterial invasion (561). The cytokine TNF-α has been described to have diverse IEC effects, such as modulation of mucus secretion, tight junction control and cell death (562). Overall, the response of the iPSC-derived IECs is a plausible reaction towards the bacterial toxins LPS and nigericin and resembles an *in vivo* reaction to bacterial invasion of the gut.

Furthermore, our study assessed whether the inflammatory reaction of iPSC-derived IECs towards LPS and nigericin differs between apical and basolateral exposure. The presence and location of specific TLRs on IECs can vary based on tissue region and disease state (563), while TLRs are generally expressed on both apical and basolateral membranes of IECs (564). Despite subtle differences in the cytokine expression and release after apical and basolateral exposure, we cannot conclude any side to be more susceptible towards bacterial toxins. Both scenarios are physiologically relevant, as (fragments of) bacteria

might either breach the intestinal mucus layer and interact with the apical membrane of the intestinal epithelium, or breach the intestinal epithelial layer itself and interact with receptors on the basolateral side. In contrast, no effects on cytokine secretion were observed in differentiated Caco-2 cells. It has been previously described that Caco-2 cells show very limited responses towards inflammatory stimuli such as LPS (343), which in part can be attributed to a lack of *TLR4* expression (534). However, nigericin exposure did not cause any effects in Caco-2 cells as well, suggesting a dysfunction of a nigericin-associated pathway. Overall, our results demonstrate immunocompetence of iPSC-derived IECs towards the microbial toxins LPS and nigericin, even without a specific immunocompetent cell type present. Notably, the basal mRNA expression of *IL-6*, *IL-8*, and *TNF-α*, and their respective secretion, was significantly elevated in the cell layers of iPSC-derived IECs compared to that in Caco-2 cell layers, indicating a constant state of low-level inflammation in iPSC-derived IECs without additional stimuli. A possible explanation could be the activation of transcription factor STAT3, which is involved in IL-6 production, but also in the establishment of pluripotency in iPSCs (565). iPSC-derived cells often represent an immature phenotype compared to cells directly collected from *in vivo* material, as iPSC-IECs are not exposed to the physiologically-relevant tissue microenvironment that might play a major role in fine-tuning gene expression patterns (566). The iPSC-IECs immature and more proliferative state could explain its significantly higher cytokine expression compared to Caco-2.

A true recapitulation of intestinal immune responses involves the interplay between epithelial and immune cells and thus requires the incorporation of intestinal tissue-residing immune cells in future research. Tissue-resident immune cells, most notably macrophages and dendritic cells, underlie the intestinal epithelial cells and induce hyporesponsiveness to bacteria (567, 568). If the intestinal barrier is breached, tissue-resident immune cells release cytokines and chemokines to induce mucosal inflammation. Several groups have reported this interplay between the epithelial lining and immune cells in the intestine, often using the THP-1 cell line (343, 530). To fully recapitulate the intestinal inflammatory response induced by luminal content, a co-culture of epithelial and tissue-resident immune cells (*e.g.* macrophages (569)) must be further explored, potentially derived from the same donor.

Moreover, initial results from multicenter studies, using complex iPSC models for drug screening, showed acceptable variability, overcoming a main hurdle for the broader acceptance of the outcome of iPSC-based studies (570). Recent examples show that iPSC-based cell models have successfully studied the transport and effects of PFAS (541), paving the way for other transport studies using iPSC-based models (571, 572). In addition, iPSC-derived models have the potential to study individual donor differences, which are particularly important in the context of disease modelling, such as IBD. Alleles that

increase disease susceptibility often show low penetrance in individuals carrying them, indicating that IBD is primarily caused by the interplay between host factors and environmental influences (573). To distinguish between genetic predisposition and overlapping pathogenic exposure, cellular models should include donors with disease-susceptibility alleles for disease modelling and risk analysis. Cells from patients with IBD could be collected using non-invasive methods and transformed into iPSCs, which could then be differentiated into iPSC-derived intestinal cells, similar to how it was demonstrated for iPSCs derived from osteoarthritis patients (574). The iPSC differentiation protocol and readout methods described in the present study could aid in the development of such personalized models that emulate the inflammation-related perturbations and subsequent treatment options.

3.6 Conclusions

Overall, our study showed that iPSC-derived IEC layers are a suitable immunocompetent model of the intestinal epithelial cell layer, capable of emulating pro-inflammatory responses towards microbial toxins. This model could be further developed and used to emulate inflammation-related perturbations of the human intestinal epithelium *in vitro*, stemming from drugs, chemicals, particulate matter, dietary components or disease susceptibility.

3.7 Acknowledgements

We would like to express our gratitude to Arjan Bader for his guidance with confocal microscopy. The authors declare that they have not used AI-generated work in this manuscript.

3.8 Funding

This publication is part of the LymphChip project (number NWA-ORC 2019 1292.19.019) of the NWA research program 'Research on Routes by Consortia (ORC)', which is funded by the Netherlands Organization for Scientific Research (NWO). This study also received funding from the Plasticheal project under the European Union's Horizon 2020 research and innovation program (grant no. 965196) and the Netherlands Organization for Health Research and Development (ZonMw) and Health-Holland, Top Sector Life Sciences & Health within the MOMENTUM (Microplastics and Human Health Consortium) project (grant no. 458001101).

3.9 Supplementary information

Table S1 – Key resources

REAGENT or RESOURCE	SOURCE	IDENTIFIER
Antibodies		
Anti-Villin antibody for Immunofluorescence (1:200)	Santa Cruz Biotechnology	Cat# sc-58897 RRID: AB_2304475
Anti-MUC2 for immunofluorescence (1:100)	Santa Cruz Biotechnology	Cat# sc-7314 RRID: AB_627970
Anti-Lyzozyme for immunofluorescence (1:100)	DAKO	Cat# A009902-2 RRID: AB_2341230
Anti-ZO-1 for immunofluorescence (1:200) – used in combination with Anti-Villin and Anti-MUC2.	Fisher Scientific	Cat# PA585256 RRID: AB_2792399
ZO-1 Monoclonal Antibody (ZO1-1A12), Alexa Fluor™ 594 (1:200) – used in combination with Anti-Lyzozyme.	Fisher Scientific	Cat# 339194 RRID: AB_2532188
Goat anti-Mouse IgG (H+L) Highly Cross-Adsorbed Secondary Antibody, Alexa Fluor™ Plus 488 (1:250)	Fisher Scientific	Cat# A32723 RRID: AB_2633275
Donkey anti-Rabbit IgG (H+L) Highly Cross-Adsorbed Secondary Antibody, Alexa Fluor™ 647 (1:250)	Fisher Scientific	Cat# A-31573 RRID: AB_2536183
Chemicals, Peptides, and Recombinant Proteins		
Matrigel hESC-Qualified Matrix	Corning	354277
Matrigel Growth Factor Reduced	Corning	354230
mTeSR plus	Stem cell technologies	662640
Gentle Cell Dissociation Reagent	Stem cell technologies	100-0485
Y-27632	Stem cell technologies	72304
Recombinant Human Activin A	Cell guidance systems	GFH6-100
Recombinant Human BMP-4 Protein	R&D systems	314-BP-010/CF
Recombinant Human FGF2 Protein	R&D systems	233-FB-025/CF
Recombinant Human EGF Protein	R&D systems	236-EG-200/CF
Forskolin	Merck	F3917
5-aza-2′-deoxycytidine (5mM)	Merck	A3656
A 83-01	Stem cell technologies	72022
PD98059	Stem cell technologies	72174
RPMI-1640 Medium	Merck	R8758
DMEM/F-12 with 15 mM HEPES	Stem cell technologies	36254
Advanced DMEM/F-12	Fisher Scientific	12634010
GlutaMAX™ Supplement	Fisher Scientific	35050038
B-27™ Supplement (50X), minus vitamin A	Fisher Scientific	12587010
N-2 Supplement	Fisher Scientific	17502048

Table S1 – Continued

REAGENT or RESOURCE	SOURCE	IDENTIFIER
HepExtend™ Supplement	Fisher Scientific	A2737501
Accutase™ Cell Dissociation Reagent	Fisher Scientific	A1110501
L-Glutamine (200 mM)	Fisher Scientific	25030024
Penicillin and Streptomycin (5,000 U/mL)	Fisher Scientific	15070063
Triton X-100	Merck	T8787
Tween20	Merck	P9416
Bovine Serum Albumin	Merck	A2153
Lithium L-lactate	Merck	L2250
β-Nicotinamide adenine dinucleotide sodium salt	Merck	N0632
Iodonitrotetrazolium chloride	Merck	I8377
Phenazine methosulfate	Merck	P9625
Trizma hydrochloride	Merck	T3253
Trizma base	Merck	T4661
Sulfuric acid solution	Honeywell International Inc.	84741
Lipopolysaccharides from *Escherichia coli* O111:B4	Merck	L4391
Nigericin	Merck	N7143
Hoechst 33342	Fisher Scientific	H3570
Defined Fetal Bovine Serum	Hyclone	SH30070.01
GAPDH primer	Qiagen	PPH00150F-200
TNFα primer	Qiagen	PPH00341F-200
Acetic acid	Merck	695092
Alcian Blue solution	Merck	B8438
Periodic acid	Merck	P7875
Schiff's reagent	Merck	1.09033.0500
Critical Commercial Assays		
RLT buffer	Qiagen	79216
RNeasy mini kit	Qiagen	74106
QuantiTect Reverse Transcription Kit	Qiagen	205311
Rotor-Gene® SYBR® Green PCR kit	Qiagen	204174
ProLong™ Gold Antifade Mountant	Fisher Scientific	P36934
Human IL-6 DuoSet ELISA	R&D systems	DY206
Human IL-8/CXCL8 DuoSet ELISA	R&D systems	DY208
Human TNF-alpha DuoSet ELISA	R&D systems	DY210
Experimental Models: Cell Lines		
Caco-2 cells	ATCC	HTB-37
hiPSC CS83iCTR-33nxx	Cedars-Sinai Medical Center	CS83iCTR-33nxx

Table S1 – Continued

REAGENT or RESOURCE	SOURCE	IDENTIFIER
Equipment		
Orbital Shaker	Fisher Scientific	10309644
Nanodrop™	Fisher Scientific	13-400-525
Rotor-Gene Q®	Qiagen	9001862
EVOM3 Trans Epithelial Electrical Resistance (TEER) meters	WPI	EVOM3
Electrode blades for STX4 EVOM™	WPI	STX4-BLADES
SpectraMax	Molecular Devices	iD3
Re-scan confocal microscope	Confocal.nl	RCM1
Inverted phase contrast microscope	Olympus	CKX53
Software and Algorithms		
Fiji-ImageJ	Schindelin et al., 2012 PMID: 22743772	https://imagej.net/Fiji/Downloads
GraphPad Prism 10.2.3	GraphPad	N/A
Disposables		
Millicell Cell Culture Insert, 12 mm, polycarbonate, 3.0 µm	Millipore	PITP01250
Microscope slide 26x76x1mm	Fisher Scientific	15998086
Microscope cover glass, 170 µm thick	Fisher Scientific	10039670
QiaShredder	Qiagen	79656
Nunc™ MaxiSorp™ ELISA Plates, Uncoated	Biolegend	423501

Table S2 – Primers used for RT-qPCR

Gene symbol	GeneBank Accession No.	Primer sequence (5'-3')	PCR efficiency (%)	Regression coefficient (R2)	Source
POU5F1	NM_002701.6	F: TGGAGTTTGTGCCAGGGTTT R: TCACCTTCCCTCCAACCAGT	106	0.995	This paper
SOX17	NM_022454.4	F: GCAAGATGCTGGGCAAGTC R: CTTGTAGTTGGGGTGGTCCTG	92	0.990	This paper
CDX2	NM_001265.6	F: CCAGCGGCGGAACCTGTG R: GTCTTTCGTCCTGGTTTTCAC	110	0.995	(236)
LGR5	NM_003667.4	F: GGAAATCATGCCTTACAGAGC R: CACTCCAAATGCACAGCACTG	109	0.995	(236)
LYZ	NM_000239.3	F: CCCTGGTCAGCCTAGCACTC R: CCTTGCCCTGGACCGTAACA	97	0.998	(236)
VIL1	NM_007127.3	F: CGGAAAGCACCCGTATGGAG R: CGTCCACCACGCCTACATAG	109	0.997	(236)
MUC2	NM002457.4	F: AGAAGGCACCGTATATGACGAC R: CAGCGTTACAGACACACTGCTC	107	0.999	(236)
CHGA	NM_001275.4	F: TCCGACACACTTTCCAAGCC R: TTCTGCTGATGTGCCCTCTC	99	0.997	(236)
IL6	NM_000600.3	F: AGCCACTCACCTCTTCAGAAC R: GCCTCTTTGCTGCTTTCACAC	105	0.992	(575)
IL8	NM_000584.2	F: CTGATTTCTGCAGCTCTGTG R: GGGTGGAAAGGTTTGGAGTATG	103	0.997	(576)
TNF-α	NM_000594	PPH00341F-200	-	-	Qiagen
GAPDH	NM_002046	PPH00150F-200	-	-	Qiagen
ACTB	NM_001101.5	QT00095431	-	-	Qiagen

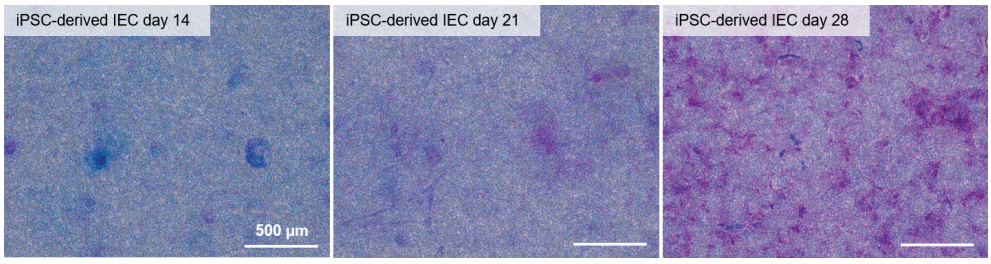

Fig. S1 – Histochemical staining with Alcian blue and Periodic acid–Schiff reaction was performed on paraformaldehyde-fixed iPSC-derived intestinal-like epithelial cells for acidic (blue) and neutral (magenta) mucus, respectively.

Images were acquired on an Olympus CKX53 inverted phase contrast microscope. Images were taken at 20x magnification, scalebar represents 500 µm.

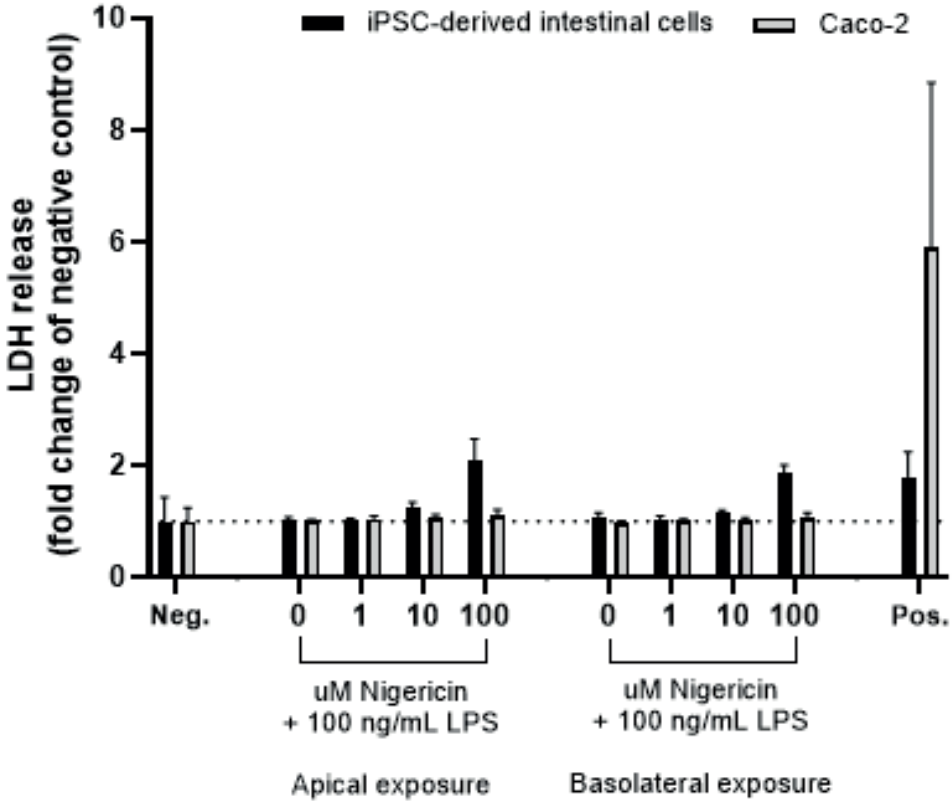

Fig S2 – Basolateral LDH levels after exposure to LPS plus nigericin on the apical or basolateral sides.

Data are expressed as the percentage change compared to the negative control as the mean ± SD (N=4).

CHAPTER 4

Toxicity of true-to-life microplastics to human iPSC-derived intestinal epithelia correlates to their protein corona composition

Hugo Brouwer, Mathias Busch, Shuo Yang, Tom Venus, Germaine Aalderink, Juan Francisco Ferrer Crespo, Aliro Villacorta, Alba Hernández, Irina Estrela-Lopis, Sjef Boeren, Hans Bouwmeester

Based on Brouwer H, Busch M, Yang S, Venus T, Aalderink G, Crespo JFF, Villacorta A, Hernández A, Estrela-Lopis I, Boeren S, Bouwmeester H. Toxicity of true-to-life microplastics to human iPSC-derived intestinal epithelia correlates to their protein corona composition. J Hazard Mater. 2025

doi: 10.1016/j.jhazmat.2025.138908.

4.1 Abstract

Humans are continually exposed to microplastics, now pervasive in the environment. The intestinal epithelium, as a primary barrier tissue, frequently faces high microplastic exposure, yet health implications remain elusive. Using an intestinal epithelial cell model derived from human induced pluripotent stem cells, we show intestinal toxicity upon exposure to true-to-life polyethylene terephthalate-TiO_2, polypropylene-Talc, polyvinyl chloride and polyamide microplastics. These materials compromised barrier integrity, elevated intracellular reactive oxygen species and stimulated intestinal cytokine secretion. Epithelial perturbations were not observed upon exposure to polystyrene microplastics, which frequently serve as a proxy for product-derived microplastic exposure. Proteomics analysis identified unique protein corona compositions for each microplastic, which correlated with *in vitro* effects. For example, the abundance of biocorona proteins involved in inflammation strongly correlated to the degree of cytokine secretion. These findings underscore the need for routine availability of true-to-life microplastics and protein corona analysis in hazard assessment to enable safe-by-design plastic development.

4.2 Graphical abstract

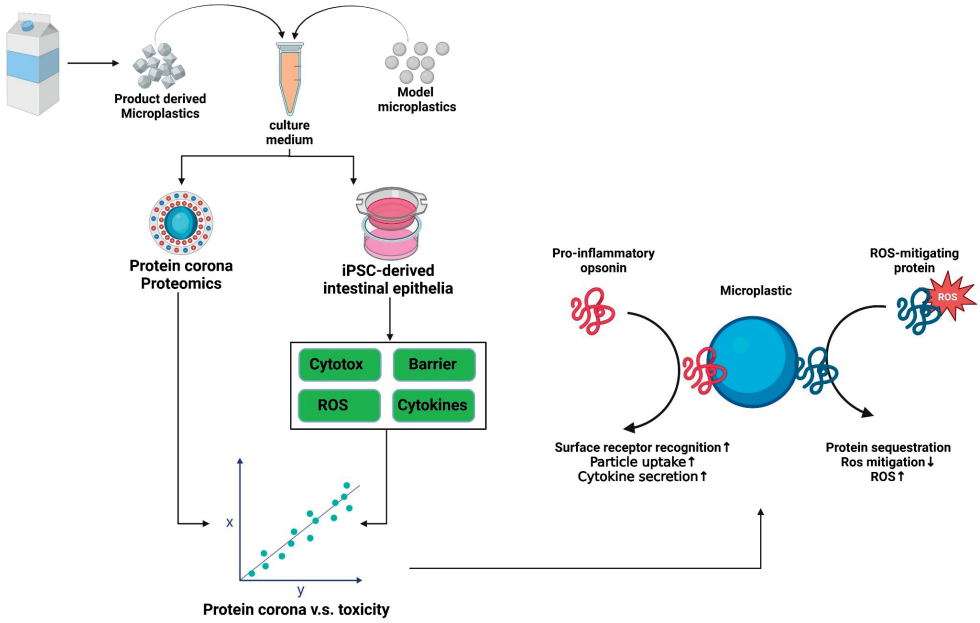

4.3 Introduction

The production of fossil-based plastics is estimated to increase from 460 million tons in 2019, to a stunning amount of 1.4 billion tons by 2060 (577, 578). Of all globally produced plastics, only 9 % is recycled, 19 % is incinerated and the remaining 72 % eventually gets deposited in the environment (4, 577, 578). Exposure of plastic debris to harsh environmental conditions (i.e. UV light and physical stress through abrasion) causes the plastic waste to degrade into micro (<5 mm) and nanosized (<0.1 mm) plastic particles, which persist in the environment, can accumulate in the food chain (13, 579) and have been found in human organs including blood placenta and brain (14, 16, 17). The variety of sizes and shapes of microplastics and the highly diverse presence and composition of additives and fillers (13) highlights the challenges of exhaustive toxicity testing and necessitated the use of *in vitro* screening approaches.

Ensuring the human relevance of *in vitro* methods and test materials is essential for obtaining mechanistic insight into the potential human toxicity of environmentally ubiquitous microplastics (580, 581). Additionally, comprehensive understanding of the impact

of (bio)physicochemical properties on health outcomes are required to allow read-across approaches that reduce unnecessary animal testing and enable safe and sustainable by design plastic development (582). While much remains to be studied regarding the impact of microplastics on human health, their capacity to induce reactive oxygen species and inflammatory responses in exposed tissues likely represent key events in the (suspected) adverse health outcomes (583, 584).

Humans are exposed to microplastics daily through contaminated foodstuffs, swallowing of microplastics that are cleared from the lungs via the mucociliary escalator and microplastic that are released from food-contact materials(168). As a result the intestinal epithelium as the primary barrier faces the highest microplastic exposure of all human tissues (13). Microplastics are limited in their capacity to translocate across the intestinal epithelium (<0.3 % of the applied dose) and microplastics larger than 1.5 µm are not systemically available (13, 580). Conversely, the luminal side of the intestinal epithelium is exposed to all of the ingested microplastics, irrespective of their sizes, making it a likely target organ for microplastic-induced toxicity. Intestinal toxicity of microplastics is typically studied using immortalized intestinal cell lines like Caco-2, which have well-recognized physiological and inflammatory shortcomings (231, 585) that limit the translation of *in vitro* effects to *in vivo* effects (237, 585). Here we set out to use induced pluripotent stem cell (iPSC) derived intestinal epithelial cells (IECs) grown as cell layers as an advanced human-relevant intestinal epithelial cell model.

To address urgent risk assessment needs and eminent societal concerns, human relevant true-to-life microplastics resulting from the degradation of plastic products or waste are to be included in microplastic hazard studies (583, 584). Emerging evidence suggests that relying only on studies with readily available polystyrene (PS) microplastics as the basis for risk assessment of microplastics does not capture the diversity of cellular responses to differing microplastic polymer types (263, 580, 586). True-to-life microplastics on the other hand contain realistic amounts of additives and fillers and thus are representative of real human microplastic exposure (587). In this study we therefore included six highly relevant polymer types including their fillers, being polylactic-acid (PLA) derived from PLA pellets, polyethylene terephthalate with titanium dioxide filler (PET-TiO_2) derived from opaque plastic bottles (587), polypropylene with talc filler (PP-Talc), polyvinyl chloride (PVC) and polyamide (PA) derived from plastic pellets (588), and commercially available 1µm PS as reference particles. Together, this panel of microplastics represents the major polymer types that contaminate our food and the environment (4).

Physiological relevance of the microplastic exposure was further increased by taking the microplastic specific protein corona into account, which forms spontaneously on the microplastic surface in biological environments and can either alleviate or exacerbate

particle toxicity (151-153, 589). The protein corona shields the cell from the reactive particle surface, however the presence of misfolded or immunogenic proteins at the particle surface can trigger increased particle phagocytosis and cytokine secretion(151, 158). Additionally, the protein binding capacity of microplastic surfaces can disrupt cellular protein homeostasis, either by shuttling harmful proteins into the cell interior (i.e., Trojan horse principle) (590) or by sequestering intracellular proteins, rendering them incapable of performing their biological function (591).

Here, we used an iPSC-derived IEC model, comprised of multiple cell types, to study intestinal interactions with a panel of well characterized true-to-life microplastics and a 1 µm PS reference particle. An extensive characterization of the formed protein corona in exposure media was performed using semi-quantitative LC-MS-MS based proteomics. The endpoints assessed were cytotoxicity, barrier disrupting capacity, the ability to generate reactive oxygen species (ROS), and the induction of cytokine secretion, as these represent key events in the adverse outcome upon microplastics exposure (592). Finally, correlations between the composition of the biocorona and observed effects were studied.

4.4 Material and methods

4.4.1 Materials

Phosphate-buffered saline (PBS), paraformaldehyde (PFA), sodium bicarbonate, hydrochloric acid, RPMI-1640 medium, Triton® X-100, Tris-HCL, Tween-20, phenazine methosulfate, and sulphuric acid were obtained from Merck (Amsterdam, The Netherlands). Accutase Cell Detachment solution, penicillin/streptomycin, L-glutamine, non-essential amino acids (NEAA), B27 supplement minus vitamin A, DMEM/F12 medium, glutamax, advanced DMEM, hepExtend supplement, N2 supplement and 5-aza-2'-deoxycitidine were obtained from Fisher Scientific (Landsmeer, The Netherlands). Defined fetal bovine serum (dFBS) was obtained from Cytivia (Medemblik, The Netherlands). Millicell® 24-well inserts with 3 µm pore size were obtained from Millipore, Sigma (Darmstadt, Germany). Whatman filters, trifluoroacetic acid, KCl, dithiothreitol and iodoacetamide were obtained from Sigma Aldrich (Zwijndrecht, The Netherlands). Sequencing-grade trypsin was obtained from Boehringer Mannheim (Mannheim, Germany). mTeSR™ Plus medium, Gentle Cell Dissociation Reagent, Y-27632 Rock-inhibitor, Forskolin, PD98059 A-83-01 were obtained from Stem Cell Technologies (Saint-Egrève, France). Matrigel hESC-Qualified Matrix and Matrigel Growth Factor Reduced Basement Membrane Matrix were obtained from Corning, (New York, USA). Epidermal growth factor, BMP4, FGF2 and the duoset ELISA kits for IL-1β, IL-6, IL-8, IL-18 and TNF-α were obtained from R&D Systems (Dublin, Ireland). Activin A was obtained from Cell Guidance Systems (Cambridge, United Kingdom).

4.4.2 Micro and nanoplastics

Non-fluorescent PS microspheres of 1 µm were obtained from Polysciences (Hirschberg an der Bergstraße, Germany), polylactic acid (PLA) microplastics were provided by AIMPLAS (Valencia, Spain) and titantium dioxide-doped polyethylene terephthalate (PET-TiO_2) microplastics were generated from opaque plastic bottles as described previously (587) and were generously provided by Universitat Autònoma de Barcelona. Polypropylene-Talc (PP-Talc), Polyvinyl-chloride (PVC) and polyamide 6.6 particles (PA) were generated and provided by the Dutch organization for applied scientific research (TNO) as described previously (588).

4.4.3 Characterization of particle suspensions

The particle size and zeta potential of microplastics were determined using a ZS-nano Zetasizer (Malvern Panalytical, Malvern, Great Britain). Microplastic size was determined in intestinal cell differentiation (ICD) medium prepared as described below in section "Differentiation of iPSCs into intestinal epithelial cell layers" and Milli-Q water at a temperature of 37 °C. Zeta-potential was measured at a temperature of 25 ºC in a 10 mM solution of KCl, filtered through a 0.2 µm nylon Whatman filter. Prior to suspension in ICD medium or 10 mM KCl, microplastics were sonicated for 2 min at 70% amplitude using a FB505 cuphorn sonicator (Fisher Scientific, Landsmeer, The Netherlands). Microplastics were diluted to a concentration of 20 µg/ml for both zeta-potential and hydrodynamic size determination. Prior to the measurement, suspensions were mixed using manual pipetting and were transferred to a 1.5 mL PS cuvette. At least three measurements for both size and zeta potential were obtained for each sample.

4.4.4 Prediction of degree of microplastic sedimentation using *in silico* dosimetry

The degree of microplastic sedimentation was determined through *in silico* dosimetry simulations using the distorted grid model (435). The dish depth was set to 6.6 mm as this corresponds to the medium height in Millicell inserts and the particle size was set to the intensity-weighted size average in IEC medium obtained through DLS. The following densities were used for calculating the sedimentation; 1.09 g/ml for PS, 1.68 g/ml for PP-Talc, 1.25 g/ml for PLA, 1.38 g/ml for PVC, 1.14 g/ml for PA and 1.454 g/ml for PET-TiO_2. No dissolution or agglomeration was considered and the remaining settings were left at their default values.

4.4.5 Culture of human induced-pluripotent stem cell (iPSC)

The human induced pluripotent stem cell line CS83iCTR-33n1 was obtained from Cedars-Sinai Medical Center (Los Angeles, CA, United States). Undifferentiated iPSCs were seeded in hESC-Qualified Matrigel Matrix-coated 6-well plates under feeder-free conditions and cultured in mTeSR™ Plus medium (Stem Cell Technologies, Saint-Egrève, France), at

95 % humidity, 5% CO_2 and 37 °C. mTeSR™ Plus medium was replaced every 2-3 days and routine passaging of cells was performed by detaching the iPSCs using Gentle Cell Dissociation Reagent for 5 min at room temperature followed by transfer to a new matrigel hESC-coated 6 well plate. Confocal fluorescence microscopy was used to confirm the presence of VIL^+ enterocytes, $MUC2^+$ goblet cells and LYZ^+ Paneth cells in the iPSC-derived IECs (Supplementary Fig. 3).

4.4.6 Differentiation of iPSCs into intestinal epithelial cell layers

Intestinal epithelial cell induction was performed as previously described (593). First, iPSCs were dissociated as single cells with Accutase for 6 min at 37 °C and 140.000 cells were seeded into each well of a hESC Matrigel-coated 24-well plates. Cells were incubated in 500 µL mTeSR™ Plus medium containing 10 µM Y-27632 Rock-inhibitor for 24 h. Endoderm differentiation was induced using RPMI-1640 medium supplemented with 1% pen/strep (10,000 U/mL), 2 mM L-glutamine, 1 % NEAA, 2 % B27 supplement minus vitamin A, 100 ng/mL Activin A, and 50 ng/mL BMP4. On the second day of differentiation, the medium was changed to BMP-4 free medium and refreshed every day for two consecutive days. Hindgut induction was performed between day 4-8 of differentiation using DMEM/F12 medium supplemented with 2 % dFBS, 1 % glutamax and 250 ng/mL FGF2. On day 8, the cells were dissociated using Accutase for 6 min. Millicell 24-well inserts with 3 µm pore size were coated with growth factor reduced Matrigel basement membrane matrix and seeded on the apical side with 300000 cells/well in Advanced DMEM supplemented with 2 % dFBS, 2 % B27 supplement minus vitamin A, 2 % HepExtend supplement, 1 % N2 supplement, 1 % non-essential amino acids (NEAA), 1 % penicillin-streptomycin, 2 mM L-glutamine and supplemented with 20 ng/mL epidermal growth factor and 3 µM Forskolin (ICD medium) with 10 µM Y-27632 for 3 days. Cells were placed on an SH-200D-O Mini Orbit Shaker (Antylia scientific, Illinois, USA) set at 60 rpm in a humidified stove at 37 °C, and the medium was replaced with ICD medium without Y-27632 every 2-3 days. ICD medium was supplemented from day 14 with the small molecules 5 µM 5-aza-2'-deoxycitidine, 20 µM PD98059 and 15 µM A-83-01 until 26-28 days of differentiation. Cell culture was performed at 37 °C with 5 % CO_2 for all differentiation steps. iPSCs derived from a single donor were differentiated three times between passages 16-18. Each independent iPSC differentiation into IEC layers is considered a biological replicate, denoted as n=3 in the figure legends.

4.4.7 Immunostaining

The differentiated IEC layers were fixed with 3.7 % paraformaldehyde in phosphate-buffered saline (PBS) at room temperature for 15 min, washed twice with PBS, and stored in Milli-Q water at 4 °C. The cells were permeabilizated just prior to staining with 0.3 % Triton® X-100 for 10 minand non-specific binding sites were blocked with 2 % FBS, 2 % bovine serum albumin (BSA) and 0.1 % Tween20 in PBS for 30 min. The membranes

containing the fixed IEC layers were subsequently cut out of the Millicell inserts with a scalpel and were incubated with primary antibodies Villin, Mucin 2 or Lysozyme and Hoechst 33342 for 2 h at room temperature. Chromogranin A expression was also assessed but is excluded from the results due to lack of expression. Thereafter, the IEC layers were washed twice with PBS containing 4 % FBS and were incubated with secondary antibodies for 30 min followed by two more washing steps. The antibodies used are listed in Supplementary Table 2. The filters were placed on a microscopic slide with cells facing up and covered with a drop of Prolong Gold antifade mounting agent and a cover slip. Images were captured with a re-scan confocal microscope (confocal.nl, Amsterdam, The Netherlands). The images were analysed using Fiji version 1.53t.

4.4.8 Trans-epithelial electrical resistance measurements

Transepithelial electrical resistance (TEER) was measured using the EVOM3 Manual Epithelial Volt Ohm Meter and STX4 EVOM™ Electrode (World precision instruments, Florida, USA). The TEER was measured according to the manufacturer's instructions using a 10 µA current. Matrigel coated, cell-free transwells were used to estimate the background TEER. The 24 well plates were kept on water-filled T175 flasks pre-heated to 37 °C to prevent temperature fluctuations during the measurement. TEER values of the IEC layers were measured before and after exposure. No difference in TEER values of any of the conditions was observed prior to exposure (Supplementary Fig. 5)

4.4.9 Microplastic exposure and sample harvesting

Microplastics were sonicated and were subsequently diluted to a final concentration of 125 µg/ml in ICD medium supplemented with 5 µM 5-aza-2'-deoxycitidine, 20 µM PD98059 and 15 µM A-83-01. During exposure, the cells were kept in a humidified incubator at 37 °C for 24 h without orbital shaking. TEER was measured and all IEC layers were apically exposed to 5 µM of cellrox green dye followed by 30-min incubation on a rotary shaker at 37 °C in a humidified incubator. The apical and basolateral media were collected and stored at -80 °C for LDH-based cytotoxicity assessment and measurement of cytokine secretion using enzyme-linked immunosorbent assay (ELISA). The IEC layers were subsequently washed once with PBS and cells were detached from the transwell membrane by addition of 500 µl Accutase followed by a 5-min incubation at 37 °C and scraping using a cell scraper. The cell suspension was collected in 1.5 mL low-protein binding Eppendorf tubes and was centrifugated at 300 RCF for 6 min followed by two PBS washes and resuspension in PBS with 1 % BSA and 1.5 mM EDTA. The cells were measured using an Attune flow-cytometer (ThermoFisher, Massachusetts, USA) directly after harvesting. Microplastic exposures were repeated thrice with iPSC passages between 15-20.

4.4.10 LDH cytotoxicity assay

Cytotoxicity was assessed using a lactate dehydrogenase assay (LDH assay) as was described previously(212). Briefly, 50µl of apical supernatant was transferred to 96 well plates and 150µl of LDH reaction solution consisting of 200 mM Tris buffer (pH 8), 50 mM Li-lactate solution, 5 mM NAD+ solution, 65 mM INT solution, and 29 mM PMS solution was added. The plates were incubated at room temperature for 10 min in the dark. The reaction was stopped by adding 50 µl of 1 M H_2SO_4. Absorbance was measured with SpectraMax id3 and SoftMax Pro 7.1 using 490 nm as the detection wavelength and 680 nm as the control wavelength. Positive controls for cytotoxicity were exposed to 0.1 % triton for 30 min prior to the LDH assay. The final percentage of cytotoxicity was calculated by subtracting measured A680 from the A490 and by subsequently interpolating between the positive control (0.1 % triton X-100) and negative control (ICD medium).

4.4.11 Enzyme-linked immunosorbent assay (ELISA)

The secretion of proinflammatory cytokines by IEC layers upon microplastic exposure was analysed using Duoset ELISA kits for human IL-1β, IL-6, IL-8, IL-18 and TNF-α as described elsewhere (34). The supernatants were diluted if necessary. To exclude any possibility of particle interference we included particle only-controls which consisted of particles in ICD medium without cells (Supplementary Fig. 6).

4.4.12 Flow cytometry-based ROS determination

The cell pellets were used to measure intracellular ROS using an attune flow cytometer. In order to distinguish microplastics from cellular material, first 0.1mm, 0.2 mm, 0.5 mm and 1.0 mm PS spheres (Polysciences, Hirschberg an der Bergstraße, Germany) were analysed using a flow cytometer to determine the forward scatter and side scatter values of microplastics. Cells were distinguished from unbound microplastics by gating out the events which overlapped with the microplastics using the FSC-H and SSC-H channels and singlet cells were distinguished from doublet events based on their FSC-H and FSC-A (Supplementary Fig. 7). The relative level of ROS was determined using cellrox green, a dye that becomes fluorescent upon oxidation. The 525/40 channel was used to determine the relative fluorescence of cellrox green. The obtained relative light units were expressed as fold change increase compared to unexposed control cells to correct for differences in fluorescence background between differentiations.

4.4.13 Microplastic imaging in IEC layers by confocal Raman microscopy

Confocal Raman microspectroscopy (CRM) analyses was performed using an Alpha300 R microscope (WITec GmbH, Germany) equipped with a piezo-scanner (P-500, Physik Instrumente, Karlsruhe, Germany), 532 nm laser source, 63x water immersion objective (Zeiss, W Plan- Apochromat, NA = 1.0), multi-mode fiber (50 µm diameter) and a charge-coupled device (CCD) cooled down to -61 °C. Raman spectra were collected pixel-wise

using a 600 g mm^{-1} grating, a laser power set on ca. 35 mW with an integration time of 0.07 seconds. The cells were measured under wet conditions using sterile PBS. The extracted spectra from images were further analysed in the Project SIX PLUS software (WITec GmbH, Ulm, Germany), where cosmic ray correction, background subtraction, decomposition and de-mixture of recorded spectra were performed. The data set of the mapping field was decomposed into images of different cell components or biomolecules by the fitting procedure, component or cluster analysis as described elsewhere (594).

4.4.14 Proteomics of the protein corona on microplastic in ICD medium

To assess the protein corona formed on the microplastics, we performed LC-MS-MS based proteomics as described previously (595). All microplastics were suspended in ICD medium as described before. The particles were left shaking head over heels for 2 h at 37 °C to stimulate corona formation. Afterwards, the microplastic samples were pelleted using a tabletop centrifuge set at 30000 RCF for 30 minutes. The microplastics were washed twice with 1 M ammonium bicarbonate and once with 50 mM ammonium bicarbonate. The pellet was suspended in 50 µl 50 mM ammonium bicarbonate and peptides were generated using an on-bead protein digestion protocol as described before (596). Briefly, 5 µl of freshly prepared 150 mM dithiothreitol was added and samples were incubated for 30 min at 45 °C while shaking at 500 RPM. Proteins were alkylated by addition of 5 µl of 200 mM iodoacetamide and incubation at 20 °C in the dark for 30 min. Alkylation was terminated by addition of 6 µl of 200 mM of cysteine in ammonium bicarbonate buffer and proteins were digested by addition of 500 ng of sequencing grade trypsin and overnight incubation. The enzymatic digestion was stopped by the addition of 3 µl of 10 % trifluoro acetic acid. Microplastics were separated from tryptic peptides by centrifugation at 30000 RCF for 30 minutes and the peptide samples were cleaned using a C18 µ-column method as previously described (596). Leftover solvent was removed using a rotary evaporator, and the peptides were resuspended in 50 µl of 0.1 % formic acid in demi water. A peptide sample originating from ICD medium without particles was included to distinguish between unbound proteins and proteins part of the protein corona of microplastics. The samples were measured using a nano LC–MS-MS protocol as previously described (596, 597). Briefly, 5 µl of tryptic peptide solution was injected into a 0.10 × 250 mm ReproSil-Pur 120 C18-AQ 1.9 µm beads analytical column (prepared in-house) at 800 bar. A gradient from 9 to 34 % acetonitrile in water with 0.1 % formic acid in 50 min was used. Full scan Fourier transformed mass spectrometry (FTMS) spectra were obtained using an Orbitrap Exploris 480 Thermo electron in positive mode between 380 and 1400 m/z. The 25 most abundant positively charged peaks in the MS scan were fragmented (HCD) with an isolation width of 1.2 m/z and 24 % normalized collision energy. Samples were measured in triplicate. Proteins in each sample were identified by comparing the identified peptides to the uniprot bovine database.

4.4.15 Analysis of LC–MS-MS-based proteomics data

Protein identification and label-free quantification (LFQ) was obtained with MaxQuant (598) (598) using a 2 step approach. In the first step data were analysed with default proteomics settings with enzyme mode set to Trypsin using bovine and porcine databases downloaded from Uniprot. The proteinGroups result obtained was used to create sample specific peptidomics databases from all proteins (excluding contaminants and reversed hits) found. These databases together with a contaminants database were used for the second search that was done in the peptidomics "Unspecific" enzyme mode. ProteinGroups from the second search and were subsequently analysed using an in house developed R-script. First, unreliable proteins, i.e. non-bovine contaminant, proteins identified in less than 2 samples or proteins only identified by modified peptides, were removed from the dataset. The LFQ values were log2 transformed, and missing values were imputed from a normal distribution using a downshift of 3.0 and default band narrowing of 0.3 was used. The ICD-medium sample from the section above was considered background (unbound protein-control) and only proteins which were significantly enriched on microplastics were kept. Differential enrichment analysis was performed using an empirical Bayes procedure as available in the limma package (599) and no multiple testing correction was applied to reduce false negatives. A Venn diagram was generated using the online Venn tool (VIB/UGent Bioinformatics & Evolutionary Genomics group https://bioinformatics.psb.ugent.be/webtools/Venn/) to visualize the overlap of proteins identified on microplastics. The log2 transformed values were used to generate a PCA plot using built-in-R functions, and a hierarchical clustering of the Pearson correlation coefficient between plastics was generated using the DEP R package. We performed differential protein enrichment comparing LFQ values of PS1000 to all true-to-life microplastics using the DEP R package. Differentially enriched proteins were identified using an empirical Bayes procedure as described above, but with Benjamini, Hochberg, Yukuelti FDR based multiple testing correction. Proteins were considered enriched or depleted at an adjusted p value smaller than 0.05 and an absolute log2-fold change larger than 2 and were visualized using a volcano plot. For each protein gene ontology(GO) biological process and molecular function(600), functions, were retrieved using UniProt batch search (601). Functional overrepresentation of GO functions in differentially enriched proteins was determined using a Fishers exact test. No multiple testing correction was applied as the high redundancy in functional annotation can lead to a sharp increase in false negatives (602). GO functions with a p-value equal or smaller than 0.05 were considered significantly overrepresented. The Pearson correlation between the protein LFQ values and the *in vitro* ROS generation, IL-8 secretion and barrier disruption was computed. Finally, a Fisher's exact based functional overrepresentation analysis was performed on the proteins found significantly correlated with ROS, TEER or IL-8 secretion as described above. The results of the proteomics and all analyses are listed in Supplementary file 1.

4.4.16 Statistics and data analysis

Data were analysed using R version 4.4.1 and GraphPad Prism software version 10 (GraphPad Software, CA, USA). Due to a lack of homoscedasticity of the standard deviation of the LDH, TEER, ELISA and ROS data, a non-parametric Kruskal Wallis with Multiple testing correction was done using the FDR-correction method by Benjamini, Krieger and Yukutieli was used for determining significance. The statistics for the proteomics were done as described above. Unless stated otherwise, values are expressed as mean ± standard deviation (SD).

4.5 Results

4.5.1 Exposure of true-to-life microplastics to iPSC derived monolayers.

Before exploring the interactions of microplastics with the iPSC derived epithelia, the physicochemical properties of the microplastic were comprehensively characterized in exposure medium, the fraction of microplastics expressed as microplastic surface deposited reaching the cells was predicted and cellular internalization was confirmed (Experimental design is summarized in Fig. 1 a). True-to-life microplastics and the reference polystyrene microplastics were suspended in intestinal cell differentiation medium (ICD medium) at a concentration of 125 µg/ml and the particle size was measured using dynamic light scattering (DLS) (Supplementary Fig. 1 & Supplementary Table 1). The hydrodynamic sizes of the microplastics ranged between 317 nm for PLA and 1152 nm for PS1000 particles (Fig. 1 b). The particle size was used as an input for *in silico* dosimetry modelling, predicting the effective amount of microplastics reaching cells within 24h under the experimental conditions used (Supplementary Fig. 2 & Materials and methods). The lowest sedimentation was observed for PA (1.07 microplastic cm^2 / IEC surface cm^2), while the highest sedimentation was observed for PVC (3.4 cm^2/cm^2) (Fig. 1 c). The presence of enterocytes, goblet cells and Paneth cells, constituting the major types of IEC cell types was confirmed in the iPSC derived IEC model (Supplementary Fig. 3). Internalization of microplastics by the iPSC derived intestinal epithelia was confirmed by exposure to 125 µg/ml of microplastics for 24 h and visualization of the unlabelled microplastics using the specific Raman bands of the polymers and biomolecules (Supplementary Fig. 4). All microplastic types were found within the cytoplasm in close proximity to the nucleus (Fig. 1 d)

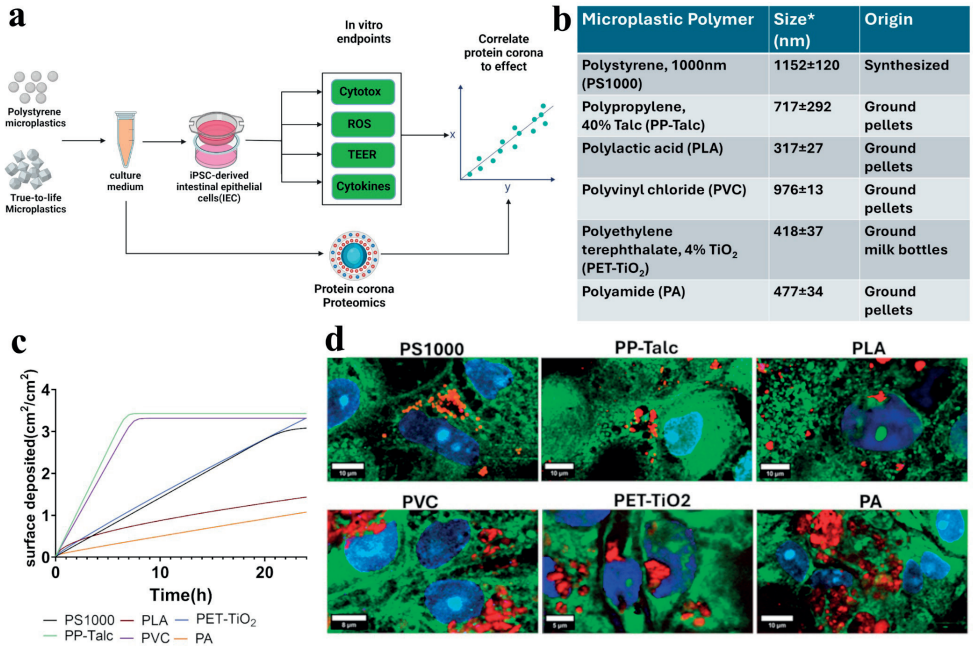

Microplastic Polymer	Size* (nm)	Origin
Polystyrene, 1000nm (PS1000)	1152±120	Synthesized
Polypropylene, 40% Talc (PP-Talc)	717±292	Ground pellets
Polylactic acid (PLA)	317±27	Ground pellets
Polyvinyl chloride (PVC)	976±13	Ground pellets
Polyethylene terephthalate, 4% TiO_2 (PET-TiO_2)	418±37	Ground milk bottles
Polyamide (PA)	477±34	Ground pellets

Fig. 1. Overview of method, materials and exposure characterization

(a) Graphical overview of methodology, briefly true-to-life or polystyrene microplastics were added to ICD medium and iPSC-derived IECs were exposed for 24h. Afterwards the degree of cytotoxicity, barrier disruption, intracellular ROS generation and IL-6/IL-8 cytokine secretion was assessed. Proteomics on the protein corona formed in ICD medium was assessed semi-quantitatively using LC-MS-MS and the microplastic protein corona composition was correlated to observed in vitro effects. (b) Overview of the microplastics used in this study and their origin. * The size represents the intensity-weighted size in ICD medium as measured by DLS ± SD. (c) In silico sedimentation prediction using the distorted grid model (435) of all microplastics shown as total microplastic surface deposited (in cm2) per cm2 of IEC surface. The X-axis indicates the duration of exposure, and the Y-axis indicates degree of deposition. The colour of each line indicates the respective microplastic as shown in the legend. (d) Cellular internalization of all microplastics used in this study was assessed employing confocal Raman microscopy. The blue colour indicates the distribution of DNA (nuclei), the green colour indicates the distribution of proteins (cytoplasm) and the red colour indicates the respective microplastic shown above each image. The scale bars of each respective image represent 10 µm for PS1000, PP-Talc, PLA and PA, 8µm for PVC and 5 µm for PET-TiO2. The spectra used to discriminate each microplastic are shown in Supplementary Fig 4.

4.5.2 Effects of microplastic exposure on human iPSC-derived IEC layers

After 24 h of microplastic exposure to 125 µg/ml, the cytotoxicity, barrier integrity, intracellular ROS generation and pro-inflammatory cytokine secretion by the iPSC-derived IEC layers was determined (Fig. 2). Absence of cytotoxicity upon exposure to 125 µg/ml of each microplastic for 24 h was shown by a lack of lactate dehydrogenase (LDH) leakage, a

proxy for cytotoxicity (Fig. 2 a). Exposure to PP-Talc or PVC microparticles induced barrier disruption as demonstrated by a significantly reduced the average TEER from 1058 Ωcm^2 to 272 Ωcm^2 and 430 Ωcm^2, respectively (Fig. 2 b). Exposure to the other microplastics did not affect the barrier integrity. Exposure of the iPSC-derived IECs to PP-Talc, PET-TiO_2 or PA microplastics significantly increased the intracellular ROS levels by 1.9, 4.0 and 2.4-fold compared to medium control, respectively (Fig. 2 c). Exposure to PS1000, PLA or PVC microplastics did not induce cellular ROS generation. A significant increase in apical secretion of IL-6 from 57 pg/ml to 253 pg/ml was observed after exposure to PP-Talc microplastics, while no differences in basolateral IL-6 secretion were observed (Fig. 2 d-e). PP-Talc and PVC microplastics exposure significantly increased apical IL-8 secretion from 183 pg/ml to 1008 pg/ml and 559 pg/ml respectively (Fig. 2 f). PP-Talc, PVC and PA microplastic exposure induced a significant increase in basolateral IL-8 secretion from 311 pg/ml to 746, 529 and 522 pg/ml respectively (Fig. 2 g). No IL-1β, IL-18 or TNF-a was detected in the cell culture media of either exposed or unexposed iPSC-derived IECs (data not shown).

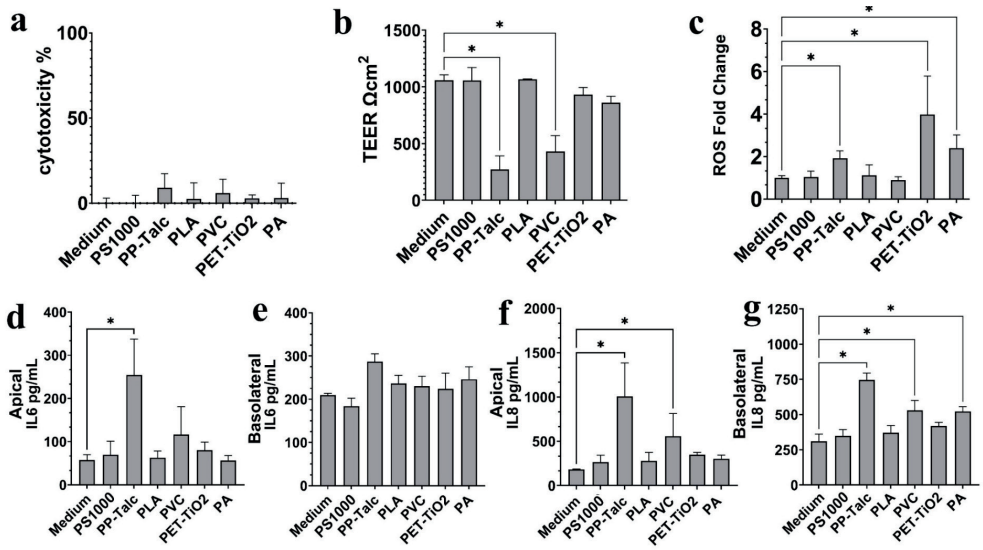

Fig. 2. Response of human iPSC-derived IEC layers to microplastic exposure.

(a) cytotoxicity determined by LDH leakage, (b) Barrier integrity assessed by measuring Transepithelial Electrical Resistance(TEER), (c) Intracellular ROS formation assessed by flow cytometry(n=6) (d) apical IL-6 secretion, (e) basolateral IL-6 secretion, (f) apical IL-8 secretion, (g) basolateral IL-8 secretion. * $p < 0.05$. Unless indicated otherwise data shows mean ± SD of n=3.

4.5.3 Proteomics of the protein corona on microplastics in ICD medium

A semiquantitative proteomics assessment of the microplastic-associated protein corona was performed using LC-MS-MS. PLA microplastics were excluded from the proteomics dataset and all subsequent analyses due to the low presence of proteins on the microplastic surface (see Supplementary Table 3). Only high confidence proteins, i.e. non contaminant, not identified by single peptide, present in at least two technical replicates and significantly different from medium control were considered (596). First, the global proteome of the protein corona on the microplastics was compared using a Venn diagram, hierarchical clustering and principal component analysis, followed by an analysis of differentially enriched proteins on true-to-life microplastics compared to PS1000 (Fig. 3).

In total, 461 high confidence proteins were identified of which 277 on PS1000, 322 on PP-Talc, 226 on PVC, 345 on PET-TiO_2 and 414 on PA microplastics. The protein corona of PA, PP-Talc, PET-TiO_2 and PVC microplastics contained 49, 7, 11 and 5 unique proteins respectively, while 166 proteins were shared between all microplastic coronas (Fig. 3 a). A Pearson correlation was performed to indicate similarities observed between the protein LFQ values (Fig. 3 b). The highest correlation was observed between PP-Talc and PET-TiO_2 (0.77) followed by PP-talc and PA (0.75), while the lowest correlation was observed between PA and PVC (0.58). A high consistency in protein LFQ values was observed between replicates (Fig. 3 c). High similarity in LFQ values was observed between the protein coronas on PET-TiO_2 and PP-Talc, as well as PS1000 and PVC while the least similarity was observed between PA and PVC (Fig. 3 b-c). The top 10 corona proteins with the highest influence on the variance explained by Principal component 1 (i.e., 43.8 %) contained 4 proteins involved in chemokine binding and immune response while the variance explained by Principal component 2 (i.e., 16 %) was dominated by proteins involved in immune reaction (3/10) and heme biosynthesis and coagulation (2/10) (Supplementary file 1). The differential enrichment analysis comparing the LFQ values of true-to-life microplastics to PS1000 revealed that most enriched proteins were found in the corona on PA>PET-TiO_2>PP-Talc>PVC with 88, 57, 52 and 17 differentially enriched proteins respectively (Fig. 3 d-g). The list of all differentially enriched proteins and their functional annotations are provided in Supplementary file 1.

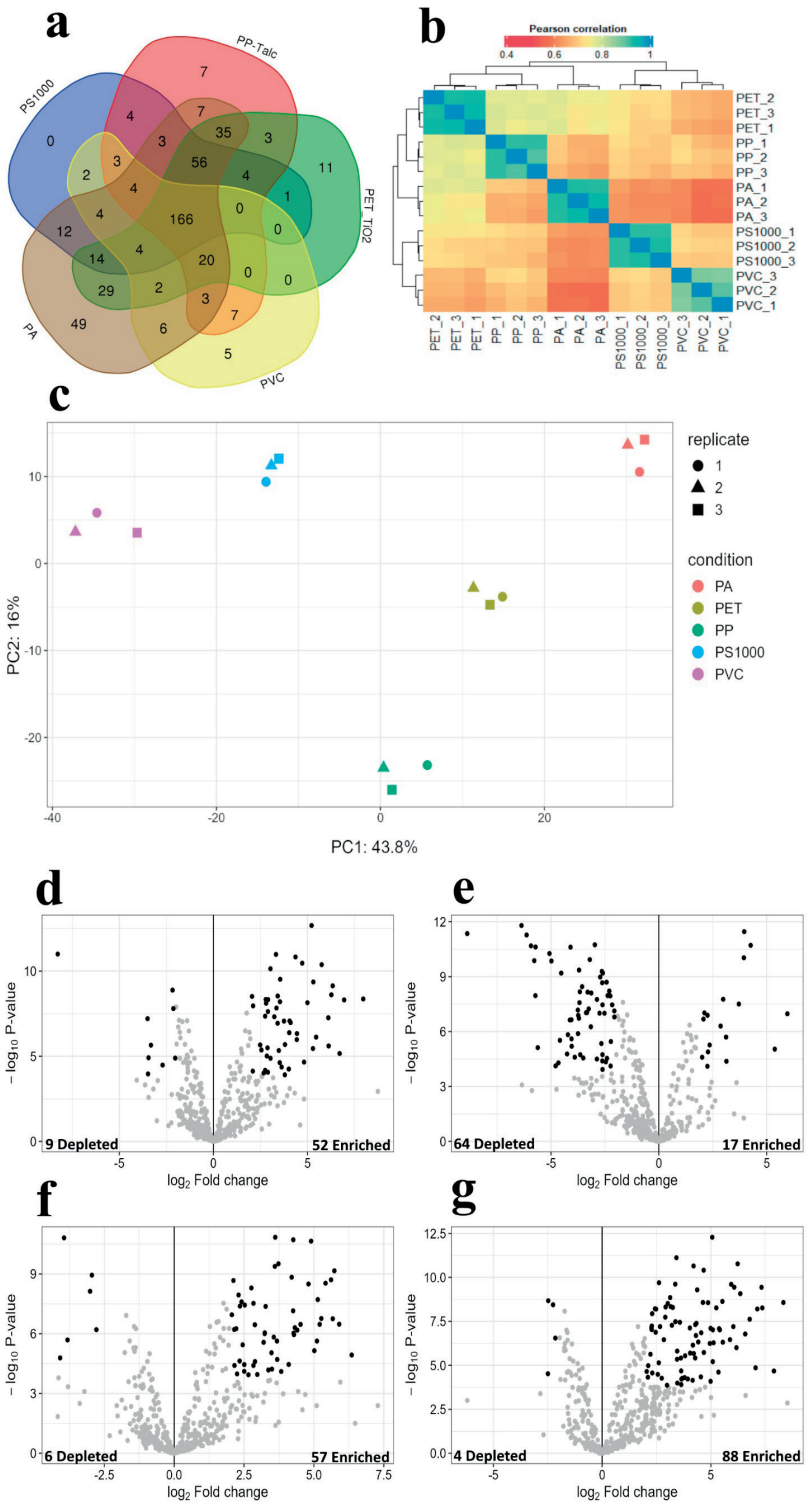
a
PS1000
PP-Talc
PET_TiO2
PA
PVC
b
Pearson correlation
0.4
0.6
0.8
1
PET_2
PET_3
PET_1
PP_1
PP_2
PP_3
PA_1
PA_2
PA_3
PS1000_1
PS1000_2
PS1000_3
PVC_3
PVC_2
PVC_1
c
PC2: 16%
PC1: 43.8%
replicate
1
2
3
condition
PA
PET
PP
PS1000
PVC
d
9 Depleted
52 Enriched
e
64 Depleted
17 Enriched
f
6 Depleted
57 Enriched
g
4 Depleted
88 Enriched
− log10 P-value
log2 Fold change

Fig. 3. Global overview of protein corona composition on the microplastics.

(a) Venn diagram showing the number of proteins identified in the microplastic protein coronas. Each microplastic is represented by an ellipsoid and overlap between the ellipsoids represents the number of shared proteins. (b) Hierarchical clustering of label-free-quantification (LFQ) values of proteins. The scale indicates the r-value of the Pearson correlation. PP is shorthand for PP-Talc (c) Principal component analysis the LFQ values of identified proteins. The legend to the right indicates the sample and microplastic polymer type. (D-G) Number of significantly depleted or enriched proteins in corona's on (d) PP-Talc, (e) PVC, (f) PET-TiO2 and (g) PA compared to PS1000 microplastics. On the Y-axis the –log transformed p-value is depicted plotted against the Log2 fold change compared to PS1000 microplastics on the X-axis. Black dots indicate significantly enriched or depleted proteins compared to PS1000 microplastics, while the grey dots are not significantly different compared to PS1000 microplastics. A protein was considered significantly enriched or depleted if the holm-corrected p-value ≤ 0.05. The number of enriched or depleted proteins in the coronas is shown on the bottom of each panel. PLA is not shown in this figure as it was excluded from the proteomics assessment due to lack of protein binding. (n=3).

A Fisher's exact test was performed on all proteins enriched on the true-to-life microplastics to determine whether there was an overrepresentation of protein functions that match the effects observed upon exposure of the iPSC-derived IECs (Fig. 4). The abundance of overrepresented protein functions followed a similar pattern as previously seen with the differential expression analysis; namely PA> >PP-Talc>PET-TiO_2>PVC with 15 overrepresented functions for PA, 5 for PP-Talc, 4 for PET-TiO_2 and 2 for PVC (Fig. 4 a-d). The corona on PP-talc and PVC microplastics contained an overrepresentation of functions in inflammatory and innate immune response respectively, while enriched proteins on PA showed overrepresentation of numerous protein functions related to innate immunity and complement cascade activation. Enriched proteins on PET-TiO_2 showed an overrepresentation of cellular oxidant detoxification functions and hydrogen peroxide detoxification.

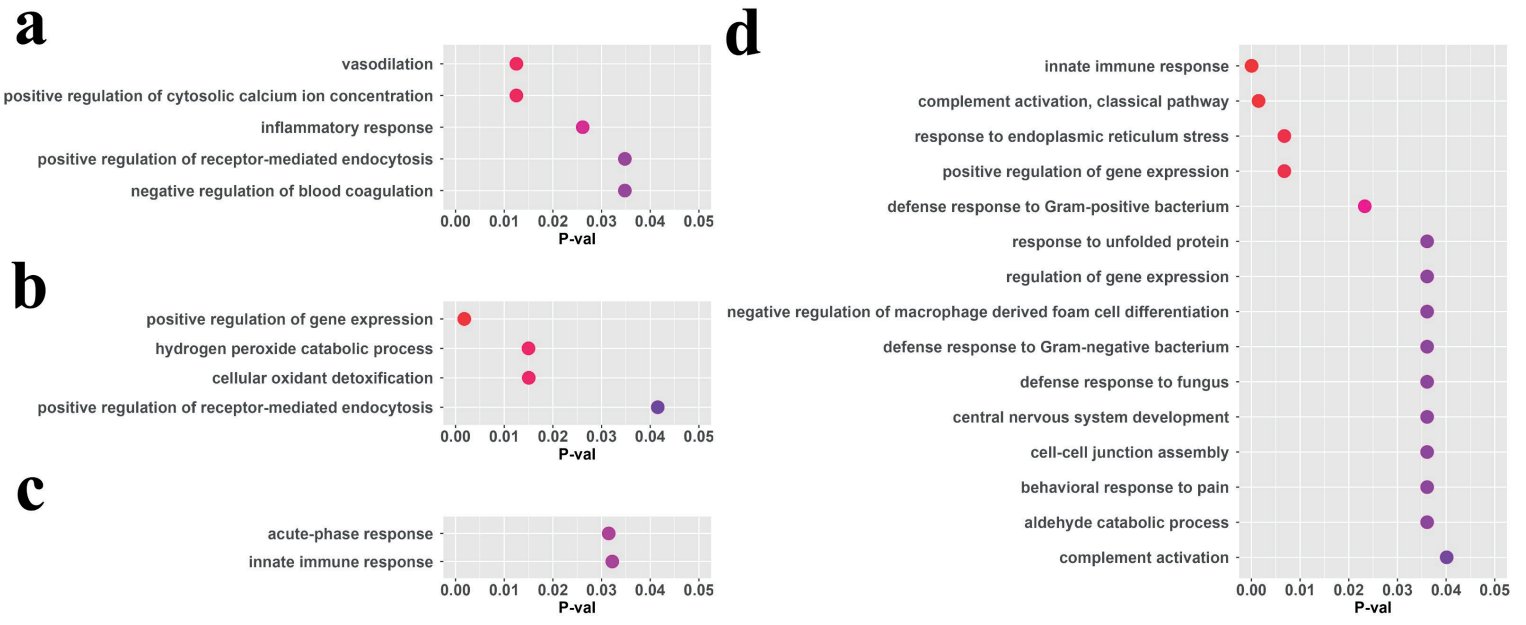

Fig. 4. Overrepresented protein functions of enriched proteins on true-to-life microplastics compared to PS1000 microplastics.

Protein functions which were overrepresented on proteins enriched on (a) PP-Talc, (b) PET-TiO_2, (c) PVC and (d) PA compared to PS1000. The Y- axis indicates the name of the function and the X-axis and colour of the dots indicate the p-value after a Fisher's exact-test without multiple testing correction. (n=3)

4.5.4 Correlation of corona protein composition and effects to iPSC-derived IECs

To assess whether the proteins identified on the protein corona on the respective microplastics may be predictive of the effects observed in iPSC-derived IEC, a Pearson correlation between the protein abundance and all *in vitro* effects to iPSC-derived IECs was determined (Fig. 5).

In total, 41 proteins were positively correlated to ROS, 4 proteins were correlated to reduced TEER values, 22 proteins to total IL-6 secretion and 15 proteins to total IL-8 secretion (Fig. 5). All significant correlations showed a strength of correlation between 0.88 and 0.99 with the effects observed in iPSC-derived IECs. Numerous key proteins involved in ROS detoxification (i.e., catalase, glutathione peroxidase A) and inflammation (i.e., kinogens, complement proteins), were amongst the proteins most correlated to ROS (Fig. 5 a) and cytokine secretion respectively (Fig. 5 c-d). To determine whether any specific protein functions were overrepresented amongst correlated proteins, a Fisher's exact test was performed (Table 1).

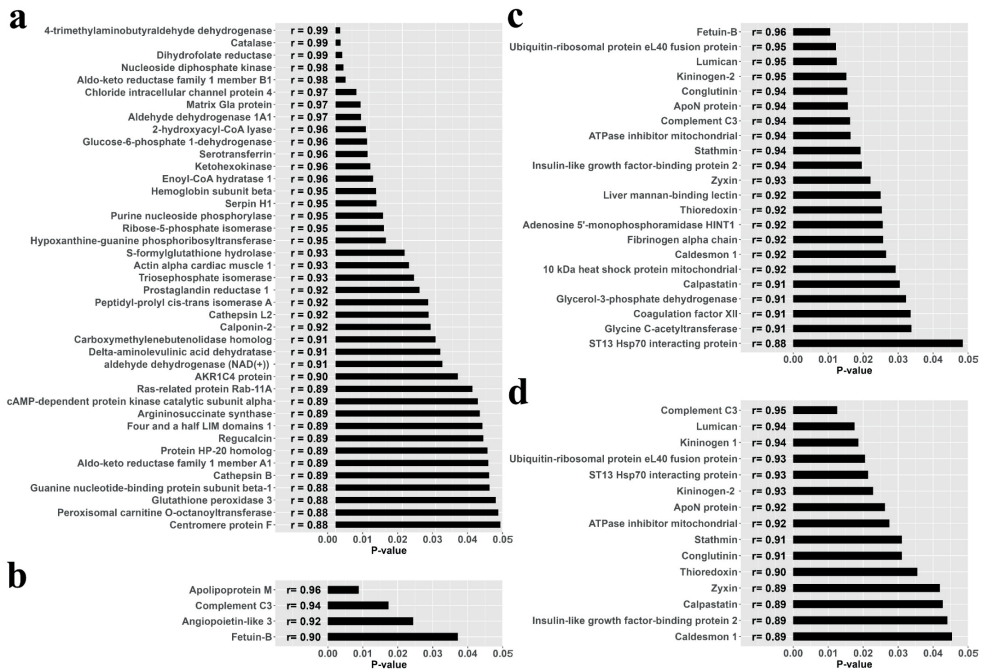

Fig. 5. Corona proteins significantly correlated with *in vitro* effects.

Proteins whose presence was significantly correlated with (a) cellular ROS, (b) TEER, (c) IL-6 secretion, and (d) IL-8 secretion. The Y-axis indicates the protein and the X-axis indicates the p-value of the correlation. The strength of the correlation, the Pearson correlation coefficient "r" is shown to the right of the respective protein name. only positive correlations are shown. A correlation was considered significant if the p-value ≤ 0.05 (n=3).

Table 1. Functional enrichment of proteins correlated to iPSC-derived IEC effects

Protein function	Over enriched in	p-value
Hydrogen peroxide catabolic process	ROS generation	0.006
Cellular detoxification of aldehyde	ROS generation	0.008
L-ascorbic acid biosynthetic process	ROS generation	0.008
Proteolysis involved in protein catabolic process	ROS generation	0.041
Fatty acid metabolic process	TEER decrease	0.001
Positive regulation of cytosolic calcium ion concentration	IL-6 secretion	0.003
Vasodilation	IL-6 secretion	0.003
Negative regulation of blood coagulation	IL-6 secretion	0.008
Inflammatory response	IL-6 secretion	0.016
Positive regulation of cytosolic calcium ion concentration	IL-8 secretion	0.001
Vasodilation	IL-8 secretion	0.001
Negative regulation of blood coagulation	IL-8 secretion	0.004
Inflammatory response	IL-8 secretion	0.006

For proteins correlated with ROS generation, four protein functions were significantly overrepresented of which two could be clearly linked to ROS; cellular detoxification of aldehyde and hydrogen peroxide catabolic process. The only protein function overrepresented in TEER correlated proteins was fatty acid metabolic process. Protein functions correlated to IL-6 and IL-8 secretion were identical; potentially indicating a shared mechanism of action. Finally, to visualize that proteins correlated to *in vitro* endpoints showed upregulation in the true-to-life microplastic protein coronas compared to the PS corona, we plotted their protein abundances (Fig. 6). Proteins correlated with ROS generation showed the highest fold change in PET-TiO_2, followed by PA and PP-Talc (Fig. 6 a), proteins correlated with a TEER decrease were most abundant for PP-talc followed by PVC (Fig. 6 b) and proteins correlated with either IL-6-secretion (Fig. 6 c) or IL-8 (Fig. 6 d) secretion were most abundant in PP-Talc followed by PET-TiO_2 and PA.

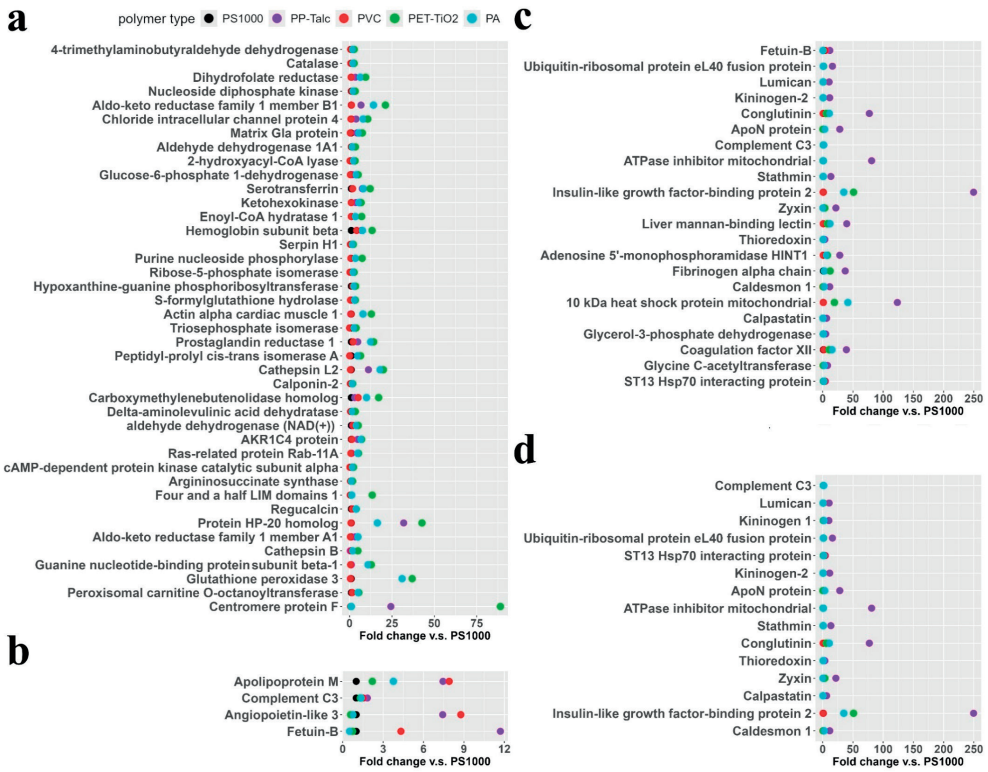

Fig. 6. Abundance of proteins correlated with iPSC-derived IEC endpoints in microplastic protein coronas

Abundance of proteins significantly correlated with (a) cellular ROS generation, (b) TEER decrease, (c) IL-6 secretion and (d) IL-8 secretion. The Y-axis indicates the respective protein and the order of proteins is from strongest correlation to weakest correlation. The X-axis indicates the fold change in LFQ value compared to PS microplastics. The colour of the dots indicates the respective particle as indicated in the legend at the top left of the figure (n=3).

4.6 Discussion

Here we report (polymer-specific) true-to-life microplastics toxicity to human iPSC-derived IEC layers and correlate observed toxic effects to the protein corona composition. Specifically, we found that PP-Talc and PVC microplastics reduced the barrier integrity of IEC layers apparent by the reduced TEER, PET-TiO_2, PP-Talc and PA microplastics increased cellular ROS generation, PP-Talc induced the secretion of the pro-inflammatory cytokine IL-6, and that PP-Talc, PVC and PA microplastics increased the secretion of the pro-inflammatory cytokine IL-8. These effects were not induced upon exposure to PS microplastics. The semiquantitative proteomics analysis of the microplastic coronas revealed the polymer-specific enrichment of proteins. Lastly, significant correlation between the

abundance of specific proteins and the observed *in vitro* effects on the iPSC-derived IEC layers were established. Overall, the outcome of this study shows the need to incorporate true-to-life microplastics in future hazard studies and to include the contribution of the protein corona on these outcomes.

Based on lessons learned from studies with engineered nanomaterials, we first comprehensively characterised the microplastic suspension in the cell culture medium and predicted the fraction of the microplastics deposited on the iPSC-derived IEC cell layers using the distorted grid sedimentation model (435). The hydrodynamic diameter in the cell culture medium was different for each microplastic and ranged between 0.3 µm for PLA to 1.15 µm for PS1000 (Fig. 1 b & Supplementary table 1). As biochemical reactions take place at surfaces of materials (170), we consider the predicted deposited microplastic surface/cm^2 as the most relevant metric to express the effective microplastic concentration deposited. The largest difference in sedimented particle surface was a 3.2-fold lower microplastic surface/cm^2 between PA and PP-talc microplastics (Fig. 2 b). The calculated deposition in terms of microplastic surface area could be used to correct the microplastics concentrations for future toxic potency ranking of the microplastics. In addition, we confirmed cellular internalisation of all used microplastic polymer types by using confocal Raman microscopy, which currently is the only visualisation methodology for true-to-life microplastics in cells (603, 604). Based on the polymer type specific Raman spectra we showed the presence of microplastics in the cytoplasm, confirming that all microplastics used in this study were internalized by iPSC-derived IECs.

Next, we confirmed absence of cytotoxicity due to microplastic exposure of the iPSC-derived IEC layers by measuring LDH leakage (Fig. 2 a). None of the microplastics induced significant cytotoxicity upon 125 µg/ml microplastic exposure for 24h. Previously, a significant increase in apoptosis after exposure to 10 µg/ml of 50 nm PS nanoplastics for 14 days in iPSC-based organoid-derived intestinal monolayers was observed (605), which emphasises that microplastic toxicity is size specific. No other studies could be identified that have used iPSC-derived intestinal models to examine the cytotoxic effects of microplastics. A general lack of intestinal cytotoxicity after true-to-life or PS microplastic exposure was previously demonstrated, using 100-400 µg/ml of 0.1-0.25 mm PLA (39, 606), 30 µg/ml of 0.8 mm PET (607), 110 µg/ml of 1.2 mm PVC (212) or 50-1000 µg/ml of PS microplastics of various sizes ranging between 0.025 mm and 10 mm (206, 212, 321, 608, 609) using co-cultures of Caco-2 and HT29-MTX. As no general cytotoxicity upon microplastic exposure was observed, we further explored barrier disruption, cellular ROS formation and cytokine secretion, which are regarded as key events in putative adverse outcome pathways for nano- and microplastics (135, 592).

A polymer-specific reduction in barrier integrity, increased cellular ROS generation and increased secretion of the pro-inflammatory cytokines IL-6 and IL-8 upon exposure to 125 mg/ml true-to-life microplastics for 24 hours was observed in iPSC-derived IECs. PP-Talc and PVC microplastics reduced the TEER of the iPSC-derived IEC layer by 74 % and 59 % respectively, while the other microplastics did not affect the TEER (Fig. 2 b). Previous studies describing the exposure of intestinal Caco-2/HT29-MTX cell cultures showed no effect on barrier integrity after 24h exposure to PS microplastics 0.05-1µm, 50 µg/cm^2 (~110 µg/ml) of 1.2 µm PVC or 0.35-1.1 µm polyethylene (PE) microplastics or 50 µg/ml of PLA microplastics (39, 212, 263, 610, 611), indicating that microplastics generally do not compromise barrier properties. Effects of PA, PP and PET-TiO_2 microplastic exposure on intestinal barrier properties have not been reported before. The intestinal barrier disruption by PP and PVC has not previously been reported in vitro, but is in line with what has been reported in mice (612, 613). The discrepancy in the barrier disruption by PVC reported here and previously reported lack of barrier disruption in Caco-2 and HT29-MTX co-cultures (212) indicates an increased sensitivity of the iPSC-derived IEC layer towards barrier disruption. Studies making a direct comparison between iPSC derived epithelia and Caco-2 models are required to confirm the relative sensitivity of the models. The strong reduction in barrier capacity by PP-Talc and PVC reported here raises concerns, as both PVC and PP microplastics with talc fillers are frequently used for food-contact materials (614, 615). The strong reduction in barrier capacity by PP-Talc and PVC reported here raises concerns, as both PVC and PP microplastics with talc fillers are frequently used for food-contact materials (614, 615).

PP-Talc microplastic exposure increased both IL-6 and IL-8 secretion while exposure to PA and PVC microplastic exposure only increased IL-8 secretion (Fig. 2 d-g). Increased IL-6 levels can disrupt the function of tight junctions on intestinal cells leading to increased barrier permeability, while upregulation of IL-8 is frequently associated with increased barrier permeability through an, as of yet, unelucidated mechanism (216, 217). The observed decrease in TEER after exposure to PVC or PP-talc may therefore in part be due to the increased IL-6 and IL-8 secretion. No effects on IL-1β, IL-6, IL-8 cytokine secretion was observed upon exposure of Caco-2 cells to 282 µm PP and 72 µm PA microplastics at concentrations approximately 10-fold higher than those used here (322). However, as the particles used in those studies are larger than the upper limit of endocytosis (i.e. larger than 10 mm, (616)), it is difficult to generalise these findings to smaller particles. Exposure of an intestinal triple cell culture model consisting of Caco-2, HT29-MTX and THP-1-derived macrophages for 24h to 50 µg/cm^2 of 0.05 mm PS or 1 µm PVC microplastics did not affect IL-6, IL-8, IL-1β or TNF-α secretion (212). Exposure of Caco-2 to polydisperse true-to-life PP microplastics derived from heat-treated baby-bottles increased gene expression of IL-6, IL-1β and TNF-α (617). Overall, this suggest that PP-Talc, PVC and PA

microplastics, which are polymer types that are abundantly used by consumers (580) , specifically induce cytokine secretion.

We found that PET-TiO_2, PP-Talc and PA microplastic exposure increases intracellular ROS by 4.0, 1.9 and 2.4-fold respectively (Fig. 2 c). The strong ROS generation upon PET-TiO_2 and PP-Talc microplastics exposure raises the question whether the ROS is generated by the polymer itself or by the TiO_2 or Talc fillers present in the microplastics. Previously, polydisperse PP was shown to induce ROS in Caco-2 cells, however, due to poor material characterisation the presence of fillers or other contaminants could not be excluded (617). Likewise, talc has been suggested to be carcinogenic through a ROS mediated mechanism, however this remains a matter of controversy (618). Exposure of mouse macrophages, human lung epithelial cells, primary human mononuclear cells, monocytes or lymphocytes to true-to-life PET microplastics derived from food-contact materials resulted in a significant increase in ROS, underpinning the results found here (619-621). Food-grade TiO_2 particles have been reported to induce ROS in the intestine, though only at concentrations >50 µg/ml (135, 622), thus making it unlikely that the TiO_2 present in the PET-TiO_2 (4 % of total plastic weight (587)), generates ROS in this study. The data presented here show that PET-TiO_2 microplastics derived from food-contact materials, as well as PP-Talc and PA derived from plastic pellets increase ROS on iPSC-derived IECs which might point at a hazard for consumers.

While it is well established that the protein corona contributes significantly to the biological effect of microplastics(151-153, 589), there is little information on the composition of non-polystyrene microplastic protein coronas or how the composition of the protein corona is affecting *in vitro* outcomes. First, we compared the abundance of proteins found on true-to-life microplastics to those on PS1000 (Fig 3. d-e). We found enrichment of proteins with inflammatory or immune functions on PVC, PP-Talc and PA microplastics (Fig. 4 a,c-d), while proteins on PET-TiO2 were enriched for cellular oxidant detoxification and hydrogen peroxide catabolism functions (Fig. 4 b). Significant enrichment of immunomodulatory proteins and proteins that regulate oxidative stress, was previously found on the protein corona of poly-vinyl-acetate and SiO_2 nanoparticles after incubation in respiratory tract lining fluid (623), supporting the results found here. To identify the proteins which most likely contribute to the in vitro effects we calculated the Pearson correlation between protein abundance and degree of ROS formation, barrier disruption, Il-6 secretion and IL-8 secretion (Fig. 5 & Table 1).

ROS generation correlated with the abundance of proteins involved in hydrogen peroxide catabolism including catalase, numerous aldehyde dehydrogenases, which mitigate tissue damage due to ROS (624) and proteins that biosynthesise L-ascorbic acid, a ROS scavenging metabolite which can mitigate nanoparticle-induced tissue damage (625)

(Fig. 5 a). The correlation between protein abundance and ROS reported here is stronger than previously reported for metallic nanoparticles (626), which may be due to the large number of proteins identified here or the lower inherent ROS generation by microplastics compared to metallic nanoparticles due to the lack of Fenton reactions at the surface (627). The protein functions that correlated well with ROS matched the protein functions found overrepresented in the protein corona of PET-TiO_2 microplastics, the strongest ROS inducer within our panel of microplastics. Proteins that were correlated to increased ROS generation are known to be involved in ROS mitigation or the mitigation of downstream effects of ROS. Increased activity of these proteins would be expected to reduce ROS generation, yet their presence on the protein corona correlated positively with ROS generation. This leads us to postulate that the binding of intracellular ROS mitigating proteins to microplastics like PET-TiO_2 renders them inactive, effectively leading to the increasing ROS generation observed here.

Similarly, we assessed the correlation between cytokine secretion and protein abundance (Fig. 5 c-d). Proteins correlated to either IL-6 or IL-8 secretion exhibited overrepresentation of pro-inflammatory proteins like kininogens 1&2 (628), complement C3, a strong activator of phagocytosis and local inflammation (629) and lumican, which is an extracellular matrix protein that regulates inflammation in response to TLR-4 ligands (630). Kininogen 1&2, fibrinogen and complement C3, are opsonins which were shown before to be abundant in nanoparticle protein coronas and lead to increased phagocytotic particle uptake(153, 596, 631). The Fisher's exact test showed that the proteins correlated to either IL-6 or IL-8 secretion showed overrepresentation of proteins involved in the inflammatory response, which matches protein functions overrepresented in the protein corona of PP-Talc and is related to protein functions enriched on PVC and PA microplastics. In addition, enrichment of positive regulators of cellular calcium, vasodilating proteins, and proteins reducing blood coagulation was observed. While it is well known that increased cellular calcium plays a role in many biological processes including inflammation (632), the role of proteins related to vasodilation in cellular IL-6 or IL-8 secretion is less apparent. While *in vivo* vasodilation is commonly observed in acute inflammation and may be involved in vascular stiffening upon chronic inflammation (633, 634), the relevance to *in vitro* is unclear.

The majority of proteins which correlated to cytokine secretion are either involved in the onset of immune reactions or are opsonins involved in recognition and phagocytosis of particles and as such increased presence of these proteins is expected to increase cytokine secretion, as observed here. We therefore postulate that protein corona induced cytokine secretion is due to a direct interaction of proteins on the surface of microplastics with iPSC-derived IEC surface receptors resulting in the observed increased cytokine secretion. In Addition, an increased uptake of microplastics due to the enriched presence

of opsonins might shuttle pro-inflammatory proteins into the cell via a presumed "Trojan horse principle", further increasing the cellular inflammatory response. The potential role of the protein corona in driving in vitro effects is supported by previous studies that report that the protein corona of diesel exhaust, SiO_2 and TiO_2 particles may enhance IL-6 and IL-8 secretion in macrophages (635, 636) and that heat shock proteins and complement and coagulation factors on TiO_2 and SiO_2 protein coronas correlated with IL-8 secretion, ROS induction and IL-1β secretion (626). Lastly, we found that proteins correlated with reduced TEER value showed a functional enrichment for fatty acid metabolic process, but no clear relation with barrier integrity could be established based on existing literature.

While this study highlights the differences in toxicity between PS and true-to-life microplastics, there are still important limitations which should be addressed in future studies. In the intestine, microplastics will be exposed to the harsh and complex digestive environment and will interact with the intestinal microbiota. Recently, we showed that the protein corona formed during *in vitro* gastrointestinal digestion is retained in cell culture medium and can significantly increase the uptake of microplastics (596). iPSC-derived IEC models thus far have not been exposed to *in vitro* intestinal digesta which are toxic to intestinal cells in vitro(637) and require extensive optimization which was outside of the scope of this study. Additionally, the assessment of lipid components of the biocorona in future studies would be of interest, as it was shown that microplastics can have a strong affinity for lipids, thus forming distinct lipid coronas (121) with, as of yet, unknown biological effects. While we have shown strong correlations between the protein composition and in vitro effects, further studies are required to prove causation. Previous studies confirmed the importance of albumin and apolipoprotein for particle uptake by artificially coating the microplastics in absence of other proteins (638, 639). While confirmation of causation lies outside the scope of this study, a similar approach could be used to assess if microplastics interfere with ROS scavenging capacity or if specific proteins trigger cytokine secretion. An inherent limitation of assessing true-to-life microplastic toxicity is the heterogeneity of particle sizes and polydispersity of the material. While the inclusion of *in silico* dosimetry as implemented in the current study can help to offset particle differences by calculating the deposited dose, differences in cellular uptake due to size-specific pathways cannot be excluded.

4.7 Conclusion

Here we show clear differences in toxicity induced by microplastic-biocorona complexes of true-to-life microplastics compared with the most frequently studied PS microplastics. The marked difference in toxicity observed between PS and true-to-life microplastics cautions us to critically interpret previous findings that predict microplastic toxicity solely

using PS particles. We show that true-to-life microplastics have a unique and distinct protein corona composition that correlates well with observed *in vitro* effects. Previously, we showed that intestinal digestive proteins were retained in the microplastic corona upon *in vitro* gastrointestinal digestion of PS microplastics increased the cellular uptake, underpinning the importance of the protein corona for cellular interactions (596). The results presented here emphasize the need for a polymer type specific hazard assessments and open possibilities for defining criteria for future safe by design plastics.

4.8 Acknowledgements

The authors would like to thank prof.dr.ir. Ivonne M.C.M. Rietjens for valuable suggestions on the manuscript, supervision and stimulating discussions. The authors would like to thank Raquel Llorens-Chiralt for her aid in the obtention of polylactic acid produced by AIMPLAS. This project has received funding from the European Union's Horizon 2020 research and innovation program under grant agreement No. 965196 [H.Br/T.V./I.E.L.], the Horizon Europe project "European Partnership for the Assessment of Risk from Chemicals (PARC)" under grant agreement No. 101057014 [H.Bo], from the MOMENTUM project (project number 458001101) which has been made possible by ZonMw Programme Microplastics and Health, and Health-Holland, Top Sector Life Sciences & Health[M.B/S.Y./H. Bo.] and from the Lymphchip NWO grant No. NWA-ORC 2019 1292.19.019 [G.A].

4.9 Supplementary information

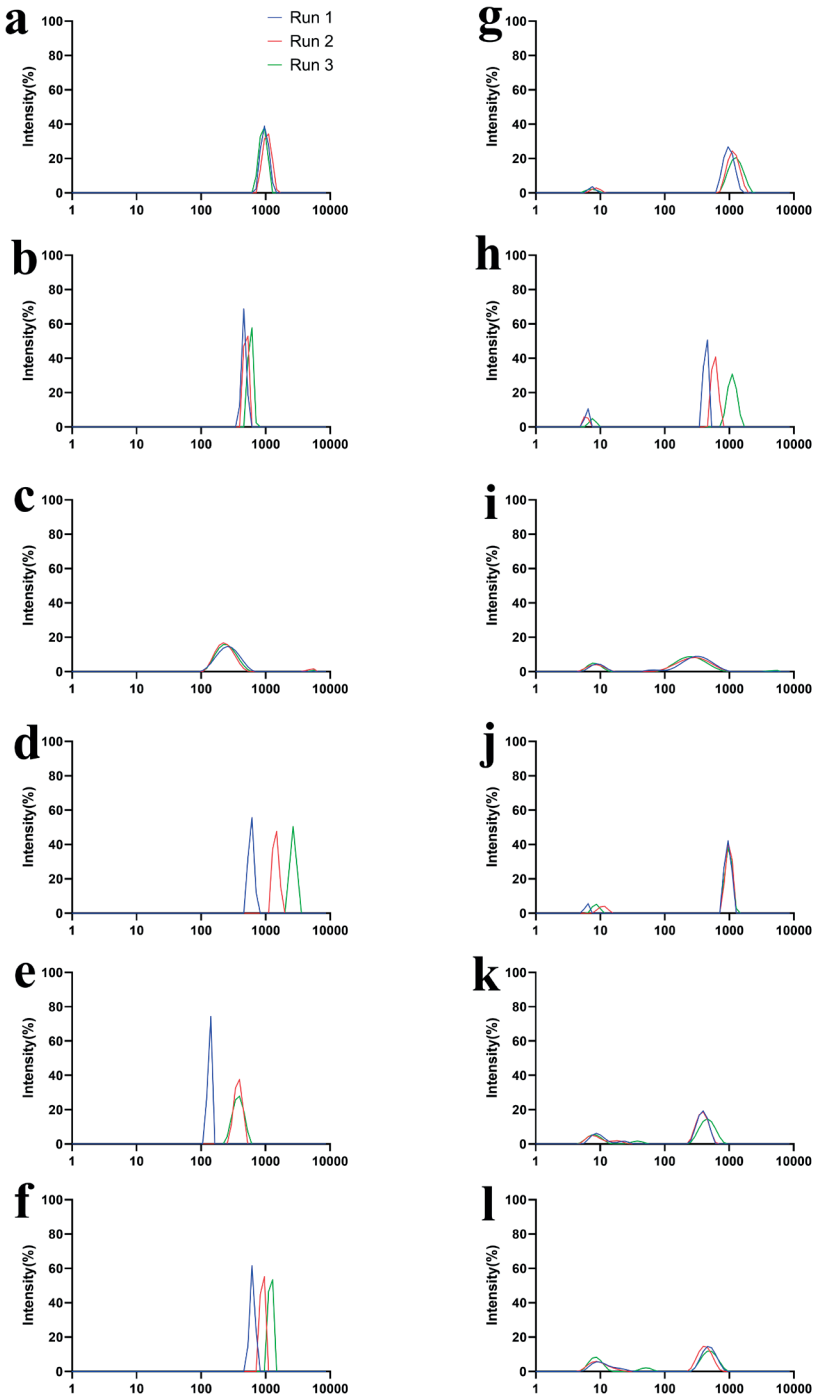

Supplementary Fig. 1. intensity weighted size distribution DLS of microplastics

Intensity based size distribution in H2O of (a) PS1000, (b) PP-Talc, (c) PLA, (d) PVC, (e) PET-TiO2 and (f) PA and intensity-weighted size distribution in ICD medium of (g) PS1000, (h)PP-Talc, (i) PLA, (j) PVC, (k) PET-TiO2 and (l) PA. The X-axis indicates the diameter in nm while the y-axis indicates the probability density in percentage. N=3

Supplementary Table 1. Physicochemical characterization of used microplastics

Particle name	Suspended in dH2O		Suspended in ICD medium		Suspended in 10 mM KCl
	Hydrodynamic size* (nm)	PDI	Hydrodynamic size* (nm)	PDI	Zeta potential (mV)
PS1000	985 ± 58	0.42	1152 ± 120	0.36	-49.8 ± 4.31
PP-Talc	515 ± 50	0.80	717 ± 292	0.68	-35.3 ± 2.0
PLA	259 ± 14	0.17	317± 27	1.0	-1.0 ± 0.4
PVC	1578 ± 859	0.51	976 ± 13	0.66	-36.4 ± 2.5
PET-TiO_2	300 ± 115	0.91	418 ± 37	0.39	-22.7 ± 4.8
PA	907 ± 391	0.78	477 ± 34	0.45	-27.9 ± 1.4

* All sizes listed represent the average of the intensity-weighted size distribution as obtained by DLS. n=3. PDI=polydispersity index, dH2O is demi water.

In ICD medium, suspensions of all microplastics except PLA showed moderate polydispersity, while PLA suspensions were highly polydisperse (PDI ≥ 0.7). For all microplastics, the hydrodynamic sizes in ICD medium remained below 1.5 µm, the commonly set upper size limit for cellular uptake (13). The zeta-potential of PLA microplastics was neutral while the remaining microplastics displayed a zeta potential between -20 and -50 mV. The hydrodynamic sizes in ICD medium were used as input for *in silico* dosimetry (Supplementary Fig. 2) using the distorted grid model (435).

Within 24 h after microplastic addition, maximal sedimentation was reached only by PP-talc and PVC. PVC and PP-Talc showed 90 % of total mass deposited, PS1000 showed 78 % of mass deposition, PET-TiO_2 showed 41 % mass deposition while PLA and PA showed 12 % of mass deposition within 24 h. Despite large differences in the fraction deposited (Supplementary Fig. 2 a) and particle sizes (Supplementary Table 1), the deposited surface area, were within a 3.2 fold difference for all particles(Supplementary Fig. 2 b-c).

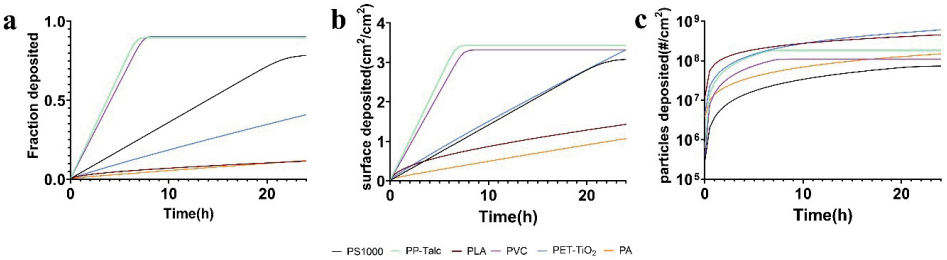

Supplementary Fig. 2. Predicted microplastic deposition on iPSC-derived IEC layers during exposure

In silico sedimentation prediction using the distorted grid model (435) of all microplastics shown as (a) fraction of mass deposited, (b) total microplastic surface deposited per cm2 of transwell surface and (c) number of particles deposited per cm2 of transwell surface. The X-axis indicates the duration of exposure, and the Y-axis indicates degree of deposition. The colour of each line indicates the respective microplastic as shown in the legend.

Supplementary Table 2 - Immunostaining antibodies

Antibodies	Supplier	Reference number
Anti-Villin antibody for Immunofluorescence (1:200)	Santa Cruz Biotechnology	Cat# sc-58897
Anti-MUC2 for immunofluorescence (1:100)	Santa Cruz Biotechnology	Cat# sc-7314
Anti-Chromogranin A for immunofluorescence (1:200)	Immunostar	Cat# 20085
Anti-Lysozyme for immunofluorescence (1:100)	DAKO	Cat# A009902-2
Goat anti-Mouse IgG (H+L) Highly Cross-Adsorbed Secondary Antibody, Alexa Fluor™ Plus 488 (1:250)	Fisher Scientific, Landsmeer, Netherlands	Cat# A32723
Donkey anti-Rabbit IgG (H+L) Highly Cross-Adsorbed Secondary Antibody, Alexa Fluor™ 647 (1:250)	Fisher Scientific, Landsmeer, Netherlands	Cat# A-31573

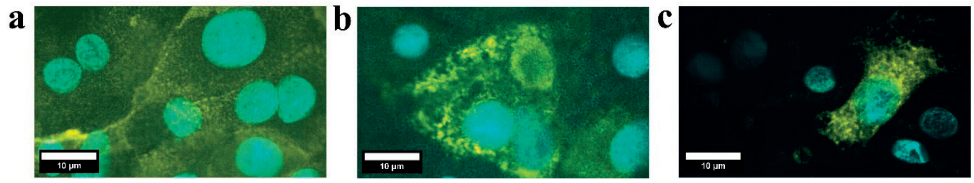

Supplementary Fig. 3. Cellular diversity in iPSC-derived IEC layers

(a-c) Representative images of confocal fluorescence microscopy showing expression of (a) VIL+ enterocytes, (b) MUC2+ goblet cells and (c) LYZ+ Paneth cells. The blue colour indicates the nuclei and the yellow colour indicates respective marker expression. n=3.

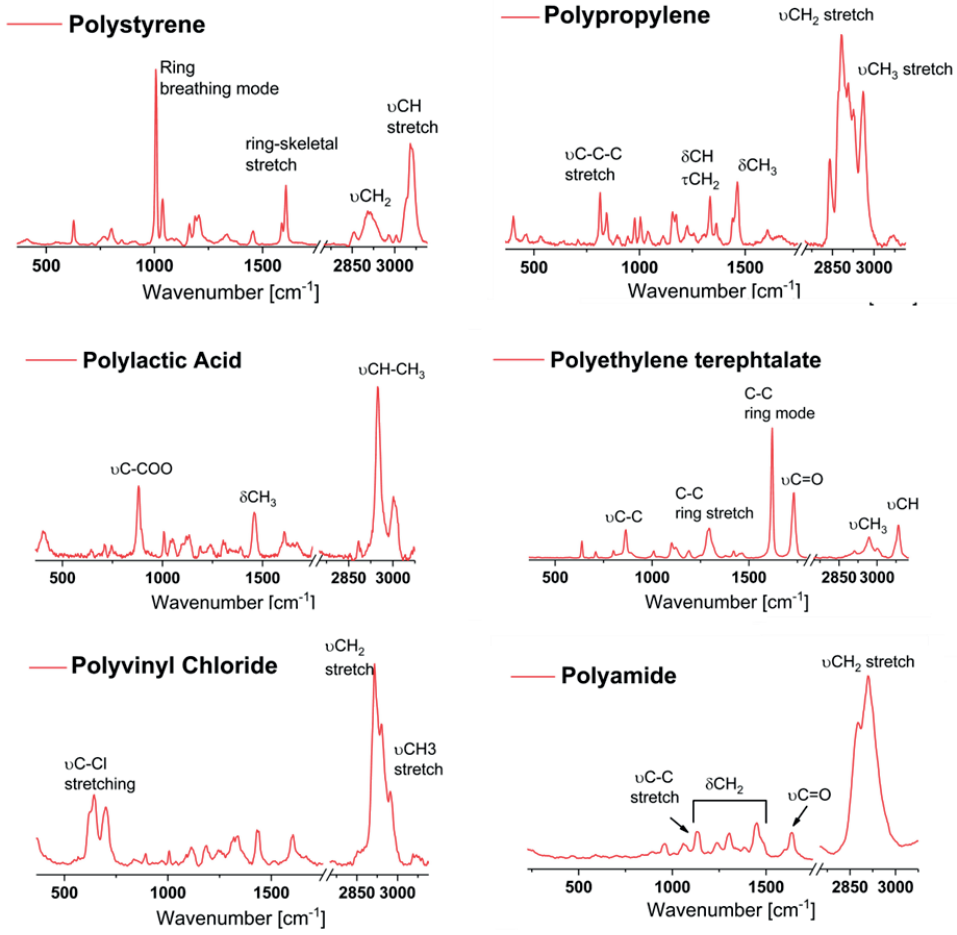

Supplementary Fig. 4. Molecular spectra used to distinguish microplastic polymers.

The microplastic specific Raman bands used for visualizing unlabeled microplastics. The Raman bands of the polymers as reported previously (640-645).

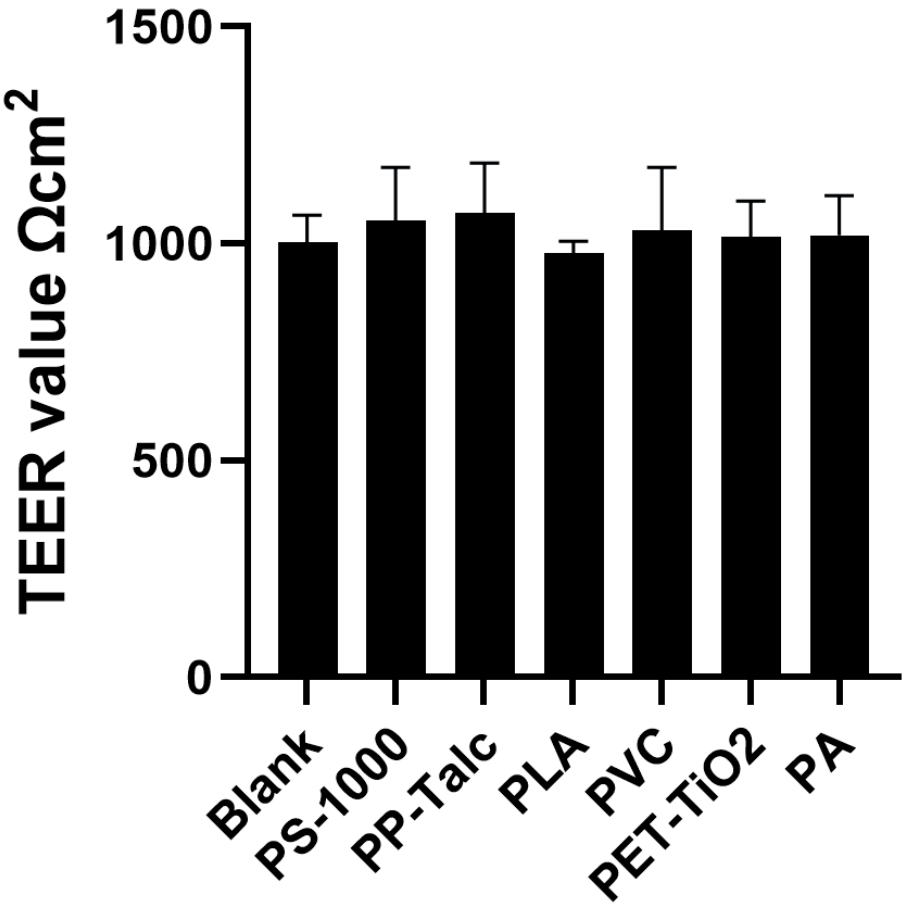

Supplementary Fig. 5. TEER values prior to experiment.

The TEER values of the IEC layers just prior to microplastic addition. No significant differences were found. N=3

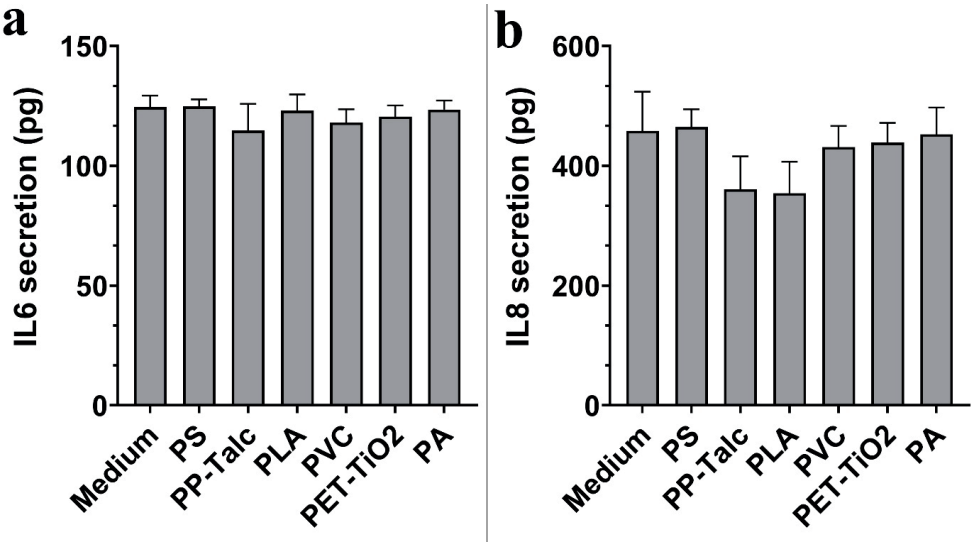

Supplementary Fig. 6. Particle interference with ELISA.

(a) Particle interference with IL-6 ELISA 125 µg/ml of IL-6 was diluted in ICD medium with or without 125 µg/ml of MNPs. no significant effects were found (b) Particle interference with IL-8 ELISA. 500 µg/ml of IL-8 was diluted in ICD medium with or without 125 µg/ml of microplastics, no significant effects were found. N=3

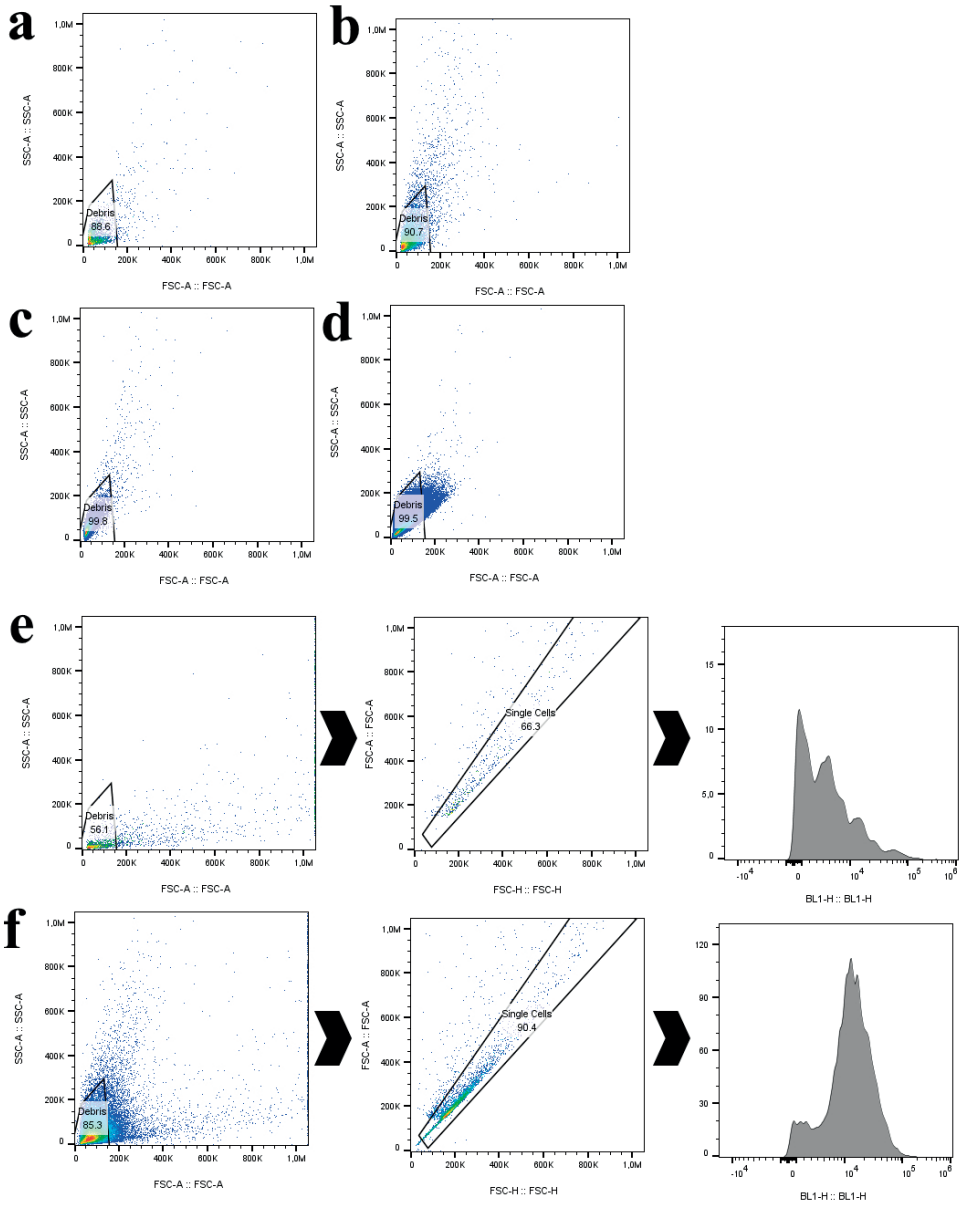

Supplementary Fig. 7. Particle sorting strategy FACS

(a-d) Determination of the particle discrimination gate based on the sizes of (a) PS100, (b) PS200, (c) PS500 and (d) PS1000. The debris gate drawn was chosen as it eliminated over 90% of large particles. (e) Sorting strategy for ROS determination; First particles were distinguished from cells by taking the debris gate set in A-D and discarding all events within this gate. Then the non-debris fraction was used for singlet discrimination using FSH-H and FSC-A. Finally the ROS was determined using the BL-1H channel. (f) representative result for microplastic exposed samples.

Supplementary Table 3 – protein numbers identified in each of the protein corona's

Particle	Number of proteins identified*	Number of proteins different from unbound protein control**
PS1000	310	277
PP-Talc	397	322
PLA	101	25
PVC	253	226
PET-TiO_2	413	345
PA	488	414
Carryover-control	121	0
Total	588	461

* The total number of unique proteins identified on each microplastic using LC-MS-MS after correction for unreliable protein idenfication i.e. contaminant proteins, proteins only identified site or proteins present in less than 2 replicates in any of the microplastics. ** The total number of proteins identified after an additional correction for non-particle bound proteins. An ICD sample without microplastics was included in all sample preparation steps and all unbound proteins were identified. Proteins on microplastics which were not significantly different from the ICD sample as assessed by an empirical bayes classifier were not considered part of the protein corona and were removed from further analysis. N=3

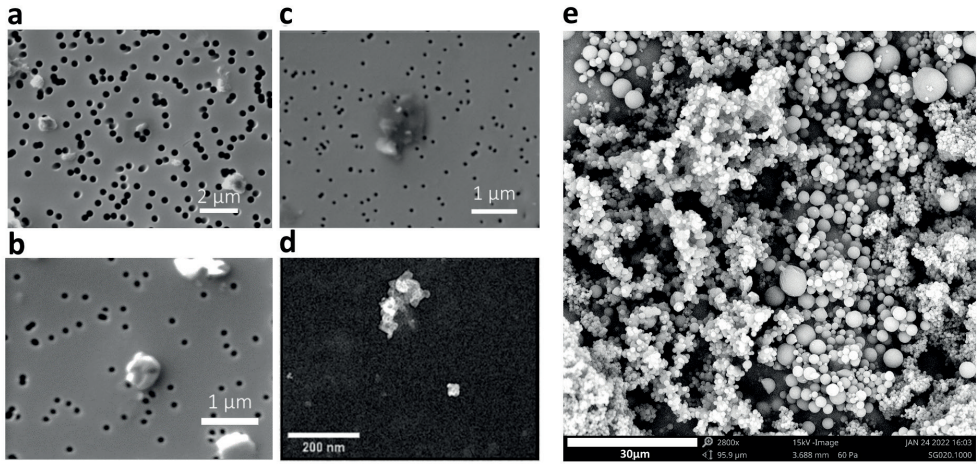

Supplementary Fig. 8. Electron microscopy images of micro and nanoplastics

(a-e) Representative electron microscopy images of (a) PA, (b) PVC, (c) PP-Talc, (d) PET-TiO2 and (e) PLA. The plastic material is shown in white, black dots are pores of the filter used for imaging. The relative size of the microplastics is indicated by the scale bar at the bottom of each figure. Figure 8 a-c was adapted from the momentum particle passports (646) and Figure 8 d was adapted from Villacorta et. al. (587).

CHAPTER 5

5

The *in vitro* gastrointestinal digestion-associated protein corona of polystyrene nano- and microplastics increases their uptake by human THP-1-derived macrophages.

Hugo Brouwer, Mojtaba Porbahaie, Sjef Boeren, Mathias Busch, and Hans Bouwmeester

Based on Brouwer H, Porbahaie M, Boeren S, Busch M & Bouwmeester H.
The in vitro gastrointestinal digestion-associated protein corona of polystyrene nano- and microplastics increases their uptake by human THP-1-derived macrophages.
Part Fibre Toxicol. 2024

5.1 Abstract

Background: Micro- and nanoplastics (MNPs) represent one of the most widespread environmental pollutants of the 21st century to which all humans are orally exposed. Upon ingestion, MNPs pass harsh biochemical conditions within the gastrointestinal tract, causing a unique protein corona on the MNP surface. Little is known about the digestion-associated protein corona and its impact on the cellular uptake of MNPs. Here, we systematically studied the influence of gastrointestinal digestion on the cellular uptake of neutral and charged polystyrene MNPs using THP-1-derived macrophages.
Results: The protein corona composition was quantified using LC–MS-MS-based proteomics, and the cellular uptake of MNPs was determined using flow cytometry and confocal microscopy. Gastrointestinal digestion resulted in a distinct protein corona on MNPs that was retained in serum-containing cell culture medium. Digestion increased the uptake of uncharged MNPs below 500 nm by 4.0- to 6.1-fold but did not affect the uptake of larger sized or charged MNPs. Forty proteins showed a good correlation between protein abundance and MNP uptake, including coagulation factors, apolipoproteins and vitronectin.
Conclusion: This study provides quantitative data on the presence of gastrointestinal proteins on MNPs and relates this to cellular uptake, underpinning the need to include the protein corona in hazard assessment of MNPs.

5.2 Graphical abstract

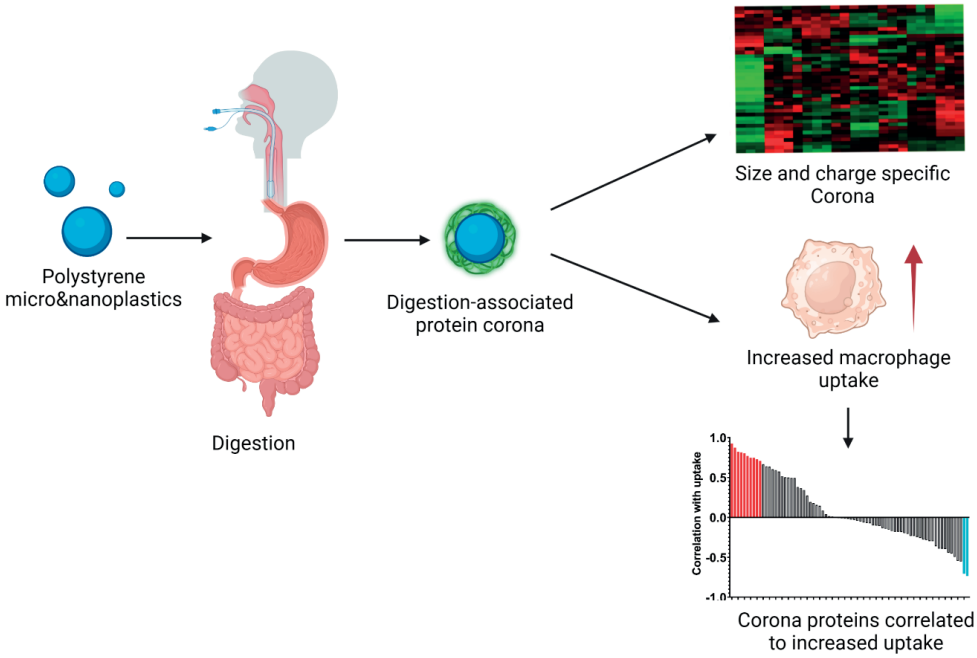

5.3 Background

Micro- and nanoplastics (MNPs) are one of the most widespread pollutants in the environment and are considered one of the five most concerning contaminants in food (13). MNPs are mostly generated from plastic waste spilled into the environment where its continuous exposure to chemical and physical stress, such as abrasion or UV light, causes the plastic waste to fragment into smaller particles (13). A second source of environmental MNPs arises from MNPs that are intentionally added to industrial and consumer products and spill into the environment during the product life cycle (647, 648). Plastic particles with a size <5 mm are defined as microplastics, while particles with a size <100 nm are defined as nanoplastics (13, 649). Currently, MNPs have been detected in virtually all environmental compartments (106), including inside and outside air (85), in household dust (650), and in food commodities, including meat (13, 106), honey (108), salt (109), shellfish (110), fish (111), beer (112) and drinking water (113). Human exposure to MNPs by ingestion or inhalation is thus unavoidable, and reports indicating the presence of MNPs in human blood and placenta highlight the ubiquity of human exposure and the systemic availability of MNPs (14, 651).

MNP exposure via ingestion (including swallowing of respirable MNPs trapped in mucus cleared from the lungs) is the dominant route of exposure for humans (652). Before MNPs reach the intestinal epithelial barrier, they pass through the stomach and intestinal luminal content, which is dynamic in pH and ionic strength and contains complex digestive fluids and food-derived molecules. This exposure results in spontaneous coverage of the MNP surface by a complex cocktail of intestinal proteins and peptides, which is collectively referred to as the protein corona (152, 153). The protein corona has been shown to affect the interaction of MNPs with cells either by shielding the reactive surface of the MNPs or by facilitating uptake through membrane receptor interactions (156-158). Importantly, the presence of a protein corona and its composition have been shown to be more predictive of cellular effects than nanoparticle properties themselves (152, 160). Despite recognition of the importance of the protein corona for the hazards of engineered (metal) nanomaterials (149-152), little is known about the influence of gastrointestinal digestion on the protein corona on MNPs or on the resulting biological impact. Previously, we showed that the cellular association of 50 nm polystyrene (PS) MNPs (149, 377) and 50 nm silver nanoparticles (149) with Caco-2 cells was increased after *in vitro* gastrointestinal digestion. However, the implications for larger-sized MNPs are unknown. Given the great diversity of MNPs that consumers can be exposed to, we studied the relationship between *in vitro* gastrointestinal digestion of well-characterized PS MNPs of different sizes and surface charge and their cellular uptake. By doing so, we address the need for systematic data required to implement read-across methodologies based on the particle size and surface properties and relate this to the cellular uptake needed to advance MNP hazard assessment (161-164).

A realistic intestinal protein corona can be created on MNPs using well-established *in vitro* gastrointestinal digestion approaches. In this study, we used the validated and standardized INFOGEST-2 protocol as the basis for the *in vitro* digestion protocol (653). Several cell-based *in vitro* models can be used to assess the impact of the protein corona on cellular uptake. *In vivo*, the intestinal uptake of most MNPs is thought to be facilitated by M-cells, which have a high phagocytotic capacity (654). Yet current cell culture protocols cannot produce M-cells in the absence of other cell types, and no protocols are available that generate M-cells that show surface marker expression similar to that of *in vivo* M-cells (164, 655, 656). For this reason, we decided to use a THP-1-derived macrophage model emulating tissue-resident macrophages that are located downstream of M-cells and thus represent a highly exposed cell population. Furthermore, macrophages are capable of accumulating nanoplastics (657, 658) and are the main cell type involved in systemic transport and blood clearance of MNPs (659-667). Therefore, uptake kinetics obtained using THP-1-derived macrophages can be used to estimate endocytosis uptake by cells present in highly exposed tissues *in vivo*.

The aim of the current study was to assess the impact of *in vitro* gastrointestinal digestion on the MNP protein corona composition and its consequences on uptake by THP-1-derived macrophages. To study this, we used seven representative PS MNPs with different sizes and surface charges. PS MNPs were digested *in vitro* using a modified INFOGEST-2 protocol (653), and the resulting protein corona was analyzed using SDS–PAGE and LC–MS-MS. THP-1 derived macrophages were subsequently exposed to noncytotoxic PS MNP concentrations, and flow cytometry combined with confocal microscopy was used to determine PS MNP uptake. Finally, the protein abundance in the corona was correlated with particle uptake to investigate which proteins play a role in PS MNP internalization.

5.4 Materials and Methods

5.4.1 Materials

Phosphate-buffered saline (PBS), paraformaldehyde, potassium chloride, sodium bicarbonate, sodium chloride, monopotassium phosphate, magnesium dichloride hexahydrate, ammonium carbonate, calcium chloride dihydrate, hydrochloric acid, bovine bile, porcine pepsin, porcine pancreatin and p-toluene-sulfonyl-L-arginine methyl ester (TAME) were obtained from Merck (Amsterdam, Netherlands). Laemmli sample buffer (2×) was obtained from Bio-Rad (Lunteren, The Netherlands). Non-heat inactivated non-irradiated fetal bovine calf serum(FBS) with product number FBS-12a was obtained from Capricorn Scientific (Ebsdorfergrund, Germany). Trifluoroacetic acid, dithiothreitol and iodoacetamide were obtained from Sigma Aldrich (Zwijndrecht, The Netherlands), and sequencing grade trypsin was obtained from Boehringer Mannheim (Mannheim, Germany). Precast SurePAGE MOPS-Tris PAGE gels were obtained from Genscript (Rijswijk, The Netherlands). Alexa-fluor 594-conjugated wheat germ agglutinin was obtained from Thermo Fisher (Bremen, Germany).

5.4.2 Particles

Green fluorescent (Ex 441, Em 485) and nonfluorescent polystyrene (PS) MNPs (50 nm, 100 nm, 200 nm, 500 nm, 1000 nm) were obtained from Polysciences (Hirschberg an der Bergstraße, Germany). Green fluorescent and nonfluorescent carboxyl- and amine-modified PS MNPs (100 nm) were obtained from Magsphere (Pasadena, USA). Throughout the rest of the manuscript, the particles will be referred to as shown in Table 1.

Table 1: MNPs used in this study with the respective abbreviations

Particle	Abbreviation
Polystyrene, 50 nm	PS50
Polystyrene, 100 nm	PS100
Amine-modified polystyrene, positive charge, 100 nm	PS100 (+)
Carboxyl-modified polystyrene, negative charge, 100 nm	PS100 (-)
Polystyrene, 200 nm	PS200
Polystyrene, 500 nm	PS500
Polystyrene, 1000 nm	PS1000

5.4.3 In vitro gastrointestinal digestion of MNPs

For the *in vitro* gastrointestinal digestion, the INFOGEST-2 protocol (653) was used with minor modifications. Briefly, the digestion protocol consists of 3 steps, namely, the sequential addition of simulated salivary fluid (SSF), simulated gastric fluid (SGF) and simulated intestinal fluid (SIF) to the sample of interest, representing the oral, gastric and intestinal digestive phases, respectively (table 2).

Table 2: Composition of digestive fluids

Component	Simulated salivary fluid (SSF) (pH = 7.0)	Simulated gastric fluid (SGF) (pH = 3.0)	Simulated intestinal fluid (SIF) (pH = 7.0)
KCl	30.2 mM	6.9 mM	6.8 mM
$NaHCO_3$	27.2 mM	25.0 mM	85.0 mM
NaCl	-	47.2 mM	38.4 mM
KH_2PO_4	7.4 mM	0.9 mM	0.8 mM
$MgCl_2.(H_2O)_6$	0.3 mM	0.1 mM	0.3 mM
$(NH_4)_2CO_3$	0.1 mM	0.5 mM	-
$CaCl_2(H_2O)_2$	1.5 mM	0.15 mM	0.6 mM
Pepsin	-	0.8 mg/ml	-
Bovine Bile	-	-	4.0 mg/ml
Porcine Pancreatin	-	-	14.0 mg/ml

After dissolution of all the salts, the pH of the SSF, SGF and SIF was adjusted to 7.0 ± 0.5, 3.0 ± 0.5, and 7.0 ± 0.5 for each fluid, respectively, using 1 mM HCl, and subsequently, all fluids were autoclaved. Prior to *in vitro* gastrointestinal digestion, 1000 U/ml pepsin was added to SGF, while 4 mg/ml bile and 100 U/ml pancreatin were added to SIF. Bile and pancreatin were dissolved by incubation at room temperature (RT) while rotating head-over-heels for 1 h (at 25 RPM), and pepsin was dissolved by head-over-heels rotation for 5 min at RT. After addition of the proteins, the SIF was centrifuged at 3000 g for 5 min to remove undissolved pancreatin fibers and bile. No loss in enzyme activity was observed

upon centrifugation using a trypsin activity assay as described in the INFOGEST2 protocol (653) (data not shown). Just prior to the *in vitro* gastrointestinal digestion, a 0.3 M $CaCl_2$ solution was added to simulated salivary, gastric and intestinal fluid in 1:200th, 1:2000th and 1:500th part respectively.

At the start of the digestion, 125 µl of a 2.5% MNP suspension (i.e., 3.125 mg total MNP mass) was sonicated in an ultrasonic bath (VWR, Amsterdam, Netherlands) to ensure a homogeneous suspension and was added to a 2 mL Eppendorf vial. First, 125 µl of 2X concentrated SSF was added to the MNPs in each sample, followed by manual mixing through inversion and a 5 min incubation at RT. Then, 250 µl of SGF was added to each sample, and the pH was adjusted to pH 3.0 ± 0.5 using 1 mM HCl. The samples were incubated at 37°C for 2 h while rotating head-over-heels at 25 RPM. Finally, 500 µl of SIF was added to each sample and the pH was adjusted to 7.0 ± 0.5 using 1 mM HCl, and the samples were incubated for 2 h at 37°C while rotating head-over-heels. For each experiment, a digestion blank including demi-water instead of MNP suspension was included. The digestion matrix needed to be diluted 25X in complete cell culture medium (CCM) before cell exposure to prevent matrix cytotoxicity (Supplementary Fig. S1).

To assess the protein corona formed upon *in vitro* gastrointestinal digestion or upon incubation (of nondigested) PS MNPs in CCM, PS MNPs were also incubated in CCM for 2 h while rotating head-over-heels at 37°C. We will refer to PS MNPs that were suspended in serum-free medium as pristine MNPs and those that were subjected to *in vitro* gastrointestinal digestion as digested MNPs. PS MNPs that were incubated in FCS-containing CCM will be referred to as serum-coated MNPs, and PS MNPs that underwent digestion and subsequent incubation in CCM will be referred to as digested+serum-coated MNPs (see Table 3). After digestion or incubation with serum, the samples were used immediately for MNP characterization or cell exposure.

Table 3: Nomenclature of MNPs according to their pretreatment and incubation in medium

	Without *in vitro* intestinal digestion	**Upon *in vitro* intestinal digestion**
Medium without serum	Pristine MNPs	Digested MNPs
Medium with serum	Serum-coated MNPs	Digested+serum-coated MNPs

5.4.4 Characterization of particle suspensions

The hydrodynamic sizes of the PS MNPs before and after *in vitro* gastrointestinal digestion were determined by dynamic light scattering (DLS) using a ZS-nano zetasizer (Malvern Panalytical, Malvern, Great Britain). Cell culture medium without serum was filtered through a 0.2 µm nylon Whatman filter to remove background particulate matter. Pristine MNPs, digested+serum-coated MNPs and serum-coated MNPs were diluted to a concentration of 125 µg/ml in serum-free cell culture medium. The suspensions were sonicated for 1 min using a sonication bath and were subsequently loaded into a 1.5 mL polystyrene cuvette. The particle sizes were determined under a scattering angle of 173° and at a temperature of 25°C. At least 5 autocorrelation curves were obtained for each sample, and all particles were measured in triplicate. The remaining zeta-sizer settings were left at their default value. For each set of measurements, a medium blank was included to determine background particulate matter. Data were analyzed using two-way ANOVA with Bonferroni post-hoc correction using graphpad prism 9.

To determine potential fluorophore leaching from the MNPs upon *in vitro* gastrointestinal digestion, MNPs were removed from the gastrointestinal digestion supernatant using centrifugation at 30,000 g for 30 min, and the fluorescence intensity of the supernatant was measured using a Spectramax iD3 Multi-Mode Microplate Reader (Molecular Devices, Birkshire, United Kingdom). Leaching of fluorophores from the MNPs was not detected (Supplementary Fig. S2).

5.4.5 Assessing particle dosimetry

We assessed the fraction of MNPs deposited on the cells using the *in vitro* sedimentation, diffusion and dosimetry (ISDD) model (432). The ISDD model was run assuming a particle density of 1.05 g/ml, and assuming no agglomerate formation, the effect of protein binding was not considered for predicting particle sedimentation. The column height was set to 2.631 mm (corresponding to a 48-well plate format), and the medium volume was set to 0.5 ml. The grid was set to consist of 300 compartments, and sedimentation up to 24 h after cell exposure was simulated. The remaining settings were left at their default conditions. The predicted deposited dose is shown in the Supplementary materials (Supplementary Fig. S3).

5.4.6 Cell culture

THP-1 cells were obtained from ATCC (Manassas, USA) and were grown in RPMI 1640 medium (A10491, Thermo Fisher, Waltham, USA) supplemented with 10% fetal calf serum and 1% penicillin/streptomycin. The cells were cultured in a humidified incubator at 37°C at 5% CO_2. Cells were maintained at a cell density between $2*10^5$ and $8*10^5$ cells/ml in an upright T75 grainer culture flask and were passaged twice a week. THP-1 cells were seeded at $5*10^5$ cells/ml in all experiments. For cell viability experiments, 100 µl THP-1

cells were seeded in 96-well plates and subsequently differentiated to M0 macrophages by the addition of 20 ng/ml phorbol 12-myristate 13-acetate (PMA) and were incubated for 48 h in a humidified incubator (668). After that, the PMA-containing medium was replaced with PMA-free complete cell culture medium, and the cells were allowed to rest for 24 h. On the subsequent day, the cells were exposed to MNPs or blanks for up to 24 h.

5.4.7 Cell viability assessment

To derive noncytotoxic concentrations of the gastrointestinal digestion matrix and MNPs to THP-1-derived macrophages, a water-soluble tetrazolium dye 1 (WST-1) assay was performed. Briefly, THP-1 cells were seeded and differentiated to macrophages in 96-well plates as described above (see section 2.6). Only nonfluorescent MNPs were used for the cell viability assay to prevent potential interference of the fluorescent label with the WST-1 viability assay. Based on the cytotoxicity of the digestion matrix (Supplementary Fig. S1), the digested MNPs and serum-coated MNPs were diluted 1:25 with complete culture medium to a concentration of 125 µg/ml. THP-1-derived macrophages were exposed to digested+serum-coated-MNPs or serum-coated-MNPs at concentrations of 7.8, 15.6, 31.3, 62.5, and 125 µg/ml for 24 h. Next, the medium was aspirated, and the cells were washed with PBS to remove MNPs that were not associated with the cells. Then, 100 µl of culture medium containing 5% WST-1 reagent was added to each well, and the plates were incubated for 1 h at 37°C while shaking at 300 RPM. After 1 h, the absorbance at 440 nm was measured using a Spectramax iD3 Multi-Mode Microplate Reader. The MNPs showed no signal in a cell-free WST-1 assay (data not shown), excluding potential particle interference.

For each experiment, a positive control containing 0.5% Triton X-100 and a negative control consisting of complete culture medium were included. The viability was calculated by comparing the absorbance at 440 nm to the negative control and expressing the resulting absorbance as a percentage of the negative control. The data were analyzed using GraphPad Prism 9.3.1 (GraphPad Software, LLC, San Diego, CA, USA), and a two-way ANOVA using Bonferroni post hoc correction was performed to assess significant differences from the medium control. Experiments were performed in triplicate.

5.4.8 Quantitative measurements of cell association

MNP cell association was measured using flow cytometry. Briefly, THP-1 cells were seeded in a 48-well Nunclon plate (Thermo Fisher) and were differentiated to macrophages as described above (see section 2.6). The THP-1-derived macrophages were exposed to digested+serum-coated or serum-coated MNPs for up to 24 h. The cells were subsequently fixed using 4% paraformaldehyde in PBS for 15 minutes at room temperature and washed twice using PBS. After fixation, the cells were stored at 4°C until measurement using flow cytometry for at most 24 h. Prior to flow cytometry, 1 mM EDTA was added

to the cell suspension, and the cells were detached from the bottom of the well using a curved Pasteur pipette and transferred to a 96-well Nunclon plate. Cell fluorescence was measured in triplicate, each consisting of 3 technical replicates, using a Cytoflex LX flow cytometer in plate mode (Beckman Coulter NL, Woerden, Netherlands). MNP cell association was assessed based on the fluorescein isothiocyanate (FITC) channel (525 nm:20), which corresponds to the green fluorescence emitted by the MNPs. Cells were distinguished from cell debris based on their forward and side scatter, singlet cells were distinguished based on their forward scatter height and width and at least 5000 cells were analyzed for each of the samples. Cells that had a FITC signal higher than 99% of the cells in the negative control were considered FITC positive. The cell association of MNPs over time of two different concentrations of MNPs (i.e., 15.6 and 62.5 µg/ml) was analyzed to determine the optimal measurement time (Supplementary Fig. S4 & S5). Next, the cell association upon 24 h incubation with 7.8, 15.6, 31.3, 62.5 or 125 µg MNPs/ml was assessed (n=3). To correct for differences in fluorescence intensity between the different MNPs, the obtained relative light unit (RLU) values were divided by the relative fluorescence intensity of each of the MNPs at 525 nm as determined using a luminometer (Supplementary Fig. S6). Then, the corrected fluorescence was expressed as the fold change compared to the average fluorescence intensity of unexposed cells. The flow cytometry sorting panel is shown in Supplementary Figure S8.

5.4.9 Determination of cellular internalization

Internalization of fluorescent MNPs into THP-1-derived macrophages was assessed using a Rescan fluorescence confocal microscope (Amsterdam, The Netherlands). First, THP-1 cells were seeded and differentiated into macrophages as described above (section 2.6) in 8-well µ-slides with a tissue culture-treated glass bottom designed for confocal imaging (Ibidi GmbH, Gräfelfing, Germany). The cells were subsequently exposed to 125 µg/ml of serum-coated or digested+serum-coated MNPs. A digestion blank and negative control containing only culture medium and cells were also included. After 1 h of MNP exposure, the cells were washed once with 300 µl of PBS, and the cell surface was stained with 10 ng/ml wheat-germ agglutinin in blocking buffer (2% FBS in PBS) for 1 h. The cells were fixed and washed as described in section 2.8.

5.4.10 Sodium dodecyl sulfate–polyacrylamide gel electrophoresis

The composition of the protein corona was qualitatively assessed using sodium dodecyl sulfate–polyacrylamide gel electrophoresis (SDS–PAGE), based on the protocol published by Walczak et al. 2015 (150). Digested, digested+serum-coated and serum-coated MNPs were separated from the unbound proteins by centrifugation at 30,000 g for 30 min using a tabletop centrifuge. The supernatant was discarded, and the pellet was washed with 1 mL of PBS followed by manual resuspension through pipetting and 10 seconds of vortexing followed by another centrifugation. The washing step and subsequent

centrifugation were repeated twice. Next, the pellet was resuspended in 100 µl of 1X Laemmli sample buffer using a sonication bath followed by vortexing for 10 seconds, and the samples were subsequently boiled at 95 °C for 5 min. To reduce the amount of MNPs loaded into the SDS–PAGE gel, MNPs were separated from the protein fraction dissolved in Laemmli buffer by centrifugation at 30,000 g for 5 min. An equal volume of protein of each MNP sample was loaded into a SurePAGE MOPS-Tris 10-well PAGE gel (Genscript EU, Netherlands), and the gel was run at 120 V. Afterwards, the gels were washed twice with demi-water for 10 min to remove excess SDS. The gels were submerged into fixation solution (10% glacial acetic acid, 40% methanol, 50% demi-water) for 20 min followed by a washing step with demi-water for 10 min. The gels were stained using Biosafe G-250 Coomassie for 2 h and were destained with water overnight. An Odyssey gel-imaging system (Li-COR, Homburg vor der Höhe, Germany) was used to capture the fluorescence at 700 nm originating from Coomassie blue, and subsequent images were analyzed using Fiji 2.9.0 as previously published (669).

5.4.11 Semiquantitative protein corona determination by proteomics

The composition of the protein corona was quantified after *in vitro* gastrointestinal digestion, serum incubation or the combination using an on-bead protein digestion protocol based on the protocol described by Wendrich et al. (2017) (595). After *in vitro* gastrointestinal digestion or incubation in culture medium, the MNPs were centrifuged at 30,000 g for 30 min. The supernatant was discarded, and the pellet was washed with 1 mL of 1 M ammonium bicarbonate buffer followed by 5 seconds of sonication and 10 seconds of vortexing. The washing step was repeated once with 1 M ammonium bicarbonate buffer, and afterwards, the pellet was washed with 50 mM of ammonium bicarbonate buffer. The supernatant was removed, and the MNPs were resuspended in 50 µl of 50 mM ammonium bicarbonate buffer. The protein sample was chemically reduced by adding 5 µl of freshly prepared 150 mM dithiothreitol and was incubated for 30 min at 45°C while shaking at 500 RPM. Five microliters of 200 mM iodoacetamide was added, and the sample was incubated at 20°C in the dark for 30 min. Six microliters of 200 mM of cysteine in ammonium bicarbonate buffer was added to stop the alkylation by iodoacetamide, followed by the addition of 500 ng of sequencing grade trypsin for an overnight digestion at 25°C while shaking at 350 RPM. The following day, the enzymatic digestion was stopped by the addition of 3 µl of 10% tri-fluoro acetic acid to the samples. The peptide samples were cleaned using the µ-column method as previously described (670). The solvent remaining after µ-column sample clean-up was removed using a rotary evaporator, and the peptide samples were redissolved in 50 µl of 1% formic acid in demi water. The samples were subsequently measured using a nano LC–MS-MS protocol as previously described (149). Briefly, 5 µl of tryptic peptide solution was injected into a 0.10 × 250 mm ReproSil-Pur 120 C18-AQ 1.9 µm beads analytical column (prepared in-house) at 800 bar. A gradient from 9 to 34% acetonitrile in water with 0.1% formic

acid in 50 min (Thermo Vanquish Neo) was used. Full scan FTMS spectra were obtained using an Orbitrap Exploris 480 Thermo electron (San Jose, CA, USA) in positive mode between 380 and 1400 m/z. The 25 most abundant positively charged peaks in the MS scan were fragmented (HCD) with an isolation width of 1.2 m/z and 24% normalized collision energy. Samples were measured in triplicate. Since the *in vitro* digestion protocol contains proteases in addition to trypsin, nonspecific digestion was assumed. To account for peptides originating from digestion by non-trypsin proteases, an in-house database of nonspecific porcine and bovine peptides was generated by heat inactivation of mixed bovine serum, bile and porcine pancreatin followed by tryptic digestion. The found tryptic peptides were mapped against the bovine and porcine Uniprot database to obtain a minimal library of potential proteins which could be encountered in the sample. Proteins in each sample were identified by comparing the identified peptides to the in-house bovine and porcine databases.

5.4.12 Analysis of LC–MS-MS-based proteomics data

The label-free quantification (LFQ) values were obtained from MaxQuant (598) and were analyzed using Perseus (671). First non-bovine or porcine contaminant proteins, proteins that did not have at least 2 valid values in any condition and proteins only identified by modified peptides (only identified by site) were removed from the dataset. Then, protein annotations, including GO biological process, molecular function, protein family and KEGG function, were retrieved using the Bos Taurus and Sus Scrofa UniProt databases (601). To visualize proteins present on the PS MNPs upon different treatment conditions, a Venn diagram and upset plot were generated in R using the R Graph gallery VennDiagram (672) and the UpSetR (673) packages. The raw LFQ values were log2 transformed, and missing values were imputed from a normal distribution using a downshift of 3.0 and default band narrowing. The log2 transformed values were used to generate a PCA plot, a heatmap of the Pearson correlation coefficient and a hierarchical clustering of the protein abundance. Differentially abundant proteins were identified using a two-tailed T test with permutation-based false discovery rate (FDR) correction using 250 simulations. Proteins were considered differentially abundant if they had a p value smaller than 0.05 and an absolute log2-fold change larger than 2. The results were plotted as volcano plots using the volcano plot function of Perseus. The correlation between particle uptake and protein abundance was computed in GraphPad 9 by taking the luminescence values obtained from flow cytometry for cells treated with the highest concentration of MNPs and by subsequently using the GraphPad 9 correlation function to correlate this to the averaged protein LFQ value obtained for each of the treatment-particle combinations. Proteins that showed a Pearson correlation coefficient larger than 0.5 were considered correlated, and the resulting correlated proteins were manually compared to previous publications (639, 674) and the annotations obtained from the UniProt database (601). To assess enrichment of protein functions in differentially abundant proteins and proteins

correlated with uptake, a Fischers exact test with Benjamini–Hochberg-based FDR correction was performed to determine if there was a significant association between the proteins of interest and specific GO terms. KEGG and GO functions with an FDR smaller than 0.05 were considered significantly enriched.

5.5 Results

5.5.1 In vitro gastrointestinal digestion does not significantly affect particle size

To characterize the hydrodynamic sizes of the MNPs upon *in vitro* gastrointestinal digestion, we used DLS. The hydrodynamic size of pristine, digested+serum-coated and serum-coated MNPs was measured in serum-free culture medium (Table 4).

Table 4: Hydrodynamic size distribution of pristine, serum-coated, and digested+serum-coated MNPs

	Pristine MNPs		Serum-coated MNPs		Digested+serum-coated MNPs	
MNP	**z-avg ± SD [nm]**	**PDI ± SD**	**z-avg ± SD [nm]**	**PDI ± SD**	**z-avg ± SD [nm]**	**PDI ± SD**
PS50	84 ± 13	0.08 ± 0.05	117 ± 9	0.17 ± 0.01	285 ± 55	0.52 ± 0.11*
PS100	109 ± 1	0.02 ± 0.01	142 ± 4	0.08 ± 0.01*	165 ± 32	0.17 ± 0.08
PS100 (-)	106 ± 1	0.04 ± 0.01	160 ± 8	0.16 ± 0.03	255 ± 27	0.26 ± 0.10
PS100 (+)	1494 ± 214	0.24 ± 0.04	608 ± 6*	0.73 ± 0.29	1630 ± 304	0.63 ± 0.35
PS200	191 ± 1	0.02 ± 0.01	221 ± 2	0.03 ± 0.01	234 ± 2	0.09 ± 0.01*
PS500	561 ± 51	0.07 ± 0.04	544 ± 2	0.17 ± 0.02	531 ± 11	0.17 ± 0.02
PS1000	1160 ± 143	0.10 ± 0.04	1038 ± 61	0.27 ± 0.10	1009 ± 41	0.28 ± 0.13

The sizes are the z-average hydrodynamic size of each of the MNPs and the polydispersity index (PDI). The particle size of pristine MNPs was measured in serum-free RPMI 1640 culture medium. The sizes and PDIs shown are the average of 3 replicates, each consisting of 5 measurements. A two-way ANOVA with Bonferroni post hoc correction was performed to assess significant differences from the pristine particles. Mean ± SD, n=3, * indicates $P<0.05$.

While an increase in the average sizes of MNPs was observed upon digestion, these increases were not statistically significant. The hydrodynamic size of the PS100 (+) MNPs was larger than the 'nominal' sizes (i.e., 100 nm) in all incubation conditions. The only significant incubation-related difference in average hydrodynamic MNP size was found for serum-coated PS100 (+), potentially due to the stabilization of MNPs by surrounding proteins.

5.5.2 Viability of THP-1-derived macrophages was unaffected by serum-coated or digested+serum-coated MNPs

A WST-1 assay was performed to assess the viability of THP-1-derived macrophages upon exposure to differently treated MNP (Fig. 1).

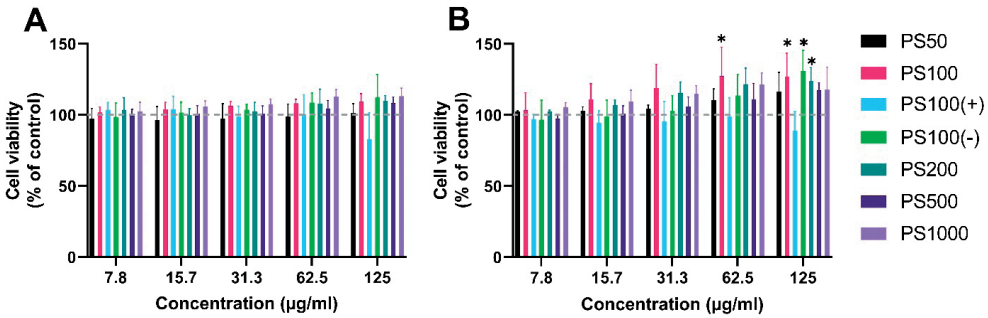

Fig. 1. Effect of digested+serum-coated or serum-coated MNPs on THP-1 cell viability.

(A) Cell viability after 24 h of exposure to serum-coated MNPs. (B) Cell viability after 24 h of exposure to digested+serum-coated-MNPs. Viability is expressed as the relative absorption at 440 nm compared to the negative control. A two-way ANOVA with Bonferroni post hoc correction was performed to assess significant differences from the medium control. Mean ± SD, n=3, * indicates $P<0.05$.

Exposure of THP-1-derived macrophages to serum-coated MNPs did not significantly affect the viability of the cells (Fig. 1A) at any of the tested concentrations. Incubation of the THP-1-derived macrophages for 24 h with digested+serum-coated MNPs also did not reduce the cell viability for any of the MNPs (Fig. 1B), although an increase in mitochondrial activity was observed after exposure to digested+serum-coated PS100, PS100 (-) PS100 (+) MNPs at 62.5 and 125 µg/ml. Based on these results, for the MNP cell association and uptake studies, a maximal MNP concentration of 125 µg/ml was used. Predictions obtained using the ISDD model indicated that the fractions deposited after 24 h of incubation for the PS50 MNPs were 77.6% and 58.1% for PS100, 45% for PS200, 63% for PS500 and 100% for PS1000 (Supplementary Fig. S6). The influence of the charge of the PS100 (-) and PS100 (+) MNP on sedimentation was not considered in the ISDD model.

5.5.3 In vitro gastrointestinal digestion increases the cell association of small but not of large or charged MNPs

The cell association and uptake of PS MNPs by THP-1-derived macrophages exposed to serum-coated and digested+serum-coated PS MNPs were assessed by flow cytometry (Fig. 2). For PS50, PS100 and PS200, the cell association was significantly higher at all concentrations for the digested+serum-coated MNPs compared to the serum-coated MNPs, being 6.1, 6.0 and 4.0 times higher for the highest concentration of PS50, PS100 and PS200, respectively. For PS500, a similar trend was observed, but significance was

only reached at the lowest concentration used. No significant differences between serum-coated and digested+serum-coated MNP cell associations were observed for the PS1000, PS100 (-) and PS100 (+) MNPs.

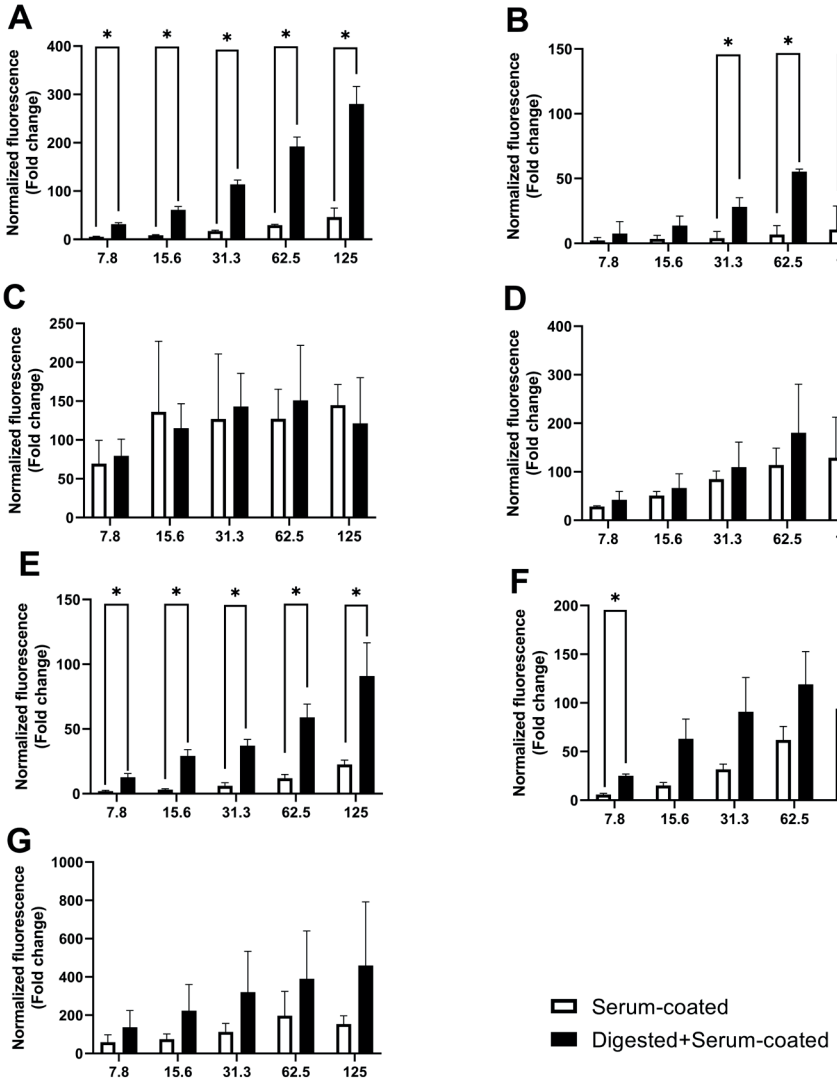

Fig. 2. Concentration-dependent THP-1-derived macrophage association of MNPs.

MNP cell association after 24 h of exposure to 7.8, 15.6, 31.3, 62.5 or 125 µg/ml of serum-coated or digested+serum-coated MNPs. The graphs show the cell association of serum-coated (white bars) or digested+serum-coated (black bars) (A) PS50, (B) PS100, (C) PS100 (+), (D) PS100 (-), (E) PS200, (F) PS500 and (g) PS1000 MNPs. The y-axis shows the fold change increase in fluorescence compared to untreated cells that has been corrected to reflect the difference in fluorescence per µg of MNPs as determined by fluorimetry (Supplementary Fig. S5). A two-way ANOVA with Bonferroni post hoc correction was performed to assess significant differences from the medium control. Mean ± SD of n=3, * indicates $P<0.05$.

5.5.4 Both digested+serum-coated and serum-coated PS MNPs are rapidly internalized by THP-1-derived macrophages.

To differentiate between cell association and cellular uptake, THP-1-derived macrophages were exposed to serum-coated MNPs (Fig. 3) or digested+serum-coated MNPs (Fig. 4). Cell membranes were stained with wheat germ agglutinin, and the MNP-exposed cells were analyzed using confocal microscopy.

For all types of PS MNPs, we observed cell internalization within 1 h of exposure to digested+serum-coated MNPs or serum-coated MNPs. Some cell surface-bound MNPs can be observed for the digested+serum-coated PS100 (+) and PS1000 MNPs, but overall, the majority of the MNPs are localized intracellularly. The washing steps removed nearly all of the unbound MNPs, allowing us to conclude that the flow cytometry results can be interpreted as MNP cellular uptake rather than (only) membrane association.

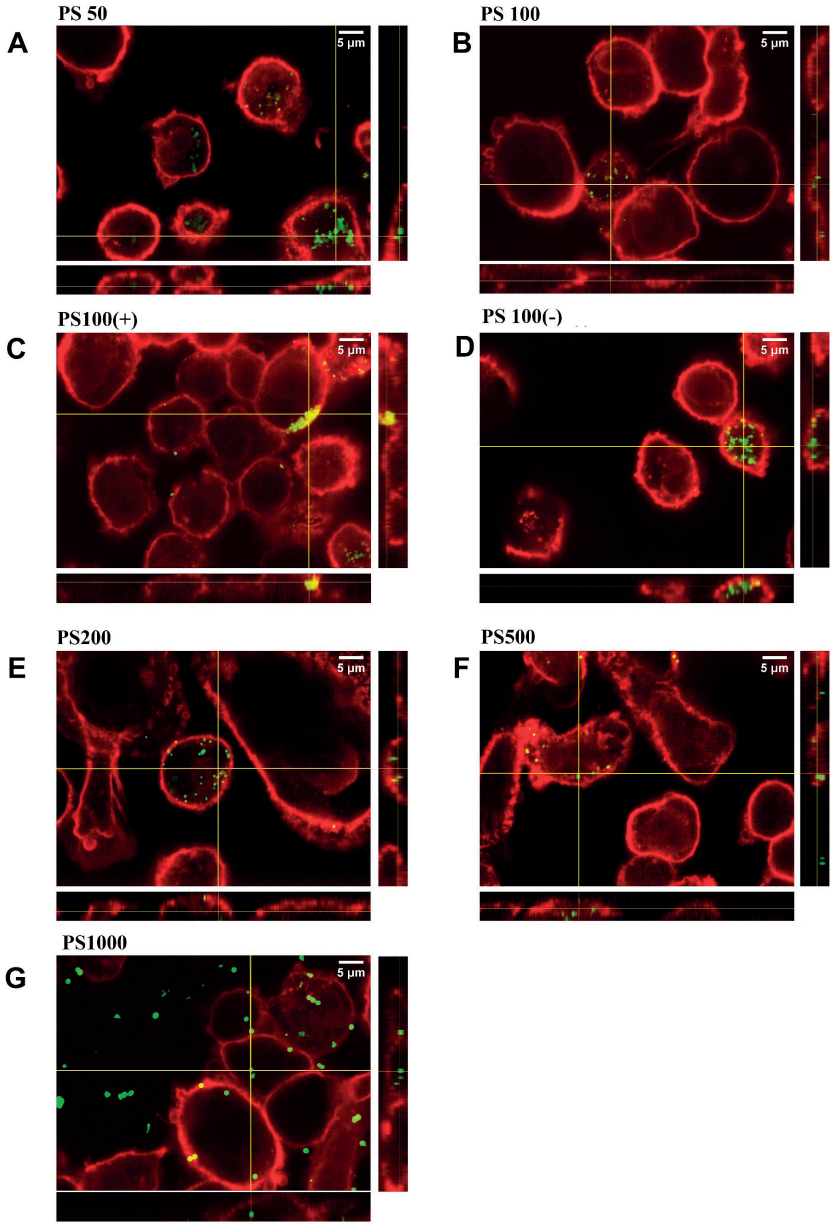

Fig. 3. Internalization of serum-coated MNPs by THP-1-derived macrophages after 1 h of exposure.

Cells were exposed to 125 µg/ml of serum-coated MNPs (A) PS50, (B) PS100, (C) PS100 (+), (D) PS100 (-), (E) PS200, (F) PS500 and (g) PS1000. At the side of each image, the orthogonal Y-Z and at the bottom, the orthogonal X-Z views are shown, which represent slices through the Y-Z and X-Z planes. The yellow cross in the X-Y image indicates the origin of the orthogonal images. The red stain corresponds to the wheat germ agglutinin cell surface coating, and the green stain corresponds to the fluorescent PS MNPs.

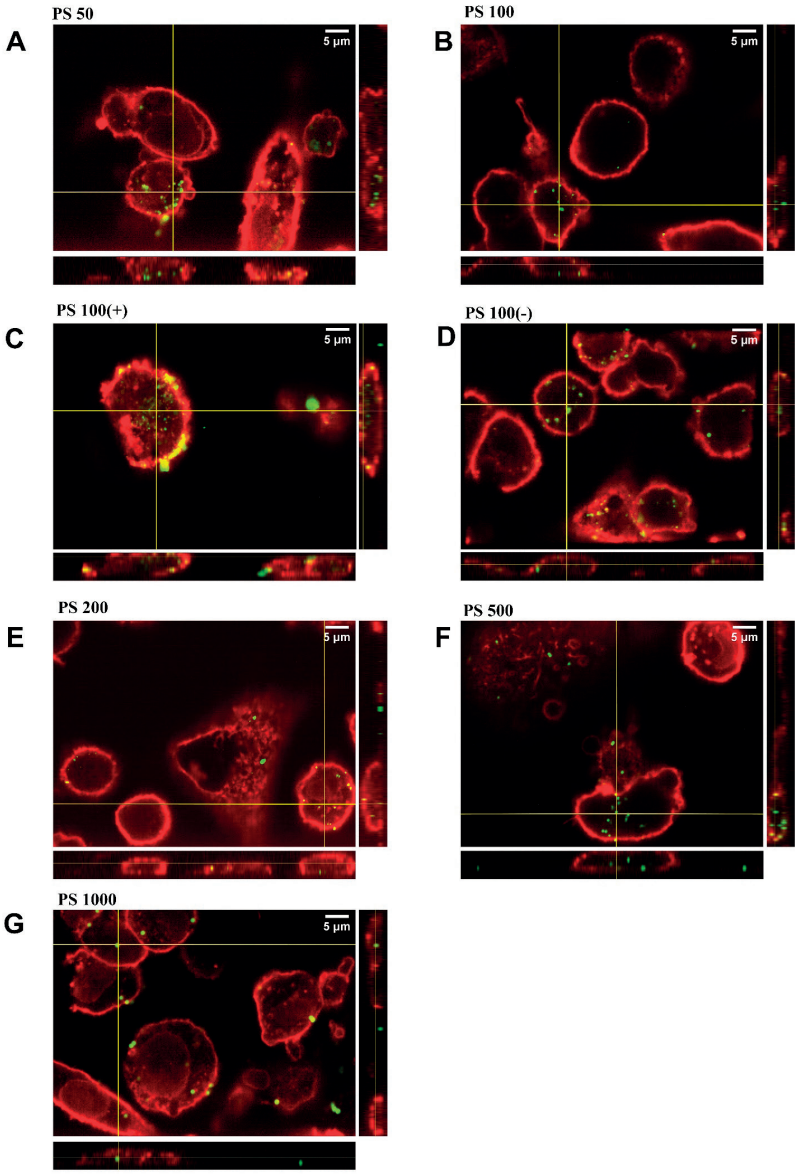

Fig. 4. Internalization of digested+serum-coated MNPs by THP-1-derived macrophages after 1 h of exposure.

Cells were exposed to 125 µg/ml of digested+serum-coated or MNPs (A) serum-coated PS50, (B) PS100, (C) PS100 (+), (D) PS100 (-), (E) PS200, (F) PS500 and (g) PS1000. At the side of each image, the orthogonal Y-Z and at the bottom, the orthogonal X-Z views are shown, which represent slices through the Y-Z and X-Z planes. The yellow cross the X-Y image indicates the origin of the orthogonal images. The red stain corresponds to the wheat germ agglutinin cell surface coating, and the green stain corresponds to the fluorescent PS MNPs.

5.5.5 The digestion corona is retained upon serum incubation and affects the subsequent binding of serum proteins.

For the assessment of the biomolecular corona on the MNPs, the protein composition was first assessed using SDS–PAGE (Fig. 5A-C). Upon incubation of the MNPs in serum containing medium (Fig. 5A), a high intensity and broad band between 50 and 60 kDa was observed for most MNPs except for the PS500 and PS1000 MNPs, which showed low overall protein content of their corona.

Upon *in vitro* gastrointestinal digestion (Fig. 5B), the different MNPs showed little variation in the protein bands observed on the gel, which largely corresponded to proteins and peptides smaller than 30 kDa. The only exception is for PS100 (+), which shows a smear of proteins and peptides ranging between 15 and 60 kDa and a much more pronounced band at 20 kDa.

Lastly, MNPs were transferred from the *in vitro* gastrointestinal digestion matrix into complete cell culture medium, which represents the exposure conditions used in the viability and uptake studies (Fig. 5C). The resulting digested+serum-coated MNP corona was loaded on the gel. Most of the bands observed for the MNPs are similar to the patterns observed in the digestion corona, indicating that the digestion-associated corona is retained in high serum conditions. PS50 and the PS100 (+) MNPs show faint retention of serum protein. When comparing Fig. 5B to Fig. 5C, it can be seen that the serum protein pattern was greatly reduced by the presence of the digestion-associated corona.

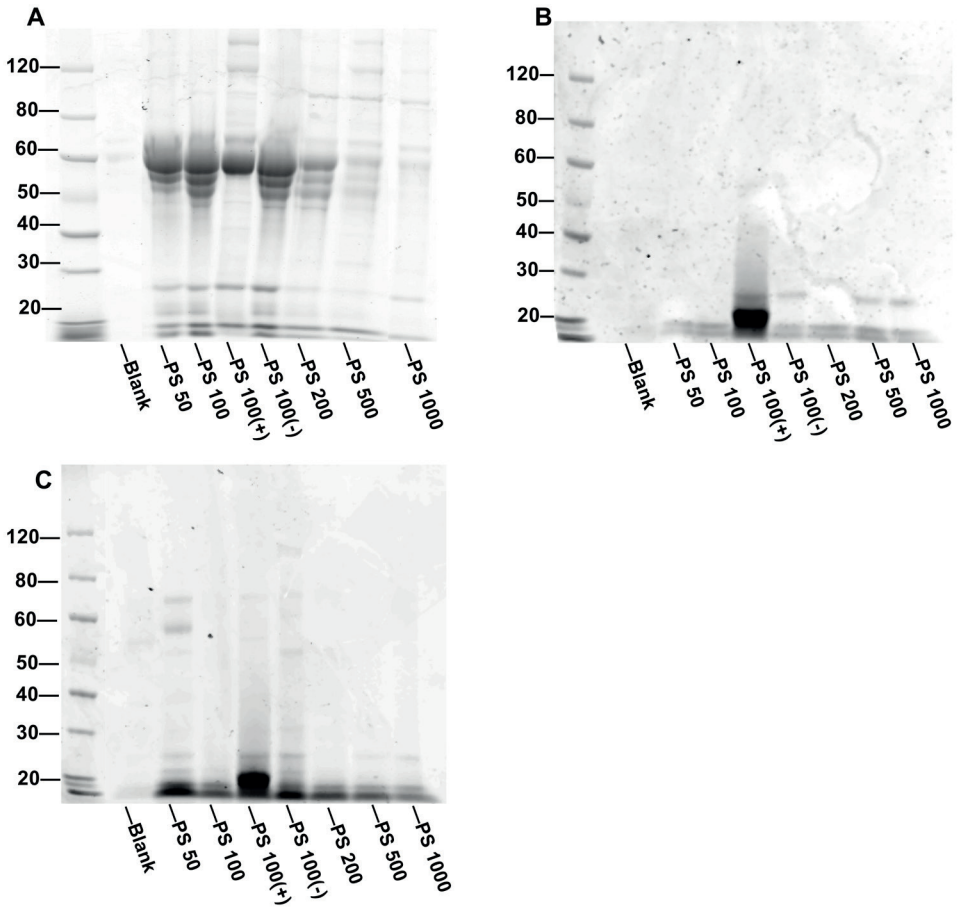

Fig. 5. Protein corona composition of MNPs with different incubation histories.

(A) SDS–PAGE of proteins isolated from serum-coated MNPs. (B) SDS–PAGE of proteins isolated from in vitro intestinal digested MNPs. (C) SDS–PAGE of proteins isolated from digested+serum-coated MNPs. The protein sizes in kDa are shown to the left of each image. The samples corresponding to each lane are shown at the bottom of each image. Blank = H2O addition instead of MNP addition. Representative image of n=3.

5.5.6 Proteomic analysis of the serum and digested+serum-coated protein corona on PS MNPs.

LC–MS-MS-based proteomics was performed to investigate potential treatment-related alterations in the protein corona on a subset of PS MNPs. From the MNPs for which *in vitro* digestion significantly affected uptake, we selected the PS100 MNPs. To study the influence of the charge of MNPs, we included PS100 (+) and PS100 (-) MNPs. Lastly, the PS1000 MNPs were included in the corona proteomics analysis to represent larger PS MNPs.

First, the global protein similarity between samples was assessed. Then, all proteins that showed a significant increase in abundance between treatment types were identified. Finally, the Pearson correlation coefficient between protein abundance and particle uptake at 125 µg/ml (based on flow cytometry) was calculated.

5.5.7 Global overview of the PS MNP protein corona.

In total, 280 proteins were identified in the corona of the PS MNPs, of which 219 proteins were found on serum-coated PS MNPs and 173 proteins were found on the digested+serum-coated PS MNPs (Table 5).

Table 5. Number of proteins identified during semiquantitative LC–MS-MS proteomics

Particle	Proteins on serum-coated MNPs	Proteins on digested+serum-coated MNPs
Total	219	173
PS100	169	105
PS100 (+)	192	157
PS100 (-)	167	113
PS1000	191	125

Similarity between samples was assessed by computing the Pearson correlation coefficient between inter-sample protein abundances (Fig. 6A) and by performing a principal component analysis (Fig. 6B). Then, proteins unique to any of the particle-treatment combinations were identified and visualized using a Venn diagram (Fig. 7A) and UpSet plot (Fig. 7B).

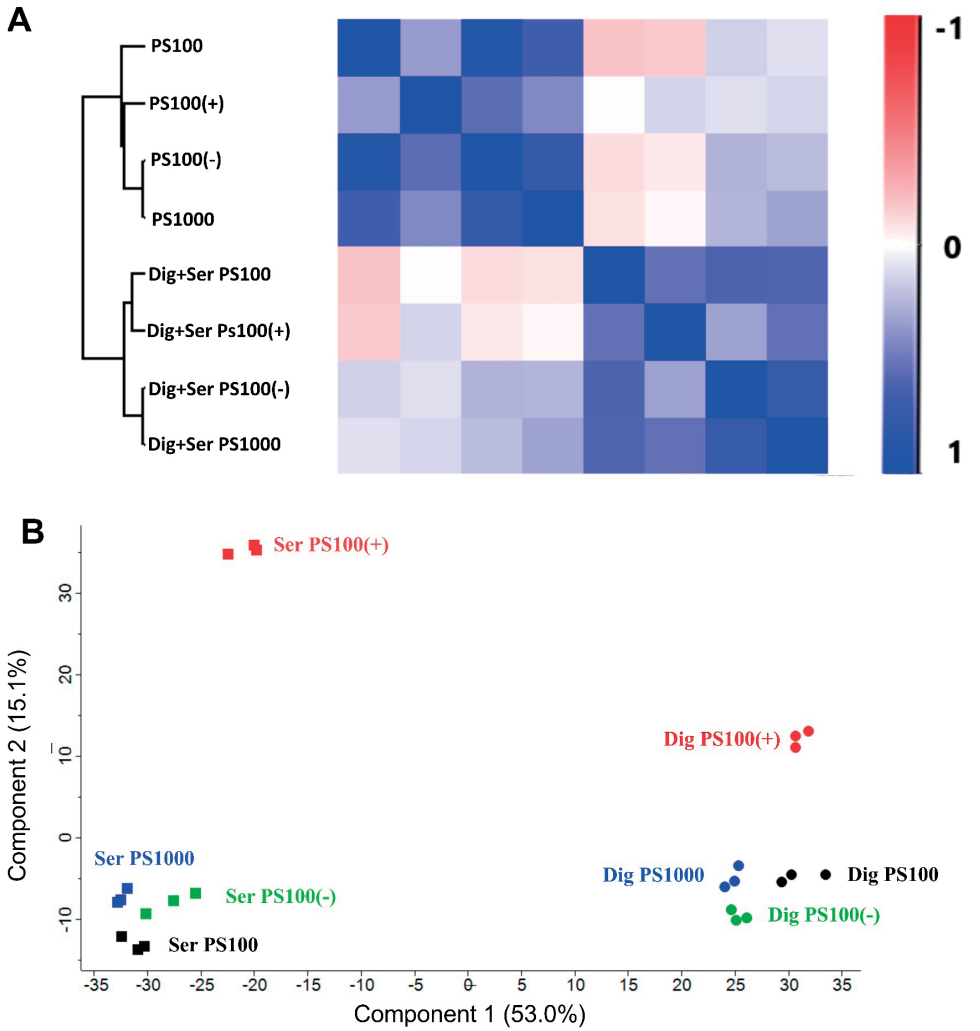

Fig. 6. Similarity between the protein coronas identified on MNPs.

(A) Heatmap indicating the Pearson correlation coefficient between the median amount of all identified proteins identified on each PS MNP type. The dendrogram shown to the left of the heatmap indicates hierarchical clustering of the different MNPs, and the X- and Y-axes indicate the treatment-particle combination. The bar to the right of the heatmap indicates the Pearson correlation coefficient corresponding to each color. In the legend on the X- and Y-axes, Ser refers to serum-coated particles, while DIG+Ser refers to digested+serum-coated particles. (B) Principal component analysis of proteomics samples. Filled squares represent serum-coated MNPs, and filled circles represent digested+serum-coated MNPs. Each symbol represents an LC–MS-MS sample. The color of each symbol indicates the MNP type, with black corresponding to PS100, red corresponding to PS100 (+), green corresponding to PS100 (-) and blue corresponding to PS1000 MNPs. (n=3)

As shown in Fig. 6A, the serum-coated and digested+serum-coated PS MNPs showed a high correlation within but a low correlation between treatment groups. Of the digested+serum-coated MNPs, the PS100 MNPs were most different from the serum-coated MNPs (average correlation -0.06), while the PS100 (-) MNPs showed the highest average correlation of 0.19. The PS100 (+) MNPs showed the highest correlation with the digested+serum-coated MNPs (0.09). Interestingly, the serum-coated PS100 MNPs showed the lowest correlation with the digested+serum-coated MNPs (-0.18), indicating a larger impact of digestion compared to the other MNPs.

The principal component analysis revealed that 53.0% of all variation in protein abundances could be explained by the treatment. The second largest source of variation comprising 15.1% was linked to the presence or absence of a positive charge.

We next assessed which proteins were unique to the serum corona or digested+serum corona (Fig. 7).

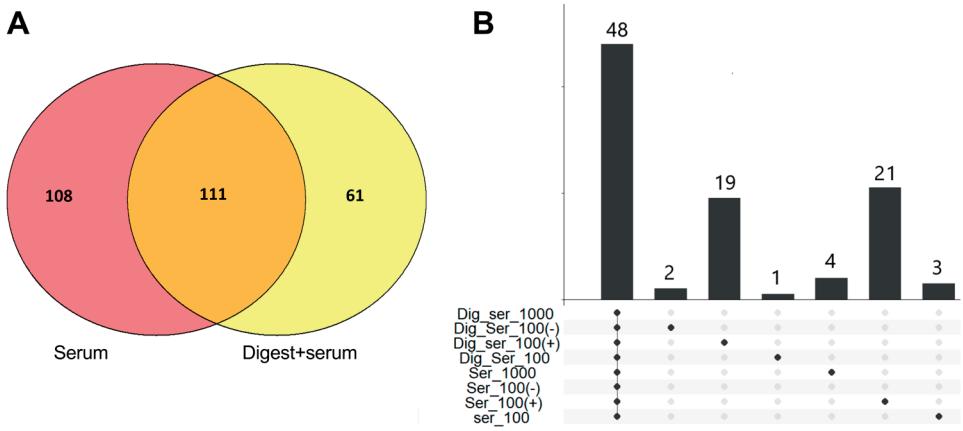

Fig. 7. Number of identified proteins present in the protein corona on PS MNPs.

(A) Venn diagram illustrating overlap between proteins identified on serum-coated and digested+serum-coated PS MNPs. The numbers in each circle indicate the number of unique proteins identified. The area where both circles overlap indicates proteins identified in both serum-coated and digested+serum-coated PS MNPs. (B) An upset plot indicating the number of proteins found on all types of PS MNPs and the number of proteins found only in one of the treated MNPs. The dots indicate the combinations of MNPs, while the bar chart on top shows the number of proteins identified in this respective group. Serum-coated PS100 (-) and digested+serum-coated PS1000 MNPs had no unique proteins and are not shown as individual columns in the upset plot.

Of the 280 proteins that we identified in the MNP corona, 108 were found only in the corona of serum-coated MNPs, 62 were found only in the digested+serum corona, and 111 proteins were shared among the two types of MNP coronas (Fig. 7A). Looking in more detail, 48 proteins were found to be present on all MNPs (Fig. 7B). The PS100 (+) MNPs contained the highest number of unique proteins, 21 in the serum-coated and 19 unique proteins on the digested+serum-coated PS100 (+) MNPs. The proteins that were unique to any of the particle treatment combinations are listed in Supplementary Table 1.

5.5.8 Identifying differentially abundant proteins in the corona on PS MNPs.

To assess which proteins were differentially abundant on the different MNPs, a differential expression analysis of the samples was performed using a two-tailed T test with permutation-based FDR correction (Fig. 8 and Supplementary file 1).

The differential expression analysis showed 166, 174, 134 and 163 differentially abundant proteins on PS100, PS100 (+), PS100 (-) and PS1000 MNPs, respectively. Of these, 48, 62, 42 and 51 proteins were significantly more abundant in the digested+serum-coated PS MNPs, while 118, 112, 92 and 112 proteins were significantly more abundant in the serum corona on PS100, PS100 (+), PS100 (-) and PS1000 MNPs, respectively (Fig. 8, and Supplementary file S1). A protein set enrichment analysis showed that the overrepresented proteins in the serum-coated PS100 corona were significantly enriched for proteins involved in the complement and coagulation cascades, while the remaining serum-coated particles had no significant enrichment of KEGG or GO functions. Proteins overrepresented in the digested+serum corona of PS MNP had no specific functional protein set enrichment (supplementary file 1). Proteins that were differentially abundant in one of the particle treatment combinations are shown in Supplementary Table S1. For PS100, PS100 (+), PS100 (-) and PS1000, 15, 29, one and nine proteins were found to be uniquely more abundant in serum-coated conditions, and five, 21, three and one proteins were uniquely more abundant in the digested+serum-coated conditions (Fig. 8 & Table 6).

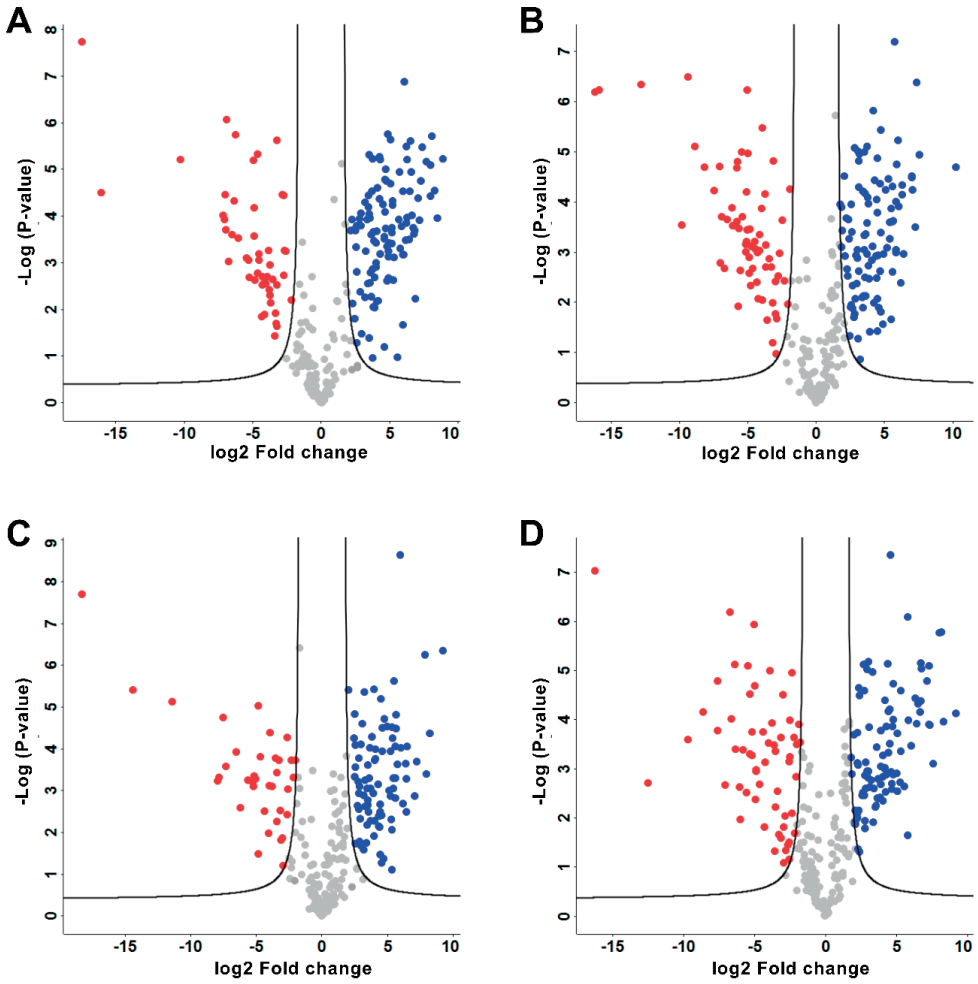

Fig. 8. Differential abundance of proteins between serum-coated and digested+serum-coated MNPs.

Differential abundance of proteins in serum-coated vs. digested+serum-coated PS MNPs (A) PS100, (B) PS100 (+), (C) PS100 (-), (D) PS1000 MNPs. Every dot represents a unique protein identified. The X-axis represents the log2 (fold change) between the serum-coated and digested+serum-coated MNPs. The y-axis indicates the -log of the P value. The black lines indicate the P value threshold and fold-change threshold used to consider a protein as differentially abundant. Colored dots are differentially abundant, while dots in gray are considered equal between treatments. A negative log2-fold change (red dots) represents proteins that are more abundant in the digested+serum-coated protein corona, while a positive log2-fold change (blue dots) represents proteins more abundant in the serum-coated protein corona. Differential expression testing was done by multiple T-tests with permutation based FDR correction at FDR=0.05. Proteins with an absolute log2fold difference larger than 2 and a P-value below 0.05 were considered significantly differentially abundant.

Table 6. Proteins uniquely differentially present in a specific PS MNP corona

Condition	Unique differentially abundant proteins		
Serum-coated PS 100	F1N045 (Complement C7)	Q3MHL4 (Adenosylhomocysteinase)	F1MB08 (phosphopyruvate hydratase)
	F1MW44(coagulation factor 13 chain)	Q2HJ57 (Coactosin like protein)	Q27967 (Secreted phosphoprotein 24)
	Q2KJ83 (carboxypeptidase N-catalytic chain)	G3MZI7 (Collagen type V alpha chain)	P80012 (von willebrand factor)
	Q28085 (complement factor H)	P17697 (Clusterin)	Q0VCM5 (ITIH 1)
	P00735 (Prothrombin)	A5D7R6 (ITIH-2)	A0A3Q1NJR8 (Antithrombin-3)
Serum-coated PS100 (+)	A0A0A0MP92 (Endopin 2)	E1BF81 (Corticosteroid binding globulin)	A0A0A0MPA0 (Serpin domain containing protein)
	P13605 (Fibromodulin)	F6RMV5 (Leucine rich alpha-2-glycoprotein 1)	Q9TT36 (Thyoxine-binding globulin)
	P01267 (Thyroglobulin)	F1MPD1 (Mannose receptor C type 2)	A6QPQ2 (Serpin A3)
	P01017 (Angiotensinogen)	O77742 (Osteomodulin)	I2E4T6 (MBL assosciated serine protease 2)
	Q09TE3 (ILGF-binding protein labile subunit)	Q95M17 (Acidic mamalian chitinase)	A0A287BDF8 (Inositol-3-phosphate synthase 1)
	F1MPE1 (CD109)	F1RU49 (Actinin alpha 3)	F1MJQ3 (alpha amylase)
	A7YWG4 (gamma-glutamyl hydrolase)	E1BH94 (peptidoglycan recognicion protein 2)	Q58CQ9 (Pantetheinase)
	F1MVK1 (uncharacterized protein)	A5PKC2 (SHBG protein)	A0A287AY54 (60S acidic ribosomal protein)
	G5E5T5 (Ig-like domain containing protein)	A5PK77 (Serpin A11 protein)	P56652 (ITIH-3)
	F1MMD7 (ITIH-4)	F1MJK3 (Pregnancy zone protein)	-
Serum-coated PS100 (-)	A0A287AFA5 (Ras homolog member F)	-	-
Serum-coated PS 1000	P33072 (Protein-lysine-6-oxidase)	P35445 (Cartilage oligomeric matrix protein)	F1SHM0 (pyruvate kinase M1/2)
	Q2KIT0 (Protein HP20-homolog)	P19879 (Mimecan)	I3LQ84 (Collagen type 6 alpha 2 chain)
	P07224 (Vitamin K dependent protein S)	Q5E946 (Parkinson disease protein 7 homolog)	F1N0I3 (Coagulation factor 5)
Digested+serum-coated PS 100	F1N5M2 (Vitamin D binding protein)	Q32KY0 (apolipoprotein D)	A0A3Q1MFR4 (Apolipoprotein B)
	P15497 (Apolipoprotein A-1)	A0A3Q1M1Z4 (Ig-like domain containing protein)	-

Table 6. Continued

Condition	Unique differentially abundant proteins		
Digested+serum-coated PS 100(+)	E1B9F6 (Elongation factor 2-alpha)	F1SML4 (SND-domain containing) protein)	Q29375 (Large ribosomal subunit eL8)
	A0A5G2QSB4 (ribosomal protein S3)	P01846 (Ig lambda chain C region)	K7GLN4 (Peroxyredoxin 4)
	F2Z4Y8 (40S ribosomal protein S11)	P28839 (cytosol aminopeptidase)	Q29036 (DAD-1)
	A0A5G2Q9S0 (Nucleoside diphosphatase kinase)	F1SQT3 (mitochondrial phosphate carrier protein)	A0A287A014 (40S ribosomal protein S15a)
	A0A5G2R5F8 (KDEL endoplasmic reticulum protein retention receptor)	F1SQW6 (endoplasmic reticulum protein 27)	P80021 (ATP synthase mitochondrial subunit)
	A0A286ZKG9 (Peptidyl-prolyl cis-trans isomerase)	A0A286ZW72 (60S ribosomal protein L14)	P26779 (Proaposin)
	K7GNY4 (60S ribosomal protein L8)	F1RW28 (hydroxysteroid 17-beta dehydrogenase)	F1SFA7 (collagen type 1 alpha 2 chain)
Digested+serum-coated PS 100(-)	A0A287AYH9 (Palmtioyl-protein thioesterase 1)	F1MZ96 (Ig-like domain containing protein)	G3MYZ3 (Afamin)
Digested+serum-coated PS 1000	G3N0S9 (Sushi domain containing protein)	-	-

This table highlights differentially abundant proteins which were only enriched on one single particle treatment combination. The leftmost column shows the corresponding particle and treatment while the 3 rightmost columns indicate the Uniprot identified and full name of the identified protein.

5.5.9 Correlation of corona proteins with cellular uptake of PS MNPs

To verify whether the proteins identified in the differential expression analysis contribute to differences in the observed uptake by THP-1-derived macrophages, the Pearson correlation coefficient was calculated for the relation between the protein abundances identified through LC–MS-MS and the uptake in relative light units identified through flow cytometry. Figure 9 and Table 7 show the Pearson correlation coefficient of the 40 proteins most correlated with the uptake of PS MNPs. In total, 40 proteins were identified that had a correlation larger than 0.5 with uptake; for 12 proteins, this correlation was statistically significant (Fig. 9 and Table 7). A graphical representation of the protein correlation is also shown in the supplementary figure (Fig S. 7).

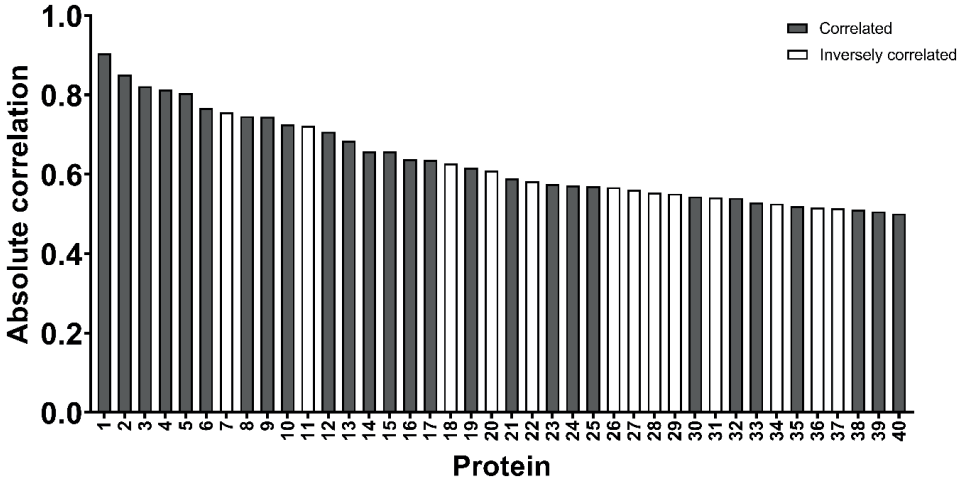

Fig. 9. Overview of proteins present in a PS MNP corona that correlated with particle uptake.

Pearson correlation coefficient of the protein abundance with MNP uptake of the 40 most correlated proteins. Correlated proteins were defined as having an absolute correlation if the coefficient >0.5. MNP uptake was determined using flow cytometry and was defined as the average relative light unit per treatment condition. Protein abundance in the MNP corona was obtained using LC–MS-MS and was defined as the average LFQ of the triplicate samples. The numbers shown on the x-axis refer to the proteins listed in Table 7. The y-axis shows the Pearson correlation coefficient. A positive coefficient indicates that the protein is correlated with uptake, while a negative correlation coefficient indicates that the protein is inversely correlated with uptake. The color (black or white) indicates whether the protein is correlated or inversely correlated ($p<0.05$, see Table 7).

Table 7. Proteins showing a significant correlation with PS MNP uptake

Protein ID	Protein name	R-coefficient	P value	upregulated in	Fig. 9 label
P81644	Apolipoprotein A-II	0.90	0.002	Digested+serum-coated PS100 Digested+serum-coated PS100 (-) Serum-coated PS100 (+)	1
A0A3Q1MGI2	Apolipoprotein E	0.85	0.007	-	2
P19034	Apolipoprotein C-II	0.82	0.012	Serum-coated PS100 (+) Serum-coated PS1000	3
P02081	Hemoglobin fetal subunit beta	0.81	0.014	-	4
P02639	Protein S100-A1	0.80	0.015	Serum-coated PS100 (+) Serum-coated PS1000	5
A0A5G2QL09	S-adenosylmethionine synthase	0.77	0.026	Serum-coated PS100 (+) Serum-coated PS1000	6
G3MZI7	Collagen type V alpha 1 chain	-0.76	0.030	Serum-coated PS100	7
P01965/P01966	Hemoglobin subunit alpha	0.75	0.033	all	8
P62833	Ras-related protein Rap-1A	0.75	0.034	-	9
Q3ZBS7	Vitronectin	0.73	0.041	-	10
Q58D62	Fetuin-B	-0.72	0.043	-	11
P19879	Mimecan	0.71	0.049	Serum-coated PS1000	12
Q3MHN5	Vitamin D-binding protein	0.68	0.061	Digested+serum-coated PS100 Digested+serum-coated PS100 (+)	13
Q28035	Glutathione S-transferase A1	0.66	0.076	Serum-coated PS100 (+) Serum-coated PS1000	14
F1SHM0	pyruvate kinase M1/2	0.66	0.076	Serum-coated PS1000	15
A0A286ZNV2	Elongation factor 1-alpha 2	0.64	0.089	Digested+serum-coated PS100 Digested+serum-coated PS100 (+)	16
P33072	Protein-lysine 6-oxidase	0.64	0.090	Serum-coated PS1000	17
F1N1W7	Neural cell adhesion molecule 1	-0.63	0.096	Serum-coated PS100 Serum-coated PS100 (+) Serum-coated PS100 (-)	18

Table 7. Continued

Protein ID	Protein name	R-coefficient	P value	upregulated in	Fig. 9 label
P01035	Cystatin-C	0.62	0.103	Serum-coated PS100 (-) Serum-coated PS1000	19
Q9TTE1	Serpin A3-1	-0.61	0.109	-	20
P15497	Apolipoprotein A-I	0.59	0.124	Digested+serum-coated PS100	21
P07224	Vitamin K-dependent protein S	-0.58	0.130	Serum-coated PS1000	22
A0A287AK65	Argininosuccinate synthase	0.58	0.136	Serum-coated PS100 (+) Serum-coated PS1000	23
F1N0I3	Coagulation factor V	0.57	0.138	Serum-coated PS1000	24
F1N102	Complement C8 beta chain	0.57	0.140	All serum-coated MNPs	25
G5E513	Ig-like domain-containing protein	-0.57	0.142	-	26
Q3SZV7	Hemopexin	-0.56	0.148	-	27
A0A3Q1M1Z4	Ig-like domain-containing protein	-0.55	0.155	Digested+serum-coated PS100	28
P80012	von Willebrand factor	-0.55	0.157	Serum-coated PS100	29
P10096	Glyceraldehyde-3-phosphate dehydrogenase	0.54	0.163	-	30
A0A3Q1M3L6	Ig-like domain-containing protein	-0.54	0.165	Serum-coated PS100, Serum-coated PS100 (-) Serum-coated PS1000	31
Q5E946	Parkinson disease protein 7 homolog	0.54	0.167	Serum-coated PS1000	32
Q2KIT0	Protein HP-20 homolog	0.53	0.177	Serum-coated PS1000	33
F1SUP2	Signal peptidase complex subunit 2	-0.53	0.180	Digested+serum-coated PS100 Digested+serum-coated PS100 (+)	34
P00735	Prothrombin	0.52	0.187	Serum-coated PS100	35
E1B805	Complement C3	-0.52	0.190	Serum-coated PS100 Serum-coated PS100 (-) Serum-coated PS1000	36
A0A3Q1MFR4	Apolipoprotein B	-0.51	0.191	Digested+serum-coated PS100	37
P81947	Tubulin alpha-1B chain	0.51	0.195	-	38

Table 7. Continued

Protein ID	Protein name	R-coefficient	P value	upregulated in	Fig. 9 label
F1MW44	Coagulation factor XIII A chain	0.51	0.200	Serum-coated PS100	39
P02676	Fibrinogen beta chain	0.50	0.206	Serum-coated PS100 Serum-coated PS100 (+)	40

The columns show the UniProt protein IDs and protein names of all of the proteins that were found to be correlated with MNP uptake. Correlation was defined as having an absolute Pearson correlation coefficient (R) > 0.5, with a positive R-coefficient indicating a positive correlation and a negative R-coefficient indicating an inverse correlation. The table is ordered from highest absolute correlation to lowest absolute correlation. The enriched in the column indicates whether the protein was enriched in any of the particle treatment combinations (Supplementary file 1). The numbers in the last column provide a link to the x-axis label in Fig. 9.

To visualize the abundance distribution of the correlated proteins, a hierarchical clustering of the samples based on the protein abundance of the 40 correlated proteins is shown in Fig. 10. Most of the correlated proteins were enriched in the serum-coated conditions, specifically the serum-coated PS100 or PS1000 MNPs. Four major protein clusters can be identified, of which the orange cluster is most abundant in serum-coated PS100, the blue cluster is most abundant in digested+serum-coated PS100, the yellow cluster is highly abundant in serum-coated PS100 (+) and low abundance in serum-coated PS1000 and finally a pink cluster which is the most abundant in PS1000. Both proteins in the blue cluster are inversely correlated with uptake. Based on the clustering distances between serum-coated and digested+serum-coated MNPs, the charged PS MNPs show the most similarity in abundance patterns of proteins correlated with uptake between treatments, while the PS1000 MNPs and the PS100 MNPs show the most differences.

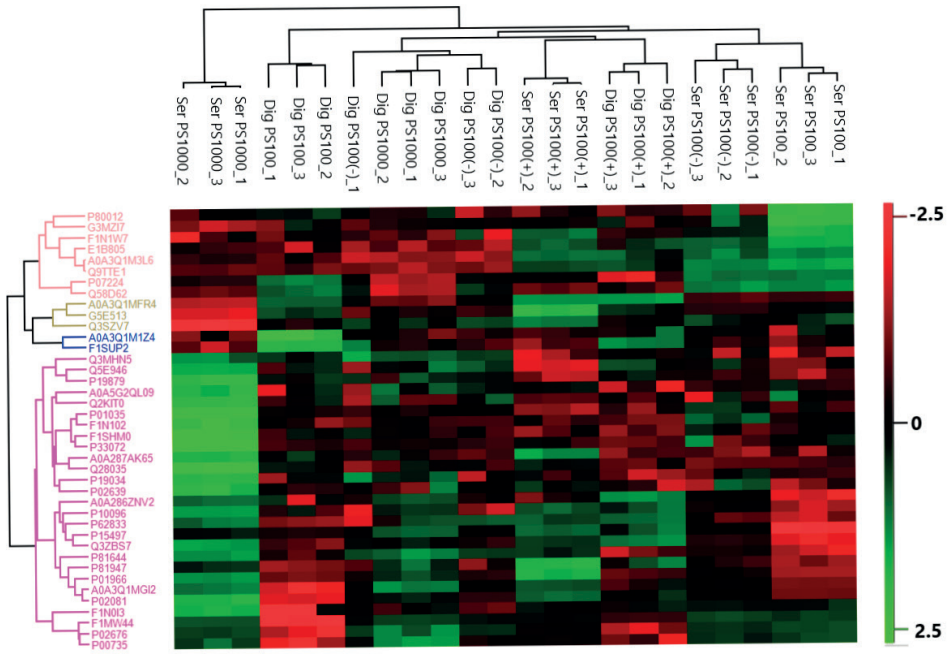

Fig. 10. LFQ profiles of the 40 most correlated proteins in the protein corona.

Heatmap indicating the normalized log LFQ value of all the proteins correlated with uptake. The dendrogram to the top of the heatmap shows hierarchical clustering of each sample based on the Euclidian distance between protein abundance. The dendrogram to the left of the heatmap indicates hierarchical clustering of the 40 identified proteins correlated with uptake. The bar to the right of the histogram indicates the normalized log LFQ value that corresponds to each color in the heatmap. Missing values were imputed from a normal distribution.

Of the correlated proteins, 30 proteins were differentially abundant in at least one particle (Table 7 & Fig. 10). Proteins enriched in digested+serum-coated PS100 included apolipoprotein A-II, vitamin D-binding protein, elongation factor 1-alpha 2, apolipoprotein A-I and Ig-like domain-containing protein, while serum-coated PS100 was enriched in fetuin-b, neural cell adhesion molecule 1, von Willebrand factor and collagen type V alpha chain. These proteins showed good correlation with the different uptake patterns observed for serum-coated and digested+serum-coated PS100 MNPs. The remaining significantly correlated proteins had a similar protein abundance between serum-coated and digested+serum-coated PS100 MNPs or did not fit well with the observed differences between the uptake of digested+serum-coated and serum-coated MNPs.

5.6 Discussion

The aim of this paper was to identify whether *in vitro* gastrointestinal digestion of MNPs affects their uptake into THP-1-derived macrophages and whether uptake differences could be explained by the protein corona composition. Here, we found that *in vitro* gastrointestinal digestion led to an increased uptake of PS50, PS100 and PS200, while *in vitro* gastrointestinal digestion had little effect on the uptake of PS500 and PS1000 MNPs and did not affect the uptake of PS100 (+) and PS100 (-) MNPs. LC–MS-MS-based proteomics showed that complement and coagulation proteins and transporter proteins such as apolipoproteins, hemoglobin, fetuin and ITIH2 proteins were differentially abundant on PS MNPs that were either digested *in vitro by* gastrointestinal digestion or only incubated in serum. A Pearson correlation coefficient analysis confirmed that the presence of 40 proteins correlated with cellular uptake, including the proteins mentioned above. The data presented here represent the first report that the digestion-associated protein corona is retained on PS MNPs of different sizes and charges and consequently affects the incorporation of serum proteins in the PS MNP corona, modifying PS MNP cellular uptake in a particle size- and charge-dependent manner.

First, we determined the hydrodynamic sizes of the PS MNPs in the different treatment conditions. While the z-average hydrodynamic sizes of the pristine and digested PS MNPs suspended in serum-containing medium were seemingly larger, these differences were not significant, with the exception of the reduced hydrodynamic sizes of the PS100 (+) MNPs suspended in serum-containing medium. We also confirmed that no fluorescence was leaking from the PS MNPs during any of the treatments, which allows interpretation of fluorescence signals obtained from the flow cytometry and confocal microscopy experiments as coming from the PS MNPs. The cellular association of MNPs cannot easily be separated from cellular uptake using flow cytometry (457); thus, confocal microscopy analysis was used to confirm the cellular uptake of PS MNPs by THP-1-derived

macrophages. All particles except serum-coated and digested+serum-coated PS100+ MNPs showed a high degree of internalization after one hour, allowing interpretation of an increased cellular fluorescence as increased PS MNP uptake.

The uptake of uncharged MNPs with sizes <500 nm was significantly increased upon *in vitro* gastrointestinal digestion compared to only serum incubation. This corroborates earlier studies that showed that *in vitro* digestion increases the uptake of 50-100 nm polystyrene particles into various blood cells, including THP-1 monocytes; however, larger particles or particles with surface modifications were not considered in that study (119). The *in vitro* digestion-associated increased cellular uptake was most apparent for the PS50, PS100 and PS200 MNPs, while for the PS500 MNPs, this treatment-related difference was only significant for the lowest concentration used. The cellular uptake of both charged (PS100 (+) and PS100 (-)) MNPs was unaltered upon *in vitro* gastrointestinal digestion compared to serum incubation alone. For PS100 (+) confocal images suggest a preference for membrane association, while upon *in vitro* digestion more MNPs are seemingly internalized in the THP-1 derived macrophages. The increased propensity for membrane association of aminated positively charged MNPs can be ascribed to their higher affinity for the negatively charged cell membrane (675). We hypothesize that the size- and charge-dependent effects of *in vitro* digestion found here can largely be explained by differences in the protein corona.

To verify whether the protein corona might be linked to alterations in uptake, the constituent proteins were first assessed at the global level. We first observed that the digestion-associated protein corona was sparser (i.e., fewer and more faint bands on the SDS page), more homogenous in protein composition and of lower molecular weight compared to the serum-coated corona. PS500 and PS1000 had a sparser protein corona compared to the PS50-PS200 MNPs upon incubation in serum, while for digested+serum-coated MNPs, there was no clear relation between protein abundance in the corona and size. The charge of the MNPs had a strong effect on the protein corona composition, where an increased presence of proteins in both the serum-coated, digested and digested+serum-coated PS100 (+) coronas was found, confirming previous studies reporting that increased surface charge leads to increased protein binding (676) and that surface charge is a major determinant of protein corona composition (589). The impact of size on protein corona composition in the 100 nm-1 µm range is poorly understood, but particle size was reported to affect both the total amount and composition of serum proteins of 50-100 nm PS particles (589). The low variety in protein sizes in digestion coronas compared to the serum corona has previously been reported for 50 nm neutral, carboxylated and aminated polystyrene nanoplastics (150).

The reduced presence of serum proteins in the corona of digested+serum-coated MNPs indicates that the prior presence of digestion proteins impaired subsequent incorporation of serum proteins into the corona of all tested MNPs. Such a shielding effect of a preexisting protein corona has previously been applied to reduce blood clearance of targeted mesoporous silica by phagocytes (677). The presence of a protein corona is known to reduce nonspecific interactions with the cellular membrane, which in turn reduces nonreceptor-mediated uptake (678), and studies have reported an inverse correlation between the amount of MNP-bound protein and cellular uptake (678, 679). The reduced amount of protein bound to the digested+serum-coated PS MNPs may therefore contribute to their higher internalization compared to serum-coated PS MNPs. The larger MNPs showed a less pronounced difference in protein abundance in their corona between serum-coated and digested+serum-coated conditions, which may explain the similar cellular uptake between the different treatments of PS500 and PS1000 MNPs. Previously it has been shown that particle surface curvature can induce protein denaturation which stimulates uptake through misfolded protein receptor mediated endocytosis(158, 680, 681). The surface curvature is inversely proportional to the squared radius of a sphere and thus larger protein denaturation is expected for small MNPs compared to large MNPs. Additionally it was shown that increased misfolding of coronated proteins was related to increased cytotoxicity in isolated blood cells, highlighting the importance of this effect(682). Future studies assessing protein denaturation on in vitro digested MNPs and whether this causes increased recognition by misfolded protein receptors may help elucidate this effect.

To investigate whether specific proteins may drive the effect of *in vitro* digestion on cellular uptake, the protein corona composition was characterized in detail using LC–MS-MS-based proteomics. The PS100, PS1000, PS100 (+) and PS100 (-) MNP subset was chosen to elucidate the influence of size and charge on the treatment-related protein corona composition. We identified 280 proteins, of which 173 proteins were found in the digested+serum-coated MNP corona, and 219 proteins were present in the serum-coated MNP corona. Based on the Pearson correlation between the protein abundance of different samples, PCA and hierarchical clustering of global protein abundance, PS100 MNPs showed the largest difference between only serum-coated and digested+serum-coated conditions. Corona on the PS100 (+) MNPs were most different in protein composition compared to all other tested MNPs, confirming the SDS–PAGE results.

We performed differential expression analysis to identify proteins that were significantly differentially abundant between serum-coated and digested+serum-coated PS MNPs. PS100, PS100 (+), PS100 (-) and PS1000 MNPs showed 166, 174, 134 and 163 differentially abundant proteins, respectively. The majority of the differentially abundant proteins showed a higher abundance in the serum-coated MNP corona than in the

digested+serum-coated MNP corona. Using a Fischers exact test, we found that the serum-coated PS100 particles were functionally enriched for proteins involved in the coagulation and complement cascade, while no other particle had a functional enrichment in the differentially abundant proteins. The coagulation and complement cascade has been intensively studied in the context of nanomedicine, and the presence of these proteins was found to increase particle phagocytosis of liposomes and PMMA nanoplastics (683, 684). The complement proteins found on serum-coated PS100 included proteins with a known role in phagocytosis or that have previously been related to nanoparticle uptake, such as plasminogen (685, 686), complement factor C3 (684), complement factor H (683), coagulation factor XIII A (687), prothrombin (688), alpha-1-antitrypsin (688) and von Willebrand factor (689).

Next, we investigated proteins that were only differentially abundant on one particle, focusing on proteins with a known role in particle uptake. In total, we found 20, 51, 4 and 10 proteins that were only differentially present for PS100, PS100 (+), PS100 (-) and PS1000, respectively. Digested+serum-coated PS100 MNPs contained an increased amount of apolipoproteins A-I, B and D, while the serum-coated PS100 had an increased amount of the aforementioned complement proteins as well as ITIH-1 and 2, clusterin and collagen type V alpha chain. For PS100 (+), we found an increased abundance of ITIH3, ITIH4, Serpin-A3-8 and Pantetheinase in serum-coated conditions and proaposin in digested+serum-coated conditions. PS100 (-) had no unique proteins that have a known role in phagocytosis, and PS1000 had an increased abundance of mimecan and coagulation factor V in serum-coated conditions. Among the identified proteins, apolipoproteins and complement proteins have most firmly been implicated in nanoparticle uptake. Apolipoproteins have previously been shown to be involved in nanoparticle uptake (690, 691) by neutrophils and macrophages (resulting in blood clearance of MNPs) and were shown to correlate well with nanoparticle uptake in numerous studies (639, 674). The specific differential presence of these proteins on digested+serum-coated PS100 was unexpected, as apolipoproteins originate from the serum component. The increased abundance of ITIH proteins on serum-coated PS100 and PS100 (+) is also of interest, as ITIH hyaluronan transporter proteins have previously been postulated to facilitate the binding of liposomes to the cell surface (674, 692) and were shown to correlate well with PS MNP uptake in the current study.

The proteomics dataset in our study uniquely allowed a calculation of Pearson correlation coefficients between identified corona proteins and MNP uptake by THP-1-derived macrophages to determine whether the identified proteins are related to particle uptake patterns. For 40 proteins, we found correlation coefficients > 0.5 with uptake, of which 30 were differentially abundant on at least one particle, with 14 being differentially abundant on exactly 1 particle. The most positively correlated proteins included apolipoprotein A-II,

C-II and E and hemoglobin subunits a and b, while the corona proteins that inversely correlated with uptake were fetuin-b, vitronectin, neural cell adhesion molecule 1 and collagen type V alpha chain. Additionally, apolipoprotein-A1 and B, complement and coagulation factors C8, C3, V, XIII-a, fibrinogen, von Willebrand factor and prothrombin were correlated with uptake. Overall, the Pearson correlation, differential expression analysis and Fischer's exact test support the notion that uptake differences observed between serum-coated particles and digested+serum-coated particles are driven by members of the coagulation and complement cascade and apolipoproteins such as opsonins. The proteins identified here show good concordance with previous studies and known roles in endocytotic processes (639, 674, 683-688). Thus, they represent a likely cause for the difference in particle uptake between digested+serum-coated and serum-coated PS MNPs. The proteins identified in the protein coronas of our studied MNPs that had a well-established relationship with phagocytosis were differentially abundant on PS100 but also on the larger PS1000 MNPs. We, however, did not observe striking treatment-related PS1000 MNP uptake differences. Potentially, the relative importance of the protein corona for PS1000 for uptake is less pronounced than that for PS100, which was also indicated by the reduced number of proteins in the larger PS MNPs. This is supported by previous studies that reported that increasing particle size reduces the effect of surface functionalization on particle clearance by macrophages (693, 694).

The current study shows that the *in vitro* gastrointestinal digestion-associated protein corona increases the uptake of PS MNPs in THP-1-derived macrophages in an MNP size- and charge-dependent manner. It was shown that *in vitro* intestinal digestion alters the binding of serum proteins on these MNPs, but the mechanism behind this is still unclear. It might be possible that the presence of digestion proteins in the corona causes steric hindrance for serum proteins or competition for binding of serum proteins in terms of affinity. Alternatively, digestion-related proteases present on the surface of MNPs are partially shielded from serum-borne protease inhibitors such as serpins and might actively degrade serum proteins bound to the surface. Based on the retention of digestive proteins on MNPs, it can be predicted that proteins from food components might also be retained on MNPs; however, this has not been studied thus far. The retention of food-bound components on MNPs may hold relevance to food immunity and warrants further studies. In addition, humans are exposed through their diet to MNPs with different polymer types, such as PET, PE and PP, as well as MNPs weathered by the environment. Little is known on the physicochemical characteristics of environmental MNPs, however larger plastic fragments are known to undergo photodegradation, biodegradation and mechanical abrasion ultimately resulting in MNPs (695-697). Artificial weathering of MNPs resulted in an increased hydrophilicity of such MNPs compared to pristine MNP, which may alter the protein corona formation and thus the cellular uptake of environmental MNPs (698, 699). Furthermore environmental components comprising the so-called eco corona may also

increase cellular uptake(700). Further studies investigating the role of MNP polymer type, environmental weathering and food components present during (in vitro) gastrointestinal digestion on nanoparticle uptake can help elucidate these questions (701, 702).

Based on the LC–MS-MS-based proteomics results, we postulate that altered binding of complement and coagulation cascade proteins to nanoplastics caused the increased uptake of nanoplastics after *in vitro* digestion. The alteration in complement and coagulation components was less pronounced in charged PS MNPs or in MNPs of 1000 nm, resulting in a minimal effect of digestion on their uptake. The increased uptake of digested MNPs may lead to increased mitochondrial membrane potential, of macrophages as an increased internal dose (of 40-90 nm nm 0.7-0.9 µm and polystyrene MNPs) has been associated with perturbed mitochondrial potential, ROS production and alterations in surface marker expression of J774A.1 mouse macrophages (703), although other studies revealed no obvious increase in toxicity after THP-1 monocyte exposure to in vitro digested 50-100 nm PS MNPs (119).

5.7 Conclusions

We have shown that *in vitro* digestion significantly alters the uptake of 50 and 100 nm uncharged PS MNPs by THP-1-derived macrophages but not charged 100 nm MNPs or MNPs larger than 500 nm. We found that the presence of digestion proteins in the protein corona alters the subsequent binding of serum components to MNPs. Forty proteins were correlated with uptake. The proteins identified here have known roles in phagocytosis, and apolipoproteins such as A-1, A-II, and C-II and complement and coagulation cascade proteins such as von Willebrand factor, complement C3 and fibrinogen may cause differences in uptake. This is the first study that quantitatively measured the effect of *in vitro* digestion on micro- and nanoplastic uptake in THP-1-derived macrophages, linking this to alterations to the protein corona. Our results indicate that digestion should be taken into account when estimating cellular uptake, and using serum-coated MNPs can lead to a significant underestimation of MNP internalization by cells.

5.8 Acknowledgments

This project has received funding from the European Union's Horizon 2020 research and innovation program under grant agreement No. 965196. Laura de Haan is acknowledged for her contribution in setting up cellular experiments, Coen Govers for his guidance on flow cytometry, and Arjen Bader for his guidance on confocal microscopy. Ivonne Rietjens is acknowledged for her contribution to reviewing the manuscript.

5.9 Supplementary information

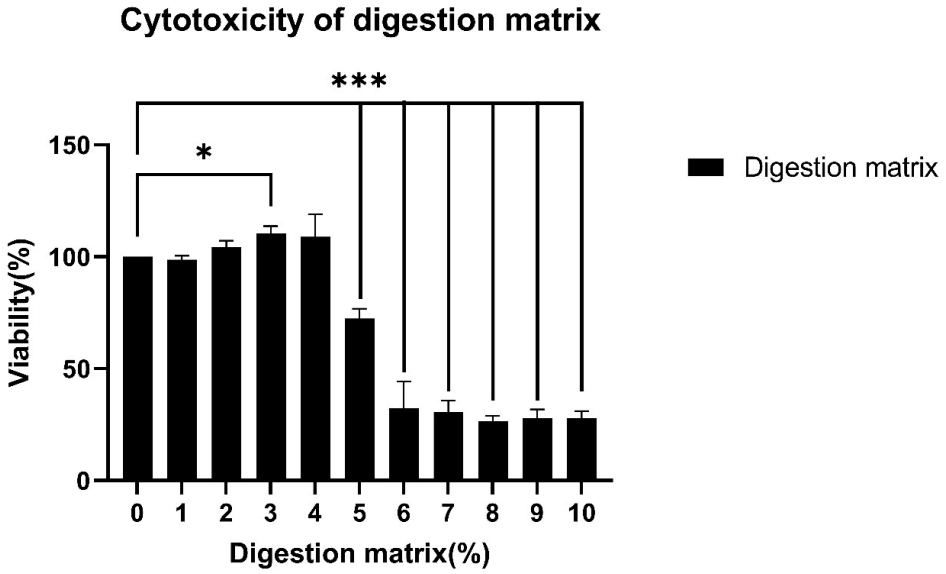

Fig. S1: digestion matrix toxicity.

The y-axis shows relative viability of THP-1 derived macrophages after exposure to 1-10 % of digestion matrix diluted in serum-containing medium as measured using WST-1. Viability is expressed in the relative absorption at 440nm compared to the medium control. The error bars show the standard deviation of the measurement. A two tailed ANOVA using Dunnett's post-hoc correction was performed to assess significant differences from the medium control, n=3. Significance is indicated: * ($P<0.05$) **($P<0.01$), ***($P<0.001$).

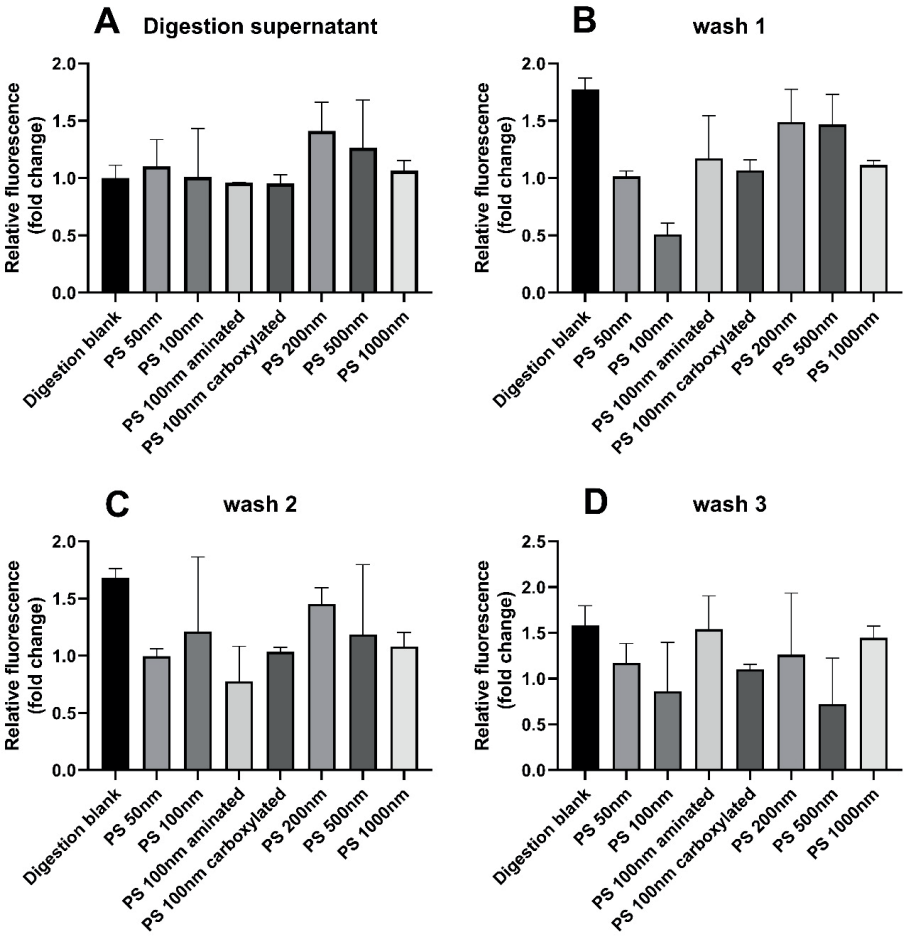

Fig. S2: Fluorophore leaching after digestion and subsequent washes

The y-axis shows the relative fluorescence measured after 30 minutes of centrifugation at 30,000 RCF in (A) the supernatant of the digestion, (B) the supernatant after the 1st PBS wash, (C) the supernatant after the 2nd PBS wash and (D) the supernatant after the 3rd PBS wash. The excitation was set at 485nm while the emission was measured at 525 nm using a Promega spectramax iD3 luminometer. the Y-axis shows the fold change of each sample compared to the digestion blank in graph A.

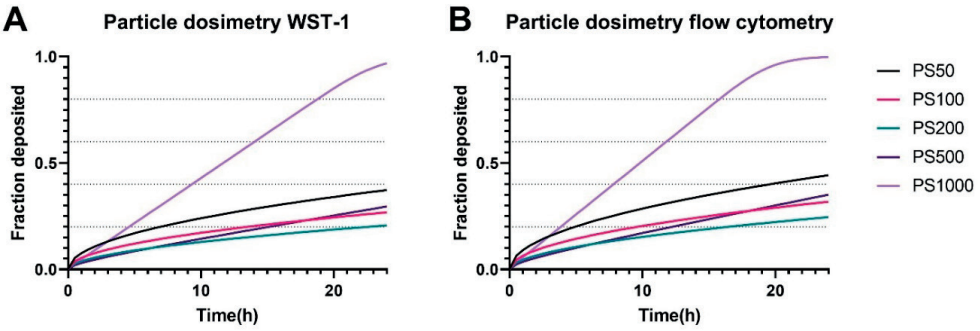

Fig. S3: Particle dosimetry for cell exposure to micro/nanoplastics

The predicted particle sedimentation during the WST-1 assay and Flow-cytometry based particle adhesion tests. The Y-axis shows the fraction of total particles that are deposited and the X-axis shows the time in hours.

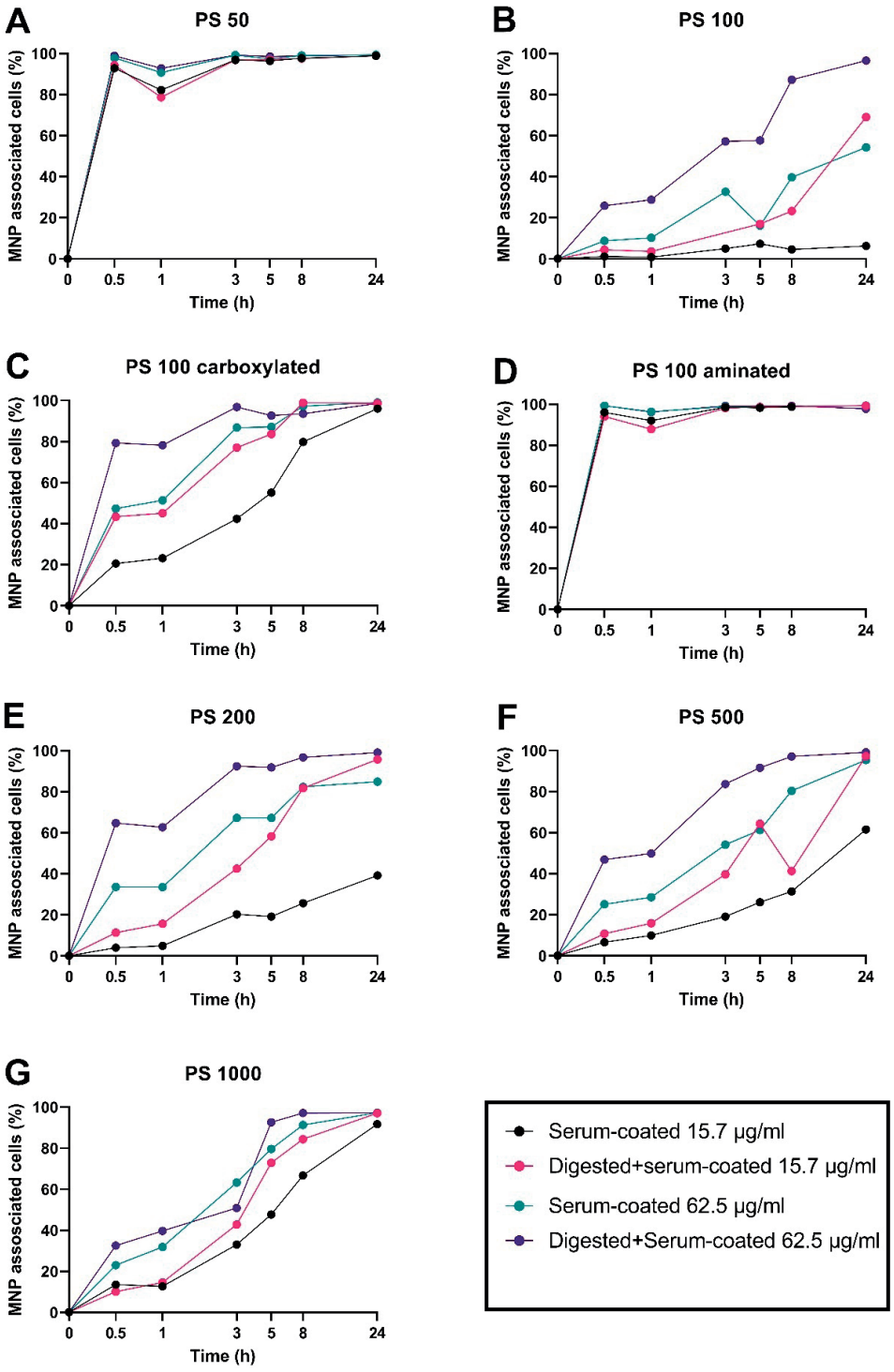
A
PS 50
B
PS 100
C
PS 100 carboxylated
D
PS 100 aminated
E
PS 200
F
PS 500
G
PS 1000
MNP associated cells (%)
Time (h)
0
0.5
1
3
5
8
24
Serum-coated 15.7 µg/ml
Digested+serum-coated 15.7 µg/ml
Serum-coated 62.5 µg/ml
Digested+Serum-coated 62.5 µg/ml

Fig. S4: Percentage of THP-1 derived macrophages associated with MNPs in time.

MNP cell association after 0.5,1,3,5,8 or 24 h exposure to digested+serum-coated or serum-coated MNPs at a concentration of 15.7 or 62.5 µg/ml. The graphs indicate association of (A) PS 50, (B) PS 100, (C) aminated PS 100, (D) carboxylated PS 100, (E) PS 200, (F) PS 500, (G) PS 1000. The y-axis indicate the percentage of cells associated with at least 1 fluorescent particle, defined as having a fluorescence intensity higher than 99% of the unexposed cells. n=1

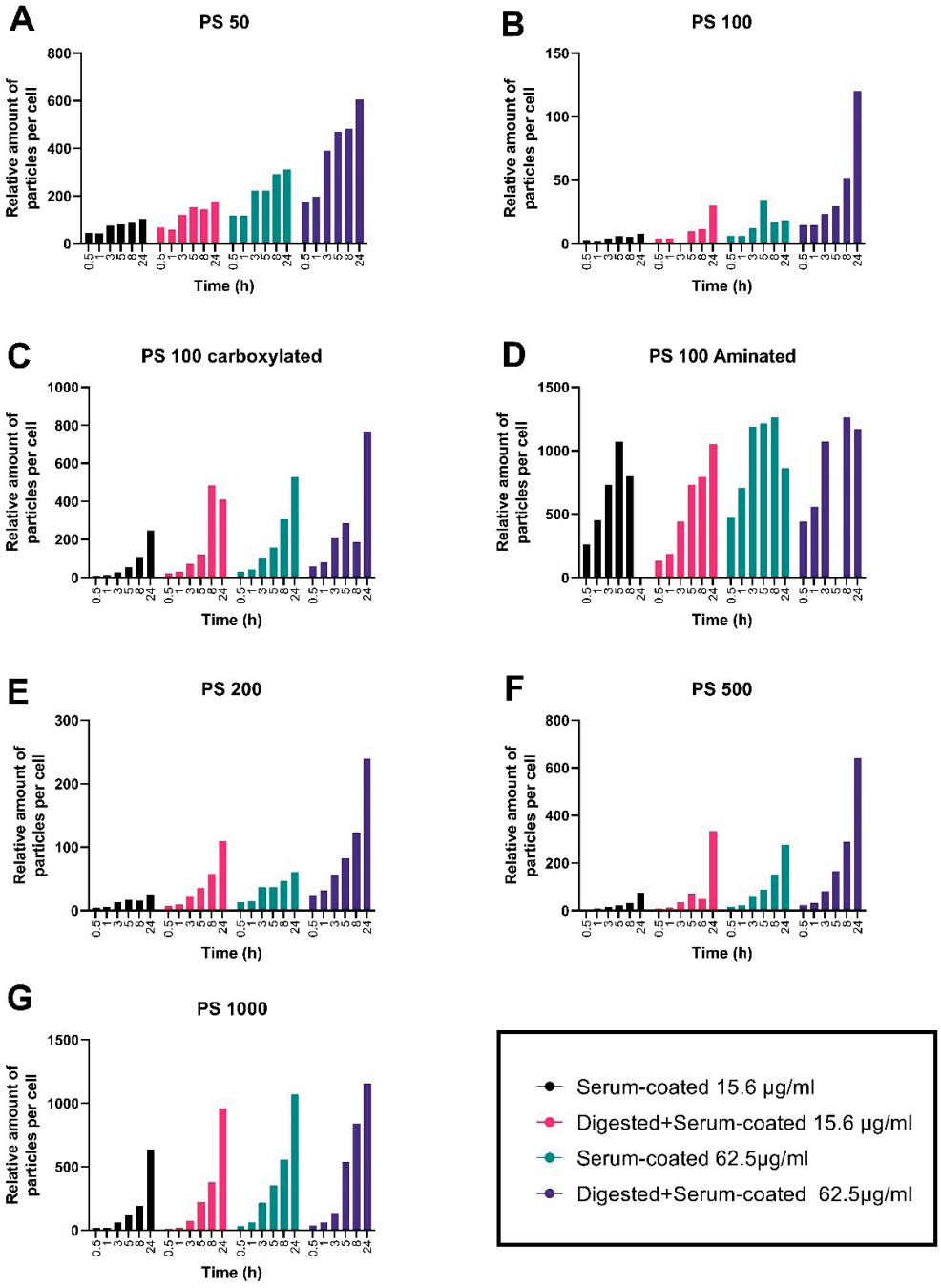
A
PS 50
Relative amount of particles per cell
800
600
400
200
0
Time (h)
B
PS 100
150
100
50
C
PS 100 carboxylated
1000
D
PS 100 Aminated
1500
E
PS 200
300
F
PS 500
G
PS 1000
0.5 1 3 5 8 24
Serum-coated 15.6 µg/ml
Digested+Serum-coated 15.6 µg/ml
Serum-coated 62.5µg/ml
Digested+Serum-coated 62.5µg/ml

Fig. S5: Amount of MNPs associated with THP-1 derived macrophages in time.

MNP cell association after 0.5,1,3,5,8 or 24 hour exposure to digested or serum-coated MNPs. The bar graphs show the average relative fluorescence originating from MNPs per cell after 0.5,1,3,5,8 or 24 hour exposure to digested or serum-coated MNPs. The graphs indicate association of (A) PS 50, (B) PS 100, (C) aminated PS 100, (D) carboxylated PS 100, (E) PS 200, (F) PS 500, (G) PS 1000. The relative fluorescent intensity is the fold change in the 525:20 channel compared to the unexposed cells. The cells were exposed to either 15.6 µg/ml or 62.5 µg/ml of MNPs. The legend on the left indicates the concentration and particle treatment. n=1

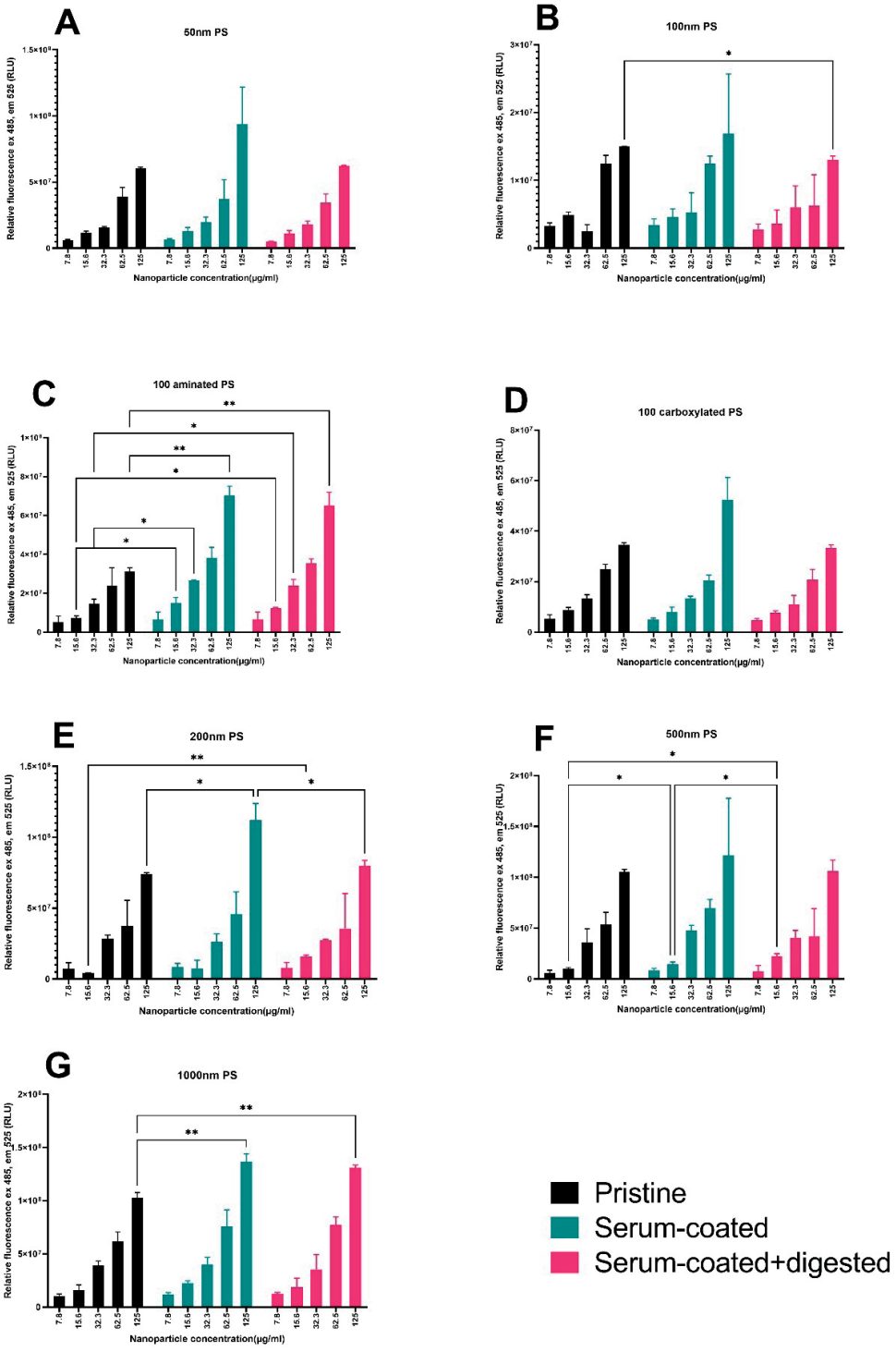
A
50nm PS
B
100nm PS
C
100 aminated PS
D
100 carboxylated PS
E
200nm PS
F
500nm PS
G
1000nm PS
Relative fluorescence ex 485, em 525 (RLU)
Nanoparticle concentration(μg/ml)
7.8
15.6
32.3
62.5
125
Pristine
Serum-coated
Serum-coated+digested

Fig. S6: Relative luminescence of pristine, serum coated and digested particles

This figure shows the relative fluorescence of pristine, serum-coated and serum-coated+digested particles. The excitation was at 485nm while the emission was measured at 525 nm. The figures show the fluorescence of (A) 50nm PS, (B) 100nm PS, (C) 100nm aminated PS, (D) 100nm carboxylated PS, (E) 200nm PS, (F) 500nm PS, (H) 1000nm PS. Fluorescence was measured using a spectramax iD3 luminometer

Supplementary table S1: Proteins uniquely enriched in any of the conditions

Unique to	Protein name	Abbreviation	Literature
Serum-coated PS100	Coactosin-like protein	Q2HJ57	(704)
Serum-coated PS100	Collagen type V alpha 1 chain	G3MZI7	(705)
Serum-coated PS100	von Willebrand factor	P80012	(677)
Serum-coated PS100 (+)	Leucine rich alpha-2-glycoprotein 1	F6RMV5	-
Serum-coated PS100 (+)	Serpin domain-containing protein	A0A0A0MPA0	-
Serum-coated PS100 (+)	60S acidic ribosomal protein P0	A0A287AY54	-
Serum-coated PS100 (+)	Inositol-3-phosphate synthase 1	A0A287BDF8	-
Serum-coated PS100 (+)	SERPINA11 protein	A5PK77	-
Serum-coated PS100 (+)	SHBG protein	A5PKC2	-
Serum-coated PS100 (+)	Serpin A3-8	A6QPQ2	(677)
Serum-coated PS100 (+)	Gamma-glutamyl hydrolase	A7YWG4	-
Serum-coated PS100 (+)	Corticosteroid-binding globulin	E1BF81	(677)
Serum-coated PS100 (+)	Peptidoglycan recognition protein 2	E1BH94	-
Serum-coated PS100 (+)	Alpha-amylase, 3.2.1.1	F1MJQ3	(704)
Serum-coated PS100 (+)	Mannose receptor C type 2	F1MPD1	-
Serum-coated PS100 (+)	CD109 molecule	F1MPE1	-
Serum-coated PS100 (+)	Actinin alpha 3	F1RU49	-
Serum-coated PS100 (+)	Ig-like domain-containing protein	G5E5T5	(706) (674)
Serum-coated PS100 (+)	MBL associated serine protease 2	I2E4T6	-
Serum-coated PS100 (+)	Osteomodulin	O77742	(677)
Serum-coated PS100 (+)	Fibromodulin	P13605	(704)
Serum-coated PS100 (+)	Insulin-like growth factor binding protein 2	Q09TE3	(707)
Serum-coated PS100 (+)	Pantetheinase	Q58CQ9	(677, 707)
Serum-coated PS100 (+)	Acidic mammalian chitinase	Q95M17	(677, 707, 708)
Serum-coated PS1000	pyruvate kinase M1/2	F1SHM0	-
Serum-coated PS1000	Protein-lysine 6-oxidase	P33072	(704)
Serum-coated PS1000	Protein HP-20 homolog	Q2KIT0	(677)
Serum-coated PS1000	Parkinson disease protein 7 homolog	Q5E946	-
Digested+serum-coated PS100	Ig-like domain-containing protein	A0A3Q1M1Z4	-
Digested+serum-coated PS100 (+)	Peptidyl-prolyl cis-trans isomerase	A0A286ZKG9	-
Digested+serum-coated PS100 (+)	60S ribosomal protein L14	A0A286ZW72	-
Digested+serum-coated PS100 (+)	40S ribosomal protein S15a	A0A287A014	-
Digested+serum-coated PS100 (+)	Nucleoside diphosphate kinase	A0A5G2Q9S0	-
Digested+serum-coated PS100 (+)	Ribosomal protein S3	A0A5G2QSB4	-
Digested+serum-coated PS100 (+)	KDEL endoplasmic reticulum protein retention receptor 2	A0A5G2R5F8	-

Supplementary table S1: Continued

Unique to	Protein name	Abbreviation	Literature
Digested+serum-coated PS100 (+)	Hydroxysteroid 17-beta dehydrogenase 13	F1RW28	-
Digested+serum-coated PS100 (+)	Staphylococcal nuclease domain-containing protein	F1SML4	-
Digested+serum-coated PS100 (+)	Phosphate carrier protein, mitochondrial	F1SQT3	-
Digested+serum-coated PS100 (+)	Endoplasmic reticulum protein 27	F1SQW6	-
Digested+serum-coated PS100 (+)	40S ribosomal protein S11	F2Z4Y8	-
Digested+serum-coated PS100 (+)	Peroxiredoxin 4	K7GLN4	-
Digested+serum-coated PS100 (+)	60S ribosomal protein L8	K7GNY4	-
Digested+serum-coated PS100 (+)	Ig lambda chain C region	P01846	(589)
Digested+serum-coated PS100 (+)	Prosaposin	P26779	(709)
Digested+serum-coated PS100 (+)	Cytosol aminopeptidase	P28839	-
Digested+serum-coated PS100 (+)	ATP synthase subunit alpha	P80021	-
Digested+serum-coated PS100 (+)	Dolichyl-diphosphooligosaccharide--protein glycosyltransferase	Q29036	-
Digested+serum-coated PS100 (+)	Large ribosomal subunit protein eL8	Q29375	-
Digested+serum-coated PS100 (-)	Palmitoyl-protein thioesterase 1	A0A287AYH9	-
Digested+serum-coated PS100 (-)	Ig-like domain-containing protein	F1MZ96	-
Serum-coated PS1000	pyruvate kinase M1/2	F1SHM0	-
Serum-coated PS1000	Protein-lysine 6-oxidase	P33072	(704)
Serum-coated PS1000	Protein HP-20 homolog	Q2KIT0	(677)
Serum-coated PS1000	Parkinson disease protein 7 homolog	Q5E946	-

Proteins uniquely identified on one of the MNP protein coronas using LC-MS-MS. The Literature column indicates sources which have previously implied the protein as being assosciated with altered uptake of nanomaterials or altered phagocytosis.

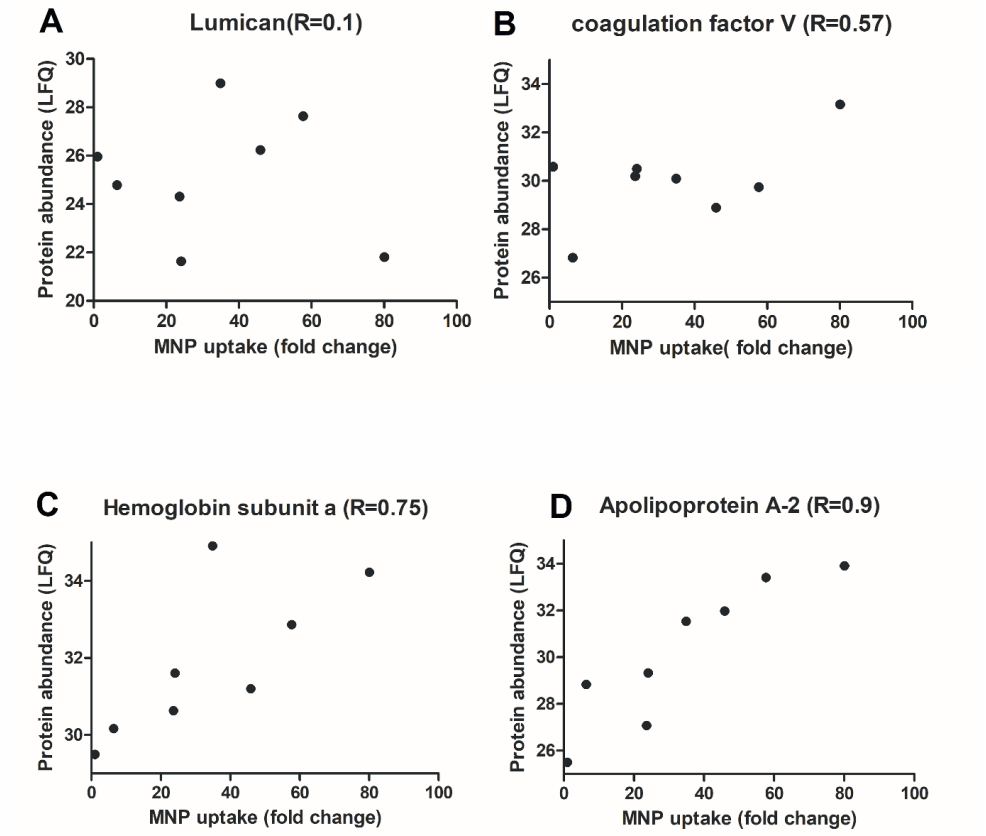

Fig. S7: Overview of correlation patterns of poorly, moderately and well correlated proteins

This figure shows the correlation of the protein abundance in LFQ with the fold change in MNP uptake for (A) Lumican, (B) Coagulation factor V, (C) Hemoglobin subunit a and (D) Apolipoprotein A-2. The R-value at the title of each graph indicates how high the pearson correlation between protein abundance and uptake was with R=1 being perfectly correlated and R=0 having no correlation.

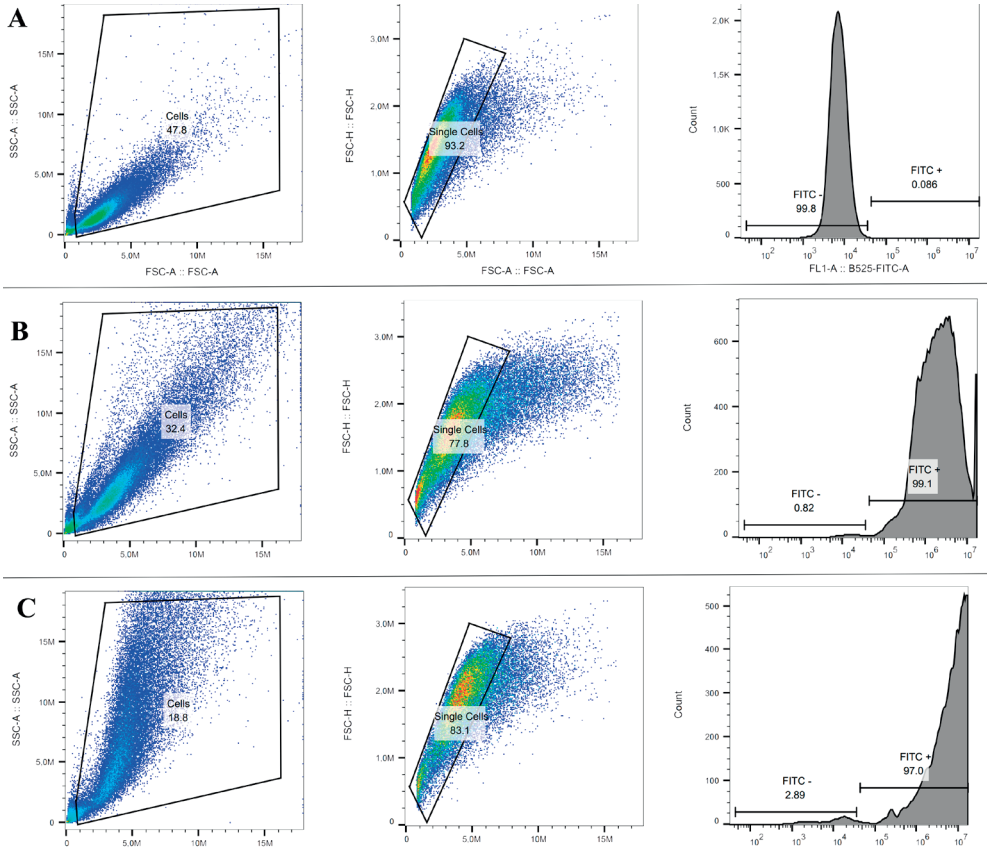

Fig. S8: Flow cytometry sorting strategy and alterations in forward side scatter after treatment

This figure shows the sorting strategy to determine the mean fluorescence intensity of cells exposed to A) cell culture medium, B) cell culture medium and 31.3 µg/ml of digested+serum coated PS50 and C) 31.3 µg/ml digested+serum-coated PS1000. The first column of figures show the gating to separate cells from debris, the y-axis shows the side-scatter area and the X-axis shows the forward scatter area. The second column of figures shows the isolation of singlet cells, the y-axis shows the forward scatter height and the X-axis shows the forward scatter area. The third column of figures shows a histogram of the particle fluorescence in single cells, the y-axis shows the count and the X-axis shows the area of the fluorescence at 525/20 nm.

CHAPTER 6

6

Mechanistic PBK Modelling for Biodistribution Prediction of Ingested Micro- and Nanoplastics

Hugo Brouwer, Mathias Busch, Nynke Kramer and Hans Bouwmeester

Manuscript in preparation

Abstract

6.1 Abstract

Background: Micro- and nanoplastic (MNP) contaminants are abundant in our diet, resulting in continuous consumer exposure. Accumulating evidence indicates that MNPs reach the human body, yet there are no controlled human exposure studies relating external MNP exposure with internal organ concentrations. Physiologically based kinetic (PBK) models are increasingly being developed to predict the biodistribution of MNPs. However, most existing colloid-PBK models are fitted on datasets obtained from animal studies. Such empirically fitted models have limited applicability for read across to other data-poor MNPs and other exposure scenarios, and are therefore of little use in a risk assessment framework for MNPs.

Methods: Here, we implement a mechanistic colloid-PBK model for size-agnostic modelling of MNP biokinetics. We benchmarked the mechanistic model to conventionally fitted empirical models and evaluated if the mechanistic model accurately predicts organ concentrations of MNPs after oral exposure in mice or humans. The ability to predict organ biodistribution after oral MNP ingestion was validated using eight mouse datasets. Additionally, the mechanistic human PBK model was used to simulate a realistic scenario of oral MNP exposure, and results were compared with observed tissue concentrations in human blood, kidney, brain and liver.

Results: The mechanistic mouse model accurately predicted observed tissue concentrations within a 10-fold difference for blood (94%), lung (88%), kidney (75%), heart (75%) and gut (75%) when used to predict tissue concentrations after single oral administration of radiolabelled PS. When both the mechanistic and empirical models were validated with eight mouse studies spanning acute and chronic exposure scenarios, we found that the mechanistic model was able to predict murine blood concentrations after oral exposure to MNPs in 52% of cases and showed a mean fold change of 1.5 compared to the observed concentration. This in part reflects the variability in the reported murine *in vivo* data. Contrastingly, the empirically fitted model showed worse prediction of validation data for all organs except spleen. Both mechanistic and empirical models predicted low overall tissue internalization of MNPs, regardless of size. Simulation of lifelong human exposure to 5 µg of MNPs per week resulted in predicted tissue concentrations of 5-9400 pg/g, 0.23-460 pg/g, 2-3500 pg/g and 5.3-11000 pg/g for blood, brain, kidney and liver, respectively (depending on the size of the MNP exposure).

Conclusion: Overall, the mechanistic model was broadly applicable to spherical MNPs between 20-6000 nm and was used to generate a preliminary prediction of human tissue concentrations after lifetime exposure to MNPs. Simulation of human MNP exposure indicates that MNP tissue concentrations are lower than previously reported and that the blood concentration may serve as a biomarker for tissue concentrations of MNPs. The improved predictability of the mechanistic colloid-PBK model compared to fitted models is promising for read-across needed for future incorporation into a risk assessment framework for MNP.

6.2 Graphical abstract

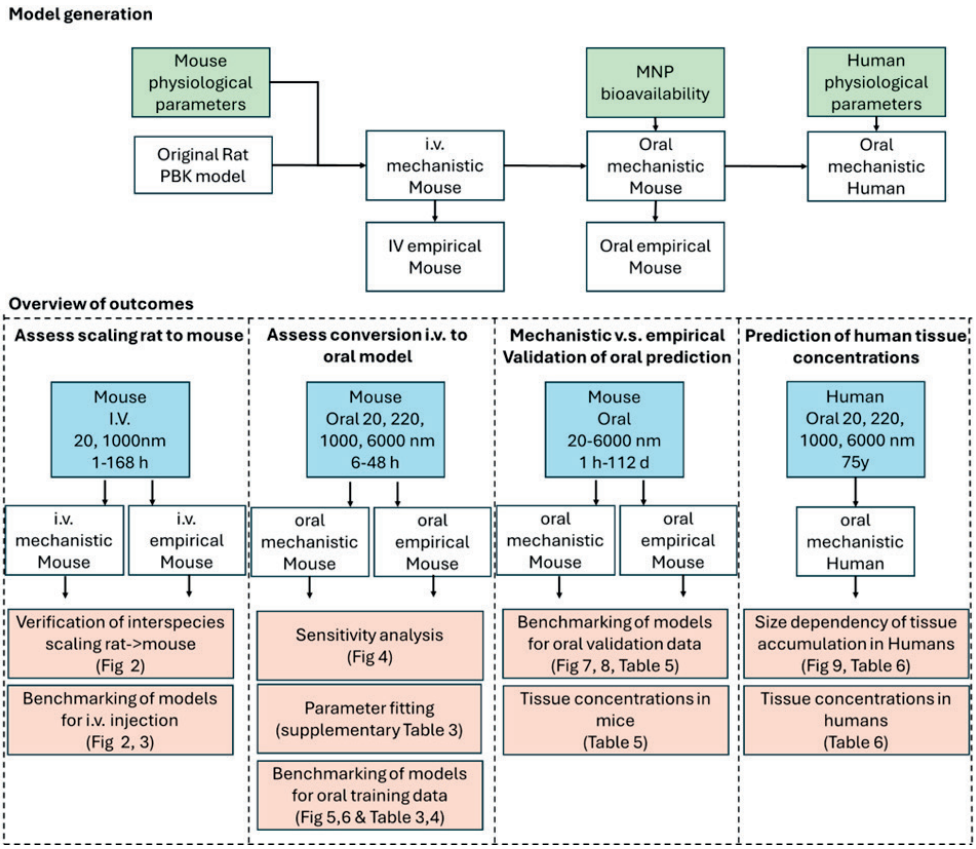

6.3 Introduction

Micro- and nanoplastics (MNPs), resulting from fragmentation of plastic waste, have become an omnipresent contaminant in all environments found on earth (8-11). Humans are continually exposed to MNPs through ingestion of contaminated foodstuffs and drinking water (13, 109, 113, 710, 711). Recent reports showing the presence of MNPs in human blood (712), placenta (17) and brain (16) are concerning and raise questions on the potential health impact of MNP exposure. Yet, no controlled exposure studies in humans are available relating external exposure to internal exposure.

Physiologically based kinetic (PBK) models are *in silico* representations of the human body that can be used to predict the biokinetics of compounds, thus connecting the external exposure and internal organ concentrations. PBK models represent organs as compart-

ments and describe the uptake, distribution, metabolism and excretion of chemicals between organs through differential equations. The solution of these differential equations requires a set of species-specific physiological parameters and compound specific physicochemical parameters and compound specific biokinetic parameters (241). For small-molecule chemicals, biokinetic parameters can be accurately predicted based on their chemical structure using quantitative structure activity relationships (QSARs) (241). However, QSARs for colloids (particles <10 µm) are still in their infancy and derivation of biokinetic properties is not yet possible. Instead, colloid-PBK models typically derive biokinetic parameters by fitting the model to best match empirically observed animal organ concentrations (i.e. the training dataset) (244-246). Empirical fitting limits the applicability domain of developed colloid-PBK models, as such a model is only valid for particles with physicochemical characteristics and exposure scenarios that are highly similar to those in the training dataset used for fitting (713). The strict reliance on empirical (animal derived) data of current colloid-PBK models hinders the prediction of data-poor materials such as environmental MNPs and precludes interspecies extrapolation, for instance from laboratory animals to humans, where data scarcity is a given.

Recently, mechanistic colloid-PBK modelling approaches have been introduced to reduce the reliance on animal data. These mechanistic colloid-PBK models derive particle toxicokinetic rates using hydrodynamic and thermodynamic functions derived from fluid dynamics (714-716). Mechanistic colloid-PBK models typically regard MNP transport as a predominantly passive process dominated by the passage through capillary fenestrations and the uptake by phagocytes (715, 716). The hydro- and thermodynamic functions are size-dependent, broadening the applicability domain of mechanistic colloid-PBK models. Through incorporation of species-specific physiological parameters, mechanistic models can be extrapolated from one species to another (i.e. from mice to humans) (716). Furthermore, the use of mechanistic models allows the prediction of particle biokinetics in a data-independent manner, bypassing the need for animal experiments. Lastly, mechanistic models are fully defined which allow future improvements like inclusion of *in vitro*-derived phagocytic uptake rates of tissue-residing macrophages (716), which is not possible with black-box models such as empirical PBK models. So far, mechanistic colloid-PBK models have only been developed for intravenous administration of nano-sized particles up to 160 nm (715).

Here, we aimed to develop a mechanistic colloid-PBK model to predict the internal fate of MNPs in a size range of 20 nm to 6000 nm upon oral exposure for mice and humans. We benchmarked the prediction of our mechanistic model towards empirically fitted colloid-PBK models. The mechanistic model was validated using eight oral mouse biokinetic studies and two human studies.

6.4 Materials and methods

6.4.1 Data sources

A literature search was performed to identify biodistribution datasets which could serve for empirical model training or model validation. First, biodistribution studies were identified using the following search condition using scopus; "(microplastic OR nanoplastic OR polystyrene) AND (kinetic OR biodistribution OR distribution OR accumulat* OR pbpk OR pbtk OR pbk OR pbbk) AND mouse". In total 704 studies were identified which were manually curated based on the following selection criteria: the underlying dataset is publicly available or can be visually estimated from the graphs; the study showed an oral bioavailability between 0.0001%-20%, which was deemed biologically plausible based on expert judgement; the dosing scheme was clearly described; organ concentrations were quantitatively reported in mass-based units; the study includes particles with a size below 6000 nm, and the study includes some form of particle characterization. After applying these selection criteria, nine studies remained including one intravenous administration study and 8 oral gavage studies which are summarized in Table 1. The organ concentrations from all datasets are included in Supplementary File 1.

Where available, tabulated MNP organ concentrations were directly taken from the original publication, otherwise organ concentration data was estimated from graphs using the online webplot digitizer tool (723). Radiolabelled data was first converted from the percentage of administered dose (%ID)/g to mg/g. When multiple sub-compartments of the gastrointestinal tract (such as stomach or small intestine) were reported separately, the total gastrointestinal tissue concentration was determined by scaling the concentrations with the relative gastrointestinal tract weights (724). The dataset of Keinanen et. al. was used as training dataset, as it comprised the largest range of MNP sizes and timepoints and as it used radiotracers which are less prone to false positive detection by fluorophore leaching (144).

6.4.2 PBK model structure

The PBK model used here was based on previously published mechanistic nanoparticle PBK models (715). The PBK model used here consists of 11 organ compartments: blood, lymph, lung, brain, heart, spleen, liver, kidney, muscle, gastrointestinal tract and a grouped compartment for other organs. The rate of MNPs internalization into organs is considered small compared to the blood flow and thus a permeability-limited model is assumed. Each organ compartment is comprised of a separate exterior blood compartment and interior tissue compartment (Figure 1). The blood compartments of all organs are connected to a central blood compartment and the tissue compartments are connected to a central lymph compartment which subsequently flows into the central blood compartment. A phagocytic sub-compartment is included in the lung and organs

belonging to the reticuloendothelial system (RES) i.e. the liver and spleen. Particles can enter the PBK model either from the blood compartment (for i.v. administration) or in a separate lumen compartment in the gastrointestinal tract (oral administration). MNP elimination can either occur through urinary excretion from the kidney interior into the urine or through biliary excretion from the liver interior into the gastrointestinal lumen. It is assumed that MNPs are not metabolized within the body. An overview of the model structure is shown in Figure 1.

Table 1: Biokinetic studies with datasets compatible with mechanistic PBK model.

Particle size (nm)	Route	Polymer type	Dose (mg/kg)	# of doses	Sampling times*	Detection	Tissues analysed	Ref
20, 1000	i.v.	PS-$NH_2^{\#}$	1.75	1	1, 6, 24, 168 h	^{89}Zr PET	Blood, Brain, Heart, Lung, Liver, Spleen, Kidney, Muscle, Gut	(145)
20, 220, 1000, 6000	Oral	PS-$NH_2^{\#}$	5	1	6, 12, 24, 48 h	^{89}Zr PET	Blood, Heart, Lung, Liver, Spleen, Kidney, Muscle, Gut	(144)**
220	Oral	PS-$NH_2^{\#}$	3	1	1, 6, 12, 24, 48 h	^{64}Cu PET	Blood, Brain, Lung, Liver, Spleen, Kidney, Gut	(717)
500	Oral	PS	5, 25, 50	14	14 d	Fluorescence	Liver, Kidney, Gut	(718)
50, 500, 5000	Oral	PS	250	1	24 h	Fluorescence	Blood, Brain, Lung, Liver, Spleen, Kidney, Muscle, Gut	(719)
800	Oral	PS	30	35	35 d	Fluorescence	Blood, Brain, Lung, Liver, Spleen, Kidney, Gut	(720)
25, 50, 100	Oral	PS	50	7	7 d	Fluorescence	Blood, Brain, Heart, Lung, Liver, Spleen, Kidney, Gut	(721)
500, 5000	Oral	PS	25	56	56 d	Fluorescence	Heart, Lung, Liver, Spleen, Kidney	(183)
2500	Oral	PLA	25	28	28 d	Fluorescence	Blood, Brain, Heart, Lung, Liver, Spleen, Kidney, Muscle	(722)

* Time after initial administration, # amine group used for conjugation of radiotracer. ** Dataset used as training dataset for oral empirical model

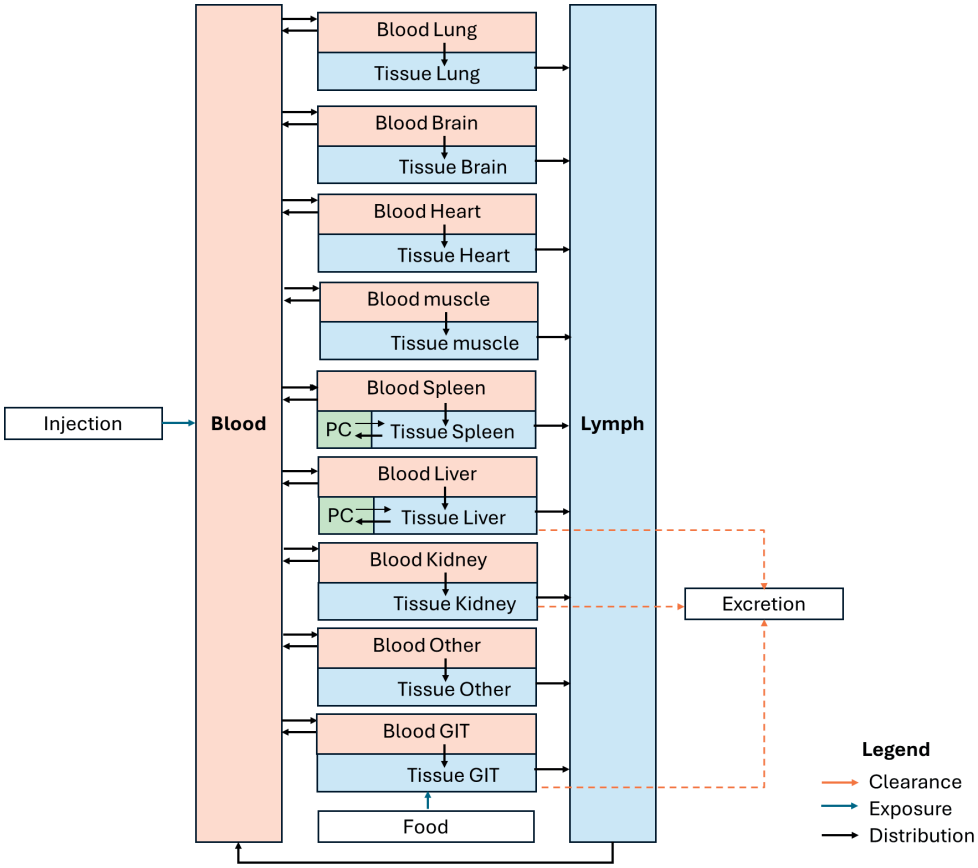

Fig 1. Topology of PBK model structure

Overview of the PBK model structure. Each organ is divided into a blood compartment comprising the capillaries and an interior tissue compartment. The liver, spleen and lung tissues contain an additional phagocytic cell (PC) compartment. Blue arrows indicate uptake processes, black arrows indicate biodistribution processes, orange arrows indicate elimination processes (i.e. clearance).

6.4.3 PBK model equations

The distribution of MNPs between organs is governed by four processes: 1) Convection of MNPs with the blood flow to the organ capillaries; 2) Binding of MNPs to the capillary wall (margination); 3) Passage of MNPs through capillary pores (extravasation) and 4) Phagocytosis by macrophages. Convection of MNPs is a result of the relative blood flow rate to each organ and the time-dependent blood concentration of each organ.

The binding of plastics to the capillary wall is governed by the rate of particle binding to the wall (K_{on}) and the release rate (K_{off}) as previously described by Dogra et. al. (715).

Briefly, K_{on} was considered to be equal to the sedimentation rate of particles in still liquids according to the Stokes-Einstein equation, corrected for the Peclet number describing the diffusivity of particles due to blood flow (Equation 1). As K_{on} relies on the blood flow speed, it was considered to be both size- and organ- specific. K_{off} was considered to be equal to the rate required for particles to move away from the capillary cell wall (i.e. the glycocalyx) assuming unimpeded passive diffusion and was set equal to the particle diffusivity obtained from the Stokes-Einstein-Sutherland equation, divided by the square of the typical length of diffusion, i.e. the capillary glycocalyx thickness (assumed at 20 nm) (Equation 2). K_{off} has no organ-specific parameters and is thus only particle size-dependent.

For the mechanistic model, the following equations were used for parameter derivation:

Equation 1: $K_{On} = \frac{2}{9}\left(\frac{\Delta\rho}{\mu_m}\right)\frac{gr^2Dl}{vR^3}$; from literature(715)

Equation 2: $K_{Off} = \frac{K_BT}{6\pi\eta r}/l_g^2$; from literature(715)

Where:
g is the gravitational acceleration constant
v is the terminal sedimentation velocity
r is the MNP radius
$\Delta\rho$ is the difference in density between medium and the MNP
μ_m is the dynamic viscosity of medium
l is the length of a capillary
$l_g$is the thickness of the glycocalyx i.e. the diffusion distance
R is the radius of a capillary
K_B is the boltzman coefficient
T is the remperature
η is the sheer rate

To model MNP capillary extravasation, the reflection coefficient due to drag and frictional forces by the capillary wall is considered to be a function of the particle size relative to the capillary pore size. Briefly, transport through a pore was considered to be similar to particles moving through a hollow tube, where the passage of particles is impeded by drag due to the fluid moving within the tube and sheer stress from the walls of the tube (715) (Equation 3).

Equation 3: $a = \frac{r}{r_p}$, $\max a = 1$; from (715)

Where
r is the radius of the MNP
r_p is the radius of the pore

The reflection coefficient was calculated as the sum of the steric hindrance as described by the empirical formula F(a) from the Faxen correction (Equation 4), and the frictional hindrance due to drag which is described by the empirical formula G(a) as described by the Curry equation (Equation 5) (725-727).

Equation 4: $F(a) = 1 - 2.10444a + 2.08877a^3 - 0.94813a^5 - 1.372a^6 + 3.87a^8 - 4.19a^9$; from (725)

Equation 5: $G\left(a\right) = \frac{1-\frac{2a^2}{3}-0.20217a^5}{1-0.75851a^5}$; from (728)

Where
a is the ratio of nanoparticle to pore radius (obtained from Equation 3)

Passage through capillary pores represents the transport of capillary-bound particles into the organ interior and is represented by an organ-specific reflection coefficient (σ) (Bean equation (727)) which functions similar to a plasma:tissue partition coefficient (Equation 6).

Equation 6: $\sigma = 1 - \left[2(1-a)^2 - (1-a)^4\right]G(a) + \frac{16}{9}(1-a)^2 F\left(a\right)$; from (715)

Where
σ is the reflection coefficient
a is the ratio of nanoparticle to pore radius (obtained from Equation 3)
$F(a)$ is the empirical Faxen correction (obtained from Equation 4)
$G(a)$ is the empirical Curry equation (obtained from Equation 5)

Finally, the macrophage uptake rate and release rate were calculated as described before by Lunov et. al. (657). Briefly, macrophage uptake is considered as a passive process where the minimal energy required for membrane deformation leading to particle internalization is compensated by the typical force applied by cytoskeletal motor proteins resulting in a phagocytosis rate constant (Kp_i) (Equation 7).

Equation 7: $k_{pi} = \frac{p}{4\pi r^2 \Upsilon}$

Where
k_{pi} *is the phagocytosis rate constant*
p *is the motor protein power*
r *is the MNP radius*
Υ *is the surface tension of a macrophage*

In addition to phagocytosis,, macrophages can also actively exocytose particles and will lose particles due to cellular turnover. In the original publications on the nanoparticle PBK model (715, 716), the exocytosis rate was set to 0.01 to account for both radioactive decay and particle degradation in the body. Here, we have assumed that particle degradation by the body is negligible and that the release of particles from macrophages is solely due to cell turnover and degradation. A modest exocytosis rate of 10^{-6} was assumed.

Urinary excretion is assumed to occur unimpeded from MNPs internalized into the kidneys. As such, the urinary excretion is limited by the kidney-specific reflection coefficient σ_k which converges to 1 as MNP size approaches the fenestration size (70 nm). The most relevant excretion pathway for microplastics is biliary excretion, yet little is known about the rate and upper size limit. Particles up to 3 µm have been reported in bile, however, the canalicular ducts that transport bile have a diameter of approximately 1 µm (729). Therefore, we have included an additional reflection coefficient σ_{bile} which is based on a pore radius of 1.5 µm in the bile duct.

For the empirical PBK model, K_{on}, K_{off}, σ, K_{pi} and K_{po} were considered to be constants with an initial value equal to the values obtained by the mechanistic model and were subsequently optimized to fit the *in vivo* data in the training dataset in Table 1.

The PBK models were written and implemented in R version 4.5.1 using the mrgSolve package (730).

6.4.4 Physiological parameters used for modelling biodistribution in mice

Physiological parameters, including organ blood flow fractions, organ volume and weight fractions, urinary flow rate and bile flow rate for mice, were obtained from (724, 731) and scaled to body weight and are shown in Supplementary Table 1. The gastric emptying rate was based on the typical residence times in the mouse gastrointestinal tract and was set to 6 h according to (732). The pore sizes used for the mechanistic model were based on (142, 733). Organs were divided into continuous capillaries with pores of 5 nm (heart, brain, lung, muscles and other slowly perfused organs), discontinuous capillaries

with pores of 12 nm (gastrointestinal tract) and fenestrated organs with pores of 280 nm for liver, 70 nm for kidney. As the blood flow ends in the spleen, a pore size equal to the average diameter of a capillary was chosen and set to 5 µm.

6.4.5 Generation and validation of human model

A human PBK model was generated by replacing the murine physiological parameters with human data and by replacing the rodent fenestration sizes with sizes reported in humans according to literature(142, 734). The physiological parameters used for the human model are shown in Supplementary table 2. The humanized PBK model was validated using the most plausible current scenario of human exposure, predicting 5 µg/week per person (80). Thus, to simulate tissue concentrations, a daily exposure of 714 ng/day (5 µg/week) was simulated for 75 years. Tissue concentrations were validated using the only current mass-based estimates of tissue exposure in blood, brain, kidney and liver as taken from (14, 16).

6.4.6 Sensitivity analysis

To assess the importance of the parameters on the model output, a local sensitivity analysis was performed on the empirical mouse model. Briefly, the local sensitivity to all parameters was performed by modifying the parameters up or down by 10% in a one-at-a-time approach and assessing the impact on the maximal tissue concentration (C_{max}). The sensitivity coefficient was calculated by comparing the change in input variables to the resulting change in the C_{max} of each organ using the following formula:

Equation 8: $SC_i = \frac{\Delta C_i}{\Delta P} * \frac{P}{C_i}$.

Where

SC_i= sensitivity coefficient organ i; P= parameter; C_i =maximal concentration organ i.

The total sensitivity coefficient was set to the average of the sensitivity coefficients for each organ.

The sensitivity analysis was performed separately for all particle sizes used in the oral exposure study in mice (144) i.e. 20 nm, 220 nm ,1000 nm and 6000 nm at a dose of 0.1 mg/mouse (5 mg/kg bw/day).

The differential equations determining the amount of MNPs moving into and out of each organ compartment and sub-compartment are shown in the Supplementary information.

6.4.7 Parameter fitting of the empirical PBK model

For model calibration of the empirical PBK model, all parameters having at least a normalized sensitivity of 0.01 for any particle sizes either after i.v. administration or oral exposure were considered for optimization. For parameter fitting, the following parameters were considered; σ_i , $K_{on,i}$, K_{off}, fraction absorbed (f_{abs}), macrophage fraction liver (Mf_{Li}), macrophage fraction spleen (Mf_S), Kp_i, Kp_o, biliary flow rate (B) and urinary flow rate (U). Fitting was separately performed against the biodistribution data of four particle sizes (20 nm, 220 nm, 1000 nm and 6000 nm) from (144). First, a cost function was created that takes the sum of squared residuals to penalize the model for having large differences with the observed data. The cost function was constructed using the modCost function of the FME package (735). The data from studies listed in Table 1 did not in all cases clearly separate the luminal gastrointestinal contents of the gut from the absorbed fraction (i.e. gastrointestinal tissue fraction), and therefore, the gut was not included in the cost function. Additionally, the urinary compartment was excluded from the cost function as it represents an external compartment and thus holds less relevance for organ concentrations.

To optimize the parameters, first the initial value was set to be equal to the values obtained with the mechanistic model, and upper and lower bounds were defined to limit how much each parameter can be altered. The bounds of physiological parameters such as biliary flow, urinary flow and macrophage fractions were set relatively narrow, as these parameters are relatively well defined. The bounds for reflection coefficients, phagocytosis rates, K_{on} and K_{off} were set at a wider range as these are particle specific and poorly defined. The upper and lower bounds of all parameters is shown in Supplementary Table 3. The parameters were optimized by first performing parameter initialization using a pseudo-random optimization algorithm (736) to obtain an optimal set of randomized parameters followed by the Nelder-Mead optimization method (737) to perform local optimization. Both the Pseudorandom optimization and Nelder-Mead algorithms were implemented through the modFit function of the FME package (735). The fitting results are shown in Supplementary Table 3.

6.4.8 Model performance evaluation

To determine model performance, the error of the model predictions was compared to the observed datasets listed in Table 1. The model performance was expressed as the root mean squared error (RMSE) calculated as $\sqrt{mean\left(Observed - Predicted\right)^2}$. A common suitability criterion for PBK models is the percentage of predictions that fall within 2, 3 or 5-fold of the observation. While the criteria is very well defined for PBK models specific to one chemical (<2-fold according to WHO), these criteria are poorly defined for generic PBK models and a 5-10 fold factor is more frequently deemed acceptable (738-740). Here, the percentage of observations lying within a 10-fold difference from the predictions

was calculated and reported as suitability criteria for generic PBK models. The mean fold change was used to determine whether the models on average show an overprediction or underprediction compared to the data.

6.5 Results

6.5.1 Scaling to mouse and prediction of intravenous administration

First, the original rat mechanistic colloid-PBK model (715) was scaled to mice because of the availability of higher quality oral mice MNP biokinetic studies (Table 1). To ensure that the model showed high accuracy after interspecies scaling (i.e. from the original rat model to the mouse model) when applied to MNPs, we first predicted organ concentrations (Figure 2 and 3) after intravenous administration of 20 nm and 1000 nm to mice (145).

The simulation by the mechanistic model showed a good prediction of the organ concentrations for 20 nm particles with all maximal observed organ concentrations (i.e. C_{max}) being within 2 orders of magnitude from the observed data. The excretion of 20 nm MNPs was overestimated in the mechanistic model, evident by the underprediction of all organs at the 168 h timepoint. For the 1000 nm MNPs, the mechanistic model predicted liver and spleen concentrations within a 2-fold difference, but underpredicted the remaining organs.

As the model could accurately predict organ concentrations upon the i.v. administration of 20 nm particles, and model accuracy was similar to those reported for the original model (715), we conclude that the model works adequately after interspecies scaling.

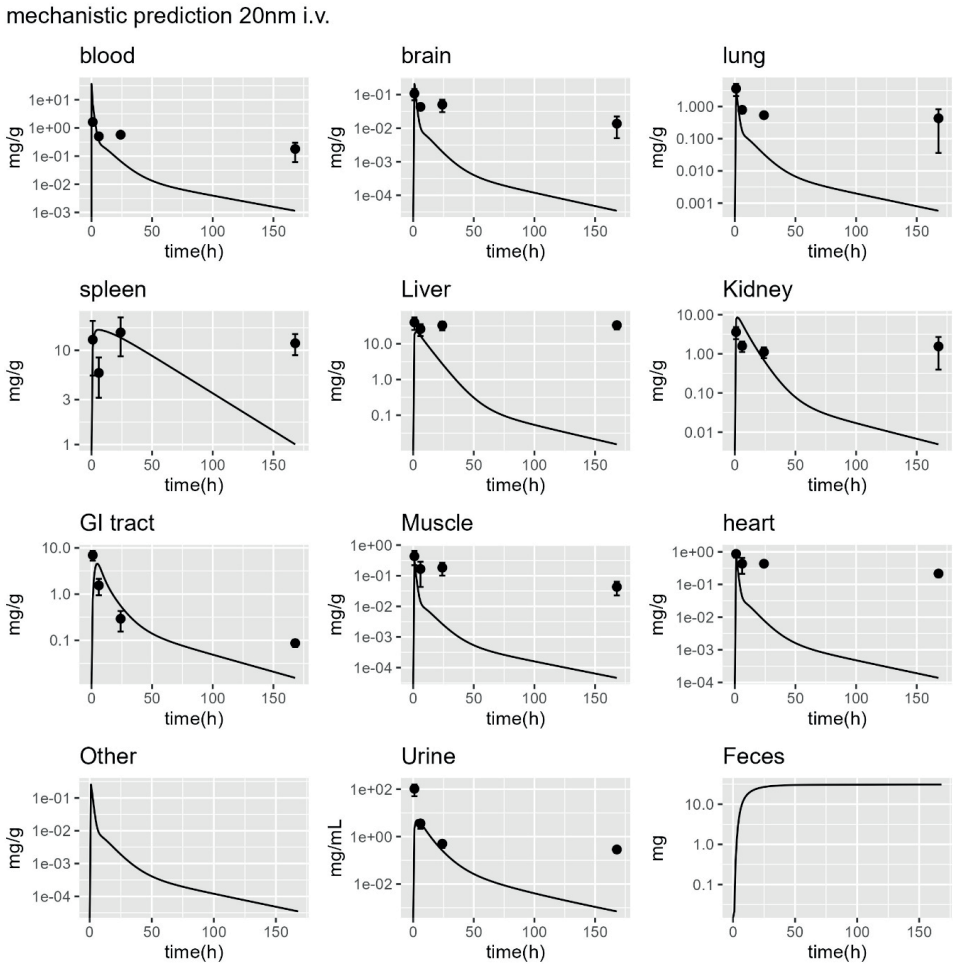

Fig 2. Mechanistic prediction of organ distribution of 20 nm polystyrene particles after intravenous administration to mice

The Y-axis indicates the concentration in each organ (mg/g), urine (mg/ml) and feces (mg). The X-axis indicates the time. The black lines indicate model predictions The black dots and error bars indicate the observed concentrations and standard deviation as retrieved from the literature (145). Note that no data from the in vivo study were reported for feces or other (carcass).

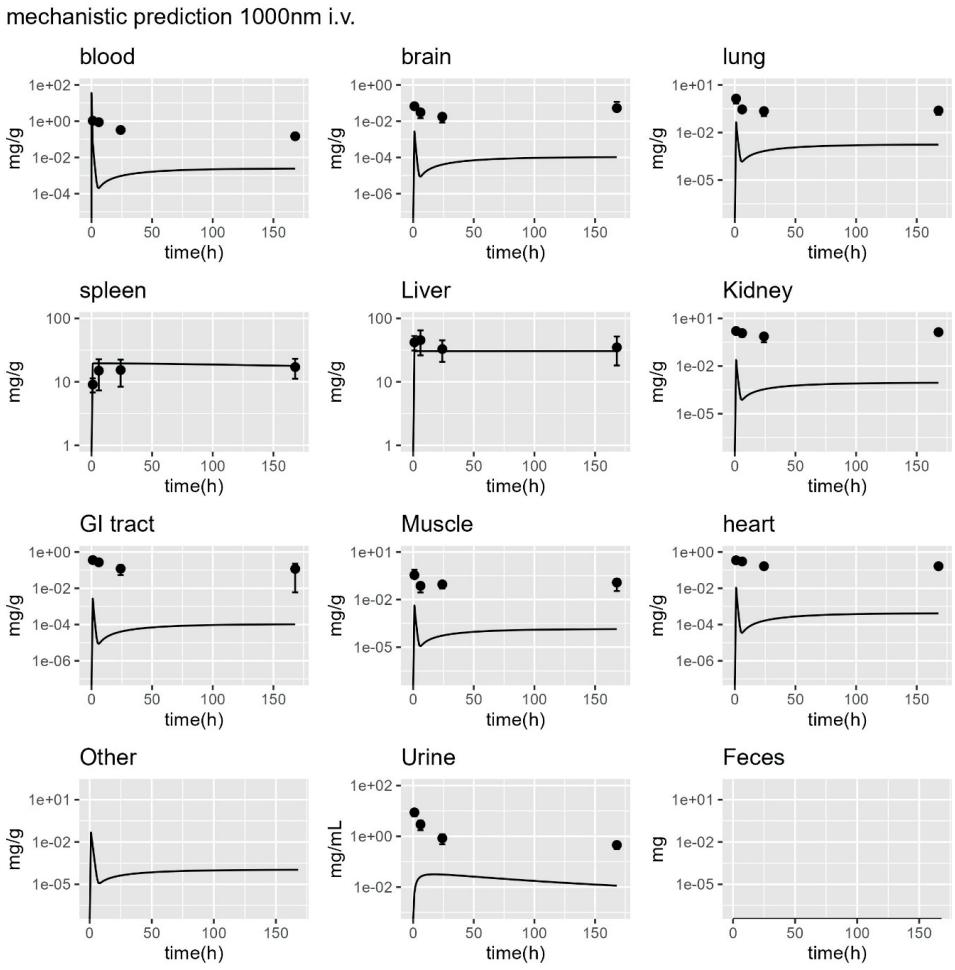

Fig 3. Mechanistic prediction of organ distribution of 1000 nm polystyrene particles after intravenous administration to mice

The Y-axis indicates the concentration in each organ (mg/g), urine (mg/ml) and feces (mg). The X-axis indicates the time. The black lines indicate model predictions. The black dots and error bars indicate the observed concentrations and standard deviation as retrieved from the literature (145). Note that no data from the in vivo study were reported for feces or other (carcass).

6.5.2 Local sensitivity analysis of the model

To determine the parameters which are most influential and should be fitted in the oral empirical model, a local sensitivity analysis was performed. The normalized sensitivity coefficient for each parameter is shown in Figure 4.

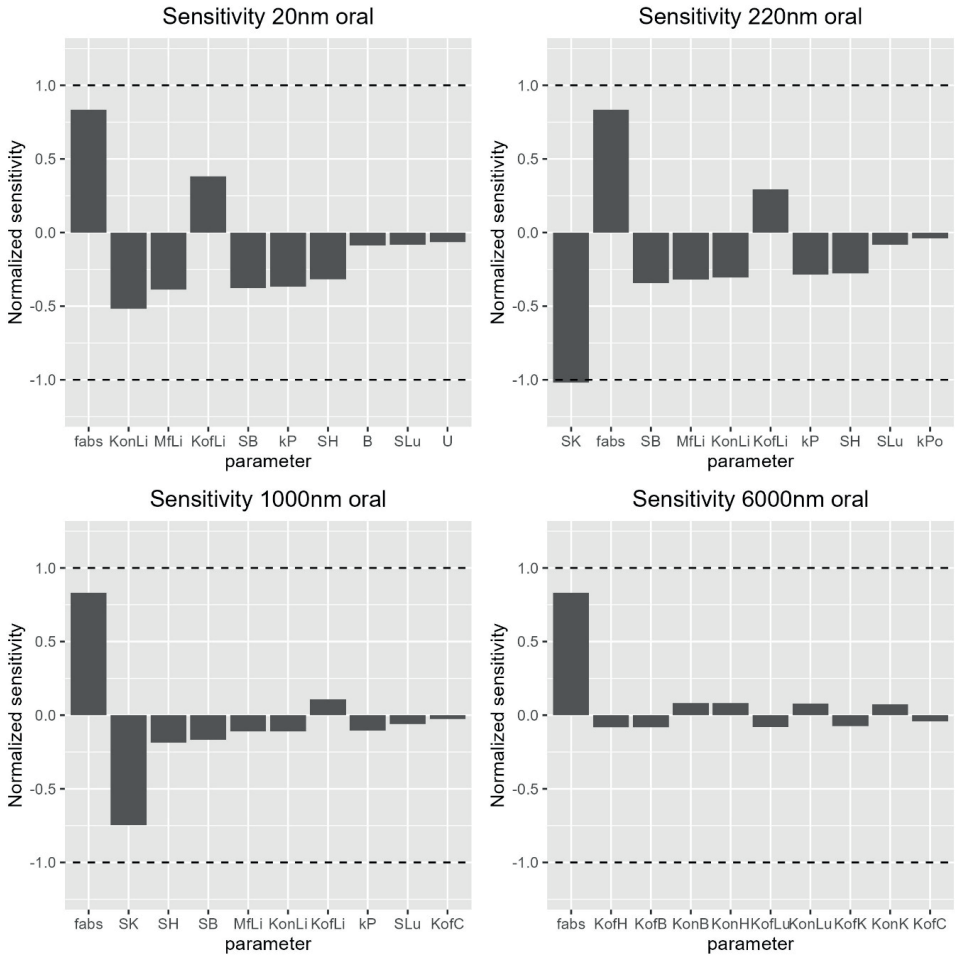

Fig 4. Parameter sensitivity for all primary parameters

The plots show the sensitivity of the organ C_{max} to all parameters for 20 nm, 220 nm, 1000 nm and 6000 nm as indicated above each plot. The Y-axis indicates the normalized sensitivity coefficient averaged over all organs and the X-axis indicates the respective parameter. U and B indicate urinary and biliary flow rates, S_i indicates reflection coefficient of organ i, Kp_i is the phagocytic uptake coefficient and kP_o is the phagocytic release coefficient, $K_{on,i}$ indicates the Kon of organ i, fabs is the fraction absorbed, Mf_{Li} and Mf_S are the macrophage fraction of liver and spleen respectively and $K_{of,i}$ is Koff in the organ i. H=heart, K=kidney, B=brain, Li=liver, S=spleen, Lu=lung, C= other (carcass).

Regardless of particle size, the f_{abs} showed a significant influence on total organ concentrations with a normalized sensitivity index above 0.5. For particles ≤1000 nm, a significant influence of the reflection coefficients for the brain, heart, lung and kidney, the fraction of macrophages in the liver and K_{on} and K_{off} of the liver was observed. Parameters

related to phagocytosis including K_p and K_{po} showed a significant influence on organ concentrations for particles below 1000 nm, but were not among the most sensitive parameters for the 6000 nm model. The 6000 nm particles showed a large influence of K_{on} and K_{off} in the kidney, brain, heart and lung. Based on these results, K_{on}, K_{off}, reflection coefficients, macrophage fractions of liver and spleen, phagocytic uptake and excretion and the fraction absorbed were used for the calibration of the empirical model (detailed in Supplementary information Table 3).

6.5.3 Benchmarking mechanistic and empirical model accuracy

Both the mechanistic and empirical PBK model were used to predict the organ concentrations after a single oral administration of 5 mg/kg bw of 20 nm PS, 220 nm PS, 1000 nm PS or 6000 nm PS. Predicted concentrations were compared against the *in vivo* data of Keinanen et. Al. (144). Figures 5 and 6 show the organ concentrations for 20 nm and 6000 nm PS MNPs while the comparisons for 220 nm and 1000 nm PS MNPs are shown in Supplementary Figures 1 and 2. The fold change between the predicted concentration and observed concentration are shown in Table 3.

Overall, the mechanistic PBK model showed a good prediction of early organ distribution for both 20 nm and 6000 nm MNPs for all organs. At later timepoints, the 20 nm model overpredicts liver, spleen and kidney concentrations and slightly underpredicts heart and muscle concentrations. The 6000 nm model showed the same overprediction of liver and spleen concentrations but shows a better prediction of heart, muscle and kidney concentrations. Like the intravenous model, microplastics of >250 nm were solely found in the organ capillaries with the exception of spleen and liver (Supplementary Figure 3 and 4).

Considering all sizes of MNPs, the mechanistic model accurately predicted observations within a 10-fold difference compared to the observed concentrations for blood (94%), lung (88%), kidney (75%), heart (75%) and gut (75%), but showed worse prediction of liver (13%), muscle (44%) and spleen (31%) concentrations. Additionally, when particles become larger than kidney fenestrations, they can no longer be excreted through urine. The empirically fitted model showed an equal quality of prediction of blood (94%) and muscle (44%), improved prediction of liver (88%), spleen (63%) and kidney (82%) concentrations, but reduced quality of the prediction of lung (69%), heart (63%) and gut (50%) concentrations.

Both models predict little accumulation of ingested MNPs in mouse organs, which is in line with the data. The 20 nm model predicts concentrations in spleen, liver and kidney within one order of magnitude, reaching 192, 91 and 31 ng/g of tissue, respectively (see Figure 5). This corresponds to 0.1%, 0.013% and 0.01% of the total oral dose. The 6000 nm model predicts a higher accumulation in the liver and spleen at 420 ng/g and 250 ng/g

of tissue, however the maximal *in vivo* observed concentrations lie at 1.5 ng/g tissue and 33.5 ng/g tissue respectively (see Figure 6), both corresponding to less than 0.01% of the oral dose.

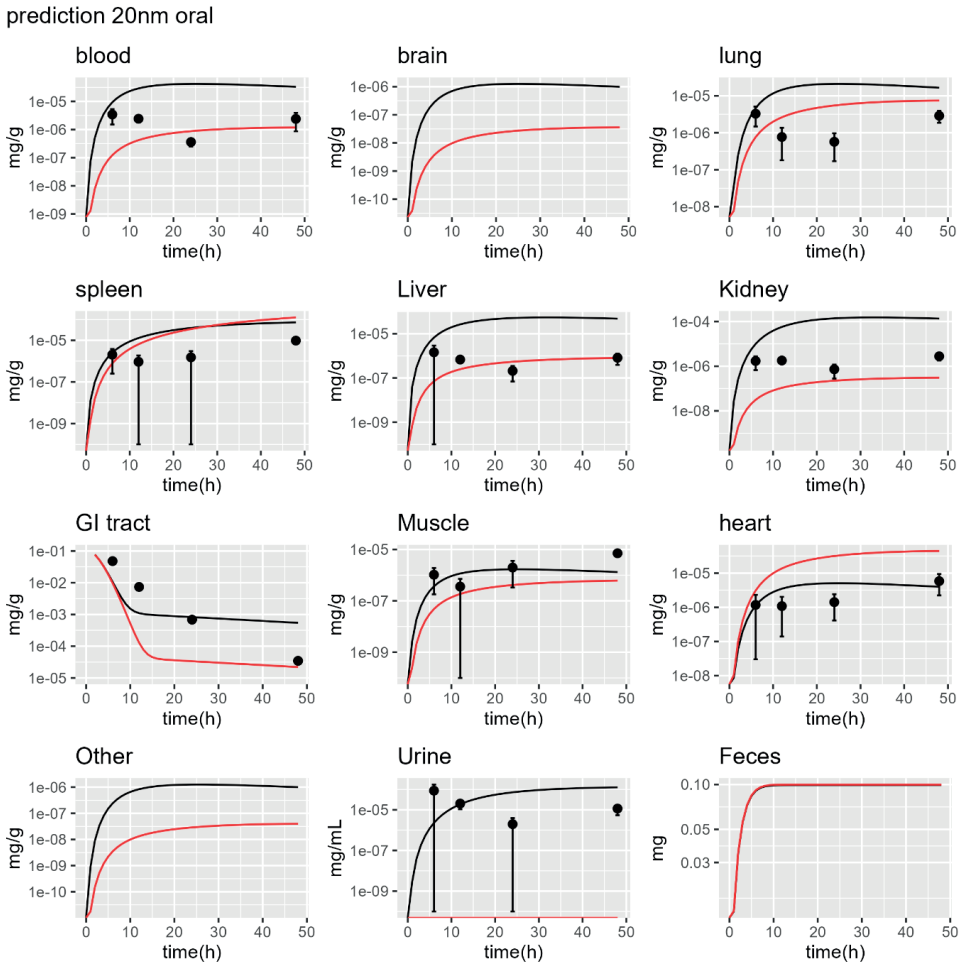

Fig 5. Prediction of organ distribution in mice upon oral exposure to 20 nm MNPs

The Y-axis indicates the concentration of each organ in mg/g and in mg/ml for urine and mg for feces and the X-axis indicates the time. The black lines indicate mechanistic model predictions while the red lines indicate the empirical model predictions. For feces the black and red lines overlap and no urinary excretion is seen with 20nm MNPs for the empirical model. The black dots and error bars indicate the observed concentrations as retrieved from the literature (144) Note that no data from the in vivo study were reported for brain, feces and other (carcass).

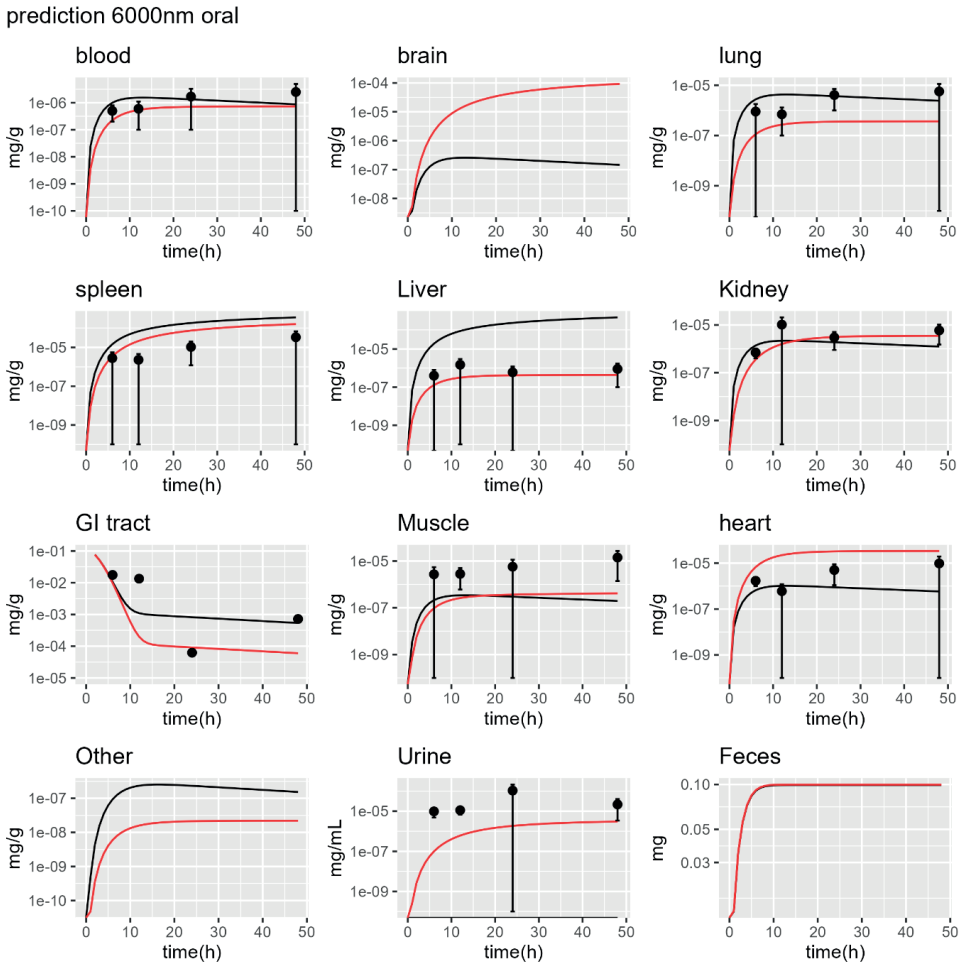

Fig 6. Prediction of organ distribution in mice upon oral exposure to 6000 nm MNPs

The Y-axis indicates the concentration of each organ in mg/g and in mg/ml for urine and mg for feces and the X-axis indicates the time. The black lines indicate mechanistic model predictions while the red lines indicate the empirical model predictions. For feces the black and red lines overlap and no urinary excretion is seen with 6000nm MNPs for the mechanistic model. The black dots and error bars indicate the observed concentrations as retrieved from the literature (144). Note that no data from the in vivo study were reported for brain, feces and other (carcass).

Table 3: Training data observations versus empirical and mechanistic oral MNP predictions (average fold changes)

	20 nm		220 nm		1000 nm		6000 nm	
	Mechanistic	Empirical	Mechanistic	Empirical	Mechanistic	Empirical	Mechanistic	Empirical
Blood	7.7	0.8	1.2	0.3	1.1	0.7	0.7	0.5
Lung	3.7	3.9	0.4	11.4	0.5	0.2	21.9	0.2
Spleen	36.9	10.8	27.4	8.0	20	8.9	9.5	5.6
Gut	4.4	0.2	1.7	0.4	0.5	0.2	3.7	0.5
Muscle	0.3	0.2	0.01	0.1	0.02	0.09	0.4	0.06
Liver	154.0	1.0	255.6	0.7	611.8	0.9	221.8	0.42
Kidney	16.6	0.1	0.2	1.8	0.2	1.0	4.9	0.6
Heart	0.6	11.3	0.08	10.8	0.09	9.7	4.9	12.7
Urine	6.2	0.08	-	0.8	-	0.02	-	0.4

The values shown in green are within a 10 fold difference with observations, the values shown in red overpredicted observed tissue concentrations more than 10-folds and the values in blue underpredicted observed tissue concentrations more than 10-folds

On average, the mechanistic model was capable of predicting the blood and gut concentrations of MNPs within a 10-fold difference of the observed value regardless of size (Table 3). The lung concentration was predicted within a 4-fold difference of the observations, but the model overpredicted the lung concentrations of 6000 nm PS particles. The concentration in the heart and muscle was adequately predicted within a 10-fold difference for both the 20 nm and 6000 nm particles, but slightly underpredicted the heart concentrations for 220 nm and 1000 nm particles and significantly underpredicted muscle accumulation of 220 nm and 1000 nm PS. Kidney concentrations were well predicted for larger particles but were overpredicted for 20 nm PS particles. Spleen concentrations were overpredicted up to 37-fold by the empirical colloid-PBK model, while concentrations predicted by the mechanistic model were within 11-fold. For the liver, concentrations of the four sizes of MNPs predicted by the empirical colloid-PBK model were within 2-fold difference regardless of size, representing a significant improvement over the mechanistic model (154-to-610-fold difference depending on the MNP size). The remaining organ concentrations were predicted with a similar accuracy by the mechanistic and empirical model (Table 3).

To assess the improvement of the empirically fitted model compared to the mechanistic model, the error in the oral prediction of the dataset of Keinanen et. Al (144). was expressed as root mean squared error (RMSE), an indication of model accuracy (Table 4). For particles of 20 nm, the empirical model showed a 2-fold reduction in total RMSE while larger particles showed a 4-fold reduction in RMSE compared to the mechanistic model, which was driven mainly by the improvement in liver and spleen prediction.

Table 4: Performance of empirical colloid-PBK model compared to mechanistic model

Organ	RMSE 20 nm		RMSE 220 nm		RMSE 1000 nm		RMSE 6000 nm	
	Mech	Emp	Mech	Emp	Mech	Emp	Mech	Emp
Blood	5.44	2.04	1.47	1.93	0.33	0.48	1.07	1.02
Lung	2.60	3.69	1.79	23.93	0.86	1.14	28.16	3.29
Spleen	110.27	60.43	185.07	69.77	161.68	81.56	122.95	70.77
Muscle	3.56	3.38	5.90	5.22	4.89	4.73	6.18	7.55
Liver	65.25	0.74	215.66	0.52	263.06	1.89	238.71	0.66
Kidney	21.19	1.74	2.03	2.11	3.01	2.38	10.12	4.53
Heart	2.58	25.26	5.07	34.41	3.29	22.84	5.05	21.28
Total	210.90	97.29	417.00	137.88	437.14	115.05	412.24	109.12

All numbers are shown in µg/kg RMSE= root mean squared error

6.5.4 Validation of mechanistic and empirical model predictions against independent datasets

Next, to assess whether the empirical and mechanistic model can predict the organ distribution of novel data, seven independent validation datasets (see Table 1) were modelled and compared. To benchmark both models, the observations were plotted against the predicted values of the mechanistic and empirical models (Figures 7 and 8) and the root mean squared error, fold change and percentage of observations predicted within a 10-fold difference and the validation data were calculated (Table 5). As the dataset of Keinanen et. al. (144) was used for training the empirical model, this dataset was not independent and was thus excluded from the validation of the empirical model.

The datasets used for validation were taken from *in vivo* studies with very different study designs, as summarized in Table 1 and Supplementary file 1. The average total bioavailability predicted vs. observed across all experiments was 0.176% (ranging between <0.001-10%) and did not show a correlation with size of the MNP (R= -0.16). The observed organ accumulation was highest in the liver (0.14 %ID/g), followed by the lung (0.05 %ID/g), kidney (0.05 %ID/g), spleen (0.04 %ID/g) and heart (0.03 %ID/g). The remaining organs showed concentrations around 0.01 %ID/g. To identify whether experimental design impacted *in vivo* bioavailability, we calculated the Pearson correlation between size and dose and observed bioavailability. No correlation between the observed bioavailability and size was observed (R=-0.17), and a weak inverse correlation between administered dose and bioavailability was observed (R= -0.48).

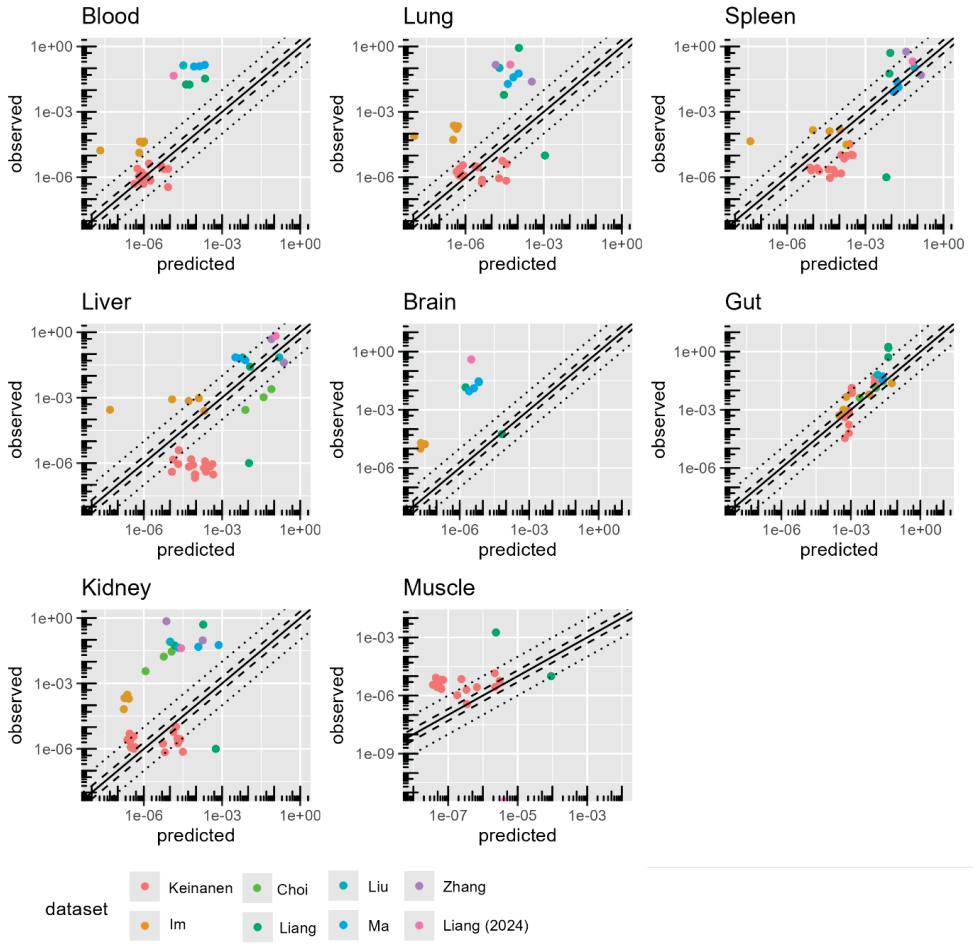

Fig. 7: Observed versus predicted organ concentrations by the mechanistic PBK model for orally ingested MNPs

The Y-axis indicates the observed concentration of each organ and the X-axis shows the predicted concentration in mg/g and mg for feces. Each dot indicates an observation-prediction pair and the colour of each dot indicates the respective dataset as shown in the legend. The black lines indicate unity between predictions and observations, the dashed black lines indicate a 2-fold and 0.5-fold difference from the observations and the dotted black line indicates a 10-fold and 0.1-fold difference from the observations. The datasets included are Keinanen (144), Im (717), Choi (718), Liang (719), Liu (720), Ma (721), Zhang (183) and Liang (2024) (722).

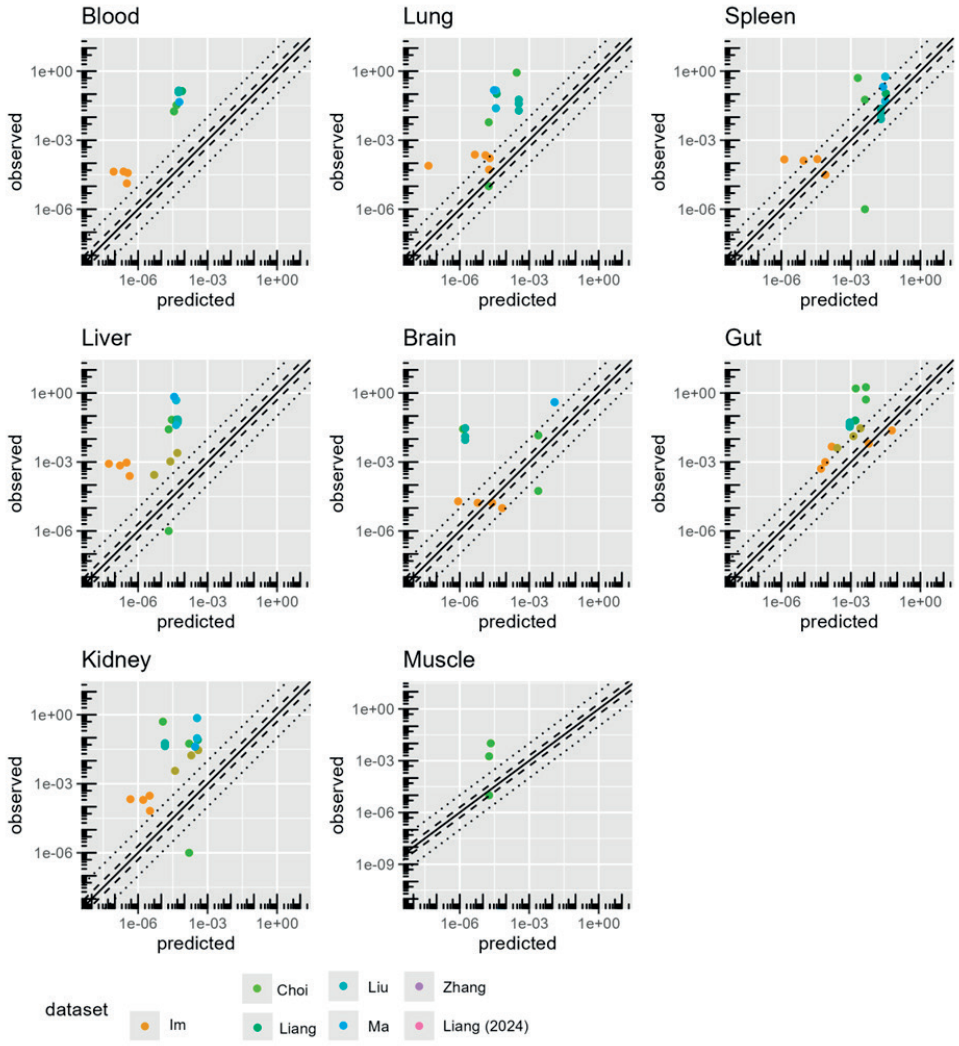

Fig. 8: Observed versus predicted organ concentrations by the empirical PBK model for orally ingested MNPs

The Y-axis indicates the observed concentration of each organ and the X-axis shows the predicted concentration in mg/g and mg for feces. Each dot indicates an observation-prediction pair and the colour of each dot indicates the respective dataset as shown in the legend. The black lines indicate unity between predictions and observations, the dashed black lines indicate a 2-fold and 0.5-fold difference from the observations and the dotted black line indicates a 10-fold and 0.1-fold difference from the observations. The datapoints from Keinanen et. al. are not included as these were not independent datapoints. The datasets included are Im (717), Choi (718), Liang (719), Liu (720), Ma (721), Zhang (183) and Liang (2024) (722).

Table 5. Performance of empirical model compared to mechanistic model for validation data

	Mechanistic model			Empirical model**			Observed
Organ	**RMSE (mg/kg)**	**Predictions <10 fold of Observation (%)**	**mean fold change**	**RMSE (mg/kg)**	**Predictions <10 fold of Observation (%)**	**mean fold change**	**mean conc. (%ID/g)***
Blood	50.0	52%	1.5	74.67	0%	0.004	0.013
Brain	110.8	7.7%	0.095	107.1	43.75%	4.2	0.014
Lung	163.8	46.7%	3.5	239.7	14.28%	0.04	0.05
Spleen	137.7	50%	13	206.0	57.14%	0.63	0.037
Gut	-	77.4%	1.6	-	16.7%	0.27	-
Muscle	3.3	36.8%	0.17	8.3	0%	0.006	0.004
Liver	129.1	30.3%	153	205.5	0%	0.00041	0.14
Kidney	155.0	36.4%	2.6	215.8	0%	0.0074	0.049
Heart	108.05	34.5%	0.78	160.2	38.5%	0.77	0.03
Total	857.6	-		1217			

* percentage of administered dose per gram of tissue. ** datapoints from Keinanen et. al. are not considered for the empirical model as these datapoints are not independent

A lower RMSE was observed for the mechanistic model compared to the empirical model for all organs except brain, indicating improved predictions of organ concentrations by the mechanistic model. The mechanistic model adequately predicted the observed concentrations in blood, lung, spleen, muscle, liver, kidney and heart in 30-50% of cases. For the GI tract 77.4% of predictions were within 10-folds of observations while for brain only 7.7% of predictions were within 10-folds of observations. The empirically fitted model did not have any datapoints within a 10-fold prediction of the blood, liver or kidney compartments, but predicted the brain and spleen concentrations better than the mechanistic model.

The average fold change (predicted vs. observed) showed that the mechanistic model overpredicted the spleen and liver concentrations, while the empirical model shows better predictions of spleen, but strongly underpredicts liver concentrations.

Overall, the mechanistic model was adequate at predicting organ concentrations of blood, lung, gut, muscle and heart concentrations after oral exposure, showed improved predictions compared to the empirical model, but showed large differences between predicted and observed liver, spleen and brain concentrations.

6.5.5 Prediction of human tissue concentrations after oral exposure

While little human data is available, we have scaled the PBK model to humans to provide an initial estimation of organ concentrations which could be expected given current estimates of human oral exposure. Only two datasets report human tissue concentrations in terms of mass per gram of organ (14, 16).

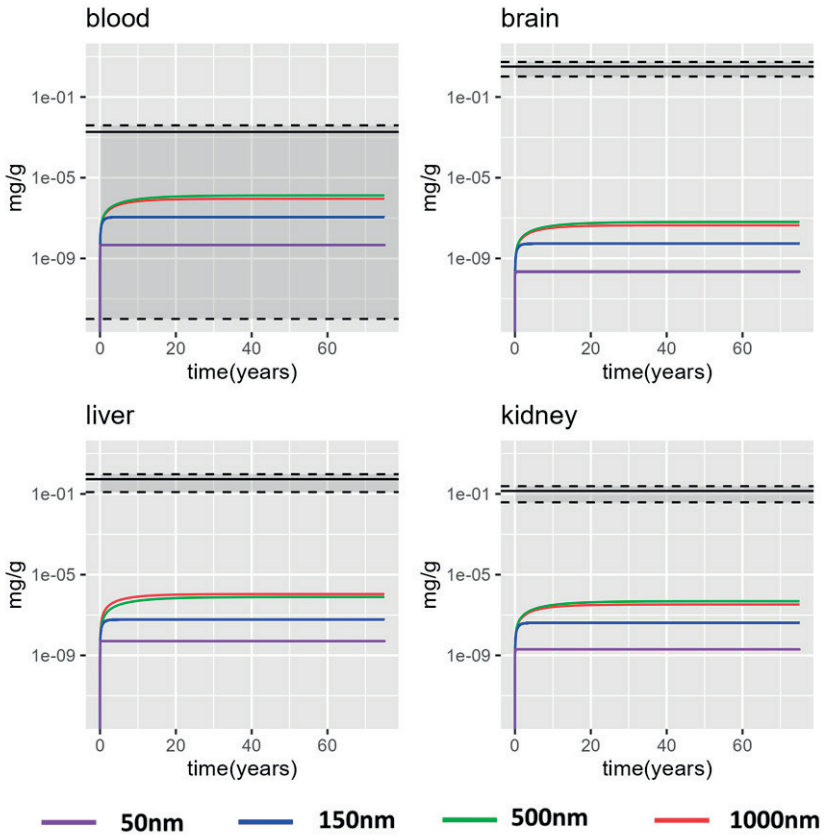

Fig. 9: Prediction of human tissue concentrations after oral MNP exposure

Predicted human tissue concentrations in blood, brain, liver and kidney after 75 years of exposure to 5 µg/week (80). The colour of the line indicates the modelled particle size with the purple line representing 50 nm particles, the blue line representing 150 nm particles, the green line representing 500 nm particles and the red line representing 1000 nm particles. The area highlighted in darker grey represents the measured mean concentration in human tissues ± the standard deviation. Values were taken from (14) and (16). The horizontal black line represents the average concentration of all individuals tested and the dashed black line represent the mean concentration ± the standard deviation. For blood, the mean-standard deviation crosses 0, but was fixed at 10-12 to allow visualization in log scale.

Depending on the MNP size, three different tissue concentration profiles were observed. Particles which were smaller than the fenestration size of the kidney (i.e. <70 nm) underwent rapid urinary excretion and quickly reached a steady state concentration without further bioaccumulation. Particles with sizes above the kidney fenestration size, but below the liver fenestration size (i.e. < 180 nm) underwent rapid biliary clearance and likewise rapidly reached a steady state. Particles above the fenestration size of the kidney showed a slow bioaccumulation over time due to the slow rate of excretion. For particles above the fenestration size of the liver, the duration before steady state occurred was dependent on the particle size and overall had a higher accumulation in all organs. The predicted tissue concentrations are shown in Table 6.

The model predictions for 50 nm, 150 nm, 500 nm and 1000 nm particles were significantly lower than the reported average blood concentration but were within the range of observed blood concentrations (please note the high standard deviation of the observed blood concentration). We predict that brain shows the lowest accumulation followed by kidney. There was a similar predicted MNP concentration in blood, liver, lung, spleen, while the highest concentration was predicted in heart. The predicted tissue concentrations ranged between 0.23 pg/g and 15 ng/g.

Table 6. Predicted tissue concentrations after lifelong exposure to MNPs

	Predicted tissue concentration (pg/g)			
Organ	**50 nm**	**150 nm**	**500 nm**	**1000 nm**
Blood	5	110	1300	9400
Brain	0.2	5.4	64	460
Heart	7.5	170	2000	15000
Kidney	2	40	490	3500
Liver	5.3	59	780	11000
Lung	5.4	120	1500	10000
Spleen	4.8	110	1400	13000

The tissue concentrations reported assume 75 years of daily exposure to 714 ng/d of MNPs with 50 nm, 150 nm, 500 nm or 1000 nm diameter.

6.6 Discussion

Here, we showed that mechanistic colloid-PBK models can be used to predict organ concentrations after oral exposure to MNPs. By using size dependent hydro- and thermodynamic functions, the resulting PBK model can be used for a broad range of MNP

sizes (here between 20-6000 nm). The mechanistic model predicted tissue concentrations within 10-fold differences of observed values in blood (94%), lung (88%), kidney (75%), heart (75%) and gut (75%) when simulating single oral administration of radiolabelled PS to mice. When the model was compared to datasets comprising both acute and sub-chronic exposure scenarios in mice, approximately 50% of tissue concentration predictions were within 10-folds of observations. Finally, we predict an initial estimate of human tissue concentrations after lifelong MNP exposure, while recognizing the uncertainty in human exposure scenarios and validation data. We predict that regardless of the tissue, MNP concentrations are below 15 ng/g, indicating low tissue burden in humans. Uncertainties in literature-reported validation data preclude conclusive determination of model accuracy, however, the model accuracy for mice is deemed acceptable for an initial generic colloid-PBK model. While there still are kinetic processes that can be improved, the flexibility of the mechanistic modelling approach is very promising for future quantitative *in vitro* to *in vivo* extrapolation of MNP risk assessment frameworks.

The mechanistic PBK model describes particle biokinetics through hydro- and thermodynamic functions capturing margination towards, and extravasation through the capillary walls followed by cellular phagocytosis in RES organs. Mathematical description of particle margination is rarely included in PBK models, but several margination models have been developed for red blood cells and injected particles (741). The capillary wall binding and release was described as a function of particle sedimentation, Brownian diffusion, shear induced diffusion and sedimentation, as published before (715). More detailed models of margination incorporate electrostatic interactions, van der Waals forces and shape effects (742, 743), which could extend the application domain of the current model to differently shaped and charged MNPs. The description of particle extravasation through pores based on hydrodynamic particle mechanics was first derived by Bean and Curry (725, 727, 744) and initially applied to mathematical models of solutes extravasation in the heart (726). More recently, it was used to describe the fate of MRI contrast agents (745-747). As the majority of colloid clearance from blood is due to interaction with macrophages (748), phagocytosis is frequently included in conventional colloid-PBK models where it is individually fitted to each particle size and organ (243, 749, 750). Instead, we modelled phagocytosis as a passive process, where a size specific energy barrier is described by the deformation energy of the phagocyte membrane required for particle internalization, which is provided by a size agnostic force applied by cytoskeletal proteins. From the obtained predictions it was shown that the mechanistic model was not able to accurately predict phagocytosis, and empirical fitting was required to accurately predict the spleen and liver concentrations. Alternative mechanistic models can be applied to more accurately describe the size-dependency of phagocytosis. Recently, a non-linear model was published that relates the fitted intestinal absorption coefficient and particle size (245), which could also be explored to predict phagocytosis coefficients.

Additionally, the phagocytosis parameters can be obtained by calibration with *in vitro* uptake data of differently sized PS and subsequently scaling the phagocytosis coefficient to the whole organ (716). The use of *in vitro* fitted phagocytosis parameters in future mechanistic PBK models is promising, as it can improve the prediction of phagocytosis when scaling to human, can capture the preferential uptake of MNPs in the low µm range and can be used to derive organ-specific phagocytosis rates.

To evaluate the model predictions, high quality biokinetic data from *in vivo* studies is needed. The *in vivo* datasets used here for model validation were obtained from studies with a great variety of study designs. The respective publications described a total oral dose range from 3 mg/kg to 1400 mg/kg, spanning both single dose acute studies and sub-chronic multiple dosing studies up to 112 days (144, 183, 717-722). The total bioavailability reported in these studies ranged from <0.001% to 2.1%. One potential confounder is that MNPs are not commonly directly detected in tissues and instead make use of covalent or non-covalent labelling to detect MNPs by proxy. It is well known that non-covalently attached labels can leach from nanoparticles, effectively causing false positives in tissue detection. While leaching of the fluorescent label is typically assumed to be negligible (~1% (719)), the tissue accumulation of MNPs reported in the validation studies are even lower, often below <0.001% of the injected dose. This gives cause for concern as it is no longer discernible if the tissue fluorescence is due to the presence of MNPs, or from detached fluorescent labels. When assessing the datasets used in this study, the bioavailability of both radiolabelled and fluorescently labelled datasets was similar (0.35% ± 0.6% and 0.27% ± 0.03% respectively), indicating that, for these studies, fluorophore leaching has little impact on bioavailability. The fluorescently labelled MNPs did show a significantly higher tissue accumulation in terms of %ID in the brain ($p=0.0007$), muscle ($p=0.046$) and liver ($p=0.0036$), but not in the remaining organs, indicating a plausible organ-specific fluorophore leaching. To compensate for potential fluorescent leakage, a sub-model for leached fluorophores could be added to the mechanistic generic PBK model, as has previously been demonstrated for hydrophobic organic chemicals leaching from plastics (80), which could improve overall specific MNP predictions.

The original mechanistic model was developed for the prediction of intravenous mesoporous silica particles (<160 nm) in tumour bearing rats (751). We extrapolated the model to mice and therefore we first assessed if the interspecies extrapolation affected model accuracy. To this end, the mechanistic model was used to predict tissue concentrations after i.v. injection of 20 or 1000 nm PS beads in mice, and predictions were compared to literature results (145). The model showed a good prediction of organ concentrations of 20 nm particles, however the concentrations of larger particles were underpredicted. In the original publication, 20 nm to 160 nm MNPs showed comparable predictive accuracy

as reported here (751). Therefore, the impact of interspecies extrapolation on model accuracy was deemed minimal.

As the majority of human exposure to MNPs occurs through our diet (168), the mechanistic model was extended to predict oral absorption in mice. First, the most extensively characterized dataset (144) was used to train an empirical model for comparison of the model performance with that of the data-independent mechanistic model. Both the mechanistic and empirical models showed predictions within a 10-fold difference form the observed value in 93.75% of blood plasma concentrations and 68.5-87.5% of lung, gut, muscle and heart concentrations. Overall, the concentrations predicted in organs downstream of intestinal absorption showed concentrations below 0.1% of the administered dose, being approximately 100 ng/g when5 mg/kg was administered to mice. Unlike the predictions of the intravenous model, no clear reduction in organ concentrations were observed upon oral exposure with increasing time.

Because of the lack of mathematical theory to predict the size dependence of intestinal absorption, the oral absorption in mice was modelled using a single size-independent absorption coefficient (set at 0.5%, based on *in vivo* studies (13)). Even though the total bioavailability in the tested datasets ranged from 0.001% to 2.1%, the assumption of one common oral bioavailability predicted 77.4% of all gut concentrations within a 10-fold error and performed better than the empirical model, which had a size specific parameter for intestinal absorption. In the mechanistic model, particle transport is assumed to mostly take place through passive processes, which interestingly yielded remarkably accurate tissue accumulation for the liver and spleen after intravenous injection, whereas the model overpredicted liver and spleen concentrations upon oral exposure to MNPs. A potential explanation for these differences might be the formation of a protein corona on the surface of MNPs as digestive proteins can strongly increase particle uptake by phagocytotic cells, as shown by *in vitro* studies (596). Despite the well-established role of the protein corona on *in vivo* biodistribution (752), no PBK models to date have managed to capture protein corona effects due to lack of *in silico* models for protein corona formation.

The oral predictions show that the mechanistic model can be used to predict oral bioavailability and tissue distribution of polystyrene MNPs up to 6000 nm. The good prediction of the tissue concentration of particles up to 6000 nm in organs with pores smaller than the particle diameter (muscle, kidney and heart) was surprising. While our model predicts accumulation in the capillary compartments of these organs, no actual internalization into the cellular compartment is predicted (Supplementary Figure 3 and 4). This raises the question whether the measured organ concentrations *in vivo* are a result of actual tissue accumulation or merely due to the presence of MNPs in the tissue capillaries. It is possible to alter *in vivo* studies to distinguish both effects by flushing the organs with

saline solution prior to organ measurement, however this is infrequently performed and, to the best of our knowledge, comparison of flushed and unflushed tissue concentrations have never been assessed for MNPs. The datasets used for validation were comprised of both studies which have flushed organs prior to MNP measurements (183, 719, 722) and studies which measured MNPs in organs with capillary blood (717, 718, 720, 721, 753). There was an observed (but insignificant) difference between the average bioavailability of studies which have perfused the animals with saline prior to measurement (0.04% ± 0.02%) compared to the studies without (0.29% ± 0.54%), indicating that blood-borne MNPs can contribute to total tissue MNP concentrations.

As a demonstration of the potential of mechanistic PBK models, we simulated human tissue concentrations after lifelong exposure to a realistic estimate of human MNP intake (80). MNPs below the fenestration size of the liver (<180 nm) show low tissue accumulation due to rapid urinary and biliary excretion, while MNPs >180 nm show a size dependent tissue accumulation. Rapid blood clearance of nanoparticles is typically only seen with nanoparticles between 6 nm and 8 nm (146), however polymeric nanoparticles up to 133 nm may also exhibit rapid renal clearance when presenting viral glycans on their surface (754). It is known that viral particles can be excreted even when they are much larger than glomerular pores (755, 756). As MNPs rapidly bind to biological components like saccharides and proteins, the presentation of viral corona components is a likely mechanism for urinary excretion of MNPs. Here, the biliary excretion was assumed to be passive with the main barrier being passage through the canaliculi. Likely, the cells lining the liver canaliculi will present an additional barrier, however it is also possible that MNPs get actively transported into the canaliculi, as bile salts can bind to the nanoparticle corona and stimulate active transport into bile as observed with chylomicron microparticles (729, 757, 758). As such, the actual biliary transport could either be higher or lower than what we predict here. Regardless of exposure scenario and particle size, we show similar concentrations in blood, heart, lung, spleen and liver, and lower concentrations in brain and kidney. If this observation is true, it would be possible to use blood MNP concentrations as a biomarker for tissue concentrations of MNPs, however due to the lack of *in vivo* data, this finding cannot be validated at this time.

We predicted tissue accumulation ranging from 0.23 pg/g in brain to 15 ng/g in heart, depending on the particle size. The predicted tissue concentrations are much lower than reported by human *in vivo* observations. However, it is unclear whether this is due to model inaccuracy or inaccuracies in reported tissue concentrations. One study reporting MNP concentration in blood indicated an average concentration of 1.6 µg/g with a standard deviation of 2.1 µg/g and most of the tested individuals had average blood concentrations below the LOQ (0.4 - 2.3 µg/ml, depending on the polymer tested) (14). Currently, it is therefore not possible to accurately derive the actual concentration of

MNPs in blood. Based on our model estimates, the LOQ of the analytical methods need to be lowered dramatically. The other human study reports tissue accumulation of 3.2 ± 2.2 mg/g in brain, 536 ± 412 µg/g in liver and 140±102 µg/g in kidney, but the authors did not specify the LOQ of the analytical workflow used (16). This study used historical samples which were never intended for MNP analysis and the use of polyethylene cutting boards, plastic buckets and plastic gloves represent realistic sources of contamination. Previous studies have shown that plastic cutting boards may release up to 4.73 mg of MNPs during regular use (759) while lab gloves release up to 0.32 mg (760) during contact with liquids. As the concentrations measured in brain, liver and kidney samples were approximately 3 mg/g, 500 µg/g and 150 µg/g in a total sample weight of 3 - 5 g, it is plausible that plastic contamination causes much of the measured tissue concentration. Additionally, measurement of polyethylene in fatty-matrices using pyrolysis GC-MS-MS can leads to errors in the measured concentration and can artificially increase the detected amount of polyethylene (761). Unfortunately, no blank samples were included to assess the magnitude of background plastic contamination and as such, the reported values may be subject to significant measurement error.

6.7 Conclusion

We have shown that the generic mechanistic colloid-PBK model for oral absorption of MNPs performs better at predicting organ concentrations than empirically fitted models. The model adequately predicts blood, lung, gut, muscle, heart concentrations, but to a lesser extent liver, spleen and brain concentrations. The model outcomes consistently show tissue accumulations less than 0.1% of the administered dose, raising questions on the relevance of the toxicity found *in vitro* at high doses of MNPs. Simulation of human MNP exposure indicates that MNP tissue concentrations likely are lower than previously reported and that the blood concentration may serve as a biomarker for tissue concentrations of MNPs. While the model did not yet perform to the same level of generic PBK models for small molecules, it represents a first step in the application of PBK modelling for read across between MNPs.

6.8 Acknowledgement and project funding.

This project has received funding from the European Union's Horizon 2020 research and innovation program under grant agreement No. 965196 [H.Br], the Horizon Europe project "European Partnership for the Assessment of Risk from Chemicals (PARC)" under grant agreement No. 101057014 [M.B, N.K, H.Bo] and Wageningen University [H.Br]. We acknowledge Ivonne Rietjens for her discussions on the model design.

6.9 Supplementary information

Supplementary Table 1. Physiological parameters for mouse

*Parameter***	*G**	*B**	*Br**	*GI**	*H**	*S**	*Lu**	*Li**	*L**	*K**	*M**
BW	*20 g*										
PlD	*1e-1 g/ cm^3*										
RBC	*2.9µm*										
HMT	*0.45*										
CF	*0.55*										
B	*0.0833 ml/h*										
U	*0.0416 ml/h*										
Kpf	*1e-17 W*										
gamma	*6e-5 N/m*										
Mf	*-*					*0.1*		*0.5*			
vl	*1 mm*										
vr	*5 µm*										
Wf		*0.049*	*0.017*	*0.042*	*0.005*	*0.004*	*0.007*	*0.055*	*0.02*	*0.017*	*0.38*
Vfc		*-*	*0.03*	*0.03*	*0.12*	*0.17*	*0.5*	*0.31*	*-*	*0.24*	*0.04*
Qf		*-*	*0.033*	*0.141*	*0.066*	*0.011*	*1*	*0.161*	*-*	*0.091*	*0.159*
Lf		*-*	*1/500*	*1/500*	*1/500*	*1/500*	*1/500*	*1/500*	*-*	*1/500*	*1/500*
r		*-*	*0.5 nm*	*6nm*	*2.5nm*	*2.5µm*	*2.5nm*	*140nm*	*-*	*35nm*	*2.5nm*
GFR	*0.28 ml/h*										

*G=generic, B=blood, Br=brain, GI=gastrointestinal tract, H=heart, S=spleen, Lu=lung, Li=liver, L=lymph, K=kidney, M=muscle ** BW=body weight, PlD=plasma density, RBC is red blood cell radius, HMT=hematocrit fraction, CF=capillary fraction used to derived capillary speed, B=bile flow rate, U=urinary flow rate, Kpf=protein force for phagocytosis, gamma=phagocyte membrane rigidity, Mf=macrophage fraction, vl=typical length of capillary, vr=typical radius of capillary, Wf=weight fraction, vfc=volume fraction of blood, Qf=fraction of blood flow, Lf= ratio lymph flow to blood flow, r=capillary pore radius, GFR=glomerular filtration rate.

Supplementary Table 2. Physiological parameters for human

*Parameter***	*G*	*B**	*Br**	*GI**	*H**	*S**	*Lu**	*Li**	*L**	*K**	*M**
BW	*70 kg*										
PlD	*1e-1 g/ cm^3*										
RBC	*3.6µm*										
HMT	*0.45*										
CF	*0.55*										
B	*29.16 ml/h*										
U	*66.6 ml/h*										
Kpf	*1e-17 W*										
gamma	*6e-5 N/m*										
Mf	*-*					*0.1*		*0.5*			
vl	*1 mm*										
vr	*7.5 µm*										
Wf		*0.080*	*0.02*	*0.017*	*0.005*	*0.003*	*0.008*	*0.026*	*0.02*	*0.004*	*0.4*
Vfc		*-*	*0.012*	*0.07*	*0.09*	*0.14*	*0.105*	*0.1*	*-*	*0.02*	
Qf		*-*	*0.12*	*0.15*	*0.04*	*0.03*	*1*	*0.255*	*-*	*0.19*	*0.17*
Lf		*-*	*1/500*	*1/500*	*1/500*	*1/500*	*1/500*	*1/500*	*-*	*1/500*	*1/500*
r		*-*	*0.5 nm*	*2.5nm*	*2.5nm*	*5µm*	*2.5nm*	*90 nm*	*-*	*35nm*	*2.5nm*
GFR	*60 ml/h*										

*G=generic, B=blood, Br=brain, GI=gastrointestinal tract, H=heart, S=spleen, Lu=lung, Li=liver, L=lymph, K=kidney, M=muscle ** BW= body weight, PlD=plasma density, RBC is red blood cell radius, HMT=hematocrit fraction, CF=capillary fraction used to derived capillary speed, B=bile flow rate, U=urinary flow rate, Kpf=protein force for phagocytosis, gamma=phagocyte membrane rigidity, Mf=macrophage fraction, vl=typical length of capillary, vr=typical radius of capillary, Wf=weight fraction, vfc=volume fraction of blood, Qf= fraction of blood flow, Lf=ratio lymph flow to blood flow, r=capillary pore size, GFR=glomerular filtration rate.

Calibration of empirical model to datasets

An empirical model was generated to predict the oral bioavailability and organ distribution of 20nm, 220nm, 1000nm and 6000nm PS particles. Initial parameters and the four optimized parameter for 20nm, 220nm, 1000nm and 6000nm PS are shown in supplementary Table 3, below. Additionally, to identify whether there were size-related patterns in the parameter values, the Spearmen correlation between particle sizes and each fitted parameter was computed.

Supplementary Table 3. Calibrated parameters of empirical model

Parameter	Initial value (20nm)	20nm	220nm	1000nm	6000nm
Intestinal absorption	0.005	0.00041	0.0016	0.001	0.002
σBrain	1	1	0.01	1.00e-05	0.19
σLung	1	1	1	1	0.26
σHeart	1	1	1	0.56	0.10
σSpleen	0.0001023	1	0.0001	1.00e-05	1
σLiver	0.0289	1	0.059	1	1
σGit	1	1	1	1	0.59
σKidney	0.6477	1	0.19	1.00e-05	1.02e-05
σMuscle	1	0.00030	1.00e-05	8.19e-05	0.17
σBile	0.000633	0.0025	1	1	0.008
K_{on} Brain	7.29	158.85	5.00e+06	4934674.93	3365.65
K_{on} Lung	6.94	171044.72	1107.20	0.09	0.14
K_{on} Heart	7.11	4624256.41	7374.85	268393.80	3720595.78
K_{on} Spleen	8.4	39.74	5000000	5000000	46507.29
K_{on} Liver	10.04	0.01	0.01	0.23	0.01
K_{on} Git	7.10	0.01	0.10	5.34	5.00e+06
K_{on} Kidney	8.17	1.33	199.18	0.01	0.01
K_{on} Muscle	9.76	154742.22	401.02	7886.75	159574.96
K_{off}	2042594	14859.17	10.06	706.13	15365.38
M_f Liver	0.5	0.20	0.20	0.32	0.30
M_f Spleen	0.1	0.07	0.80	0.02	0.02
Phagocytic uptake	477464	32102.59	0.14	2.54	193.54
Phagocytic release	4.7764	0.00014	0.37	19.15	50
Biliary excretion	0.0833	0.09	0.08	0.08	0.07
Urinary excretion	0.041667	0.044	0.04	0.05	0.04

The symbols for each parameters are as described in the materials and methods, briefly σ are reflection coefficients, Kon are capillary association constants, Koff is the capillary dissociation constant and Mf is the macrophage fraction

The fitted fraction absorbed was between 0.05% and 0.2% indicating a low overall oral bioavailability of materials. In contrast to the mechanistic model, the fitted reflection coefficients were the highest for 20nm particles and decreased as particles grow bigger, with except for muscle and bile. Both the macrophage fractions and phagocytic uptake rates were lower in the fitted model than the initial parameters used. The fitted K_{on} for brain, heart were consistently higher than the initial parameters, while liver was consistently lower. To identify factors influencing the model parameters which show a size

dependence we determined the Spearman correlation coefficients. Spearman correlation revealed inverse correlation between the ranks of size and σHeart(-0.95), σKidney(-0.8), K_{on} Lung(-0.8), mfS(-0.8) and Biliary excretion(-0.8) and positive correlations between fabs(0.8), K_{on}Git(1), and phagocytic release(1).

Supplementary Table 3. Upper and lower bounds for empirical fitting

Parameter	Upper bound	Lower bound
Fabs	0.2	1e-5
CF	0.6	0.4
B	0.09	0.07
U	0.05	0.04
σBr	1	1e-5
σGI	1	1e-5
σH	1	1e-5
σS	1	1e-5
σLu	1	1e-5
σLi	1	1e-5
σK	1	1e-5
σM	1	1e-5
σBile	1	1e-5
GFR	0.3	0.2
Kp	5e5	1e-1
Kpo	50	1e-5
K_{on}Br	5e6	1e-2
K_{on}GI	5e6	1e-2
K_{on}H	5e6	1e-2
K_{on}S	5e6	1e-2
K_{on}Lu	5e6	1e-2
K_{on}Li	5e6	1e-2
K_{on}K	5e6	1e-2
K_{on}M	5e6	1e-2
K_{off}	5e6	1e-2
MfLi	0.8	0.2
MfS	0.8	0.01

*fabs=oral absorption, CF= capillary fraction, B=biliary formation rate, U=urinary formation rate, σi=reflection coefficient of organ i, GFR= glomerular filtration rate, kP= phagocytic uptake coefficient, KpO = phagocytic excretion coefficient, K_{on}i= capillary binding coefficient of organ I, Koff= capillary release coefficient, Mfi = macrophage fraction of organ i.

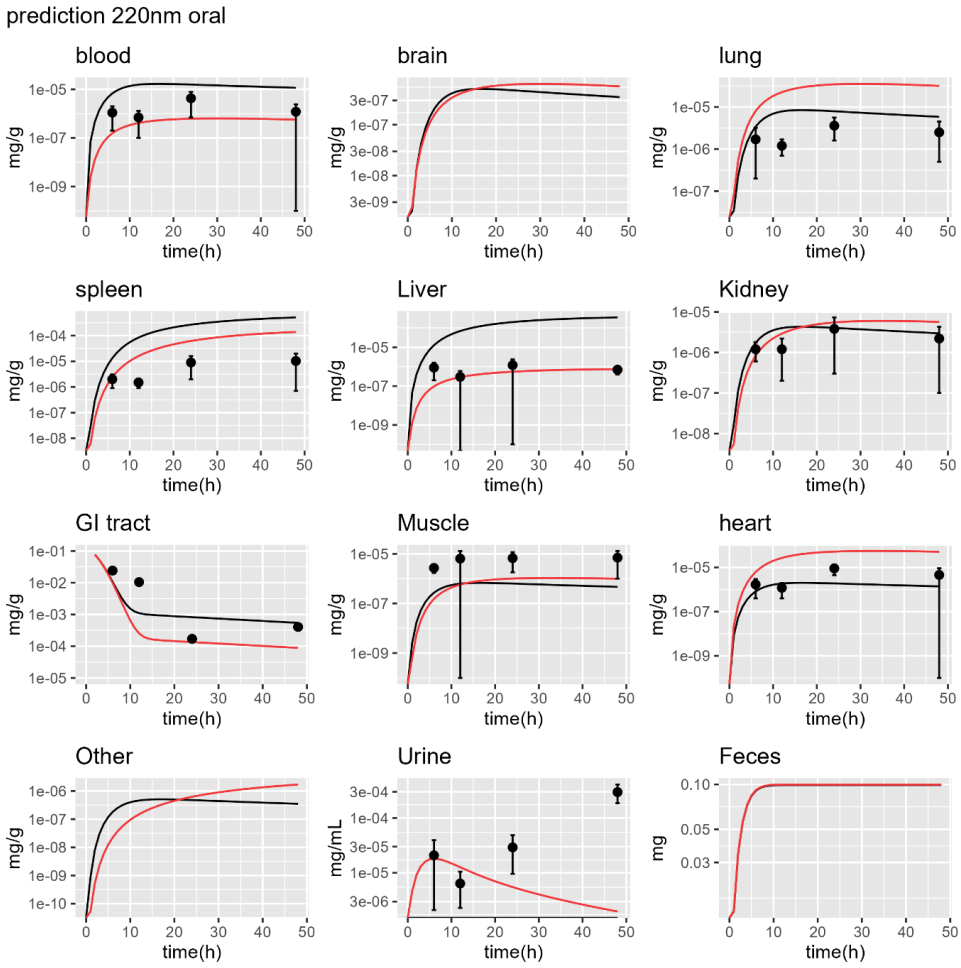

Supplementary Fig. 1. PBK predictions of organ concentration of oral exposure of 220nm nanoplastics

The Y-axis indicates the concentration of each organ in mg/g and in mg/ml for urine and mg for Feces and the X-axis indicates the time. The black lines indicate mechanistic model predictions while the red lines indicate the empirical model predictions. The black dots indicate the observed concentrations as retrieved from Keinanen et. al.(144) The error bars indicate the standard deviations of each dataset as retrieved from the supplementary information by Keinanen et. al.

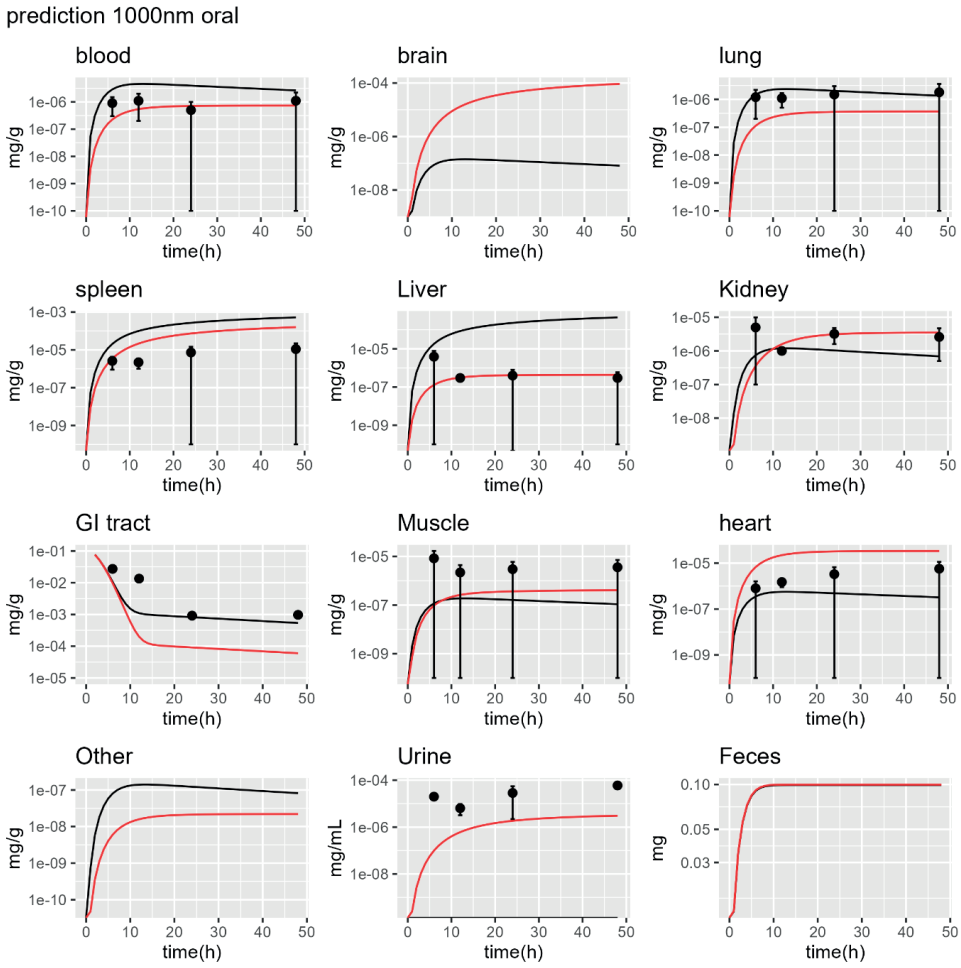

Supplementary Fig. 2. PBK predictions of organ concentration of oral exposure of 1000nm nanoplastics

The Y-axis indicates the concentration of each organ in mg/g and in mg/ml for urine and mg for feces and the X-axis indicates the time. The black lines indicate mechanistic model predictions while the red lines indicate the empirical model predictions. The black dots and error bars indicate the observed concentrations as retrieved from the literature (144) Note that no data from the in vivo study were reported in brain, feces and other (carcass).

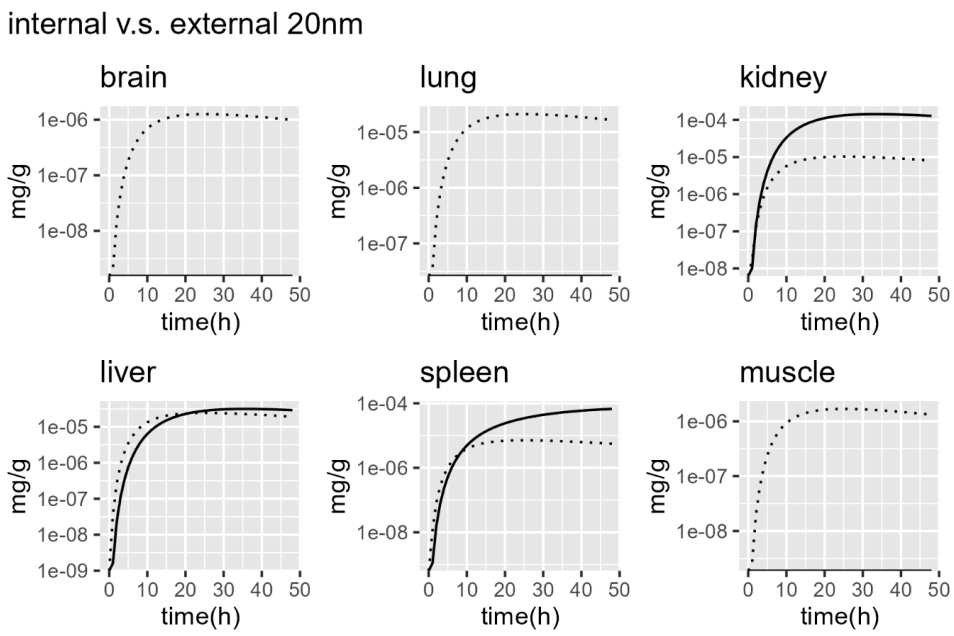

Supplementary Fig. 3. Internal versus external localization of 20nm MNPs

The Y-axis indicates the concentration of each organ in mg/g and in mg/ml for urine and mg for feces and the X-axis indicates the time. The solid black lines indicate mechanistic model predictions within the interior tissue compartment (including macrophages) while the dotted lines indicates the concentration in the external capillary compartment lines. Note that heart, blood and lymph are not included as these have no clear separation between tissue interior and exterior.

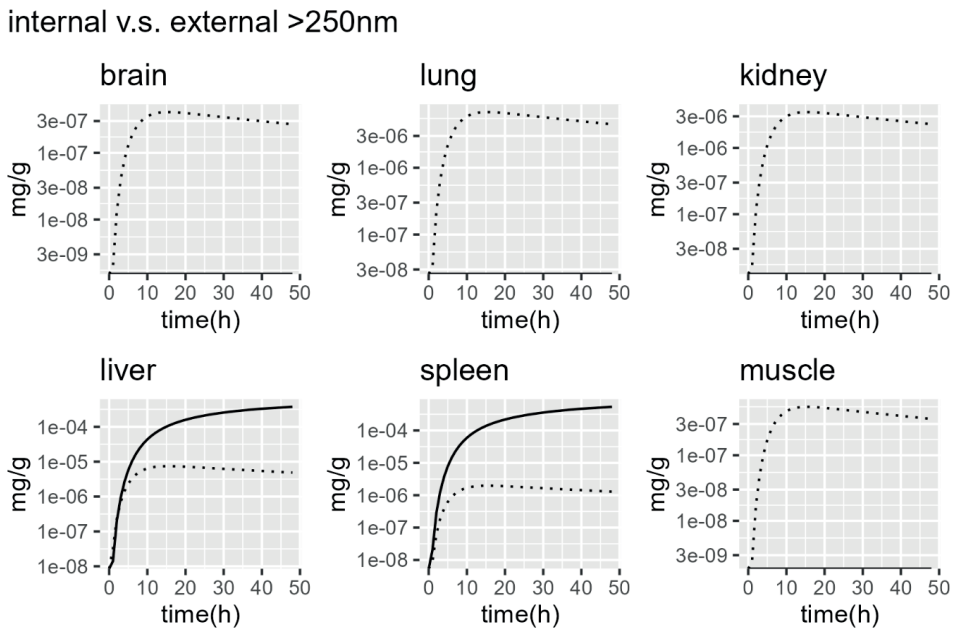

Supplementary Fig. 4. Internal versus external localization of 250nm MNPs

The Y-axis indicates the concentration of each organ in mg/g and in mg/ml for urine and mg for feces and the X-axis indicates the time. The solid black lines indicate mechanistic model predictions within the interior tissue compartment (including macrophages) while the dotted lines indicates the concentration in the external capillary compartment lines. Note that heart, blood and lymph are not included as these have no clear separation between tissue interior and exterior.

Model equations:

Blood:

$$V_B * \frac{dC_b}{dt} = -C_b * (Q_{Br} + Q_{Lu} + Q_H + Q_{Li} + Q_S + Q_G + Q_K + Q_M + Q_O) + \sum_{x \in H} C_x^{vf} * (Q_x - L_x) + \sum_{x \in H} C_L * L_x$$

Lymph:

$$V_L * \frac{dC_L}{dt} = \sum_{x \in H} C_x^{ev} * L_x - \sum_{x \in H} C_L * L_x$$

Equations for RES organs:

Spleen

vascular free

$$V_S^V * \frac{dC_S^{vf}}{dt} = C_b * Q_S - \left(C_S^{vf} * L_S * (1 - \sigma_S)\right) - (C_S^{vf} * \left(Q_S - L_S\right)) - \left(C_S^{vf} * V_S^V * K_{on,S}\right) + \left(C_S^{vb} * V_S^V * K_{off}\right)$$

vascular bound

$$V_S^V * \frac{dC_S^{vb}}{dt} = \left(C_S^{vf} * V_S^V * K_{on,S}\right) - \left(C_S^{vb} * V_S^V * K_{off}\right) - kp * Mf_S * C_S^{vb}$$

extravascular

$$V_S^E * \frac{dC_S^{ev}}{dt} = \left(C_S^{vf} * L_S * (1 - \sigma_S)\right) - C_S^{ev} * L_{Li} + kpo * Mf_S * A_S^P$$

Phagocytes

$$\frac{dA_S^P}{dt} = kp * Mf_S * C_S^{vb} - kpo * Mf_S * A_S^P$$

Liver

vascular free

$$V_{Li}^V * \frac{dC_{Li}^{vf}}{dt} = C_b * Q_{Li} - \left(C_{Li}^{vf} * L_{Li} * (1 - \sigma_{Li})\right) - (C_{Li}^{vf} * \left(Q_{Li} - L_{Li}\right)) - \left(C_{Li}^{vf} * V_{Li}^V * K_{on,Li}\right) + \left(C_{Li}^{vb} * V_{Li}^V * K_{off}\right)$$

vascular bound

$$V_{Li}^V * \frac{dC_{Li}^{vb}}{dt} = \left(C_{Li}^{vf} * V_{Li}^V * K_{on,Li}\right) - \left(C_{Li}^{vb} * V_{Li}^V * K_{off}\right) - kp * Mf_{Li} * C_{Li}^{vb}$$

extravascular

$$V_{Li}^{E} * \frac{dC_{Li}^{ev}}{dt} = \left(C_{Li}^{vf} * L_{Li} * (1 - \sigma_{Li})\right) - C_{Li}^{ev} * L_{Li} + kpo * Mf_{Li} * A_{Li}^{P} - C_{Li}^{ev} * B * \left(1 - \sigma_{bile}\right)$$

Phagocytes

$$\frac{dA_{Li}^{P}}{dt} = kp * Mf_{Li} * C_{Li}^{vb} - kpo * Mf_{Li} * A_{Li}^{P}$$

Equations for kidney

vascular free

$$V_{K}^{V} * \frac{dC_{K}^{vf}}{dt} = C_{b} * Q_{K} - \left(C_{K}^{vf} * GFR * (1 - \sigma_{K})\right) - (C_{K}^{vf} * \left(Q_{K} - GFR\right)) - \left(C_{K}^{vf} * V_{K}^{V} * K_{on,K}\right) + \left(C_{K}^{vb} * V_{K}^{V} * K_{off}\right)$$

vascular bound

$$V_{K}^{V} * \frac{dC_{K}^{vb}}{dt} = \left(C_{K}^{vf} * V_{K}^{V} * K_{on,K}\right) - \left(C_{K}^{vb} * V_{K}^{V} * K_{off}\right)$$

extravascular

$$V_{K}^{E} * \frac{dC_{K}^{ev}}{dt} = \left(C_{K}^{vf} * GFR * (1 - \sigma_{K})\right) - C_{K}^{ev} * L_{K} - C_{K}^{ev} * U$$

Equations for gut:

Lumen

$$\frac{dA_{G}^{lum}}{dt} = C_{Li}^{ev} * B * (1 - \sigma_{bile}) - \left(A_{G}^{lum} * \left(1 - \left(e^{-\frac{t}{\tau}}\right)\right)\right)$$

$$\left(1 - \left(e^{-\frac{t}{\tau}}\right)\right) = exponential\ decay\ function\ based\ on\ gastrointestinal\ transit\ time:\ \tau\ and\ time\ after\ dose:\ t$$

vascular free

$$V_{G}^{V} * \frac{dC_{G}^{vf}}{dt} = C_{B} * Q_{G} - \left(C_{G}^{vf} * L_{G} * (1 - \sigma_{K})\right) - (C_{G}^{vf} * \left(Q_{G} - L_{G}\right)) - \left(C_{G}^{vf} * V_{G}^{V} * K_{on,G}\right) + \left(C_{G}^{vb} * V_{G}^{V} * K_{off}\right)$$

vascular bound

$$V_{G}^{V} * \frac{dC_{G}^{vb}}{dt} = \left(C_{G}^{vf} * V_{G}^{V} * K_{on,G}\right) - \left(C_{G}^{vb} * V_{G}^{V} * K_{off}\right)$$

extravascular

$$V_G^E * \frac{dC_G^{ev}}{dt} = \left(C_G^{vf} * L_G * (1 - \sigma_G)\right) + f_{abs} * \left(A_G^{lum} * \left(1 - \left(e^{-\frac{t}{\tau}}\right)\right)\right)$$

Equations for remaining organs (placeholder x used to indicate organ)

vascular free

$$V_x^V * \frac{dC_x^{vf}}{dt} = C_B * Q_x - \left(C_x^{vf} * L_x * (1 - \sigma_x)\right) - (C_x^{vf} * \left(Q_x - L_x\right)) - \left(C_x^{vf} * V_x^V * K_{on,x}\right) + \left(dC_x^{vb} * V_x^V * K_{off}\right)$$

vascular bound

$$V_x^V * \frac{dC_x^{vb}}{dt} = \left(C_x^{vf} * V_x^V * K_{on,x}\right) - \left(C_x^{vb} * V_x^V * K_{off}\right)$$

extravascular

$$V_x^E * \frac{dC_x^{ev}}{dt} = \left(C_x^{vf} * L_x * (1 - \sigma_x)\right) - C_x^{ev} * L_x$$

$$\left(A_G^{lum} * \left(1 - \left(e^{-\frac{t}{\tau}}\right)\right)\right)$$

H= the set of organ tissues i.e. Brain, Lung, Heart, Liver, Spleen, Gut, Kidney, Muscle and Other
x= indicator of organ, refers to all organs that are part of H.
V_B*= volume of blood*
V_L*=volume of lymph*
V_x^V*=the vascular volume of organ x*
V_x^E*= the extravascular volume of organ x*
A_x^P*= amount captured by phagocytic cells in organ x*
A_G^{lum}*= the amount in the gut lumen*
C_B*= concentration in blood*
C_L*=concentration in lymph*
C_x^{vf}*=concentration in the free vascular compartment of organ x*
C_x^{vb}*=concentration in the bound vascular compartment of organ x*
C_x^{ev}*= concentration in the extravascular compartment of organ x*
σ_x*= capillary reflection coefficient of organ x*
σ_{bile}*= reflection coefficient for biliary excretion*
$K_{on,x}$*= the* K_{on} *coefficient of blood vessel binding for organ x*
K_{off}*= the organ independent* K_{off} *coefficient for blood vessel release*
kp*= organ independent phagocytic capture coefficient*
kpo*= organ independent phagocytic release coefficient*
Mf_S*= macrophage fraction of spleen*

Mf_{Li}= *macrophage fraction of liver*
B=*bile flow rate*
$\sum_{x \in H} y_x =$ *The sum of organ dependent values y for all organs x within H*
t=*time in hours*
Q_x= *blood flow to organ x*
L_x= *lymph flow from organ x*
GFR=*glomerular filtration rate*
e=*euler's number*
t=*time after last dose*
τ= *gastrointestinal transit time*
Specific organs are indicated with a subscript B for blood, L for lymph, S for spleen, Li for liver, K for kidney and G for gastrointestinal tract.

Model code

The model code was too voluminous to be included in the thesis, but will be made available on reasonable request.

CHAPTER 7

7

General discussion

Hugo Brouwer

7.1 Summary of main findings

Plastic products in the form of furniture, clothing, containers and tools have become an integral part of our lifestyle. However, environmental degradation of these plastic products has led to widespread micro- and nanoplastic (MNP) contamination. The small size of MNPs enables their ingestion and recent detection of MNPs in human tissues (14-16) has raised concerns with regulators, the general population and experts alike. It is now certain that we are exposed to MNPs and will be for the foreseeable future, yet the effects of MNPs on human health remain poorly understood. As a barrier organ, the intestine is exposed to some of the highest MNP concentrations of all human tissues. This makes the intestine a likely target organ for MNP toxicity.

The toxicity of nanomaterials is largely determined by their physicochemical properties and the same holds true for MNPs. MNPs of different sizes, shapes and polymer compositions will therefore likely elicit different toxicity within the intestine. There is a near limitless combination of possible MNP properties, all of which have to be assessed for human safety. It is impossible to exhaustively test this multitude of MNPs using conventional animal experiments and instead, cheap and high throughput methods need to be utilized.

In vitro and *in silico* methods are collectively referred to as New Approach Methodologies (NAMs) and have a lower associated cost and duration than animal experiments. NAMs are therefore well positioned to tackle safety testing of the great diversity of possible MNPs. The study of MNPs is relatively new and research thus far has prioritized methodological simplicity. As such, the vast majority of existing MNP literature assessed toxicity using primary MNPs and simple cell lines. Primary MNPs lack the complexity of secondary MNPs to which humans are exposed and conventional intestinal cell lines lack cellular pathways which may be relevant to MNP toxicity. This creates a dichotomy between the toxicity measured in laboratory settings and the actual toxicity of MNPs to humans. Furthermore, the protein corona is known to be one of the main determinants of nanomaterial toxicity (151, 154), yet its composition on MNPs and its role in the intestine is poorly understood. Together, these factors resulted in a noticeable scarcity of data on the toxicity of secondary MNPs, the impact of the biological matrix on MNP toxicity and the suitability of NAMs for MNP toxicity testing. As the field of MNP toxicology matures, it is becoming clearer that these data-gaps necessitate the embrace of increased complexity of NAMs and testing materials.

To address these issues, The aim of this thesis was to improve in vitro and in silico NAMs for MNP toxicity assessment and to improve understanding of the formation and effects of the protein corona on MNPs. To accomplish this, the studies presented here were designed to answer four research questions.

1. To assess the suitability of iPSC-derived intestinal models for *in vitro* MNP toxicity testing.
2. To delineate the role of the protein corona on MNPs to their cellular interaction.
3. To determine whether primary MNPs are representative of MNP toxicity as a whole.
4. To develop a mechanistic PBK model for predicting bioaccumulation after oral MNP exposure.

Societal pressure to warrant animal welfare and high costs associated with animal experiments, stimulates scientific and regulatory interest in the use of *in vitro* models for toxicity testing. In general, *in vitro* models need to be complex enough to capture key biological processes underlying toxicity, yet simple enough to allow large scale implementation. **Chapter 2** presents a review of the current use of *in vitro* NAMs for intestinal MNP toxicity testing and the potential upsides and downsides of stem cell-derived intestinal models. At present, immortalized Caco-2 enterocyte cell lines remain the most utilized intestinal model for MNP toxicity research, due to their robustness and ease of use. Additional physiological functionality is often included by co-culturing Caco-2 with HT29-MTX goblet cells to include a mucous layer, THP-1 derived macrophages to emulate inflamed intestinal models or Raji-B B lymphocytes to stimulate differentiation to M-cells. Despite their widespread use, the cancer-like origin of these cell lines is associated with genetic aberrations that impacts biological processes like cytokine secretion, DNA repair, proliferation and oxidative damage (227-232). Recently, stem cell-derived models have garnered scientific interest due to improved physiological relevance over cancer-derived cell lines and improved availability over primary tissue. In **Chapter 2**, it is described that stem cell-derived intestinal models show improvements in terms of the variety of cell-types present in the model, physiological relevance and sensitivity at the cost of a higher variability in results (762). Overall, the chapter concludes that induced pluripotent stem cell (iPSC)-derived intestinal models show promise for the study of MNP toxicity.

As highlighted by **chapter 2**, iPSC-derived intestinal models have potential for assessment of MNPs, however there is a lack of two-dimensional models (371, 763) which allow apical MNP dosing with predictable dosimetry. Therefore, **chapter 3** implements a two-dimensional iPSC-derived intestinal epithelial model and benchmarked this model against a Caco-2-derived enterocyte model. First, the physiological and morphological properties of the iPSC-derived intestinal epithelia were determined. Using gene expression and immunofluorescence it was demonstrated that the iPSC derived epithelia consisted in majority of enterocytes with minor amounts of goblet cells and Paneth cells, and secretion of both acidic and neutral mucus indicated a greater variety in secretory goblet cells (764). Next, both the iPSC-derived intestinal epithelia and differentiated Caco-2 cells were exposed to LPS and nigericin, which act as stimulatory agents for TLR-4 induced inflammation. Co-treatment of LPS and nigericin resulted in significant cytotoxicity

and barrier disruption for the iPSC-derived epithelium. Furthermore, the co-treatment increased the gene-expression and secretion of the pro-inflammatory cytokines IL-6, IL-8 and TNF-α. On the contrary, LPS and nigericin co-treatment caused no significant toxic effects in the Caco-2 model. It was concluded that the iPSC-derived intestinal epithelia shows improved sensitivity over Caco-2 models for barrier disruption, cytotoxicity and cytokine secretion.

A longstanding problem in MNP research is the lack of knowledge on effects of secondary MNPs and the impact of their protein corona on cells. Therefore, in **chapter 4**, the cytotoxicity, cytokine secretion, barrier disruption and ROS generation resulting from both primary and secondary MNP exposure were assessed and related to the MNP protein corona composition. **Chapter 3** demonstrated increased sensitivity of the iPSC-derived model, thus the same model was utilized here. Confocal Raman spectroscopy confirmed the presence of the MNPs in cells and indicated close proximity of MNPs to the nucleus. None of the tested MNPs showed acute cytotoxicity, which is in line with the general biocompatibility of plastics. Exposure to PP-Talc, PVC, PET-TiO_2 or PA resulted in significant barrier disruption, pro-inflammatory cytokine secretion and intracellular ROS, while PS and PLA showed no significant toxicity. LC-MS-MS based proteomics assessment of the protein corona showed differential binding of proinflammatory opsonins and ROS-scavenging proteins on secondary MNPs and primary PS MNPs. The pattern of protein enrichment matched observed induction of cytokine secretion and ROS, indicating a potential role for the protein corona in ROS and inflammation induced toxicity. Overall, we conclude that safety of primary PS MNPs cannot be extrapolated to secondary MNPs and that the protein corona plausibly contributes to cellular toxicity by presenting deleterious proteins and sequestering beneficial proteins.

In **chapter 4**, it was demonstrated that the protein corona in medium substantially impacts cellular toxicity, yet the composition of the digestion-associated protein corona and its effects on cells remains unknown. Thus, in **chapter 5**, we set out to determine how MNP charge and size impact the digestion-associated protein corona and whether the corona composition affects MNP uptake in a THP-1-derived model of intestinal phagocytes. Ideally, secondary MNPs would be included to assess differences in biokinetics between digested primary and secondary MNPs. However, currently there are no methods to fine tune secondary MNP properties and accurate label-free quantification of cellular internalization is not yet feasible. Instead, a panel of primary PS MNPs of various sizes and surface charges was subjected to *in vitro* digestion and the effect on cellular uptake was determined using flow cytometry. *In vitro* digestion significantly increased MNP internalization for 50 nm,100 nm and 200 nm MNPs when compared to serum-treated MNPs, but did not affect uptake of charged MNPs or MNPs of 500 - 1000 nm. These findings suggest that the protein corona becomes less important as particle size increases, or when

there is a strong charge on the MNP. Using SDS-PAGE, it was shown that *in vitro* digestion resulted in a sparse protein corona which is retained when exposed to serum and affects serum-protein binding. This finding implies that the history of the protein composition can impact subsequent protein binding, potentially leading to divergent protein coronas depending on the route of exposure, even if the final matrix is identical. Using LC-MS-MS proteomics, it was shown that *in vitro* digestion significantly affected subsequent binding of serum-borne apolipoproteins, complement and coagulation proteins to MNPs, both of which are implied in particle recognition by phagocytes (683-689). We conclude that digestion increases cellular uptake of uncharged nanoplastics and small microplastics. Therefore, *in vitro* digestion should be included in oral hazard assessment of MNPs <500 nm to prevent underestimation of uptake.

In **chapters 4 and 5,** it was shown that primary and secondary MNPs have the potential of cellular internalization and *in vitro* toxicity. To relate these *in vitro* findings to human risks, it is necessary to know at what oral human exposure these effects occur. Typically, the extrapolation of *in vitro* to *in vivo* concentrations (QIVIVE) is done using PBK models (241, 242). However, current PBK models for MNPs rely on mouse data for empirical fitting (243, 765) which does not lend itself well to interspecies scaling or QIVIVE. Therefore, **chapter 6** implemented a data-independent mechanistic PBK model, to predict tissue concentrations in mouse and humans after oral exposure to MNPs. The mechanistic mouse model accurately predicted observed tissue concentrations within a 10-fold difference for blood (94%), lung (88%), kidney (75%), heart (75%) and gut (75%) when used to predict tissue concentrations after single oral administration of radiolabelled PS. When considering both acute and chronic exposure, the mechanistic PBK model predicted mouse tissue concentrations within 10-folds in approximately 50% for blood and around 30-40% for remaining tissues. When compared to an empirically fit model, the mechanistic PBK model showed improved prediction of mouse validation data. To predict tissue concentrations in humans, lifelong (75 years) oral exposure to 5 µg/week (80) of MNPs was simulated. The model indicated three separate biokinetic patterns of MNPs. MNPs <50 nm were predicted to be rapidly excreted by urine, MNPs <150 nm were rapidly excreted through bile and MNPs >150 nm showed increased tissue accumulation which increased with increasing size. This suggests that nanoplastics may not be able to accumulate in the body and a tempered risk perception of nanoplastics may be warranted. Regardless of particle size, a steady-state concentration was predicted within 20 years and a similar concentration between blood and organs was observed. This indicates that the blood concentration may serve as a proxy for MNP tissue concentrations. The predicted MNP concentrations in internal tissues ranged from 0.23 pg/g to 15 ng/g, which was consistent with observed concentrations in blood, but over a 1000-fold lower than previously reported kidney, brain and liver concentrations (14, 16). Uncertainties in the mice data available for validation made it impossible to determine whether the difference between observed and

predicted concentrations are due to inaccuracies in the model or the measured tissue concentrations. While the lack of high-quality human validation data prevents estimation of human model accuracy, the predictions indicate considerably lower tissue concentrations than previously thought.

When taken together, **chapter 2, 3 and 4** provide evidence that stem cell-derived intestinal models are suitable for MNP testing and can have distinct advantages over cell lines in terms of sensitivity. In **chapter 4 and 5** we show that the protein corona depends both on the polymer backbone as well as size and charge of MNPs. The results show that the protein corona likely contributes to *in vitro* toxicity and transport, and improper consideration of the protein corona may lead to artificial results. From **chapter 5** we could clearly demonstrate differences in toxicity between primary PS MNPs and secondary MNPs supporting the need to routinely include secondary MNPs when assessing risk. Finally, in **chapter 6** we have, for the first time, demonstrated the applicability of mechanistic PBK models to oral uptake of MNPs. While more human data is needed to conclusively assess model quality, model estimates show that life-long oral exposure to MNPs may not lead to tissue concentrations at which toxicity occurs *in vitro*. Overall, **chapters 3-6** contributed considerably to our understanding of protein corona composition and implications for toxicity, demonstrate limitations of current *in vitro* NAMs and give clear recommendations how to improve future MNP risk assessment.

7.2 General discussion and future perspectives

The results described in **chapters 2-6** of this thesis show the applicability of advanced NAMs for MNP toxicity assessment. Furthermore, the role of the protein corona on the toxicity of primary and secondary MNPs was elucidated in terms of impact on cytokine secretion, ROS generation, barrier disruption and phagocytosis. From the conclusions of this thesis, several recommendations for the future directions of MNP toxicity testing can be derived. Specifically, the following future directions are expected to impact the field substantially and are discussed in detail in the sections below.

1. Use of advanced *in vitro* models for MNP testing
2. Accelerating MNP research with reference materials
3. Envisioned improvements to MNP associated protein corona research
4. Assessing low dose (sub)-chronic toxicity
5. Improving trust in reported *in vivo* MNP concentrations
6. Envisioned improvements to colloid PBK and dosimetry models

7.3 Use of advanced *in vitro* models for MNP testing

Chapter 2, 3 and 4 have shown the suitability of iPSC-derived intestinal models for assessing MNP hazards. While stem cell-derived models have recently gained large scientific interest, these models still see little regulatory acceptance for toxicity testing. One of the key questions to discuss is whether these models consistently offer an advantage over cell line models or whether their application domain is more limited.

The main advantages of stem cell-derived models over cell lines are the ability to differentiate into multiple cell types, which have a phenotype closer to primary cells (240, 766, 767). The ability to differentiate into rare cell types allows the assessment of differential toxicity to specific cellular subsets of the tissue. For example, **chapter 3 and chapter 4** highlight the ability of iPSCs to differentiate into Paneth cells and a gradient of acidic and basic goblet cells, neither of which can be captured in conventional cell line models. Of these cells, especially Paneth cells are relevant to MNP toxicity as they are responsible for secreting anti-bacterial peptides that can also stimulate cytokine secretion of the intestinal epithelium (768). While not performed in this thesis, *in vitro* stem cells can also be differentiated into tuft cells and enteroendocrine cells which likewise have no available cell lines (769-771). Toxicity to any of these rare intestinal cell types is likely to result in overt pathological consequences even when the remaining cell types are unaffected. Future studies should therefore assess differential toxicity to these cell types using transcriptomics endpoints like single-cell sequencing or by isolation of these cell types using fluorescence-assisted cell sorting (FACS).

In **chapter 3,** it was shown that iPSC-derived intestinal epithelia are more sensitive towards inflammation and barrier disruption than cell lines. The detection of toxicity of secondary PVC MNPs in **chapter 4,** which was not previously observed using Caco-2 co-cultures (212), provides further proof for increased sensitivity of iPSC-derived intestinal models. One question which springs forth from these observations is whether this increased sensitivity is artificial or physiologically relevant. For small chemicals, stem cell-derived models show increased correlation with intestinal permeability of primary tissues (240, 766, 767), but due to the lack of studies on nanomaterials, this conclusion cannot be extended to MNPs. Nevertheless, the barrier disruption of PVC and PP observed in **chapter 4** is in line with effects observed in mice (612, 613). While it cannot yet be established if the increased sensitivity of iPSC-derived models is artificial or not, the precautionary principle advocates for selection of the most sensitive model in the absence of strong scientific counterevidence (772).

Chapter 3 and 4 indicate potential benefits of iPSC-derived intestinal epithelia in terms of hazard assessment, but the suitability of iPSC-derived models for assessing MNP transport

was not investigated. iPSC-derived models strictly require the inclusion of extracellular matrices like Matrigel or collagen to provide the cellular cues required for proper cellular differentiation (773-776). These extracellular matrices may impede MNP transport in a size-specific manner (775, 777) and act as a sink for MNPs. For two-dimensional models, like the one used during this thesis, the extracellular matrix is located on the basolateral side. Basolateral inclusion of an extracellular matrix is physiologically relevant as it mimics the basement membrane, but the choice of the type and amount of matrix is largely arbitrary. This raises the question whether the inclusion of the extracellular matrix causes an artificially tight barrier or improves physiological relevance. Typically, Caco-2-derived nanomaterial translocation ranges between 0.1-10%, while murine bioavailability typically ranges between 0.1-2% (13). This indicates that the *in vitro* bioavailability is typically overpredicted, implying that inclusion of an extracellular matrix would improve correlation with *in vivo* results. Further research comparing the bioavailability of MNPs in iPSC-derived models will be required to definitively conclude whether iPSC-derived models are suitable for MNP translocation assessment.

Advanced *in vitro* models offer several potential improvements over conventional cell models, however there are currently concrete practical considerations hindering regulatory implementation. The first is the lack of standardization of cellular differentiation protocols. At the moment of writing, there are over a dozen of different iPSC differentiation protocols resulting in different intestinal phenotypes and cell compositions (237, 240, 371, 767, 778). This variety in models is a double-edged sword, on the one end it allows one to tune their model to the specific research question at hand, but on the other hand it creates ambiguity in the model selection. In addition to variety introduced by the choice of differentiation protocol, the donor used to derive iPSC models also impacts the final phenotype of the model. When considered optimistically, the donor dependance can be used to capture population-wide variance in toxic response, but when regarded pessimistically, it makes model outcomes inconsistent and donor selection for risk assessment would be non-trivial. While an increasing number of iPSC studies characterize their model using iPSCs derived from multiple donors, the issue of donor selection from a regulatory perspective is largely ignored. Considering these issues, it is still too soon to consider the regulatory implementation of advanced *in vitro* models for MNP testing, but these obstacles are of transient nature and will be resolved as the field matures.

7.4 Accelerating MNP research with reference materials

Chapter 4 demonstrates toxicity of secondary PET-TiO_2, PVC, PP-Talc and PA MNPs, and absence of toxicity of primary PS MNPs. These findings emphasize the need to generate more data on secondary MNP toxicity. There is currently a lack of standardization in

secondary MNPs used for laboratory studies. Because of this, extensive particle characterization is needed before any interlaboratory comparison of results can be made. The generation of such data is cumbersome and in practice, MNP characterization data is often limited or absent in toxicity studies. Improved interlaboratory comparison of results can be attained by circumventing the need for repeated particle characterization through the generation and distribution of secondary MNP "reference materials".

The generation of reference materials for nanoparticles is not a new concept, as metallic reference particles and microplastics of PP, PET , LD-PE and HD-PE were previously distributed by the European Union's Joint Research Centre (JRC) (779, 780). The size of these initial MNP reference materials surpasses the limit of human bioavailability (~10 µm) and thus a set of smaller MNP reference materials is required to be relevant to human toxicity. Such a "reference material" should be designed to address data-gaps that cannot be answered using primary MNPs. Current research with primary PS MNPs often includes a variety of sizes and differing surface charge, and there is a relative abundance of data relating these properties to toxicity. Instead, the largest data-gaps are the unknown effects of the polymer composition and MNP shape. To delineate the effect of polymer composition, the most relevant polymer types to include would be those with the highest production volume, and those that are expected to show a rapid increase in production. Specifically inclusion of LD-PE, HD-PE, PP, PVC, PUR, PS, PET and biodegradable polymers like PLA (4, 46-53) would be recommended. Additionally, **chapter 4** has shown that PP-Talc and PET-TiO_2 showed the highest magnitude of effects, indicating that inclusion of mineral or metallic fillers may aggravate toxicity. The use of filler materials in plastic products is very common and may comprise over 50% of material weight (781), yet it is rarely considered for MNP toxicity research. To fill this data gap, it is vital to generate MNPs containing the most common filler types such as talc, calcium carbonate, silicates, barium sulfate, sodium sulfate, carbon black (782) and upcoming biodegradable fillers like lignocellulose and bamboo fibers (77).

In addition to polymer composition, the generation of MNPs of various shapes will help delineate the shape effect of toxicity. In the environment, fibre-like MNPs are the most abundant followed by sheets and fragments (55). Fragments of various aspect ratios are obtained naturally during standard production methods like cryo-milling or laser-ablation (40, 783, 784), thus inclusion required no additional effort. At the time of writing, it is not possible to produce nanosized secondary MNPs like fibres or sheets, but ground-up synthesis of fibres and sheets may be possible. Recently, electrospinning was utilized to develop a polyurethane and polyester fibres and subsequent cutting of these fibres by cryotome or a santoku kitchen knife was shown to be able to generate microfibres between 100 - 2000 µm in length (785, 786). The length of fibres produced this way is similar to the length of polyester fibres derived from fabrics (787), and the diameter of

fibres obtained from these methods is approximately 15 µm, which is similar to textile derived polyethylene fibres. While standardization and validation of these methods may be required, they are currently the most promising for generation of relevant MNP fibres. Currently, there are no published methods to generate MNP sheets, which thus cannot be included as reference material until protocols become available.

7.5 Envisioned improvements to protein corona research

Chapters 4 and 5 have demonstrated the potential impact of the protein corona on pro-inflammatory cytokine secretion, ROS generation and MNP uptake. While these studies contributed to our overall understanding of protein-corona functioning, several extensions of this methodology may allow the study of currently underexplored aspects of the protein corona.

The protein corona is composed of a tightly bound hard corona and weakly bound soft corona of which the hard protein corona was the focus of **chapters 4 and 5**. The soft protein corona spatially covers the hard protein corona (152-154) and may sterically provide a cover preventing cellular interaction with the hard corona. It is therefore likely that the soft protein corona has a relevant biological impact on MNP interaction. The study of the protein corona requires separation of MNPs from the surrounding matrix to prevent carry-over due to unbound proteins (150, 152, 589, 788). Currently, centrifugal methods are the most common MNP separation method, however, subjection to high G-forces causes loss of loosely bound proteins comprising the soft protein corona. Recently, improvements to sample preparation have enabled the retention of the soft protein corona. Separation methods such as field-flow fractionation or size-exclusion chromatographic methods do not subject the MNP to strong forces and have been used to isolate MNPs without removal of the soft protein corona (789-791). Alternatively, the modification of proteins through click chemistry, photo-activated crosslinkers or traditional formaldehyde fixation can covalently crosslink the soft and hard protein corona (791-793). Of these methods, the use of fixation techniques appears most readily applicable as it does not require large material investments and therefore warrants further investigation.

When studying the interaction of MNPs with the intestine, ideally the protein corona will mimic digested MNPs as close as possible. **Chapter 5** shows that inclusion of *in vitro* digestion alters the protein corona and affects particle uptake in a size and charge dependent manner. One of the limitations in the study of *in vitro* digested MNPs is the poor tolerance of various digestive components by cell lines. Bile salts, pancreatin and trypsin are cytotoxic to intestinal cell lines if not inactivated with small molecule inhibitors or proteinaceous trypsin inhibitors, which can induce toxicity or alter the protein corona

(637). *In vivo*, the intestine is protected from digestive components through the presence of a thick mucous layer and the secretion of pancreatic and intestinal trypsin inhibitors (794-797). These components are currently not included in existing *in vitro* digestion protocols, but future inclusion may hold several potential advantages. First, inclusion of mucous and human trypsin inhibitors in the simulated intestinal fluid circumvents toxicity of the *in vitro* digesta in a physiologically relevant way. Additionally, it is likely that *in vivo*, mucous proteins will at least in part displace the digestive protein corona, which is not captured in current *in vitro* studies. Besides the inclusion of mucous, inclusion of food-matrices can simultaneously increase relevance of the digestive corona and reduce the toxicity of the digesta. In recent years, the first studies investigating the protein corona resulting from co-digestion of nanoparticles and various food matrices including bread (701), milk casein (798, 799) and a cream-based proxy for a high-fat diet (121) have appeared. These studies confirmed the binding of food-molecules various colloids and reported subsequent modulation of cellular toxicity. We argue that inclusion of mucous and food matrix in *in vitro* digestion will allow for more accurate estimation of MNP effects to the intestinal epithelium and in future models of the microbiota.

In addition to the protein component of the corona, MNPs can bind numerous other metabolites including lipids and saccharides (121, 800). In 2018, the first studies showing the formation of lipid and saccharide components of the corona (801) appeared in literature. Lipids like phospholipids, fatty acids and saccharides like glucose and LPS are abundant in the intestine and have known roles in inflammation and phagocytosis (802, 803). As such, it is reasonable to assume that these alternative metabolites may be a major component of the bio-corona and may affect biological identity. Indeed, early studies investigating the bio-corona of metal nanoparticles and primary PS have revealed a high abundance of lipids and saccharides and indicate that these components have a high particle specificity and can in return affect protein corona composition (804-808). It is therefore recommended that future studies assess the metabolite corona after *in vitro* digestion or serum-incubation.

MNPs are carriers of a multitude of associated chemicals, either as additives or by association with environmental contaminants forming an eco-corona. Among these associated chemicals are bisphenols, poly-aromatic hydrocarbons, organic pesticides, heavy metals, a multitude of antimicrobial compounds, harmful pathogenic bacteria and other contaminants of emerging concern (280, 809-813). Many of these compounds have confirmed endocrine or neuronal effects and may be transported into the body using microplastics as carriers (25, 66-74). This is called the "trojan-horse effect" and is considered one of the main potential toxicity mechanisms of MNPs (814). While the associated chemicals of MNPs have a well-established role in toxicity, they are also highly abundant in nature and humans are exposed to a relatively high background burden of these chemicals through

our daily lives (815-817). Therefore, the question becomes whether or not exposure to MNPs is able to substantially increase to the point of actual health risks for humans. Recently, the first *in silico* assessment of chemical leaching from MNPs suggested that chemical leaching is low compared to background exposure (80). However, this study only covered a small part of known contaminants and we recommend that future studies apply a similar approach to assess the contribution of MNPs to the total body burden of novel contaminants of emerging concern like PFAS.

7.6 Assessing low dose (sub)-chronic toxicity

Chapters 3, 4 and 5 aimed to assess toxicity and transport mechanics as occurring in the intestine. While barrier organs like the intestine are exposed to high concentrations of MNPs, the modelling results of **chapter 6** indicate much lower MNP concentrations in non-barrier organs. This finding holds implications for current MNP testing strategies as both *in vitro* and *in vivo* studies have focussed on high, acute MNP toxicity.

Oral rodent studies typically use a daily exposure from 5 mg/kg to 50 mg/kg per day, and most studies use doses >= 25 mg/kg/d (144, 718-720, 722). When no human exposure estimates were available, these concentrations were acceptable, however, recent estimates of human exposure call for a change in experimental design. Currently, There are some mass-based estimates of human oral MNP exposure of which the lowest is around ~5 µg/week (80) and the highest at 100-5000 mg/week (117). Assuming 5000 mg/week, the daily dose to a 70 kg human, would be 10 mg/kg, similar to current *in vivo* dosing conventions. However the estimate of 100-5000 mg/week has been discredited due to mathematical errors (818) and the exposure estimate of ~5 µg/week is more consistent with number based exposure estimates (115, 116). Assuming a 5 µg/week exposure, the daily dose to humans is approximately 0.01 µg/kg/d, i.e., over a million-fold lower than current dosing conventions. All substances become toxic at sufficiently high concentration and any toxicity measured at these concentrations holds no relevance to realistic MNP toxicity. Additionally, the use of such high doses increases the risk of false positives due to the cellular toxicity of common MNP additives like sodium-azide or fluorophores (819, 820). Thus, current design of animal studies only has a limited capacity to contribute useful data for hazard assessment and leads to unnecessary costs and animal distress. It is therefore urgently recommended to critically consider the relevance of available *in vivo* data and to design *in vivo* studies to include more relevant exposures between 0.01 µg/kg to 100 µg/kg.

In vitro studies on MNPs have also informally adopted a set of conventional concentrations which range between 5 - 250 µg/ml (~5 - 250 µg/g). **Chapter 6** predicts that tissue

concentrations in the liver, kidney, blood, spleen, brain and lung are below 15 ng/g, about a thousand-fold lower than current dosing standards. Typically, toxic effects of MNPs occur between 20 µg and 250 µg/ml, and no studies observing toxic effects below 5 µg/ml could be identified. The toxicity observed at 20 - 250 µg/ml is frequently used as basis to claim various kinds of MNP toxicity in reviews and policy briefs. However, given the tissue concentrations predicted in **chapter 6**, these findings should rather be interpreted as an indication of MNP safety at physiologically relevant concentrations. While the PBK model used here is far from validated, chapter 6 urges critical examination of available *in vitro* results, more nuanced communication to policy makers and inclusion of MNP doses <1 µg/ml for toxicity studies in non-barrier tissues.

7.7 Improving trust in in vivo tissue concentrations

An increasing number of studies report the presence of MNPs >500 nm in tissues of both human and rat. Contrastingly, **chapter 6** predicted much lower tissue concentrations than observed *in vivo* and indicated that MNPs larger >500 nm may remain trapped in the organ capillaries. This raises the question whether these discrepancies are due to inaccuracies in the PBK model or due to inaccuracies in measured tissue concentrations. Specifically, leaching of label molecules, unknown localization within tissues and methodological challenges are realistic confounders in current biokinetic studies.

The detection of MNPs in rodent studies is usually reliant on fluorescence labelling of molecules like Nile red or proprietary fluorophores. Fluorophore leaching is a well-known issue for nanoparticles and may cause false positive particle detection (821). The control for fluorescence leaching is increasingly included in studies, but this data is often not shown in the respective publication or is not critically assessed. For example, it was shown that 0.1 - 1% of total fluorophore can leach from MNPs after *in vitro* digestion (719). In the respective study this was considered negligible, however, when considering that typical MNP bioavailability is much lower than 1% (13), fluorophore leaching can significantly skew measured tissue concentrations. A solution to this problem would be covalent attachment of fluorophores to the MNP surface or correction for fluorophore tissue concentrations by extending the PBK model from **chapter 6** with a leached fluorophore sub-model.

The second major confounder of measured MNPs in tissues is the unknown localization of MNPs within an organ. In **chapter 6**, it was predicted that the vast majority of MNPs remain located within the tissue capillaries once the size exceeds 50 nm. MNP quantification *in vivo* is commonly determined in unflushed tissue homogenates (718-720, 722, 822), which destroys tissue architecture without removal of capillary blood. It is therefore

possible that all MNPs measured in tissue homogenates are due to MNPs in the capillary blood rather than the tissue itself. Furthermore, homogenization techniques such as bead-based homogenization and blending very likely generates large quantities of MNPs due to the impact of metal beads/fins and the plastic container, which has thus far not been studied. To distinguish capillary-borne and tissue-borne MNPs, it is possible to flush the animal with saline solution prior to tissue isolation, but it is likely that MNPs remain attached to the sticky glycocalyx of capillaries even after washing. The tissue localization of MNPs has large implications on the critical effects of MNPs as capillary borne MNPs are unlikely to cause toxicity in the tissue itself. Here it is recommended that future research assesses whether saline perfusion prior to tissue homogenization removes glycocalyx-bound MNPs and to assess the background MNPs generated using tissue homogenization techniques.

Recent years have seen a boom in studies investigating human tissue concentrations, however the novelty of these studies bring associated methodological challenges. To date, only two studies have quantified tissue concentrations in terms of mass. A groundbreaking study showing the application of pyrolysis GC-MS for MNP quantification in the blood of volunteers set the stage for much of the regulatory interest in MNP toxicology (14). However, there was a large inconsistency between measured MNP concentrations in participants. In duplicate blood samples of 18 volunteers, there were only 3 individuals showing the presence of MNPs in both samples and all individuals taken together, the measured plastic concentration was not significantly different from the limit of detection (14). While this study demonstrates the applicability of pyrolysis GC-MS for measuring MNPs in blood, we argue that the findings are not sufficient to make quantitative claims on MNP blood concentrations. The other study that reports mass based tissue concentrations measured MNP concentrations in samples of brain, liver and kidney (16). Here, the samples used were historic and the experimental design was not specific to the study of MNPs. As such, potential sources of MNP contamination were not taken into consideration, and polyethylene cutting boards and plastic buckets were used during tissue isolation. When using plastic cutting boards as intended, up to 4.73 mg of MNPs are generated which represents a non-negligible source of MNP contamination (759). Furthermore, it was recently described that the use of nitrile gloves can result in significant MNP generation which represents an omni-present source of contamination in both medical and laboratory studies (760). In addition to these "real" contaminations of MNPs, the use of pyrolysis GC-MS in high-fat matrices has also been reported to lead to an artificial increase in plastic signal, leading to false-positive detection of plastics (761). Until these issues are addressed, the detection of MNPs in human tissues is dubious and should not be unquestionably accepted.

7.8 Envisioned improvements to PBK and dosimetry models

In **chapter 6**, the application of mechanistic PBK models to MNP biodistribution was shown. PBK models are promising tools for read across of biodistribution between MNP types, however the accuracy of our mechanistic model is still too low for regulatory consideration. The largest factors currently limiting the application of mechanistic PBK models is the limited understanding of biokinetic processes of MNPs and the lack of high-quality animal or human validation data.

There are currently major knowledge gaps on MNP biokinetic processes in humans. First, there is a discrepancy between historical reports of particulate contamination during intravenous infusion and currently reported MNP sizes in tissues. Prior to the 80s, there was no routine filtration of liquids for intravenous infusion and particulate contamination was not uncommon (823, 824). In such cases, rapid sequestration of microparticles in the lung capillary beds was observed and lung embolisms or granulomas quickly ensued (823, 825, 826). Similarly, when a beagle dog was injected with large quantities of 3-12 µm MNPs, quick sequestration of 12 µm particles in the lung capillary beds were observed while only MNPs below 5 µm accumulated in RES organs like liver and spleen (827). Despite these historic precedents, recent studies have shown the presence of MNPs >15 µm in liver, lung, testis, semen, placenta, urine and bile and have found MNPs >1 mm in blood (147, 765). Physiologically speaking there are no know processes which allow the escape of particles >5 µm from the bloodstream, and MNPs should not be able to pass the lung capillary bed which have an average diameter of 6 µm (828). Likely, once the recommendations from section 7.7 are implemented and limits of quantification of MNPs in biological tissues are reduced, the source of these discrepancies will come to light.

As increasing amounts of high quality biokinetic data becomes available, it is expected that mechanistic PBK models will overtake empirical PBK models. As more biodistribution data becomes available, it may also be possible to develop Quantitative Structure Activity Relationships (QSARs) which can predict ADME properties based on physicochemical properties. For small molecules, QSARs are frequently used to derive tissue partition coefficients and bioavailability, both of which are currently challenging to be derived mechanistically for MNPs (242). Recent QSARs for metallic nanoparticles and carbon nanoparticles have shown to accurately predict cellular uptake, mitochondrial membrane potential disruption, cytotoxicity and genotoxicity in a variety of cell types including prokaryotes, unicellular eukaryotes and human cells (829-833), highlighting the potential applicability of these models. Additionally, the recent advancement of artificial intelligence may be promising for deriving mechanistic PBK models. The first AI-fitted PBK models have appeared for data-rich nanoparticles (834, 835). If data is abundant,

these models are much better at identifying underlying relations in data than traditional machine learning models, enabling more rapid establishment of biokinetic dependencies on material properties. As established in section 7.7, there are currently large issues with the experimental design of animal studies and reported tissue concentrations in humans and animals. Overall, the detected sizes and concentrations of MNPs in tissues contradicts our theoretical knowledge of colloid biokinetics. There is a common saying in modelling; "Garbage in, garbage out" and while the issues surrounding detection of MNPs in tissues persists, the resulting data will be unsuitable for PBK validation or training.

Dosimetry models represent another class of *in silico* models frequently used for MNPs. These models can determine how much of the added *in vitro* dose (nominal dose) reaches the target cells (delivered dose) based on the density and size of MNPs. At the moment, the three most commonly applied dosimetry models are ISDD, ISD3 and distorted grid (DG), which allow the estimation of MNP sedimentation in 2-dimensional cell culture (432, 434, 435). Through the use of these models, it is possible to determine large differences in delivered dose, which can help to align toxicity results. While the reported dose metric in MNP studies is typically still the nominal dose, inclusion of the delivered dose can help posterior alignment of *in vitro* results by regulators. Current dosimetry models allow for prediction of the delivered dose in a remarkable variety of *in vitro* setups, however several improvements can be envisioned. Current *in silico* dosimetry models are not capable of predicting the transport of MNPs through semi-permeable inserts or extracellular matrices which hinder toxicokinetic studies. The use of semi-permeable membranes like transwells is very common for determining translocation of chemicals and nanoparticles. In these studies, cells are grown on a porous membrane that separates a basolateral and apical compartment and the transport of chemicals through the pores is determined. For small molecules, the barrier posed by the permeable membrane is negligible, but this is not true for nanoparticles given that the standard pore size is 400 nm – 3 µm, and the fact that less than 1% of the total surface consists of pores. Thus, the total rate of MNP transport is a function of both the barrier posed by the cells and the barrier posed by the semipermeable insert, both of which require quantification. Potentially, the extravasation model from **chapter 6** can predict the transport of MNPs based on the ratio of MNP to pore size, however this needs to be validated in cell free conditions. When using advanced NAMs like stem cell-derived intestinal epithelia, organ-on-chip devices or organoids, an additional barrier is posed by the extracellular matrix. Current dosimetry models do not consider the extracellular matrix, however the interaction of nanoparticles and the extracellular matrix has been studied extensively from a tumor nanomedicine perspective. Existing mathematical models predicting MNP transport through the tumour or brain extracellular matrix may serve as a basis for dosimetric models (775, 836, 837). The utility of predicting MNP transport through porous matrices also extends beyond dosimetry,

as it will also aid mechanistic prediction of bioavailability by simulating the transport of MNPs through the mucous layer lining the intestine.

Extending beyond the models utilized in this thesis, numerous molecular dynamics models used to predict protein-drug interactions, are promising for MNPs. Using knowledge on the electric interaction between proteins, it is possible to predict protein-protein interactions *in silico*. As established throughout this thesis, protein corona formation is reliant on particle properties, the surrounding matrix and the history of the MNP. The prediction of protein interactions is of great value to nanotoxicology as it could allow estimation of the formation dynamics of the protein corona and can subsequently predict affinity for receptors. Molecular dynamics simulations for metallic nanoparticles and carbon-nanoparticles are already available in literature (838) and could potentially be used to tackle the complexity of protein corona formation on MNPs (160). While these methods are currently not yet able to comprehensively predict protein corona interactions, they are promising tools for future to enable future regulatory consideration of the protein corona of MNPs.

Recently, the nanoinformatics roadmap 2030 was jointly published by the European Union and American FDA (839). This roadmap describes that currently the largest obstacles to widescale implementation of nanoinformatics methods are the lack of data, the lack of access to data and regulatory requirements for validation of nanoinformatics models. These are actively being solved through the evolution of data generation through *in vitro* NAMS, the establishment of harmonized and interconnected digital data repositories like enanomapper, and efforts to generate human relevant toxicity data. Overall, nanoinformatics has seen remarkable growth in the recent years, spurred forwards by both governmental incentives and financial incentives of the nanotechnology industry. The methods described are well positioned to tackle the multiplicity of nanoparticle materials and enable understanding and prediction of complex phenomena like protein corona formation and eco-corona composition, which would not be possible using solely *in vitro* methods. As such, we recommend more frequent implementation of nanoinformatics tools and stimulation by universities and governments to train nanotoxicologists in the use of these models.

7.9 Conclusions

In conclusion, this thesis shows the applicability of new approach methodologies for MNP toxicity assessment. We present one of the earliest reports that iPSC-derived intestinal epithelia are applicable to MNP toxicity testing and show increased sensitivity of *in vitro* models compared to traditional cell lines. We confirm that secondary micro and

nanoplastics show increased toxicity compared to primary PS MNPs and indicate that especially MNPs with metallic fillers may show increased toxicity. The results suggest a role of the protein corona in determining MNP uptake, ROS generation, inflammation and barrier disruption as correlation between protein corona composition and effects was confirmed. We further provide proof that the digestion-associated protein corona affects subsequent corona formation, highlighting that the history of the protein corona can affect it's composition. Finally, we demonstrated that mechanistic PBK models can predict MNP tissue concentrations and show better predictivity than empirical models. The computed tissue concentrations indicate that lifelong accumulation of MNPs is below typically used *in vivo* and *in vitro* concentrations. This indicates a necessity to alter current *in vitro* and *in vivo* dosing standards. Overall, this thesis contributed substantially to the understanding of the protein corona in context of secondary MNP toxicity and provides concrete recommendations for future MNP risk assessment and QIVIVE strategies.

References

1. Chalmin P. The history of plastics: from the Capitol to the Tarpeian Rock. Field Actions Science Reports The journal of field actions. 2019:6–11.
2. Utracki LA. History of commercial polymer alloys and blends (from a perspective of the patent literature). Polymer Engineering & Science. 1995;35(1):2–17.
3. Weil BH, Anhorn VJ. Plastic Horizons: Jaques Cattell; 1944.
4. PlasticsEurope. Plastics the fast facts 2023 2023 [Available from: https://plasticseurope.org/knowledge-hub/plastics-the-fast-facts-2023/.
5. Barnes DK, Galgani F, Thompson RC, Barlaz M. Accumulation and fragmentation of plastic debris in global environments. Philosophical transactions of the Royal Society of London Series B, Biological sciences. 2009;364(1526):1985–98.
6. Peries SD, Sewwandi M, Sandanayake S, Kwon H-H, Vithanage M. Airborne transboundary microplastics–A Swirl around the globe. Environmental pollution. 2024;353:124080.
7. K.L P, K.R R, Joseph CJ, M.S I, Srinivas R, S H. Fate, transport and degradation pathway of microplastics in aquatic environment — A critical review. Regional Studies in Marine Science. 2022;56:102647.
8. Jamieson AJ, Brooks LSR, Reid WDK, Piertney SB, Narayanaswamy BE, Linley TD. Microplastics and synthetic particles ingested by deep-sea amphipods in six of the deepest marine ecosystems on Earth. Royal Society Open Science. 2019;6(2):180667.
9. Chiba S, Saito H, Fletcher R, Yogi T, Kayo M, Miyagi S, et al. Human footprint in the abyss: 30 year records of deep-sea plastic debris. Marine Policy. 2018;96:204–12.
10. Napper IE, Davies BFR, Clifford H, Elvin S, Koldewey HJ, Mayewski PA, et al. Reaching New Heights in Plastic Pollution—Preliminary Findings of Microplastics on Mount Everest. One Earth. 2020;3(5):621–30.
11. Bergmann M, Collard F, Fabres J, Gabrielsen GW, Provencher JF, Rochman CM, et al. Plastic pollution in the Arctic. Nature Reviews Earth & Environment. 2022;3(5):323–37.
12. Obeng EM, Hodge C, You J. Microplastic pollution: a review of specific blood-tissue barrier breaches and health effects. Environmental pollution. 2025;376:126416.
13. Alexander J, Barregard L, Bignami M, Ceccatelli S, Cottrill B, Dinovi M, et al. Presence of microplastics and nanoplastics in food, with particular focus on seafood. Efsa Journal. 2016;14(6).
14. Leslie HA, van Velzen MJM, Brandsma SH, Vethaak AD, Garcia-Vallejo JJ, Lamoree MH. Discovery and quantification of plastic particle pollution in human blood. Environ Int. 2022;163:107199.
15. Schwabl P, Koppel S, Konigshofer P, Bucsics T, Trauner M, Reiberger T, et al. Detection of various microplastics in human stool: A prospective case series. Annals of Internal Medicine. 2019.
16. Nihart AJ, Garcia MA, El Hayek E, Liu R, Olewine M, Kingston JD, et al. Bioaccumulation of microplastics in decedent human brains. Nature Medicine. 2025.
17. Ragusa A, Svelato A, Santacroce C, Catalano P, Notarstefano V, Carnevali O, et al. Plasticenta: First evidence of microplastics in human placenta. Environ Int. 2021;146:106274.
18. Liu S, Guo J, Liu X, Yang R, Wang H, Sun Y, et al. Detection of various microplastics in placentas, meconium, infant feces, breastmilk and infant formula: A pilot prospective study. Science of The Total Environment. 2023;854:158699.
19. Gomez Cortes L, Porcel Rodriguez E, Marinov D, Sanseverino I, Lettieri T. Selection of substances for the 5th Watch List under the Water Framework Directive: Publications Office of the European Union; 2025.

20. Schreiber L, Halko R, Santana-Viera S, Michalides NM, Sosa-Ferrera Z, Santana-Rodríguez JJ. Evaluation of European watch list contaminants in environmental matrices and microplastics: Analytical strategies, mechanisms of adsorption and occurrence. Trends in Environmental Analytical Chemistry. 2024;44:e00245.
21. Geissen V, Mol H, Klumpp E, Umlauf G, Nadal M, van der Ploeg M, et al. Emerging pollutants in the environment: A challenge for water resource management. International Soil and Water Conservation Research. 2015;3(1):57–65.
22. Duncan TV, Khan SA, Patri AK, Wiggins S. Regulatory Science Perspective on the Analysis of Microplastics and Nanoplastics in Human Food. Analytical Chemistry. 2024;96(11):4343–58.
23. European Food Safety A. EFSA Scientific Colloquium 25 – A coordinated approach to assess the human health risks of micro- and nanoplastics in food. EFSA Supporting Publications. 2021;18(8):6815E.
24. WHO. World Health Organization Microplastics in drinking-water. Geneva; 2019.
25. Wu P, Huang J, Zheng Y, Yang Y, Zhang Y, He F, et al. Environmental occurrences, fate, and impacts of microplastics. Ecotoxicol Environ Saf. 2019;184:109612.
26. Qun W, Shoukuan F, Tongyin Y. Emulsion polymerization. Progress in Polymer Science. 1994;19(4):703–53.
27. Pineda-Reyes AM, Hernández Delgado M, Zambrano-Zaragoza MdlL, Leyva-Gómez G, Mendoza-Muñoz N, Quintanar-Guerrero D. Implementation of the emulsification-diffusion method by solvent displacement for polystyrene nanoparticles prepared from recycled material. RSC Advances. 2021;11(4):2226–34.
28. Lovell PA, Schork FJ. Fundamentals of Emulsion Polymerization. Biomacromolecules. 2020;21(11):4396–441.
29. Gao Z, Wontor K, Cizdziel JV. Labeling Microplastics with Fluorescent Dyes for Detection, Recovery, and Degradation Experiments. Molecules. 2022;27(21).
30. Zhang Q, Han Y, Wang W-C, Zhang L, Chang J. Preparation of fluorescent polystyrene microspheres by gradual solvent evaporation method. European Polymer Journal. 2009;45(2):550–6.
31. Gouin T, Ellis-Hutchings R, Pemberton M, Wilhelmus B. Addressing the relevance of polystyrene nano- and microplastic particles used to support exposure, toxicity and risk assessment: implications and recommendations. Particle and Fibre Toxicology. 2024;21(1):39.
32. Andrady AL. The plastic in microplastics: A review. Marine pollution bulletin. 2017;119(1):12–22.
33. Vasiljevs LO, Zabarovska R, Gulevska E, Cirule D, Sansonetti E, Andersone I, et al. Changes in Wood Plastic Composite Properties After Natural Weathering and Potential Microplastic Formation. Forests [Internet]. 2024; 15(12).
34. Song YK, Hong SH, Eo S, Shim WJ. The fragmentation of nano- and microplastic particles from thermoplastics accelerated by simulated-sunlight-mediated photooxidation. Environmental pollution. 2022;311:119847.
35. Al Harraq A, Brahana PJ, Arcemont O, Zhang D, Valsaraj KT, Bharti B. Effects of Weathering on Microplastic Dispersibility and Pollutant Uptake Capacity. ACS Environmental Au. 2022;2(6):549–55.
36. Kotoyori T. Activation energy for the oxidative thermal degradation of plastics. Thermochimica Acta. 1972;5(1):51–8.
37. Zhang K, Hamidian AH, Tubić A, Zhang Y, Fang JKH, Wu C, et al. Understanding plastic degradation and microplastic formation in the environment: A review. Environmental pollution. 2021;274:116554.

38. Ducoli S, Rani M, Marchesi C, Speziani M, Zacco A, Gavazzi G, et al. Comparison of different fragmentation techniques for the production of true-to-life microplastics. Talanta. 2025;283:127106.
39. Banaei G, García-Rodríguez A, Tavakolpournegari A, Martín-Pérez J, Villacorta A, Marcos R, et al. The release of polylactic acid nanoplastics (PLA-NPLs) from commercial teabags. Obtention, characterization, and hazard effects of true-to-life PLA-NPLs. J Hazard Mater. 2023;458:131899.
40. Magri D, Sanchez-Moreno P, Caputo G, Gatto F, Veronesi M, Bardi G, et al. Laser Ablation as a Versatile Tool To Mimic Polyethylene Terephthalate Nanoplastic Pollutants: Characterization and Toxicology Assessment. ACS nano. 2018;12(8):7690–700.
41. Dias LP, Araújo CAS, Pupin B, Ferreira PC, Braga GÚ L, Rangel DEN. The Xenon Test Chamber Q-SUN(®) for testing realistic tolerances of fungi exposed to simulated full spectrum solar radiation. Fungal Biol. 2018;122(6):592–601.
42. Burrows S, Colwell J, Costanzo S, Kaserzon S, Okoffo E, Ribeiro F, et al. UV sources and plastic composition influence microplastic surface degradation: Implications for plastic weathering studies. Journal of Hazardous Materials Advances. 2024;14:100428.
43. Kim S, Sin A, Nam H, Park Y, Lee H, Han C. Advanced oxidation processes for microplastics degradation: A recent trend. Chemical Engineering Journal Advances. 2022;9:100213.
44. Hartmann NB, Hüffer T, Thompson RC, Hassellöv M, Verschoor A, Daugaard AE, et al. Are We Speaking the Same Language? Recommendations for a Definition and Categorization Framework for Plastic Debris. Environmental science & technology. 2019;53(3):1039–47.
45. International organization of standardization. ISO 80004-1:2023 Nanotechnologies – Vocabulary. 2023.
46. Obbard RW, Sadri S, Wong YQ, Khitun AA, Baker I, Thompson RC. Global warming releases microplastic legacy frozen in Arctic Sea ice. Earth's Future. 2014;2(6):315–20.
47. Kanhai LDK, Officer R, Lyashevska O, Thompson RC, O'Connor I. Microplastic abundance, distribution and composition along a latitudinal gradient in the Atlantic Ocean. Marine pollution bulletin. 2017;115(1):307–14.
48. Horton AA, Svendsen C, Williams RJ, Spurgeon DJ, Lahive E. Large microplastic particles in sediments of tributaries of the River Thames, UK – Abundance, sources and methods for effective quantification. Marine pollution bulletin. 2017;114(1):218–26.
49. Kuhn S, van Oyen A, Bravo Rebolledo EL, Ask AV, van Franeker JA. Polymer types ingested by northern fulmars (Fulmarus glacialis) and southern hemisphere relatives. Environ Sci Pollut Res Int. 2021;28(2):1643–55.
50. Kuhn S, van Oyen A, Booth AM, Meijboom A, van Franeker JA. Marine microplastic: Preparation of relevant test materials for laboratory assessment of ecosystem impacts. Chemosphere. 2018;213:103–13.
51. Abidli S, Antunes JC, Ferreira JL, Lahbib Y, Sobral P, Trigui El Menif N. Microplastics in sediments from the littoral zone of the north Tunisian coast (Mediterranean Sea). Estuarine, Coastal and Shelf Science. 2018;205:1–9.
52. Muhib MI, Uddin MK, Rahman MM, Malafaia G. Occurrence of microplastics in tap and bottled water, and food packaging: A narrative review on current knowledge. Science of The Total Environment. 2023;865:161274.
53. Geyer R, Jambeck JR, Law KL. Production, use, and fate of all plastics ever made. Sci Adv. 2017;3(7):e1700782.

54. Zhang H, Wei X, Liu L, Zhang Q, Jiang W. The role of positively charged sites in the interaction between model cell membranes and γ-Fe(2)O(3) NPs. The Science of the total environment. 2019;673:414–23.
55. Hongprasith N, Kittimethawong C, Lertluksanaporn R, Eamchotchawalit T, Kittipongvises S, Lohwacharin J. IR microspectroscopic identification of microplastics in municipal wastewater treatment plants. Environmental Science and Pollution Research. 2020;27(15):18557–64.
56. Koelmans AA, Mohamed Nor NH, Hermsen E, Kooi M, Mintenig SM, De France J. Microplastics in freshwaters and drinking water: Critical review and assessment of data quality. Water Res. 2019;155:410–22.
57. Kowalski N, Reichardt AM, Waniek JJ. Sinking rates of microplastics and potential implications of their alteration by physical, biological, and chemical factors. Marine pollution bulletin. 2016;109(1):310–9.
58. Khatmullina L, Isachenko I. Settling velocity of microplastic particles of regular shapes. Marine pollution bulletin. 2017;114(2):871–80.
59. Manojkumar N, Srimuruganandam B, Shiva Nagendra SM. Application of multiple-path particle dosimetry model for quantifying age specified deposition of particulate matter in human airway. Ecotox Environ Safe. 2019;168:241–8.
60. Schinwald A, Donaldson K. Use of back-scatter electron signals to visualise cell/nanowires interactions in vitro and in vivo; frustrated phagocytosis of long fibres in macrophages and compartmentalisation in mesothelial cells in vivo. Part Fibre Toxicol. 2012;9:34.
61. Brown SC, Kamal M, Nasreen N, Baumuratov A, Sharma P, Antony VB, et al. Influence of shape, adhension and simulated lung mechanics on amorphous silica nanoparticle toxicity. Advanced Powder Technology. 2007;18(1):69–79.
62. European chemicals agency. Plastic additives initiative, suplementary information on Scope and Methods 2019 [Available from: https://echa.europa.eu/documents/10162/17228/plastic_additives_supplementary_en.pdf/79bea2d6-8e45-f38c-a318-7d7e812890a1.
63. Hahladakis JN, Velis CA, Weber R, Iacovidou E, Purnell P. An overview of chemical additives present in plastics: Migration, release, fate and environmental impact during their use, disposal and recycling. J Hazard Mater. 2018;344:179–99.
64. Erik Hansen NN, Kristine Slot Ravnholt Vium. Hazardous substances in plastics,
Survey of chemical substances in consumer
products. In: environment Dmot, editor. 2014.
65. Yamashita R, Tanaka K, Yeo BG, Takada H, van Franeker JA, Dalton M, et al. Hazardous Chemicals in Plastics in Marine Environments: International Pellet Watch. In: Takada H, Karapanagioti HK, editors. Hazardous Chemicals Associated with Plastics in the Marine Environment. Cham: Springer International Publishing; 2019. p. 163–83.
66. Brennecke D, Duarte B, Paiva F, Cacador I, Canning-Clode J. Microplastics as vector for heavy metal contamination from the marine environment. Estuar Coast Shelf S. 2016;178:189–95.
67. Koelmans AA, Bakir A, Burton GA, Janssen CR. Microplastic as a Vector for Chemicals in the Aquatic Environment: Critical Review and Model-Supported Reinterpretation of Empirical Studies. Environmental science & technology. 2016;50(7):3315–26.
68. Li J, Zhang K, Zhang H. Adsorption of antibiotics on microplastics. Environmental pollution. 2018;237:460–7.
69. Mato Y, Isobe T, Takada H, Kanehiro H, Ohtake C, Kaminuma T. Plastic resin pellets as a transport medium for toxic chemicals in the marine environment. Environmental science & technology. 2001;35(2):318–24.

70. Mendoza LMR, Jones PR. Characterisation of microplastics and toxic chemicals extracted from microplastic samples from the North Pacific Gyre. Environ Chem. 2015;12(5):611–7.
71. Rochman CM, Kurobe T, Flores I, Teh SJ. Early warning signs of endocrine disruption in adult fish from the ingestion of polyethylene with and without sorbed chemical pollutants from the marine environment. The Science of the total environment. 2014;493:656–61.
72. Rodrigues JP, Duarte AC, Santos-Echeandia J, Rocha-Santos T. Significance of interactions between microplastics and POPs in the marine environment: A critical overview. Trac-Trend Anal Chem. 2019;111:252–60.
73. Wang W, Wang J. Different partition of polycyclic aromatic hydrocarbon on environmental particulates in freshwater: Microplastics in comparison to natural sediment. Ecotoxicol Environ Saf. 2018;147:648–55.
74. Wang Z, Chen M, Zhang L, Wang K, Yu X, Zheng Z, et al. Sorption behaviors of phenanthrene on the microplastics identified in a mariculture farm in Xiangshan Bay, southeastern China. The Science of the total environment. 2018;628-629:1617–26.
75. Zimmermann L, Dierkes G, Ternes TA, Volker C, Wagner M. Benchmarking the in Vitro Toxicity and Chemical Composition of Plastic Consumer Products. Environmental science & technology. 2019;53(19):11467–77.
76. Mahmoud Zaghloul MY, Yousry Zaghloul MM, Yousry Zaghloul MM. Developments in polyester composite materials – An in-depth review on natural fibres and nano fillers. Composite Structures. 2021;278:114698.
77. La Mantia FP, Morreale M. Green composites: A brief review. Composites Part A: Applied Science and Manufacturing. 2011;42(6):579–88.
78. Froggett SJ, Clancy SF, Boverhof DR, Canady RA. A review and perspective of existing research on the release of nanomaterials from solid nanocomposites. Particle and Fibre Toxicology. 2014;11(1):17.
79. Lau O-W, Wong S-K. Contamination in food from packaging material. J Chromatogr A. 2000;882(1):255–70.
80. Mohamed Nor NH, Kooi M, Diepens NJ, Koelmans AA. Lifetime Accumulation of Microplastic in Children and Adults. Environmental science & technology. 2021;55(8):5084–96.
81. Li P, Li Q, Lai Y, Yang S, Yu S, Liu R, et al. Direct entry of micro(nano)plastics into human blood circulatory system by intravenous infusion. iScience. 2023;26(12):108454.
82. Huang T, Liu Y, Wang L, Ruan X, Ge Q, Ma M, et al. MPs Entering Human Circulation through Infusions: A Significant Pathway and Health Concern. Environment & Health. 2025;3(5):551–9.
83. Devane PA, Bourne RB, Rorabeck CH, Hardie RM, Horne JG. Measurement of polyethylene wear in metal-backed acetabular cups. I. Three-dimensional technique. Clin Orthop Relat Res. 1995(319):303–16.
84. Nich C, Goodman SB. Role of macrophages in the biological reaction to wear debris from joint replacements. J Long Term Eff Med Implants. 2014;24(4):259–65.
85. Airborne microplastics: Consequences to human health?, (2018).
86. Alzona J, Cohen BL, Rudolph H, Jow HN, Frohliger JO. Indoor-outdoor relationships for airborne particulate matter of outdoor origin. Atmospheric Environment (1967). 1979;13(1):55–60.
87. Brown JS, Gordon T, Price O, Asgharian B. Thoracic and respirable particle definitions for human health risk assessment. Part Fibre Toxicol. 2013;10:12.

88. Asgharian B, Owen TP, Kuempel ED, Jarabek AM. Dosimetry of inhaled elongate mineral particles in the respiratory tract: The impact of shape factor. Toxicol Appl Pharmacol. 2018;361:27–35.
89. Dris R, Gasperi J, Mirande C, Mandin C, Guerrouache M, Langlois V, et al. A first overview of textile fibers, including microplastics, in indoor and outdoor environments. Environmental pollution. 2017;221:453–8.
90. Möller W, Häussinger K, Winkler-Heil R, Stahlhofen W, Meyer T, Hofmann W, et al. Mucociliary and long-term particle clearance in the airways of healthy nonsmoker subjects. J Appl Physiol (1985). 2004;97(6):2200–6.
91. Möller W, Häussinger K, Ziegler-Heitbrock L, Heyder J. Mucociliary and long-term particle clearance in airways of patients with immotile cilia. Respir Res. 2006;7(1):10.
92. Bennett WD, Wu J, Fuller F, Balcazar JR, Zeman KL, Duckworth H, et al. Duration of action of hypertonic saline on mucociliary clearance in the normal lung. J Appl Physiol (1985). 2015;118(12):1483–90.
93. Fry FA, Black A. Regional deposition and clearance of particles in the human nose. Journal of Aerosol Science. 1973;4(2):113–24.
94. Rist S, Carney Almroth B, Hartmann NB, Karlsson TM. A critical perspective on early communications concerning human health aspects of microplastics. Science of The Total Environment. 2018;626:720–6.
95. Catarino AI, Macchia V, Sanderson WG, Thompson RC, Henry TB. Low levels of microplastics (MP) in wild mussels indicate that MP ingestion by humans is minimal compared to exposure via household fibres fallout during a meal. Environmental pollution. 2018;237:675–84.
96. Noorimotlagh Z, Hopke PK, Mirzaee SA. A systematic review of airborne microplastics emissions as emerging contaminants in outdoor and indoor air environments. Emerging Contaminants. 2024;10(4):100372.
97. Vianello A, Jensen RL, Liu L, Vollertsen J. Simulating human exposure to indoor airborne microplastics using a Breathing Thermal Manikin. Scientific reports. 2019;9(1):8670.
98. Schwabl P. Microplastics in hot water. Nature Food. 2020;1(11):671–2.
99. Zimmermann L, Geueke B, Parkinson LV, Schür C, Wagner M, Muncke J. Food contact articles as source of micro- and nanoplastics: a systematic evidence map. npj Science of Food. 2025;9(1):111.
100. He Y-J, Qin Y, Zhang T-L, Zhu Y-Y, Wang Z-J, Zhou Z-S, et al. Migration of (non-) intentionally added substances and microplastics from microwavable plastic food containers. J Hazard Mater. 2021;417:126074.
101. Jin T, Liu Y, Lyu H, He Y, Sun H, Tang J, et al. Plastic takeaway food containers may cause human intestinal damage in routine life usage: Microplastics formation and cytotoxic effect. J Hazard Mater. 2024;475:134866.
102. Chae Y, Kim D, Kim SW, An Y-J. Trophic transfer and individual impact of nano-sized polystyrene in a four-species freshwater food chain. Scientific reports. 2018;8(1):284.
103. Cole M, Lindeque P, Fileman E, Halsband C, Goodhead R, Moger J, et al. Microplastic ingestion by zooplankton. Environmental science & technology. 2013;47(12):6646–55.
104. Khan A, Qadeer A, Wajid A, Ullah Q, Rahman SU, Ullah K, et al. Microplastics in animal nutrition: Occurrence, spread, and hazard in animals. Journal of Agriculture and Food Research. 2024;17:101258.
105. Beriot N, Peek J, Zornoza R, Geissen V, Huerta Lwanga E. Low density-microplastics detected in sheep faeces and soil: A case study from the intensive vegetable farming in Southeast Spain. Science of The Total Environment. 2021;755:142653.

106. Potential Health Impact of Environmentally Released Micro- and Nanoplastics in the Human Food Production Chain: Experiences from Nanotoxicology, (2015).
107. Oliveri Conti G, Ferrante M, Banni M, Favara C, Nicolosi I, Cristaldi A, et al. Micro- and nanoplastics in edible fruit and vegetables. The first diet risks assessment for the general population. Environ Res. 2020;187:109677.
108. Liebezeit G, Liebezeit E. Origin of synthetic particles in honeys. Polish Journal of Food and Nutrition Sciences. 2015.
109. Kosuth M, Mason SA, Wattenberg EV. Anthropogenic contamination of tap water, beer, and sea salt. PloS one. 2018;13(4):e0194970.
110. Davidson K, Dudas SE. Microplastic Ingestion by Wild and Cultured Manila Clams (Venerupis philippinarum) from Baynes Sound, British Columbia. Archives of Environmental Contamination and Toxicology. 2016.
111. Akhbarizadeh R, Moore F, Keshavarzi B. Investigating a probable relationship between microplastics and potentially toxic elements in fish muscles from northeast of Persian Gulf. Environmental pollution. 2018.
112. Liebezeit G, Liebezeit E. Synthetic particles as contaminants in German beers. Food additives & contaminants Part A, Chemistry, analysis, control, exposure & risk assessment. 2014;31(9):1574–8.
113. Mason SA, Welch VG, Neratko J. Synthetic Polymer Contamination in Bottled Water. Frontiers in Chemistry. 2018.
114. Duncan TV, Khan SA, Patri AK, Wiggins S. Regulatory Science Perspective on the Analysis of Microplastics and Nanoplastics in Human Food. Anal Chem. 2024;96(11):4343–58.
115. Cox KD, Covernton GA, Davies HL, Dower JF, Juanes F, Dudas SE. Human Consumption of Microplastics. Environmental science & technology. 2019;53(12):7068–74.
116. Domenech J, Marcos R. Pathways of human exposure to microplastics, and estimation of the total burden. Current Opinion in Food Science. 2021;39:144–51.
117. Senathirajah K, Attwood S, Bhagwat G, Carbery M, Wilson S, Palanisami T. Estimation of the mass of microplastics ingested – A pivotal first step towards human health risk assessment. J Hazard Mater. 2021;404:124004.
118. Koelmans AA, Redondo-Hasselerharm PE, Mohamed Nor NH, Kooi M. Solving the Nonalignment of Methods and Approaches Used in Microplastic Research to Consistently Characterize Risk. Environmental science & technology. 2020;54(19):12307–15.
119. Vela L, Villacorta A, Venus T, Estrela-Lopis I, Pastor S, García-Rodriguez A, et al. The potential effects of in vitro digestion on the physicochemical and biological characteristics of polystyrene nanoplastics. Environmental pollution. 2023;329:121656.
120. Liu S, Wu X, Gu W, Yu J, Wu B. Influence of the digestive process on intestinal toxicity of polystyrene microplastics as determined by in vitro Caco-2 models. Chemosphere. 2020;256:127204.
121. DeLoid GM, Cao X, Coreas R, Bitounis D, Singh D, Zhong W, et al. Incineration-Generated Polyethylene Micro-Nanoplastics Increase Triglyceride Lipolysis and Absorption in an In Vitro Small Intestinal Epithelium Model. Environmental science & technology. 2022;56(17):12288–97.
122. Madara J. The functional morphology of the mucosa of the small intestine. Physiology of the gastrointestinal tract. 1994:1577–622.
123. Selective permeability of mucus barriers, (2018).
124. Witten J, Ribbeck K. The particle in the spider's web: Transport through biological hydrogels. Nanoscale. 2017.

125. Xu Q, Ensign LM, Boylan NJ, Schön A, Gong X, Yang J-C, et al. Impact of Surface Polyethylene Glycol (PEG) Density on Biodegradable Nanoparticle Transport in Mucus ex Vivo and Distribution in Vivo. ACS nano. 2015;9(9):9217–27.
126. Lai SK, O'Hanlon DE, Harrold S, Man ST, Wang YY, Cone R, et al. Rapid transport of large polymeric nanoparticles in fresh undiluted human mucus. Proceedings of the National Academy of Sciences of the United States of America. 2007;104(5):1482–7.
127. Behrens I, Pena AI, Alonso MJ, Kissel T. Comparative uptake studies of bioadhesive and non-bioadhesive nanoparticles in human intestinal cell lines and rats: the effect of mucus on particle adsorption and transport. Pharmaceutical research. 2002;19(8):1185–93.
128. Carlson TL, Lock JY, Carrier RL. Engineering the Mucus Barrier. Annual Review of Biomedical Engineering. 2018;20(Volume 20, 2018):197–220.
129. Lehr C-M, Poelma FGJ, Junginger HE, Tukker JJ. An estimate of turnover time of intestinal mucus gel layer in the rat in situ loop. Int J Pharm. 1991;70(3):235–40.
130. Presence of microplastics and nanoplastics in food, with particular focus on seafood. EFSA Journal. 2016.
131. Hillyer JF, Albrecht RM. Gastrointestinal persorption and tissue distribution of differently sized colloidal gold nanoparticles. Journal of Pharmaceutical Sciences. 2001.
132. Volkheimer G. Passage of particles through the wall of the gastrointestinal tract. Environmental Health Perspectives. 1974.
133. Powell JJ, Faria N, Thomas-McKay E, Pele LC. Origin and fate of dietary nanoparticles and microparticles in the gastrointestinal tract. Journal of Autoimmunity. 2010.
134. Cornes JS. Number, size, and distribution of Peyer's patches in the human small intestine: Part I The development of Peyer's patches. Gut. 1965;6(3):225–9.
135. Rolo D, Assunção R, Ventura C, Alvito P, Gonçalves L, Martins C, et al. Adverse Outcome Pathways Associated with the Ingestion of Titanium Dioxide Nanoparticles-A Systematic Review. Nanomaterials (Basel). 2022;12(19).
136. McGuckin MA, Lindén SK, Sutton P, Florin TH. Mucin dynamics and enteric pathogens. Nature Reviews Microbiology. 2011;9(4):265–78.
137. Ermund A, Schütte A, Johansson MEV, Gustafsson JK, Hansson GC. Studies of mucus in mouse stomach, small intestine, and colon. I. Gastrointestinal mucus layers have different properties depending on location as well as over the Peyer's patches. American Journal of Physiology - Gastrointestinal and Liver Physiology. 2013.
138. Rouch JD, Scott A, Lei NY, Solorzano-Vargas RS, Wang J, Hanson EM, et al. Development of functional microfold (M) cells from intestinal stem cells in primary human enteroids. PloS one. 2016.
139. Jani P, Halbert GW, Langridge J, Florence AT. Nanoparticle uptake by the rat gastrointestinal mucosa: quantitation and particle size dependency. The Journal of pharmacy and pharmacology. 1990;42(12):821–6.
140. Walczak AP, Hendriksen PJ, Woutersen RA, van der Zande M, Undas AK, Helsdingen R, et al. Bioavailability and biodistribution of differently charged polystyrene nanoparticles upon oral exposure in rats. J Nanopart Res. 2015;17(5):231.
141. Kvietys PR, Granger DN. Role of intestinal lymphatics in interstitial volume regulation and transmucosal water transport. Ann N Y Acad Sci. 2010;1207 Suppl 1(Suppl 1):E29–43.
142. Sarin H. Physiologic upper limits of pore size of different blood capillary types and another perspective on the dual pore theory of microvascular permeability. J Angiogenes Res. 2010;2:14.

143. Steiniger BS, Pfeffer H, Gaffling S, Lobachev O. The human splenic microcirculation is entirely open as shown by 3D models in virtual reality. Scientific reports. 2022;12(1):16487.
144. Keinanen O, Dayts EJ, Rodriguez C, Sarrett SM, Brennan JM, Sarparanta M, et al. Harnessing PET to track micro- and nanoplastics in vivo. Scientific reports. 2021;11(1):11463.
145. Delaney S, Rodriguez C, Sarrett SM, Dayts EJ, Zeglis BM, Keinänen O. Unraveling the in vivo fate of inhaled micro- and nanoplastics with PET imaging. Science of The Total Environment. 2023;904:166320.
146. Zhu GH, Gray ABC, Patra HK. Nanomedicine: controlling nanoparticle clearance for translational success. Trends in Pharmacological Sciences. 2022;43(9):709–11.
147. Jani PU, Nomura T, Yamashita F, Takakura Y, Florence AT, Hashida M. Biliary excretion of polystyrene microspheres with covalently linked FITC fluorescence after oral and parenteral administration to male Wistar rats. Journal of drug targeting. 1996.
148. Zhang Y-N, Poon W, Tavares AJ, McGilvray ID, Chan WCW. Nanoparticle–liver interactions: Cellular uptake and hepatobiliary elimination. J Control Release. 2016;240:332–48.
149. Abdelkhaliq A, van der Zande M, Punt A, Helsdingen R, Boeren S, Vervoort JJM, et al. Impact of nanoparticle surface functionalization on the protein corona and cellular adhesion, uptake and transport. Journal of nanobiotechnology. 2018;16(1):70.
150. Walczak AP, Kramer E, Hendriksen PJ, Helsdingen R, van der Zande M, Rietjens IM, et al. In vitro gastrointestinal digestion increases the translocation of polystyrene nanoparticles in an in vitro intestinal co-culture model. Nanotoxicology. 2015;9(7):886–94.
151. Monopoli MP, Åberg C, Salvati A, Dawson KA. Biomolecular coronas provide the biological identity of nanosized materials. Nature nanotechnology. 2012.
152. Tenzer S, Docter D, Kuharev J, Musyanovych A, Fetz V, Hecht R, et al. Rapid formation of plasma protein corona critically affects nanoparticle pathophysiology. Nature nanotechnology. 2013;8(10):772–81.
153. Monopoli MP, Walczyk D, Campbell A, Elia G, Lynch I, Baldelli Bombelli F, et al. Physical-Chemical aspects of protein corona: Relevance to in vitro and in vivo biological impacts of nanoparticles. J Am Chem Soc. 2011.
154. Walczyk D, Bombelli FB, Monopoli MP, Lynch I, Dawson KA. What the Cell "Sees" in Bionanoscience. J Am Chem Soc. 2010;132(16):5761–8.
155. García-Álvarez R, Vallet-Regí M. Hard and Soft Protein Corona of Nanomaterials: Analysis and Relevance. Nanomaterials (Basel). 2021;11(4).
156. Shannahan JH, Podila R, Aldossari AA, Emerson H, Powell BA, Ke PC, et al. Formation of a Protein Corona on Silver Nanoparticles Mediates Cellular Toxicity via Scavenger Receptors. Toxicological Sciences. 2014;143(1):136–46.
157. Deng F, Kim KS, Moon J, Bae YH. Bile Acid Conjugation on Solid Nanoparticles Enhances ASBT-Mediated Endocytosis and Chylomicron Pathway but Weakens the Transcytosis by Inducing Transport Flow in a Cellular Negative Feedback Loop. Adv Sci (Weinh). 2022:e2201414.
158. Lara S, Perez-Potti A, Herda LM, Adumeau L, Dawson KA, Yan Y. Differential Recognition of Nanoparticle Protein Corona and Modified Low-Density Lipoprotein by Macrophage Receptor with Collagenous Structure. ACS nano. 2018.
159. Lu L, Wan Z, Luo T, Fu Z, Jin Y. Polystyrene microplastics induce gut microbiota dysbiosis and hepatic lipid metabolism disorder in mice. Science of The Total Environment. 2018;631-632:449–58.
160. Walkey CD, Olsen JB, Song F, Liu R, Guo H, Olsen DWH, et al. Protein corona fingerprinting predicts the cellular interaction of gold and silver nanoparticles. ACS nano. 2014.

161. Helma C, Rautenberg M, Gebele D. Nano-Lazar: Read across Predictions for Nanoparticle Toxicities with Calculated and Measured Properties. Front Pharmacol. 2017;8:377.
162. Toropova AP, Toropov AA. Nanomaterials: Quasi-SMILES as a flexible basis for regulation and environmental risk assessment. Sci Total Environ. 2022;823:153747.
163. Walkey CD, Olsen JB, Song F, Liu R, Guo H, Olsen DWH, et al. Protein Corona Fingerprinting Predicts the Cellular Interaction of Gold and Silver Nanoparticles. ACS Nano. 2014;8(3):2439–55.
164. Delon L, Gibson RJ, Prestidge CA, Thierry B. Mechanisms of uptake and transport of particulate formulations in the small intestine. Journal of Controlled Release. 2022;343:584–99.
165. Jiang D-H, Satoh T, Tung SH, Kuo C-C. Sustainable Alternatives to Nondegradable Medical Plastics. ACS Sustainable Chemistry & Engineering. 2022;10(15):4792–806.
166. Behzadi S, Serpooshan V, Tao W, Hamaly MA, Alkawareek MY, Dreaden EC, et al. Cellular uptake of nanoparticles: journey inside the cell. Chem Soc Rev. 2017;46(14):4218–44.
167. Buzea C, Pacheco, II, Robbie K. Nanomaterials and nanoparticles: sources and toxicity. Biointerphases. 2007;2(4):Mr17–71.
168. Bouwmeester H, Dekkers S, Noordam MY, Hagens WI, Bulder AS, de Heer C, et al. Review of health safety aspects of nanotechnologies in food production. Regul Toxicol Pharmacol. 2009;53(1):52–62.
169. Lewinski N, Colvin V, Drezek R. Cytotoxicity of nanoparticles. Small. 2008;4(1):26–49.
170. Schmid O, Stoeger T. Surface area is the biologically most effective dose metric for acute nanoparticle toxicity in the lung. Journal of Aerosol Science. 2016;99:133–43.
171. Khan FR, Clark N, Xu EG. Micro(nano)plastics in the fish gastrointestinal tract: A mini review and relevance to One Health perspective. Current Opinion in Environmental Science & Health. 2025;46:100645.
172. Toussaint B, Raffael B, Angers-Loustau A, Gilliland D, Kestens V, Petrillo M, et al. Review of micro- and nanoplastic contamination in the food chain. Food additives & contaminants Part A, Chemistry, analysis, control, exposure & risk assessment. 2019;36(5):639–73.
173. Oliveira M, Ribeiro A, Hylland K, Guilhermino L. Single and combined effects of microplastics and pyrene on juveniles (0+group) of the common goby Pomatoschistus microps (Teleostei, Gobiidae). Ecol Indic. 2013;34:641–7.
174. Oliveira M, Ribeiro A, Guilhermino L. Effects of short-term exposure to microplastics and pyrene on Pomatoschistus microps (Teleostei, Gobiidae). Comparative Biochemistry and Physiology Part A: Molecular & Integrative Physiology. 2012;163:S20.
175. Ribeiro F, Garcia AR, Pereira BP, Fonseca M, Mestre NC, Fonseca TG, et al. Microplastics effects in Scrobicularia plana. Marine pollution bulletin. 2017;122(1):379–91.
176. Lu Y, Zhang Y, Deng Y, Jiang W, Zhao Y, Geng J, et al. Uptake and Accumulation of Polystyrene Microplastics in Zebrafish (Danio rerio) and Toxic Effects in Liver. Environmental Science and Technology. 2016.
177. Chen Q, Gundlach M, Yang S, Jiang J, Velki M, Yin D, et al. Quantitative investigation of the mechanisms of microplastics and nanoplastics toward zebrafish larvae locomotor activity. Science of the Total Environment. 2017.
178. Mattsson K, Ekvall MT, Hansson LA, Linse S, Malmendal A, Cedervall T. Altered behavior, physiology, and metabolism in fish exposed to polystyrene nanoparticles. Environmental Science and Technology. 2015.
179. Pitt JA, Kozal JS, Jayasundara N, Massarsky A, Trevisan R, Geitner N, et al. Uptake, tissue distribution, and toxicity of polystyrene nanoparticles in developing zebrafish (Danio rerio). Aquatic Toxicology. 2018.

180. Cong Y, Jin F, Tian M, Wang J, Shi H, Wang Y, et al. Ingestion, egestion and post-exposure effects of polystyrene microspheres on marine medaka (Oryzias melastigma). Chemosphere. 2019.
181. Park EJ, Han JS, Park EJ, Seong E, Lee GH, Kim DW, et al. Repeated-oral dose toxicity of polyethylene microplastics and the possible implications on reproduction and development of the next generation. Toxicol Lett. 2020;324:75–85.
182. Li B, Ding Y, Cheng X, Sheng D, Xu Z, Rong Q, et al. Polyethylene microplastics affect the distribution of gut microbiota and inflammation development in mice. Chemosphere. 2020;244:125492.
183. Zhang Z, Chen W, Chan H, Peng J, Zhu P, Li J, et al. Polystyrene microplastics induce size-dependent multi-organ damage in mice: Insights into gut microbiota and fecal metabolites. J Hazard Mater. 2024;461:132503.
184. Xiao J, Jiang X, Zhou Y, Sumayyah G, Zhou L, Tu B, et al. Results of a 30-day safety assessment in young mice orally exposed to polystyrene nanoparticles. Environmental pollution. 2022;292:118184.
185. Jing J, Zhang L, Han L, Wang J, Zhang W, Liu Z, et al. Polystyrene micro-/nanoplastics induced hematopoietic damages via the crosstalk of gut microbiota, metabolites, and cytokines. Environ Int. 2022;161:107131.
186. Sun R, Xu K, Yu L, Pu Y, Xiong F, He Y, et al. Preliminary study on impacts of polystyrene microplastics on the hematological system and gene expression in bone marrow cells of mice. Ecotox Environ Safe. 2021;218:112296.
187. Mu Y, Sun J, Li Z, Zhang W, Liu Z, Li C, et al. Activation of pyroptosis and ferroptosis is involved in the hepatotoxicity induced by polystyrene microplastics in mice. Chemosphere. 2022;291:132944.
188. Deng Y, Zhang Y, Lemos B, Ren H. Tissue accumulation of microplastics in mice and biomarker responses suggest widespread health risks of exposure. Scientific reports. 2017.
189. Hou J, Lei Z, Cui L, Hou Y, Yang L, An R, et al. Polystyrene microplastics lead to pyroptosis and apoptosis of ovarian granulosa cells via NLRP3/Caspase-1 signaling pathway in rats. Ecotoxicol Environ Saf. 2021;212:112012.
190. Prata JC, da Costa JP, Lopes I, Duarte AC, Rocha-Santos T. Environmental exposure to microplastics: An overview on possible human health effects. The Science of the total environment. 2020;702:134455.
191. Toxicity of Microplastics and Nanoplastics in Mammalian Systems, (2020).
192. Rawle DJ, Dumenil T, Tang B, Bishop CR, Yan K, Le TT, et al. Microplastic consumption induces inflammatory signatures in the colon and prolongs a viral arthritis. Science of The Total Environment. 2022;809:152212.
193. Schwarzfischer M, Niechcial A, Lee SS, Sinnet B, Wawrzyniak M, Laimbacher A, et al. Ingested nano- and microsized polystyrene particles surpass the intestinal barrier and accumulate in the body. NanoImpact. 2022;25:100374.
194. Rafiee M, Dargahi L, Eslami A, Beirami E, Jahangiri-rad M, Sabour S, et al. Neurobehavioral assessment of rats exposed to pristine polystyrene nanoplastics upon oral exposure. Chemosphere. 2018.
195. Jani P, Halbert GW, Langridge J, Florence AT. The Uptake and Translocation of Latex Nanospheres and Microspheres after Oral Administration to Rats. Journal of Pharmacy and Pharmacology. 1989.
196. Abbasi S, Turner A. Human exposure to microplastics: A study in Iran. J Hazard Mater. 2021;403:123799.

197. Horvatits T, Tamminga M, Liu B, Sebode M, Carambia A, Fischer L, et al. Microplastics detected in cirrhotic liver tissue. eBioMedicine. 2022;82:104147.
198. Zhu L, Zhu J, Zuo R, Xu Q, Qian Y, An L. Identification of microplastics in human placenta using laser direct infrared spectroscopy. Science of The Total Environment. 2023;856:159060.
199. Jenner LC, Rotchell JM, Bennett RT, Cowen M, Tentzeris V, Sadofsky LR. Detection of microplastics in human lung tissue using μFTIR spectroscopy. Science of The Total Environment. 2022;831:154907.
200. Kremer AM, Pal TM, Boleij JS, Schouten JP, Rijcken B. Airway hyperresponsiveness, prevalence of chronic respiratory symptoms, and lung function in workers exposed to irritants. Occupational and Environmental Medicine. 1994;51(1):3.
201. Eschenbacher WL, Kreiss K, Lougheed MD, Pransky GS, Day B, Castellan RM. Nylon flock-associated interstitial lung disease. Am J Respir Crit Care Med. 1999;159(6):2003–8.
202. Yan Z, Liu Y, Zhang T, Zhang F, Ren H, Zhang Y. Analysis of Microplastics in Human Feces Reveals a Correlation between Fecal Microplastics and Inflammatory Bowel Disease Status. Environmental science & technology. 2022;56(1):414–21.
203. Wu D, Feng Y, Wang R, Jiang J, Guan Q, Yang X, et al. Pigment microparticles and microplastics found in human thrombi based on Raman spectral evidence. Journal of Advanced Research. 2023;49:141–50.
204. Dong C-D, Chen C-W, Chen Y-C, Chen H-H, Lee J-S, Lin C-H. Polystyrene microplastic particles: In vitro pulmonary toxicity assessment. J Hazard Mater. 2020;385:121575.
205. He Y, Li J, Chen J, Miao X, Li G, He Q, et al. Cytotoxic effects of polystyrene nanoplastics with different surface functionalization on human HepG2 cells. The Science of the total environment. 2020;723:138180.
206. Stock V, Bohmert L, Lisicki E, Block R, Cara-Carmona J, Pack LK, et al. Uptake and effects of orally ingested polystyrene microplastic particles in vitro and in vivo. Archives of toxicology. 2019;93(7):1817–33.
207. Poma A, Vecchiotti G, Colafarina S, Zarivi O, Aloisi M, Arrizza L, et al. In Vitro Genotoxicity of Polystyrene Nanoparticles on the Human Fibroblast Hs27 Cell Line. Nanomaterials (Basel). 2019;9(9).
208. Rubio L, Barguilla I, Domenech J, Marcos R, Hernández A. Biological effects, including oxidative stress and genotoxic damage, of polystyrene nanoparticles in different human hematopoietic cell lines. J Hazard Mater. 2020.
209. Fuchs A-K, Syrovets T, Haas KA, Loos C, Musyanovych A, Mailänder V, et al. Carboxyl- and amino-functionalized polystyrene nanoparticles differentially affect the polarization profile of M1 and M2 macrophage subsets. Biomaterials. 2016;85:78–87.
210. Weber A, Schwiebs A, Solhaug H, Stenvik J, Nilsen AM, Wagner M, et al. Nanoplastics affect the inflammatory cytokine release by primary human monocytes and dendritic cells. Environ Int. 2022;163:107173.
211. Busch M, Bredeck G, Waag F, Rahimi K, Ramachandran H, Bessel T, et al. Assessing the NLRP3 Inflammasome Activating Potential of a Large Panel of Micro- and Nanoplastics in THP-1 Cells. Biomolecules. 2022;12(8).
212. Busch M, Bredeck G, Kampfer AAM, Schins RPF. Investigations of acute effects of polystyrene and polyvinyl chloride micro- and nanoplastics in an advanced in vitro triple culture model of the healthy and inflamed intestine. Environ Res. 2021;193:110536.
213. Visalli G, Facciolà A, Pruiti Ciarello M, De Marco G, Maisano M, Di Pietro A. Acute and Sub-Chronic Effects of Microplastics (3 and 10 μm) on the Human Intestinal Cells HT-29. International Journal of Environmental Research and Public Health. 2021;18(11):5833.

214. Gautam RK, Laltanpuia, Singh N, Kushwaha S. A particle of concern: explored and proposed underlying mechanisms of microplastic-induced lung damage and pulmonary fibrosis. Inhal Toxicol. 2025;37(1):1–17.
215. Djouina M, Waxin C, Dubuquoy L, Launay D, Vignal C, Body-Malapel M. Oral exposure to polyethylene microplastics induces inflammatory and metabolic changes and promotes fibrosis in mouse liver. Ecotox Environ Safe. 2023;264:115417.
216. Russo RC, Garcia CC, Teixeira MM, Amaral FA. The CXCL8/IL-8 chemokine family and its receptors in inflammatory diseases. Expert Review of Clinical Immunology. 2014;10(5):593–619.
217. Alhendi A, Naser SA. The dual role of interleukin-6 in Crohn's disease pathophysiology. Front Immunol. 2023;14:1295230.
218. Chen Q, Li J, Pan Z, Meng J, Li J. Significant increase in reactive oxygen species induced by metal deposition on microplastic surfaces: A case study involving lead and enrofloxacin. Chemical Engineering Journal. 2025;506:159783.
219. Lerchner T, Jedlička J, Kripnerová M, Dejmek J, Kuncová J. Influence of micro- and nanoplastics on mitochondrial function in the cardiovascular system: a review of the current literature. Physiol Res. 2024;73(S3):S685–s95.
220. Zorov DB, Filburn CR, Klotz LO, Zweier JL, Sollott SJ. Reactive oxygen species (ROS)-induced ROS release: a new phenomenon accompanying induction of the mitochondrial permeability transition in cardiac myocytes. J Exp Med. 2000;192(7):1001–14.
221. Lehner R, Weder C, Petri-Fink A, Rothen-Rutishauser B. Emergence of Nanoplastic in the Environment and Possible Impact on Human Health. Environmental science & technology. 2019;53(4):1748–65.
222. Domenech J, Annangi B, Marcos R, Hernández A, Catalán J. Insights into the potential carcinogenicity of micro- and nano-plastics. Mutat Res Rev Mutat Res. 2023;791:108453.
223. Danopoulos E, Twiddy M, West R, Rotchell JM. A rapid review and meta-regression analyses of the toxicological impacts of microplastic exposure in human cells. J Hazard Mater. 2022;427:127861.
224. Krewski D, Acosta D, Jr., Andersen M, Anderson H, Bailar JC, 3rd, Boekelheide K, et al. Toxicity testing in the 21st century: a vision and a strategy. J Toxicol Environ Health B Crit Rev. 2010;13(2-4):51–138.
225. Sambuy Y, De Angelis I, Ranaldi G, Scarino ML, Stammati A, Zucco F. The Caco-2 cell line as a model of the intestinal barrier: influence of cell and culture-related factors on Caco-2 cell functional characteristics. Cell Biol Toxicol. 2005;21(1):1–26.
226. Gullberg E, Leonard M, Karlsson J, Hopkins AM, Brayden D, Baird AW, et al. Expression of specific markers and particle transport in a new human intestinal M-cell model. Biochem Biophys Res Commun. 2000;279(3):808–13.
227. Altman BJ, Stine ZE, Dang CV. From Krebs to clinic: glutamine metabolism to cancer therapy. Nat Rev Cancer. 2016;16(10):619–34.
228. Liberti MV, Locasale JW. The Warburg Effect: How Does it Benefit Cancer Cells? Trends Biochem Sci. 2016;41(3):211–8.
229. Saunier E, Antonio S, Regazzetti A, Auzeil N, Laprévote O, Shay JW, et al. Resveratrol reverses the Warburg effect by targeting the pyruvate dehydrogenase complex in colon cancer cells. Scientific reports. 2017;7(1):6945.
230. Ma Y, Koh JYC, Lim HK, Shi P, Tay CY. Elucidating the Size-Dependency of In Vitro Digested Polystyrene Microplastics on Human Intestinal Cells Health and Function. Macromolecular Chemistry and Physics. 2022;223(13):2100454.

231. Grouls M, van der Zande M, de Haan L, Bouwmeester H. Responses of increasingly complex intestinal epithelium in vitro models to bacterial toll-like receptor agonists. Toxicology in Vitro. 2022;79:105280.
232. Langerholc T, Maragkoudakis PA, Wollgast J, Gradisnik L, Cencic A. Novel and established intestinal cell line models - An indispensable tool in food science and nutrition. Trends Food Sci Technol. 2011;22:S11–s20.
233. Hwang J, Choi D, Han S, Choi J, Hong J. An assessment of the toxicity of polypropylene microplastics in human derived cells. The Science of the total environment. 2019;684:657–69.
234. Martin L, Simpson K, Brzezinski M, Watt J, Xu W. Cellular response of keratinocytes to the entry and accumulation of nanoplastic particles. Part Fibre Toxicol. 2024;21(1):22.
235. Adamiak K, Sidoryk-Węgrzynowicz M, Dąbrowska-Bouta B, Sulkowski G, Strużyńska L. Primary astrocytes as a cellular depot of polystyrene nanoparticles. Scientific reports. 2025;15(1):6502.
236. Janssen AWF, Duivenvoorde LPM, Rijkers D, Nijssen R, Peijnenburg AACM, van der Zande M, et al. Cytochrome P450 expression, induction and activity in human induced pluripotent stem cell-derived intestinal organoids and comparison with primary human intestinal epithelial cells and Caco-2 cells. Archives of toxicology. 2020.
237. Janssen AWF, van der Lugt B, Duivenvoorde LPM, Vos AP, Bastiaan-Net S, Tomassen MMM, et al. Comparison of iPSC-derived human intestinal epithelial cells with Caco-2 cells and human in vivo data after exposure to Lactiplantibacillus plantarum WCFS1. Scientific reports. 2024;14(1):26464.
238. Takayama K, Negoro R, Yamashita T, Kawai K, Ichikawa M, Mori T, et al. Generation of Human iPSC–Derived Intestinal Epithelial Cell Monolayers by CDX2 Transduction. Cellular and Molecular Gastroenterology and Hepatology. 2019;8(3):513–26.
239. Takenaka T, Harada N, Kuze J, Chiba M, Iwao T, Matsunaga T. Application of a Human Intestinal Epithelial Cell Monolayer to the Prediction of Oral Drug Absorption in Humans as a Superior Alternative to the Caco-2 Cell Monolayer. Journal of Pharmaceutical Sciences. 2016;105(2):915–24.
240. Negoro R, Takayama K, Kawai K, Harada K, Sakurai F, Hirata K, et al. Efficient Generation of Small Intestinal Epithelial-like Cells from Human iPSCs for Drug Absorption and Metabolism Studies. Stem Cell Reports. 2018;11(6):1539–50.
241. Rietjens IM, Louisse J, Punt A. Tutorial on physiologically based kinetic modeling in molecular nutrition and food research. Mol Nutr Food Res. 2011;55(6):941–56.
242. Punt A, Pinckaers N, Peijnenburg A, Louisse J. Development of a Web-Based Toolbox to Support Quantitative In-Vitro-to-In-Vivo Extrapolations (QIVIVE) within Nonanimal Testing Strategies. Chem Res Toxicol. 2021.
243. Physiologically based pharmacokinetic modeling of nanoparticles, (2010).
244. Bachler G, Von Goetz N, Hungerbuhler K. Using physiologically based pharmacokinetic (PBPK) modeling for dietary risk assessment of titanium dioxide (TiO2) nanoparticles. Nanotoxicology. 2015.
245. Chen C-Y, Kamineni VN, Lin Z. A physiologically based toxicokinetic model for microplastics and nanoplastics in mice after oral exposure and its implications for human dietary exposure assessment. J Hazard Mater. 2024;480:135922.
246. Lin Z, Monteiro-Riviere NA, Riviere JE. A physiologically based pharmacokinetic model for polyethylene glycol-coated gold nanoparticles of different sizes in adult mice. Nanotoxicology. 2016.

247. Gakis GP, Krikas A, Neofytou P, Tran L, Charitidis C. Modelling the biodistribution of inhaled gold nanoparticles in rats with interspecies extrapolation to humans. Toxicol Appl Pharm. 2022;457:116322.
248. de Souza Machado AA, Kloas W, Zarfl C, Hempel S, Rillig MC. Microplastics as an emerging threat to terrestrial ecosystems. Glob Chang Biol. 2018;24(4):1405–16.
249. EFSA. Statement on the presence of microplastics and nanoplastics in food, with particular focus on seafood. EFSA Journal. 2016;14(6):4501.
250. Enfrin M, Lee J, Gibert Y, Basheer F, Kong L, Dumée LF. Release of hazardous nanoplastic contaminants due to microplastics fragmentation under shear stress forces. J Hazard Mater. 2020;384:121393.
251. Cai Y, Mitrano DM, Hufenus R, Nowack B. Formation of Fiber Fragments during Abrasion of Polyester Textiles. Environ Sci Technol. 2021;55(12):8001–9.
252. Järlskog I, Jaramillo-Vogel D, Rausch J, Gustafsson M, Strömvall A-M, Andersson-Sköld Y. Concentrations of tire wear microplastics and other traffic-derived non-exhaust particles in the road environment. Environ Int. 2022;170:107618.
253. Schwaferts C, Niessner R, Elsner M, Ivleva NP. Methods for the analysis of submicrometer- and nanoplastic particles in the environment. Trends Analyt Chem. 2019;112:52–65.
254. Zhang J, Wang L, Kannan K. Microplastics in house dust from 12 countries and associated human exposure. Environ Int. 2020;134:105314.
255. Yao Y, Glamoclija M, Murphy A, Gao Y. Characterization of microplastics in indoor and ambient air in northern New Jersey. Environ Res. 2022;207:112142.
256. Van Cauwenberghe L, Janssen CR. Microplastics in bivalves cultured for human consumption. Environmental pollution. 2014;193:65–70.
257. Davidson K, Dudas SE. Microplastic Ingestion by Wild and Cultured Manila Clams (Venerupis philippinarum) from Baynes Sound, British Columbia. Arch Environ Contam Toxicol. 2016;71(2):147–56.
258. Kershaw PJ, Rochman CM. Sources, fate and effects of microplastics in the marine environment: part 2 of a global assessment. Reports and studies - IMO/FAO/Unesco-IOC/WMO/IAEA/UN/UNEP Joint Group of Experts on the Scientific Aspects of Marine Environmental Protection (GESAMP) eng no 93. 2015.
259. Liebezeit G, Liebezeit E. Origin of Synthetic Particles in Honeys. Pol J Food Nutr Sci. 2015;65(2):143–7.
260. Mason SA, Welch VG, Neratko J. Synthetic Polymer Contamination in Bottled Water. Front Chem. 2018;6:407.
261. Felipe-Rodriguez M, Bohm G, Doran R. What does the public think about microplastics? Insights from an empirical analysis of mental models elicited through free associations. Front Psychol. 2022;13:920454.
262. Coffin S, Bouwmeester H, Brander S, Damdimopoulou P, Gouin T, Hermabessiere L, et al. Development and application of a health-based framework for informing regulatory action in relation to exposure of microplastic particles in California drinking water. Microplast nanoplast. 2022;2(1):12.
263. Busch M, Kämpfer AAM, Schins RPF. An inverted in vitro triple culture model of the healthy and inflamed intestine: Adverse effects of polyethylene particles. Chemosphere. 2021;284:131345.
264. Magrì D, Veronesi M, Sánchez-Moreno P, Tolardo V, Bandiera T, Pompa PP, et al. PET nanoplastics interactions with water contaminants and their impact on human cells. Environ Pollut. 2021;271:116262.

265. Sun M, Ding R, Ma Y, Sun Q, Ren X, Sun Z, et al. Cardiovascular toxicity assessment of polyethylene nanoplastics on developing zebrafish embryos. Chemosphere. 2021;282:131124.
266. Gopinath PM, Twayana KS, Ravanan P, John T, Mukherjee A, Jenkins DF, et al. Prospects on the nano-plastic particles internalization and induction of cellular response in human keratinocytes. Part Fibre Toxicol. 2021;18(1):35.
267. Roursgaard M, Hezareh Rothmann M, Schulte J, Karadimou I, Marinelli E, Møller P. Genotoxicity of Particles From Grinded Plastic Items in Caco-2 and HepG2 Cells. Front Public Health. 2022;10.
268. Karbalaei S, Hanachi P, Walker TR, Cole M. Occurrence, sources, human health impacts and mitigation of microplastic pollution. Environ Sci Pollut Res Int. 2018;25(36):36046–63.
269. Gouin T, Ellis-Hutchings R, Thornton Hampton LM, Lemieux CL, Wright SL. Screening and prioritization of nano- and microplastic particle toxicity studies for evaluating human health risks - development and application of a toxicity study assessment tool. Microplast nanoplast. 2022;2(1):2.
270. Jani P, Halbert GW, Langridge J, Florence AT. The Uptake and Translocation of Latex Nanospheres and Microspheres after Oral Administration to Rats. J Pharm Pharmacol. 1989;41(12):809–12.
271. Walczak AP, Hendriksen PJM, Woutersen RA, van der Zande M, Undas AK, Helsdingen R, et al. Bioavailability and biodistribution of differently charged polystyrene nanoparticles upon oral exposure in rats. J Nanoparticle Res. 2015;17(5):231.
272. Hsiao T-J, Wang J-D, Yang P-M, Yang P-C, Cheng T-J. Liver Fibrosis in Asymptomatic Polyvinyl Chloride Workers. J Occup Environ Med. 2004;46(9):962–6.
273. Heldaas SS, Langård SL, Andersen A. Incidence of cancer among vinyl chloride and polyvinyl chloride workers. Br J Ind Med. 1984;41(1):25.
274. Mason TJ. Cancer mortality in U.S. counties with plastics and related industries. Environ Health Perspect. 1975;11:79–84.
275. Porter DW, Castranova V, Robinson VA, Hubbs AF, Mercer RR, Scabilloni J, et al. Acute Inflammatory Reaction in Rats after Intratracheal Instillation of Material Collected from a Nylon Flocking Plant. J Toxicol Environ Health A. 1999;57(1):25–45.
276. Warheit DB, Webb TR, Reed KL, Hansen JF, Kennedy GL. Four-week inhalation toxicity study in rats with nylon respirable fibers: rapid lung clearance. Toxicology. 2003;192(2):189–210.
277. Hesterberg TW, McConnell EE, Miiller WC, Hamilton R, Bunn WB. Pulmonary toxicity of inhaled polypropylene fibers in rats. Fundam Appl Toxicol. 1992;19(3):358–66.
278. Hartmann NB, Huffer T, Thompson RC, Hassellov M, Verschoor A, Daugaard AE, et al. Are We Speaking the Same Language? Recommendations for a Definition and Categorization Framework for Plastic Debris. Environ Sci Technol. 2019;53(3):1039–47.
279. Andrady AL, Rajapakse N. Additives and Chemicals in Plastics. In: Takada H, Karapanagioti H, editors. Hazardous Chemicals Associated with Plastics in the Marine Environment The Handbook of Environmental Chemistry. 78: Springer, Cham; 2016.
280. Bouwmeester H, Hollman PC, Peters RJ. Potential Health Impact of Environmentally Released Micro- and Nanoplastics in the Human Food Production Chain: Experiences from Nanotoxicology. Environmental science & technology. 2015;49(15):8932–47.
281. Peters R, de Jong N, de Haan L, Wright S, Bouwmeester H. Release and intestinal translocation of chemicals associated with microplastics in an in vitro human gastrointestinal digestion model. Microplast nanoplast. 2022;2(1):3.
282. Casals E, Pfaller T, Duschl A, Oostingh GJ, Puntes V. Time Evolution of the Nanoparticle Protein Corona. ACS Nano. 2010;4(7):3623–32.

283. Pulido-Reyes G, Leganes F, Fernández-Piñas F, Rosal R. Bio-nano interface and environment: A critical review. Environ Toxicol Chem. 2017;36(12):3181–93.
284. Pistollato F, Madia F, Corvi R, Munn S, Grignard E, Paini A, et al. Current EU regulatory requirements for the assessment of chemicals and cosmetic products: challenges and opportunities for introducing new approach methodologies. Arch Toxicol. 2021;95(6):1867–97.
285. EFSA. Guidance on risk assessment of nanomaterials to be applied in the food and feed chain: human and animal health. EFSA Journal. 2021;19(8):e06768.
286. Hartung T. Toxicology for the twenty-first century. Nature. 2009;460(7252):208–12.
287. Tannenbaum J, Bennett BT. Russell and Burch's 3Rs Then and Now: The Need for Clarity in Definition and Purpose. J Am Assoc Lab Anim Sci. 2015;54(2):120–32.
288. Jones CF, Grainger DW. In vitro assessments of nanomaterial toxicity. Adv Drug Deliv Rev. 2009;61(6):438–56.
289. Fröhlich E. Comparison of conventional and advanced in vitro models in the toxicity testing of nanoparticles. Artif Cells Nanomed Biotechnol. 2018;46:1091–107.
290. Wang M, Lai X, Shao L, Li L. Evaluation of immunoresponses and cytotoxicity from skin exposure to metallic nanoparticles. Int J Nanomedicine. 2018;13:4445–59.
291. Ma Y, McKay DJ, Buttitta L. Changes in chromatin accessibility ensure robust cell cycle exit in terminally differentiated cells. PLoS Biol. 2019;17(9):e3000378.
292. Janssen AWF, Duivenvoorde LPM, Rijkers D, Nijssen R, Peijnenburg AACM, van der Zande M, et al. Cytochrome P450 expression, induction and activity in human induced pluripotent stem cell-derived intestinal organoids and comparison with primary human intestinal epithelial cells and Caco-2 cells. Arch Toxicol. 2021;95(3):907–22.
293. Jackson GR, Jr., Maione AG, Klausner M, Hayden PJ. Prevalidation of an Acute Inhalation Toxicity Test Using the EpiAirway In Vitro Human Airway Model. Appl In Vitro Toxicol. 2018;4(2):149–58.
294. Zakrzewski W, Dobrzyński M, Szymonowicz M, Rybak Z. Stem cells: past, present, and future. Stem Cell Res Ther. 2019;10(1):68.
295. Urbán N, Cheung TH. Stem cell quiescence: the challenging path to activation. Development. 2021;148(3):dev165084.
296. Lyssiotis CA, Lairson LL, Boitano AE, Wurdak H, Zhu S, Schultz PG. Chemical Control of Stem Cell Fate and Developmental Potential. Angew Chem Int Ed. 2011;50(1):200–42.
297. Lairson LL, Lyssiotis CA, Zhu S, Schultz PG. Small Molecule–Based Approaches to Adult Stem Cell Therapies. Ann Rev Pharmacol Toxicol. 2013;53(1):107–25.
298. Majors AK, Boehm CA, Nitto H, Midura RJ, Muschler GF. Characterization of human bone marrow stromal cells with respect to osteoblastic differentiation. J Orthop Res. 1997;15(4):546–57.
299. Bruder SP, Jaiswal N, Haynesworth SE. Growth kinetics, self-renewal, and the osteogenic potential of purified human mesenchymal stem cells during extensive subcultivation and following cryopreservation. J Cell Biochem. 1997;64(2):278–94.
300. Drost J, Clevers H. Organoids in cancer research. Nat Rev Cancer. 2018;18(7):407–18.
301. Driehuis E, Kretzschmar K, Clevers H. Establishment of patient-derived cancer organoids for drug-screening applications. Nat Protoc. 2020;15(10):3380–409.
302. Shi Y, Inoue H, Wu JC, Yamanaka S. Induced pluripotent stem cell technology: a decade of progress. Nat Rev Drug Discov. 2017;16(2):115–30.
303. Thomson JA, Itskovitz-Eldor J, Shapiro SS, Waknitz MA, Swiergiel JJ, Marshall VS, et al. Embryonic Stem Cell Lines Derived from Human Blastocysts. Science. 1998;282(5391):1145–7.

304. Mehta RH. Sourcing human embryos for embryonic stem cell lines: Problems & perspectives. Indian J Med Res. 2014;140:106–11.
305. Wert Gd, Mummery C. Human embryonic stem cells: research, ethics and policy. Hum Reprod. 2003;18(4):672–82.
306. Lo B, Parham L. Ethical Issues in Stem Cell Research. Endocr Rev. 2009;30(3):204–13.
307. Takahashi K, Tanabe K, Ohnuki M, Narita M, Ichisaka T, Tomoda K, et al. Induction of Pluripotent Stem Cells from Adult Human Fibroblasts by Defined Factors. Cell. 2007;131(5):861–72.
308. Takahashi Y, Sato S, Kurashima Y, Yamamoto T, Kurokawa S, Yuki Y, et al. A Refined Culture System for Human Induced Pluripotent Stem Cell-Derived Intestinal Epithelial Organoids. Stem Cell Rep. 2018;10(1):314–28.
309. Miller AJ, Dye BR, Ferrer-Torres D, Hill DR, Overeem AW, Shea LD, et al. Generation of lung organoids from human pluripotent stem cells in vitro. Nat Protoc. 2019;14(2):518–40.
310. Ahmed U, Ahmed R, Masoud MS, Tariq M, Ashfaq UA, Augustine R, et al. Stem cells based in vitro models: trends and prospects in biomaterials cytotoxicity studies. Biomed Mater. 2021;16(4).
311. Abud EM, Ramirez RN, Martinez ES, Healy LM, Nguyen CHH, Newman SA, et al. iPSC-Derived Human Microglia-like Cells to Study Neurological Diseases. Neuron. 2017;94(2):278–93.
312. Spence JR, Mayhew CN, Rankin SA, Kuhar MF, Vallance JE, Tolle K, et al. Directed differentiation of human pluripotent stem cells into intestinal tissue in vitro. Nature. 2011;470(7332):105–9.
313. Grouls M, Janssen AWF, Duivenvoorde LPM, Hooiveld GJEJ, Bouwmeester H, van der Zande M. Differential gene expression in iPSC-derived human intestinal epithelial cell layers following exposure to two concentrations of butyrate, propionate and acetate. Sci Rep. 2022;12(1):13988.
314. Hartwell LH, Kastan MB. Cell Cycle Control and Cancer. Science. 1994;266(5192):1821–8.
315. Sonugur FG, Akbulut H. The Role of Tumor Microenvironment in Genomic Instability of Malignant Tumors. Front Genet. 2019;10:1063.
316. Cortés C, Domenech J, Salazar M, Pastor S, Marcos R, Hernández A. Nanoplastics as a potential environmental health factor: effects of polystyrene nanoparticles on human intestinal epithelial Caco-2 cells. Environ Sci Nano. 2020;7(1):272–85.
317. Domenech J, Cortés C, Vela L, Marcos R, Hernández A. Polystyrene Nanoplastics as Carriers of Metals. Interactions of Polystyrene Nanoparticles with Silver Nanoparticles and Silver Nitrate, and Their Effects on Human Intestinal Caco-2 Cells. Biomolecules. 2021;11(6).
318. Stock V, Laurisch C, Franke J, Donmez MH, Voss L, Bohmert L, et al. Uptake and cellular effects of PE, PP, PET and PVC microplastic particles. Toxicology in vitro : an international journal published in association with BIBRA. 2021;70:105021.
319. Pinto M, Robine-Leon SA, M.D., Kedinger M, Triadou N, Dussaulx E, Lacroix B, et al. Enterocyte-like differentiation and polarization of the human colon carcinoma cell line Caco-2 in culture. Biol Cell. 1983;47:323–30.
320. Mabbott NA, Donaldson DS, Ohno H, Williams IR, Mahajan A. Microfold (M) cells: important immunosurveillance posts in the intestinal epithelium. Mucosal Immunol. 2013;6(4):666–77.
321. Domenech J, Hernandez A, Rubio L, Marcos R, Cortes C. Interactions of polystyrene nanoplastics with in vitro models of the human intestinal barrier. Archives of toxicology. 2020;94(9):2997–3012.
322. Lehner R, Wohlleben W, Septiadi D, Landsiedel R, Petri-Fink A, Rothen-Rutishauser B. A novel 3D intestine barrier model to study the immune response upon exposure to microplastics. Archives of toxicology. 2020;94(7):2463–79.

323. Sato T, Vries RG, Snippert HJ, van de Wetering M, Barker N, Stange DE, et al. Single Lgr5 stem cells build crypt-villus structures in vitro without a mesenchymal niche. Nature. 2009;459(7244):262–5.
324. Sato T, Stange DE, Ferrante M, Vries RGJ, van Es JH, van den Brink S, et al. Long-term Expansion of Epithelial Organoids From Human Colon, Adenoma, Adenocarcinoma, and Barrett's Epithelium. Gastroenterology. 2011;141(5):1762–72.
325. Cao L, Gibson JD, Miyamoto S, Sail V, Verma R, Rosenberg DW, et al. Intestinal lineage commitment of embryonic stem cells. Differentiation. 2011;81(1):1–10.
326. Forster R, Chiba K, Schaeffer L, Regalado Samuel G, Lai Christine S, Gao Q, et al. Human Intestinal Tissue with Adult Stem Cell Properties Derived from Pluripotent Stem Cells. Stem Cell Rep. 2014;2(6):838–52.
327. Miura S, Suzuki A. Generation of Mouse and Human Organoid-Forming Intestinal Progenitor Cells by Direct Lineage Reprogramming. Cell Stem Cell. 2017;21(4):456–71.e5.
328. Hou X, Chang DF, Trecartin A, Barthel ER, Schlieve CR, Frey MR, et al. Short-term and long-term human or mouse organoid units generate tissue-engineered small intestine without added signalling molecules. Exp Physiol. 2018;103(12):1633–44.
329. Pleguezuelos-Manzano C, Puschhof J, van den Brink S, Geurts V, Beumer J, Clevers H. Establishment and Culture of Human Intestinal Organoids Derived from Adult Stem Cells. Curr Protoc Immunol. 2020;130(1):e106.
330. Stewart CJ, Estes MK, Ramani S. Establishing Human Intestinal Enteroid/Organoid Lines from Preterm Infant and Adult Tissue. In: Amarnath S, editor. Innate Lymphoid Cells : Methods and Protocols. New York, NY: Springer US; 2020. p. 185–98.
331. Treveil A, Sudhakar P, Matthews ZJ, Wrzesiński T, Jones EJ, Brooks J, et al. Regulatory network analysis of Paneth cell and goblet cell enriched gut organoids using transcriptomics approaches. Mol Omics. 2020;16(1):39–58.
332. Gerbe F, Sidot E, Smyth DJ, Ohmoto M, Matsumoto I, Dardalhon V, et al. Intestinal epithelial tuft cells initiate type 2 mucosal immunity to helminth parasites. Nature. 2016;529(7585):226–30.
333. Inaba A, Arinaga A, Tanaka K, Endo T, Hayatsu N, Okazaki Y, et al. Interleukin-4 Promotes Tuft Cell Differentiation and Acetylcholine Production in Intestinal Organoids of Non-Human Primate. Int J Mol Sci. 2021;22(15).
334. Lozoya-Agullo I, Araujo F, Gonzalez-Alvarez I, Merino-Sanjuan M, Gonzalez-Alvarez M, Bermejo M, et al. Usefulness of Caco-2/HT29-MTX and Caco-2/HT29-MTX/Raji B Coculture Models To Predict Intestinal and Colonic Permeability Compared to Caco-2 Monoculture. Mol Pharm. 2017;14(4):1264–70.
335. Kämpfer AAM, Shah U-K, Chu SL, Busch M, Büttner V, He R, et al. Interlaboratory comparison of an intestinal triple culture to confirm transferability and reproducibility. In Vitro Models. 2022.
336. Hou Z, Meng R, Chen G, Lai T, Qing R, Hao S, et al. Distinct accumulation of nanoplastics in human intestinal organoids. Sci Total Environ. 2022;838:155811.
337. Busch M, Ramachandran H, Wahle T, Rossi A, Schins RPF. Investigating the Role of the NLRP3 Inflammasome Pathway in Acute Intestinal Inflammation: Use of THP-1 Knockout Cell Lines in an Advanced Triple Culture Model. Front Immunol. 2022;13:898039.
338. Bandi SP, Kumbhar YS, Venuganti VVK. Effect of particle size and surface charge of nanoparticles in penetration through intestinal mucus barrier. J Nanoparticle Res. 2020;22(3):62.
339. Tsai Y-H, Nattiv R, Dedhia PH, Nagy MS, Chin AM, Thomson M, et al. In vitro patterning of pluripotent stem cell-derived intestine recapitulates in vivo human development. Development. 2017;144(6):1045–55.

340. Hilgers AR, Conradi RA, Burton PS. Caco-2 Cell Monolayers as a Model for Drug Transport Across the Intestinal Mucosa. Pharm Res. 1990;7(9):902–10.
341. Lesuffleur T, Barbat A, Dussaulx E, Zweibaum A. Growth Adaptation to Methotrexate of HT-29 Human Colon Carcinoma Cells Is Associated with Their Ability to Differentiate into Columnar Absorptive and Mucus-secreting Cells. Cancer Res. 1990;50(19):6334–43.
342. Susewind J, de Souza Carvalho-Wodarz C, Repnik U, Collnot EM, Schneider-Daum N, Griffiths GW, et al. A 3D co-culture of three human cell lines to model the inflamed intestinal mucosa for safety testing of nanomaterials. Nanotoxicology. 2016;10(1):53–62.
343. Kämpfer AAM, Urbán P, Gioria S, Kanase N, Stone V, Kinsner-Ovaskainen A. Development of an in vitro co-culture model to mimic the human intestine in healthy and diseased state. Toxicology in vitro : an international journal published in association with BIBRA. 2017;45(Pt 1):31–43.
344. Thant AA, Wu Y, Lee J, Mishra DK, Garcia H, Koeffler HP, et al. Role of Caspases in 5-FU and Selenium-induced Growth Inhibition of Colorectal Cancer Cells. Anticancer Res. 2008;28(6A):3579–92.
345. Ohta Y, Kazuki K, Abe S, Oshimura M, Kobayashi K, Kazuki Y. Development of Caco-2 cells expressing four CYPs via a mammalian artificial chromosome. BMC Biotechnol. 2020;20(1):44.
346. Fritz A, Busch D, Lapczuk J, Ostrowski M, Drozdzik M, Oswald S. Expression of clinically relevant drug-metabolizing enzymes along the human intestine and their correlation to drug transporters and nuclear receptors: An intra-subject analysis. Basic Clin Pharmacol Toxicol. 2019;124(3):245–55.
347. Abass K, Lämsä V, Reponen P, Küblbeck J, Honkakoski P, Mattila S, et al. Characterization of human cytochrome P450 induction by pesticides. Toxicology. 2012;294(1):17–26.
348. Takeshita A, Igarashi-Migitaka J, Nishiyama K, Takahashi H, Takeuchi Y, Koibuchi N. Acetyl Tributyl Citrate, the Most Widely Used Phthalate Substitute Plasticizer, Induces Cytochrome P450 3A through Steroid and Xenobiotic Receptor. Toxicol Sci. 2011;123(2):460–70.
349. Brachner A, Fragouli D, Duarte IF, Farias PMA, Dembski S, Ghosh M, et al. Assessment of Human Health Risks Posed by Nano-and Microplastics Is Currently Not Feasible. Int J Environ Res Public Health. 2020;17(23).
350. Coffin S, Lee I, Gan J, Schlenk D. Simulated digestion of polystyrene foam enhances desorption of diethylhexyl phthalate (DEHP) and In vitro estrogenic activity in a size-dependent manner. Environ Pollut. 2019;246:452–62.
351. Sontheimer-Phelps A, Chou DB, Tovaglieri A, Ferrante TC, Duckworth T, Fadel C, et al. Human Colon-on-a-Chip Enables Continuous In Vitro Analysis of Colon Mucus Layer Accumulation and Physiology. Cell Mol Gastroenterol Hepatol. 2020;9(3):507–26.
352. Navabi N, McGuckin MA, Lindén SK. Gastrointestinal Cell Lines Form Polarized Epithelia with an Adherent Mucus Layer when Cultured in Semi-Wet Interfaces with Mechanical Stimulation. PloS one. 2013;8(7):e68761.
353. VanDussen KL, Marinshaw JM, Shaikh N, Miyoshi H, Moon C, Tarr PI, et al. Development of an enhanced human gastrointestinal epithelial culture system to facilitate patient-based assays. Gut. 2015;64(6):911.
354. Lu W, Rettenmeier E, Paszek M, Yueh M-F, Tukey RH, Trottier J, et al. Crypt Organoid Culture as an In Vitro Model in Drug Metabolism and Cytotoxicity Studies. Drug Metab Dispos. 2017;45(7):748.
355. Belair DG, Visconti RJ, Hong M, Marella M, Peters MF, Scott CW, et al. Human ileal organoid model recapitulates clinical incidence of diarrhea associated with small molecule drugs. Toxicol in Vitro. 2020;68:104928.

356. Park SB, Jung WH, Choi KJ, Koh B, Kim KY. A Comparative Systematic Analysis of The Influence of Microplastics on Colon Cells, Mouse and Colon Organoids. Tissue Eng Regen Med. 2022.
357. Xie S, Zhang R, Li Z, Liu C, Chen Y, Yu Q. Microplastics perturb colonic epithelial homeostasis associated with intestinal overproliferation, exacerbating the severity of colitis. Environ Res. 2022:114861.
358. Leslie Jhansi L, Huang S, Opp Judith S, Nagy Melinda S, Kobayashi M, Young Vincent B, et al. Persistence and Toxin Production by Clostridium difficile within Human Intestinal Organoids Result in Disruption of Epithelial Paracellular Barrier Function. Infect Immun. 2015;83(1):138–45.
359. Sidar B, Jenkins BR, Huang S, Spence JR, Walk ST, Wilking JN. Long-term flow through human intestinal organoids with the gut organoid flow chip (GOFlowChip). Lab Chip. 2019;19(20):3552–62.
360. Co JY, Margalef-Català M, Li X, Mah AT, Kuo CJ, Monack DM, et al. Controlling Epithelial Polarity: A Human Enteroid Model for Host-Pathogen Interactions. Cell Rep. 2019;26(9):2509–20.
361. Madden LR, Nguyen TV, Garcia-Mojica S, Shah V, Le AV, Peier A, et al. Bioprinted 3D Primary Human Intestinal Tissues Model Aspects of Native Physiology and ADME/Tox Functions. iScience. 2018;2:156–67.
362. Kasendra M, Tovaglieri A, Sontheimer-Phelps A, Jalili-Firoozinezhad S, Bein A, Chalkiadaki A, et al. Development of a primary human Small Intestine-on-a-Chip using biopsy-derived organoids. Sci Rep. 2018;8(1):2871.
363. Roodsant T, Navis M, Aknouch I, Renes IB, van Elburg RM, Pajkrt D, et al. A Human 2D Primary Organoid-Derived Epithelial Monolayer Model to Study Host-Pathogen Interaction in the Small Intestine. Front Cell Infect Microbiol. 2020;10.
364. Yamada S, Kanda Y. Evaluation of Barrier Functions in Human iPSC-Derived Intestinal Epithelium. In: Turksen K, editor. Permeability Barrier: Methods and Protocols. New York, NY: Springer US; 2021. p. 27–35.
365. Breau KA, Ok MT, Gomez-Martinez I, Burclaff J, Kohn NP, Magness ST. Efficient transgenesis and homology-directed gene targeting in monolayers of primary human small intestinal and colonic epithelial stem cells. Stem Cell Rep. 2022;17(6):1493–506.
366. Yoshida S, Miwa H, Kawachi T, Kume S, Takahashi K. Generation of intestinal organoids derived from human pluripotent stem cells for drug testing. Sci Rep. 2020;10(1):5989.
367. Workman MJ, Gleeson JP, Troisi EJ, Estrada HQ, Kerns SJ, Hinojosa CD, et al. Enhanced Utilization of Induced Pluripotent Stem Cell–Derived Human Intestinal Organoids Using Microengineered Chips. Cell Mol Gastroenterol Hepatol. 2018;5(4):669–77.e2.
368. Takahashi Y, Inoue Y, Kuze K, Sato S, Shimizu M, Kiyono H, et al. Comparison of gene expression and activation of transcription factors in organoid-derived monolayer intestinal epithelial cells and organoids. Biosci Biotechnol Biochem. 2021;85(10):2137–44.
369. Wang Y, Kim R, Hwang S-HJ, Dutton J, Sims CE, Allbritton NL. Analysis of Interleukin 8 Secretion by a Stem-Cell-Derived Human-Intestinal-Epithelial-Monolayer Platform. Anal Chem. 2018;90(19):11523–30.
370. Iwao T, Toyota M, Miyagawa Y, Okita H, Kiyokawa N, Akutsu H, et al. Differentiation of human induced pluripotent stem cells into functional enterocyte-like cells using a simple method. Drug Metab Pharmacokinet. 2014;29(1):44–51.
371. Kabeya T, Mima S, Imakura Y, Miyashita T, Ogura I, Yamada T, et al. Pharmacokinetic functions of human induced pluripotent stem cell-derived small intestinal epithelial cells. Drug Metab Pharmacokinet. 2020;35(4):374–82.

372. Kabeya T, Qiu S, Hibino M, Nagasaki M, Kodama N, Iwao T, et al. Cyclic AMP Signaling Promotes the Differentiation of Human Induced Pluripotent Stem Cells into Intestinal Epithelial Cells. Drug Metab Dispos. 2018;46(10):1411–9.
373. Wilson RL, Hewes SA, Rajan A, Lin S-C, Bomidi C, Iida T, et al. A Millifluidic Perfusion Cassette for Studying the Pathogenesis of Enteric Infections Using Ex-Vivo Organoids. Ann Biomed Eng. 2021;49(4):1233–44.
374. Naumovska E, Aalderink G, Wong Valencia C, Kosim K, Nicolas A, Brown S, et al. Direct On-Chip Differentiation of Intestinal Tubules from Induced Pluripotent Stem Cells. Int J Mol Sci. 2020;21(14).
375. Nikolaev M, Mitrofanova O, Broguiere N, Geraldo S, Dutta D, Tabata Y, et al. Homeostatic mini-intestines through scaffold-guided organoid morphogenesis. Nature. 2020;585(7826):574–8.
376. Schimpel C, Teubl B, Absenger M, Meindl C, Fröhlich E, Leitinger G, et al. Development of an Advanced Intestinal in Vitro Triple Culture Permeability Model To Study Transport of Nanoparticles. Mol Pharm. 2014;11(3):808–18.
377. Walczak AP, Kramer E, Hendriksen PJ, Tromp P, Helsper JP, van der Zande M, et al. Translocation of differently sized and charged polystyrene nanoparticles in in vitro intestinal cell models of increasing complexity. Nanotoxicology. 2015;9(4):453–61.
378. Inkielewicz-Stepniak I, Tajber L, Behan G, Zhang H, Radomski MW, Medina C, et al. The Role of Mucin in the Toxicological Impact of Polystyrene Nanoparticles. Materials (Basel). 2018;11(5).
379. Wu B, Wu X, Liu S, Wang Z, Chen L. Size-dependent effects of polystyrene microplastics on cytotoxicity and efflux pump inhibition in human Caco-2cells. Chemosphere. 2019;221:333–41.
380. Wu S, Wu M, Tian D, Qiu L, Li T. Effects of polystyrene microbeads on cytotoxicity and transcriptomic profiles in human Caco-2 cells. Environ Toxicol. 2020;35(4):495–506.
381. Huang W, Yin H, Yang Y, Jin L, Lu G, Dang Z. Influence of the co-exposure of microplastics and tetrabromobisphenol A on human gut: Simulation in vitro with human cell Caco-2 and gut microbiota. Sci Total Environ. 2021;778:146264.
382. Jeon S, Lee D-K, Jeong J, Yang SI, Kim J-S, Kim J, et al. The reactive oxygen species as pathogenic factors of fragmented microplastics to macrophages. Environ Pollut. 2021;281:117006.
383. Xu X, Feng Y, Han C, Yao Z, Liu Y, Luo C, et al. Autophagic response of intestinal epithelial cells exposed to polystyrene nanoplastics. Environ Toxicol. 2022.
384. Ma Y, Koh JYC, Lim HK, Shi P, Tay CY. Elucidating the Size-Dependency of In Vitro Digested Polystyrene Microplastics on Human Intestinal Cells Health and Function. Macromol Chem Phys. 2022;223(13):2100454.
385. Steckiewicz KP, Adamska A, Narajczyk M, Megiel E, Inkielewicz – Stepniak I. Fluoride enhances polystyrene nanoparticles cytotoxicity in colonocytes in vitro model. Chem Biol Interact. 2022;367:110169.
386. Visalli G, Facciolà A, Pruiti Ciarello M, De Marco G, Maisano M, Di Pietro A. Acute and Sub-Chronic Effects of Microplastics (3 and 10 μm) on the Human Intestinal Cells HT-29. Int J Environ Res Public Health. 2021;18(11):5833.
387. Mahler GJ, Esch MB, Tako E, Southard TL, Archer SD, Glahn RP, et al. Oral exposure to polystyrene nanoparticles affects iron absorption. Nat Nanotechnol. 2012;7(4):264–71.
388. Fournier E, Leveque M, Ruiz P, Ratel J, Durif C, Chalancon S, et al. Microplastics: What happens in the human digestive tract? First evidences in adults using in vitro gut models. J Hazard Mater. 2023;442:130010.

389. Hiemstra PS, Grootaers G, van der Does AM, Krul CAM, Kooter IM. Human lung epithelial cell cultures for analysis of inhaled toxicants: Lessons learned and future directions. Toxicol in Vitro. 2018;47:137–46.
390. Crocker TT, O'Donnell TV, Nunes LL. Toxicity of Benzo(a)pyrene and Air Pollution Composite for Adult Human Bronchial Mucosa in Organ Culture. Cancer Res. 1973;33(1):88–93.
391. Craighead JE, Mossman BT, Bradley BJ. Comparative studies on the cytotoxicity of amphibole and serpentine asbestos. Environ Health Perspect. 1980;34:37–46.
392. Mohr U, Emura M. The use of cell and organ culture from the respiratory tract for testing chemicals. Food Chem Toxicol. 1985;23(2):233–8.
393. Driscoll KE, Carter JM, Iype PT, Kumari HL, Crosby LL, Aardema MJ, et al. Establishment of immortalized alveolar type II epithelial cell lines from adult rats. In Vitro Cell Dev Biol Anim. 1995;31(7):516–27.
394. Gotoh S, Ito I, Nagasaki T, Yamamoto Y, Konishi S, Korogi Y, et al. Generation of Alveolar Epithelial Spheroids via Isolated Progenitor Cells from Human Pluripotent Stem Cells. Stem Cell Rep. 2014;3(3):394–403.
395. Basil MC, Katzen J, Engler AE, Guo M, Herriges MJ, Kathiriya JJ, et al. The Cellular and Physiological Basis for Lung Repair and Regeneration: Past, Present, and Future. Cell Stem Cell. 2020;26(4):482–502.
396. Fritsche E, Haarmann-Stemmann T, Kapr J, Galanjuk S, Hartmann J, Mertens PR, et al. Stem Cells for Next Level Toxicity Testing in the 21st Century. Small. 2021;17(15):2006252.
397. Masui A, Hirai T, Gotoh S. Perspectives of future lung toxicology studies using human pluripotent stem cells. Arch Toxicol. 2022;96(2):389–402.
398. Adler KB, Cheng P-W, Kim KC. Characterization of Guinea Pig Tracheal Epithelial Cells Maintained in Biphasic Organotypic Culture: Cellular Composition and Biochemical Analysis of Released Glycoconjugates. Am J Respir Cell Mol Biol. 1990;2(2):145–54.
399. Blank F, Rothen-Rutishauser BM, Schurch S, Gehr P. An Optimized In Vitro Model of the Respiratory Tract Wall to Study Particle Cell Interactions. J Aerosol Med. 2006;19(3):392–405.
400. Lacroix G, Koch W, Ritter D, Gutleb AC, Larsen ST, Loret T, et al. Air–Liquid Interface In Vitro Models for Respiratory Toxicology Research: Consensus Workshop and Recommendations. Appl Vitro Toxicol. 2018;4(2):91–106.
401. Ding Y, Weindl P, Lenz A-G, Mayer P, Krebs T, Schmid O. Quartz crystal microbalances (QCM) are suitable for real-time dosimetry in nanotoxicological studies using VITROCELL®Cloud cell exposure systems. Part Fibre Toxicol. 2020;17(1):44.
402. Schmitz C, Welck J, Tavernaro I, Grinberg M, Rahnenführer J, Kiemer AK, et al. Mechanical strain mimicking breathing amplifies alterations in gene expression induced by SiO2 NPs in lung epithelial cells. Nanotoxicology. 2019;13(9):1227–43.
403. Yang S, Cheng Y, Chen Z, Liu T, Yin L, Pu Y, et al. In vitro evaluation of nanoplastics using human lung epithelial cells, microarray analysis and co-culture model. Ecotoxicol Environ Saf. 2021;226:112837.
404. Gupta G, Vallabani S, Bordes R, Bhattacharya K, Fadeel B. Development of Microfluidic, Serum-Free Bronchial Epithelial Cells-on-a-Chip to Facilitate a More Realistic In vitro Testing of Nanoplastics. Front Toxicol. 2021;3:735331.
405. Roshanzadeh A, Park S, Ganjbakhsh SE, Park J, Lee D-H, Lee S, et al. Surface Charge-Dependent Cytotoxicity of Plastic Nanoparticles in Alveolar Cells under Cyclic Stretches. Nano Lett. 2020;20(10):7168–76.
406. Meindl C, Öhlinger K, Zrim V, Steinkogler T, Fröhlich E. Screening for Effects of Inhaled Nanoparticles in Cell Culture Models for Prolonged Exposure. Nanomaterials. 2021;11(3).

407. Winkler AS, Cherubini A, Rusconi F, Santo N, Madaschi L, Pistoni C, et al. Human airway organoids and microplastic fibers: A new exposure model for emerging contaminants. Environ Int. 2022;163:107200.
408. Lim SL, Ng CT, Zou L, Lu Y, Chen J, Bay BH, et al. Targeted metabolomics reveals differential biological effects of nanoplastics and nanoZnO in human lung cells. Nanotoxicology. 2019;13(8):1117–32.
409. Dong C-D, Chen C-W, Chen Y-C, Chen H-H, Lee J-S, Lin C-H. Polystyrene microplastic particles: In vitro pulmonary toxicity assessment. J Hazard Mater. 2020;385:121575.
410. Lin S, Zhang H, Wang C, Su X-L, Song Y, Wu P, et al. Metabolomics Reveal Nanoplastic-Induced Mitochondrial Damage in Human Liver and Lung Cells. Environ Sci Technol. 2022;56(17):12483–93.
411. Zhang T, Yang S, Ge Y, Wan X, Zhu Y, Li J, et al. Polystyrene Nanoplastics Induce Lung Injury via Activating Oxidative Stress: Molecular Insights from Bioinformatics Analysis. Nanomaterials. 2022;12(19):3507.
412. Brown DM, Wilson MR, MacNee W, Stone V, Donaldson K. Size-Dependent Proinflammatory Effects of Ultrafine Polystyrene Particles: A Role for Surface Area and Oxidative Stress in the Enhanced Activity of Ultrafines. Toxicol Appl Pharmacol. 2001;175(3):191–9.
413. Jeon S, Clavadetscher J, Lee DK, Chankeshwara SV, Bradley M, Cho WS. Surface Charge-Dependent Cellular Uptake of Polystyrene Nanoparticles. Nanomaterials (Basel). 2018;8(12).
414. Xu M, Halimu G, Zhang Q, Song Y, Fu X, Li Y, et al. Internalization and toxicity: A preliminary study of effects of nanoplastic particles on human lung epithelial cell. Sci Total Environ. 2019;694:133794.
415. Zhu K, Jia H, Sun Y, Dai Y, Zhang C, Guo X, et al. Enhanced cytotoxicity of photoaged phenol-formaldehyde resins microplastics: Combined effects of environmentally persistent free radicals, reactive oxygen species, and conjugated carbonyls. Environ Int. 2020;145:106137.
416. Goodman KE, Hare JT, Khamis ZI, Hua T, Sang QA. Exposure of Human Lung Cells to Polystyrene Microplastics Significantly Retards Cell Proliferation and Triggers Morphological Changes. Chem Res Toxicol. 2021;34(4):1069–81.
417. Shi Q, Tang J, Wang L, Liu R, Giesy JP. Combined cytotoxicity of polystyrene nanoplastics and phthalate esters on human lung epithelial A549 cells and its mechanism. Ecotoxicol Environ Saf. 2021;213:112041.
418. Bengalli R, Zerboni A, Bonfanti P, Saibene M, Mehn D, Cella C, et al. Characterization of microparticles derived from waste plastics and their bio-interaction with human lung A549 cells. J Appl Toxicol. 2022:1–15.
419. Florance I, Chandrasekaran N, Gopinath PM, Mukherjee A. Exposure to polystyrene nanoplastics impairs lipid metabolism in human and murine macrophages in vitro. Ecotoxicol Environ Saf. 2022;238:113612.
420. Gautam R, Jo J, Acharya M, Maharjan A, Lee D, K.C PB, et al. Evaluation of potential toxicity of polyethylene microplastics on human derived cell lines. Sci Total Environ. 2022;838:156089.
421. Halimu G, Zhang Q, Liu L, Zhang Z, Wang X, Gu W, et al. Toxic effects of nanoplastics with different sizes and surface charges on epithelial-to-mesenchymal transition in A549 cells and the potential toxicological mechanism. J Hazard Mater. 2022;430:128485.
422. Shi X, Wang X, Huang R, Tang C, Hu C, Ning P, et al. Cytotoxicity and Genotoxicity of Polystyrene Micro- and Nanoplastics with Different Size and Surface Modification in A549 Cells. Int J Nanomedicine. 2022;17:4509–23.
423. Zhang H, Zhang S, Duan Z, Wang L. Pulmonary toxicology assessment of polyethylene terephthalate nanoplastic particles in vitro. Environ Int. 2022;162:107177.

424. Zhang YX, Wang M, Yang L, Pan K, Miao AJ. Bioaccumulation of differently-sized polystyrene nanoplastics by human lung and intestine cells. J Hazard Mater. 2022;439:129585.
425. da Silva Brito WA, Singer D, Miebach L, Saadati F, Wende K, Schmidt A, et al. Comprehensive in vitro polymer type, concentration, and size correlation analysis to microplastic toxicity and inflammation. Sci Total Environ. 2023;854.
426. Binder S, Cao X, Bauer S, Rastak N, Kuhn E, Dragan GC, et al. In vitro genotoxicity of dibutyl phthalate on A549 lung cells at air–liquid interface in exposure concentrations relevant at workplaces. Environ Mol Mutagen. 2021;62(9):490–501.
427. Stock V, Bohmert L, Donmez MH, Lampen A, Sieg H. An inverse cell culture model for floating plastic particles. Anal Biochem. 2020;591:113545.
428. Watson CY, DeLoid GM, Pal A, Demokritou P. Buoyant Nanoparticles: Implications for Nano-Biointeractions in Cellular Studies. Small. 2016;12(23):3172–80.
429. Upadhyay S, Palmberg L. Air-Liquid Interface: Relevant In Vitro Models for Investigating Air Pollutant-Induced Pulmonary Toxicity. Toxicol Sci. 2018;164(1):21–30.
430. Green TR, Fisher J, Stone M, Wroblewski BM, Ingham E. Polyethylene particles of a 'critical size' are necessary for the induction of cytokines by macrophages in vitro. Biomaterials. 1998;19:2297–302.
431. Ammar O, Bouaziz Y, Haddar N, Mnif N. Talc as Reinforcing Filler in Polypropylene Compounds: Effect on Morphology and Mechanical Properties. Polym Sci. 2017;3(2).
432. Hinderliter PM, Minard KR, Orr G, Chrisler WB, Thrall BD, Pounds JG, et al. ISDD: A computational model of particle sedimentation, diffusion and target cell dosimetry for in vitro toxicity studies. Part Fibre Toxicol. 2010;7(1):36.
433. Teeguarden JG, Hinderliter PM, Orr G, Thrall BD, Pounds JG. Particokinetics In Vitro: Dosimetry Considerations for In Vitro Nanoparticle Toxicity Assessments. Toxicol Sci. 2007;95(2):300–12.
434. Thomas DG, Smith JN, Thrall BD, Baer DR, Jolley H, Munusamy P, et al. ISD3: a particokinetic model for predicting the combined effects of particle sedimentation, diffusion and dissolution on cellular dosimetry for in vitro systems. Part Fibre Toxicol. 2018;15(1):6.
435. DeLoid GM, Cohen JM, Pyrgiotakis G, Pirela SV, Pal A, Liu J, et al. Advanced computational modeling for in vitro nanomaterial dosimetry. Part Fibre Toxicol. 2015;12:32.
436. Kämpfer AAM, Busch M, Buttner V, Bredeck G, Stahlmecke B, Hellack B, et al. Model Complexity as Determining Factor for In Vitro Nanosafety Studies: Effects of Silver and Titanium Dioxide Nanomaterials in Intestinal Models. Small. 2021;17(15):e2004223.
437. Sargent CY, Berguig GY, Kinney MA, Hiatt LA, Carpenedo RL, Berson RE, et al. Hydrodynamic modulation of embryonic stem cell differentiation by rotary orbital suspension culture. Biotechnol Bioeng. 2010;105(3):611–26.
438. Zhang J, Wei X, Zeng R, Xu F, Li X. Stem cell culture and differentiation in microfluidic devices toward organ-on-a-chip. Future Sci OA. 2017;3(2):FSO187.
439. Kulthong K, Hooiveld GJEJ, Duivenvoorde L, Miro Estruch I, Marin V, van der Zande M, et al. Transcriptome comparisons of in vitro intestinal epithelia grown under static and microfluidic gut-on-chip conditions with in vivo human epithelia. Sci Rep. 2021;11(1):3234.
440. Docter D, Strieth S, Westmeier D, Hayden O, Gao M, Knauer SK, et al. No king without a crown – impact of the nanomaterial-protein corona on nanobiomedicine. Nanomedicine. 2015;10(3):503–19.
441. Cao J, Yang Q, Jiang J, Dalu T, Kadushkin A, Singh J, et al. Coronas of micro/nano plastics: a key determinant in their risk assessments. Part Fibre Toxicol. 2022;19(1):55.
442. Monopoli MP, Åberg C, Salvati A, Dawson KA. Biomolecular coronas provide the biological identity of nanosized materials. Nat Nanotechnol. 2012;7(12):779–86.

443. Allen LT, Tosetto M, Miller IS, O'Connor DP, Penney SC, Lynch I, et al. Surface-induced changes in protein adsorption and implications for cellular phenotypic responses to surface interaction. Biomaterials. 2006;27(16):3096–108.
444. Ichinose T, Nishikawa M, Takano H, Sera N, Sadakane K, Mori I, et al. Pulmonary toxicity induced by intratracheal instillation of Asian yellow dust (Kosa) in mice. Environ Toxicol Pharmacol. 2005;20(1):48–56.
445. Griese M. Pulmonary surfactant in health and human lung diseases: state of the art. Eur Respir J. 1999;13(6):1455–76.
446. Liang L, Cui M, Zhang M, Zheng P, Deng Z, Gao S, et al. Nanoparticles' interference in the evaluation of in vitro toxicity of silver nanoparticles. RSC Adv. 2015;5(82):67327–34.
447. Oh SJ, Kim H, Liu Y, Han HK, Kwon K, Chang KH, et al. Incompatibility of silver nanoparticles with lactate dehydrogenase leakage assay for cellular viability test is attributed to protein binding and reactive oxygen species generation. Toxicol Lett. 2014;225(3):422–32.
448. Stone V, Johnston H, Schins RP. Development of in vitro systems for nanotoxicology: methodological considerations. Crit Rev Toxicol. 2009;39(7):613–26.
449. Ong KJ, MacCormack TJ, Clark RJ, Ede JD, Ortega VA, Felix LC, et al. Widespread nanoparticle-assay interference: implications for nanotoxicity testing. PLoS One. 2014;9(3):e90650.
450. Wilhelmi V, Fischer U, van Berlo D, Schulze-Osthoff K, Schins RPF, Albrecht C. Evaluation of apoptosis induced by nanoparticles and fine particles in RAW 264.7 macrophages: Facts and artefacts. Toxicology in Vitro. 2012;26(2):323–34.
451. Mitrano DM, Lesher EK, Bednar A, Monserud J, Higgins CP, Ranville JF. Detecting nanoparticulate silver using single-particle inductively coupled plasma–mass spectrometry. Environ Toxicol Chem. 2012;31(1):115–21.
452. Tenuta T, Monopoli MP, Kim J, Salvati A, Dawson KA, Sandin P, et al. Elution of labile fluorescent dye from nanoparticles during biological use. PLoS One. 2011;6(10):e25556.
453. Catarino AI, Frutos A, Henry TB. Use of fluorescent-labelled nanoplastics (NPs) to demonstrate NP absorption is inconclusive without adequate controls. Sci Total Environ. 2019;670:915–20.
454. Simonsen JB, Kromann EB. Pitfalls and opportunities in quantitative fluorescence-based nanomedicine studies - A commentary. J Control Release. 2021;335:660–7.
455. Nuutila J, Lilius EM. Flow cytometric quantitative determination of ingestion by phagocytes needs the distinguishing of overlapping populations of binding and ingesting cells. Cytometry A. 2005;65(2):93–102.
456. Dumont C, Czuba E, Chen M, Villadangos JA, Johnston AP, Mintern JD. DNA-based probes for flow cytometry analysis of endocytosis and recycling. Traffic. 2017;18(4):242–9.
457. Gottstein C, Wu G, Wong BJ, Zasadzinski JA. Precise Quantification of Nanoparticle internalization. ACS Nano. 2013;7(6):4933–45.
458. Smirnov A, Solga MD, Lannigan J, Criss AK. An improved method for differentiating cell-bound from internalized particles by imaging flow cytometry. J Immunol Methods. 2015;423:60–9.
459. Phanse Y, Ramer-Tait AE, Friend SL, Carrillo-Conde B, Lueth P, Oster CJ, et al. Analyzing cellular internalization of nanoparticles and bacteria by multi-spectral imaging flow cytometry. J Vis Exp. 2012(64):e3884.
460. FitzGerald LI, Johnston APR. It's what's on the inside that counts: Techniques for investigating the uptake and recycling of nanoparticles and proteins in cells. J Colloid Interface Sci. 2021;587:64–78.
461. Xing Y-F, Xu Y-H, Shi M-H, Lian Y-X. The impact of PM2.5 on the human respiratory system. J Thorac Dis. 2016;8(1):69–74.

462. Oberdorster G, Oberdorster E, Oberdorster J. Nanotoxicology: an emerging discipline evolving from studies of ultrafine particles. Environ Health Perspect. 2005;113(7):823–39.
463. Hongprasith N, Kittimethawong C, Lertluksanaporn R, Eamchotchawalit T, Kittipongvises S, Lohwacharin J. IR microspectroscopic identification of microplastics in municipal wastewater treatment plants. Environ Sci Pollut Res Int. 2020;27(15):18557–64.
464. Liang B, Zhong Y, Huang Y, Lin X, Liu J, Lin L, et al. Underestimated health risks: polystyrene micro- and nanoplastics jointly induce intestinal barrier dysfunction by ROS-mediated epithelial cell apoptosis. Part Fibre Toxicol. 2021;18(1):20.
465. Lionetto F, Corcione CE, Rizzo A, Maffezzoli A. Production and Characterization of Polyethylene Terephthalate Nanoparticles. Polymers (Basel). 2021;13(21).
466. Gouin T, Becker RA, Collot AG, Davis JW, Howard B, Inawaka K, et al. Toward the Development and Application of an Environmental Risk Assessment Framework for Microplastic. Environ Toxicol Chem. 2019;38(10):2087–100.
467. Halappanavar S, Mallach G. Adverse outcome pathways and in vitro toxicology strategies for microplastics hazard testing. Curr Opin Toxicol. 2021;28:52–61.
468. Pikuda O, Xu EG, Berk D, Tufenkji N. Toxicity Assessments of Micro- and Nanoplastics Can Be Confounded by Preservatives in Commercial Formulations. Environ Sci Technol. 2019;6(1):21–5.
469. Ajaj A, J'Bari S, Ononogbo A, Buonocore F, Bear JC, Mayes AG, et al. An Insight into the Growing Concerns of Styrene Monomer and Poly(Styrene) Fragment Migration into Food and Drink Simulants from Poly(Styrene) Packaging. Foods. 2021;10(5).
470. Gulizia AM, Patel K, Philippa B, Motti CA, van Herwerden L, Vamvounis G. Understanding plasticiser leaching from polystyrene microplastics. Sci Total Environ. 2023;857:159099.
471. Catrouillet C, Davranche M, Khatib I, Fauny C, Wahl A, Gigault J. Metals in microplastics: determining which are additive, adsorbed, and bioavailable. Environ Sci Process Impacts. 2021;23(4):553–8.
472. Petersen EJ, Barrios AC, Henry TB, Johnson ME, Koelmans AA, Montoro Bustos AR, et al. Potential Artifacts and Control Experiments in Toxicity Tests of Nanoplastic and Microplastic Particles. Environ Sci Technol. 2022;56(22):15192–206.
473. Bernauer U, Oberemm A, Madle S, Gundert-Remy U. The Use of in vitro Data in Risk Assessment. Basic Clin Pharmacol Toxicol. 2005;96(3):176–81.
474. Black MB, Stern A, Efremenko A, Mallick P, Moreau M, Hartman JK, et al. Biological system considerations for application of toxicogenomics in next-generation risk assessment and predictive toxicology. Toxicol In Vitro. 2022;80:105311.
475. Kauffman A, Gyurdieva A, Mabus J, Ferguson C, Yan Z, Hornby P. Alternative functional in vitro models of human intestinal epithelia. Front Pharmacol. 2013;4.
476. Hartung T, Daston G. Are In Vitro Tests Suitable for Regulatory Use? Toxicol Sci. 2009;111(2):233–7.
477. Ben-David U, Siranosian B, Ha G, Tang H, Oren Y, Hinohara K, et al. Genetic and transcriptional evolution alters cancer cell line drug response. Nature. 2018;560(7718):325–30.
478. Hartung T, van Vliet E, Jaworska J, Bonilla L, Skinner N, Thomas R. Systems Toxicology. ALTEX. 2012;29(2):119–28.
479. Warren HS, Tompkins RG, Moldawer LL, Seok J, Xu W, Mindrinos MN, et al. Mice are not men. PNAS. 2015;112(4):345–.
480. Kararli TT. Comparison of the gastrointestinal anatomy, physiology, and biochemistry of humans and commonly used laboratory animals. Biopharm Drug Dispos. 1995;16(5):351–80.

481. Fagerholm U, Johansson M, Lennernäs H. Comparison Between Permeability Coefficients in Rat and Human Jejunum. Pharm Res. 1996;13(9):1336–42.
482. Ermund A, Schütte A, Johansson MEV, Gustafsson JK, Hansson GC. Studies of mucus in mouse stomach, small intestine, and colon. I. Gastrointestinal mucus layers have different properties depending on location as well as over the Peyer's patches. Am J Physiol Gastrointest Liver Physiol. 2013;305(5):341–7.
483. Brouwer H, Van Oijen FLN, Bouwmeester H. Chapter 40 - Potential human health effects following exposure to nano- and microplastics, lessons learned from nanomaterials. In: Knowles ME, Anelich LE, Boobis AR, Popping B, editors. Present Knowledge in Food Safety: Academic Press; 2023. p. 590–605.
484. Lamon L, Asturiol D, Vilchez A, Cabellos J, Damásio J, Janer G, et al. Physiologically based mathematical models of nanomaterials for regulatory toxicology: A review. Comput Toxicol. 2019;9:133–42.
485. Jagiello K, Ciura K. In vitro to in vivo extrapolation to support the development of the next generation risk assessment (NGRA) strategy for nanomaterials. Nanoscale. 2022;14(18):6735–42.
486. Halappanavar S, van den Brule S, Nymark P, Gate L, Seidel C, Valentino S, et al. Adverse outcome pathways as a tool for the design of testing strategies to support the safety assessment of emerging advanced materials at the nanoscale. Part Fibre Toxicol. 2020;17(1):16.
487. Kogut I, Roop DR, Bilousova G. Differentiation of Human Induced Pluripotent Stem Cells into a Keratinocyte Lineage. In: Turksen K, editor. Epidermal Cells: Methods and Protocols. New York, NY: Springer New York; 2014. p. 1–12.
488. Castro-Viñuelas R, Sanjurjo-Rodríguez C, Piñeiro-Ramil M, Rodríguez-Fernández S, López-Baltar I, Fuentes-Boquete I, et al. Tips and tricks for successfully culturing and adapting human induced pluripotent stem cells. Mol Ther Methods Clin Dev. 2021;23:569–81.
489. Yamamoto T, Arita M, Kuroda H, Suzuki T, Kawamata S. Improving the differentiation potential of pluripotent stem cells by optimizing culture conditions. Sci Rep. 2022;12(1):14147.
490. Epelman S, Lavine Kory J, Randolph Gwendalyn J. Origin and Functions of Tissue Macrophages. Immunity. 2014;41(1):21–35.
491. Leiding JW. Neutrophil Evolution and Their Diseases in Humans. Front Immunol. 2017;8.
492. Choi YJ, Park JW, Lim Y, Seo S, Hwang DY. In vivo impact assessment of orally administered polystyrene nanoplastics: biodistribution, toxicity, and inflammatory response in mice. Nanotoxicology. 2021;15(9):1180–98.
493. He Y, Li Z, Xu T, Luo D, Chi Q, Zhang Y, et al. Polystyrene nanoplastics deteriorate LPS-modulated duodenal permeability and inflammation in mice via ROS drived-NF-kappaB/NLRP3 pathway. Chemosphere. 2022:135662.
494. Tang X, Fan X, Xu T, He Y, Chi Q, Li Z, et al. Polystyrene nanoplastics exacerbated lipopolysaccharide-induced necroptosis and inflammation via the ROS/MAPK pathway in mice spleen. Environ Toxicol. 2022;37(10):2552–65.
495. Jung BK, Han SW, Park SH, Bae JS, Choi J, Ryu KY. Neurotoxic potential of polystyrene nanoplastics in primary cells originating from mouse brain. Neurotoxicology. 2020;81:189–96.
496. Trump LR, Nayak RC, Singh AK, Emberesh S, Wellendorf AM, Lutzko CM, et al. Neutrophils Derived from Genetically Modified Human Induced Pluripotent Stem Cells Circulate and Phagocytose Bacteria In Vivo. Stem Cells Transl Med. 2019;8(6):557–67.
497. Gutbier S, Wanke F, Dahm N, Rümmelin A, Zimmermann S, Christensen K, et al. Large-Scale Production of Human iPSC-Derived Macrophages for Drug Screening. Int J Mol Sci. 2020;21(13):4808.

498. McKinney CE. Using induced pluripotent stem cells derived neurons to model brain diseases. Neural Regen Res. 2017;12(7):1062–7.
499. Noel G, Baetz NW, Staab JF, Donowitz M, Kovbasnjuk O, Pasetti MF, et al. A primary human macrophage-enteroid co-culture model to investigate mucosal gut physiology and host-pathogen interactions. Sci Rep. 2017;7(1):45270.
500. Takahashi Y, Sato S, Kurashima Y, Lai C-Y, Otsu M, Hayashi M, et al. Reciprocal Inflammatory Signaling Between Intestinal Epithelial Cells and Adipocytes in the Absence of Immune Cells. EBioMedicine. 2017;23:34–45.
501. de Rus Jacquet A. Preparation and Co-Culture of iPSC-Derived Dopaminergic Neurons and Astrocytes. Curr Protoc Cell Biol. 2019;85(1):e98.
502. Choi S, Choi J, Cheon S, Song J, Kim S-Y, Kim J-e, et al. Pulmonary fibrosis model using micro-CT analyzable human PSC–derived alveolar organoids containing alveolar macrophage-like cells. Cell Biol Toxicol. 2022;38(4):557–75.
503. Workman MJ, Mahe MM, Trisno S, Poling HM, Watson CL, Sundaram N, et al. Engineered human pluripotent-stem-cell-derived intestinal tissues with a functional enteric nervous system. Nat Med. 2017;23(1):49–59.
504. Shim K-Y, Lee D, Han J, Nguyen N-T, Park S, Sung JH. Microfluidic gut-on-a-chip with three-dimensional villi structure. Biomed Microdevices. 2017;19(2):37.
505. Ménard S, Cerf-Bensussan N, Heyman M. Multiple facets of intestinal permeability and epithelial handling of dietary antigens. Mucosal Immunol. 2010;3(3):247–59.
506. Groschwitz KR, Hogan SP. Intestinal barrier function: molecular regulation and disease pathogenesis. J Allergy Clin Immunol. 2009;124(1):3–20; quiz 1–2.
507. McGuckin MA, Eri R, Simms LA, Florin TH, Radford-Smith G. Intestinal barrier dysfunction in inflammatory bowel diseases. Inflamm Bowel Dis. 2009;15(1):100–13.
508. Peterson LW, Artis D. Intestinal epithelial cells: regulators of barrier function and immune homeostasis. Nat Rev Immunol. 2014;14(3):141–53.
509. Darwich AS, Aslam U, Ashcroft DM, Rostami-Hodjegan A. Meta-analysis of the turnover of intestinal epithelia in preclinical animal species and humans. Drug Metab Dispos. 2014;42(12):2016–22.
510. van der Flier LG, Clevers H. Stem cells, self-renewal, and differentiation in the intestinal epithelium. Annu Rev Physiol. 2009;71:241–60.
511. Barker N, van Es JH, Kuipers J, Kujala P, van den Born M, Cozijnsen M, et al. Identification of stem cells in small intestine and colon by marker gene Lgr5. Nature. 2007;449(7165):1003–7.
512. Wang Y, Song W, Wang J, Wang T, Xiong X, Qi Z, et al. Single-cell transcriptome analysis reveals differential nutrient absorption functions in human intestine. J Exp Med. 2020;217(2).
513. Lee SH. Intestinal permeability regulation by tight junction: implication on inflammatory bowel diseases. Intest Res. 2015;13(1):11–8.
514. Kim YS, Ho SB. Intestinal goblet cells and mucins in health and disease: recent insights and progress. Curr Gastroenterol Rep. 2010;12(5):319–30.
515. Johansson ME, Phillipson M, Petersson J, Velcich A, Holm L, Hansson GC. The inner of the two Muc2 mucin-dependent mucus layers in colon is devoid of bacteria. Proceedings of the National Academy of Sciences of the United States of America. 2008;105(39):15064–9.
516. Van der Sluis M, De Koning BA, De Bruijn AC, Velcich A, Meijerink JP, Van Goudoever JB, et al. Muc2-deficient mice spontaneously develop colitis, indicating that MUC2 is critical for colonic protection. Gastroenterology. 2006;131(1):117–29.
517. Bevins CL, Salzman NH. Paneth cells, antimicrobial peptides and maintenance of intestinal homeostasis. Nature Reviews Microbiology. 2011;9(5):356–68.

518. Dupont A, Heinbockel L, Brandenburg K, Hornef MW. Antimicrobial peptides and the enteric mucus layer act in concert to protect the intestinal mucosa. Gut Microbes. 2014;5(6):761–5.
519. Worthington JJ. The intestinal immunoendocrine axis: novel cross-talk between enteroendocrine cells and the immune system during infection and inflammatory disease. Biochem Soc Trans. 2015;43(4):727–33.
520. Wang M, Gao Z, Zhang Z, Pan L, Zhang Y. Roles of M cells in infection and mucosal vaccines. Hum Vaccin Immunother. 2014;10(12):3544–51.
521. Lin L, Zhang J. Role of intestinal microbiota and metabolites on gut homeostasis and human diseases. BMC Immunology. 2017;18(1):2.
522. Zhang YJ, Li S, Gan RY, Zhou T, Xu DP, Li HB. Impacts of gut bacteria on human health and diseases. Int J Mol Sci. 2015;16(4):7493–519.
523. Ivanov AI, Parkos CA, Nusrat A. Cytoskeletal regulation of epithelial barrier function during inflammation. Am J Pathol. 2010;177(2):512–24.
524. Price AE, Shamardani K, Lugo KA, Deguine J, Roberts AW, Lee BL, et al. A Map of Toll-like Receptor Expression in the Intestinal Epithelium Reveals Distinct Spatial, Cell Type-Specific, and Temporal Patterns. Immunity. 2018;49(3):560–75.e6.
525. Stephens M, von der Weid PY. Lipopolysaccharides modulate intestinal epithelial permeability and inflammation in a species-specific manner. Gut Microbes. 2020;11(3):421–32.
526. Chelakkot C, Ghim J, Ryu SH. Mechanisms regulating intestinal barrier integrity and its pathological implications. Experimental & Molecular Medicine. 2018;50(8):1–9.
527. Dignass A, Eliakim R, Magro F, Maaser C, Chowers Y, Geboes K, et al. Second European evidence-based consensus on the diagnosis and management of ulcerative colitis part 1: definitions and diagnosis. J Crohns Colitis. 2012;6(10):965–90.
528. Van Assche G, Dignass A, Panes J, Beaugerie L, Karagiannis J, Allez M, et al. The second European evidence-based Consensus on the diagnosis and management of Crohn's disease: Definitions and diagnosis. J Crohns Colitis. 2010;4(1):7–27.
529. Gonzalez-Licea A, Yardley JH. Nature of the tissue reaction in ulcerative colitis. Light and electron microscopic findings. Gastroenterology. 1966;51(5):825–40.
530. Macedo MH, Dias Neto M, Pastrana L, Gonçalves C, Xavier M. Recent Advances in Cell-Based In Vitro Models to Recreate Human Intestinal Inflammation. Adv Sci (Weinh). 2023;10(31):e2301391.
531. Pinto M, Robine-Leon S, Appay M-D, Kedinger M, Triadou N, Dussaulx E, et al. Enterocyte-like differentiation and polarization of the human colon carcinoma cell line Caco-2 in culture. Biology of the Cell. 1983;47:323–30.
532. Engle MJ, Goetz GS, Alpers DH. Caco-2 cells express a combination of colonocyte and enterocyte phenotypes. J Cell Physiol. 1998;174(3):362–9.
533. Tremblay E, Auclair J, Delvin E, Levy E, Ménard D, Pshezhetsky AV, et al. Gene expression profiles of normal proliferating and differentiating human intestinal epithelial cells: a comparison with the Caco-2 cell model. J Cell Biochem. 2006;99(4):1175–86.
534. Böcker U, Yezerskyy O, Feick P, Manigold T, Panja A, Kalina U, et al. Responsiveness of intestinal epithelial cell lines to lipopolysaccharide is correlated with Toll-like receptor 4 but not Toll-like receptor 2 or CD14 expression. Int J Colorectal Dis. 2003;18(1):25–32.
535. Ayehunie S, Landry T, Stevens Z, Armento A, Hayden P, Klausner M. Human Primary Cell-Based Organotypic Microtissues for Modeling Small Intestinal Drug Absorption. Pharmaceutical research. 2018;35(4):72.

536. Janssen AWF, van der Lugt B, Duivenvoorde LPM, Vos AP, Bastiaan-Net S, Tomassen MMM, et al. Comparison of iPSC-derived human intestinal epithelial cells with Caco-2 cells and human in vivo data after exposure to Lactiplantibacillus plantarum WCFS1. Scientific reports. 2024;14(1):26464.
537. Beumer J, Clevers H. Cell fate specification and differentiation in the adult mammalian intestine. Nature Reviews Molecular Cell Biology. 2021;22(1):39–53.
538. He G-W, Lin L, DeMartino J, Zheng X, Staliarova N, Dayton T, et al. Optimized human intestinal organoid model reveals interleukin-22-dependency of paneth cell formation. Cell Stem Cell. 2022;29(9):1333–45.e6.
539. Co JY, Margalef-Català M, Monack DM, Amieva MR. Controlling the polarity of human gastrointestinal organoids to investigate epithelial biology and infectious diseases. Nat Protoc. 2021;16(11):5171–92.
540. Lewis A, Keshara R, Kim YH, Grapin-Botton A. Self-organization of organoids from endoderm-derived cells. J Mol Med (Berl). 2021;99(4):449–62.
541. Janssen AWF, Duivenvoorde LPM, Beekmann K, Pinckaers N, van der Hee B, Noorlander A, et al. Transport of perfluoroalkyl substances across human induced pluripotent stem cell-derived intestinal epithelial cells in comparison with primary human intestinal epithelial cells and Caco-2 cells. Archives of toxicology. 2024;98(11):3777–95.
542. Brodsky A, Davio C, Shayo C, Lemos Legnazzi B, Barbosa M, Lardo M, et al. Forskolin induces U937 cell line differentiation as a result of a sustained cAMP elevation. Eur J Pharmacol. 1998;350(1):121–7.
543. Chen Y, Wen JG, Feng JJ, Wang YH, Li TF, Nurmi K, et al. Forskolin attenuates the NLRP3 inflammasome activation and IL-1β secretion in human macrophages. Pediatric Research. 2019;86(6):692–8.
544. Yan Y, Jiang W, Liu L, Wang X, Ding C, Tian Z, et al. Dopamine controls systemic inflammation through inhibition of NLRP3 inflammasome. Cell. 2015;160(1-2):62–73.
545. Volpato V, Webber C. Addressing variability in iPSC-derived models of human disease: guidelines to promote reproducibility. Dis Model Mech. 2020;13(1).
546. Deguchi S, Kosugi K, Takeishi N, Watanabe Y, Morimoto S, Negoro R, et al. Construction of multilayered small intestine-like tissue by reproducing interstitial flow. Cell Stem Cell. 2024;31(9):1315–26.e8.
547. Efe JA, Ding S. The evolving biology of small molecules: controlling cell fate and identity. Philosophical transactions of the Royal Society of London Series B, Biological sciences. 2011;366(1575):2208–21.
548. Matin MM, Walsh JR, Gokhale PJ, Draper JS, Bahrami AR, Morton I, et al. Specific knockdown of Oct4 and beta2-microglobulin expression by RNA interference in human embryonic stem cells and embryonic carcinoma cells. Stem Cells. 2004;22(5):659–68.
549. Koo BK, Clevers H. Stem cells marked by the R-spondin receptor LGR5. Gastroenterology. 2014;147(2):289–302.
550. Wang P, Rodriguez RT, Wang J, Ghodasara A, Kim SK. Targeting SOX17 in human embryonic stem cells creates unique strategies for isolating and analyzing developing endoderm. Cell Stem Cell. 2011;8(3):335–46.
551. Antonopoulos C, Russo HM, El Sanadi C, Martin BN, Li X, Kaiser WJ, et al. Caspase-8 as an Effector and Regulator of NLRP3 Inflammasome Signaling. J Biol Chem. 2015;290(33):20167–84.
552. Lei-Leston AC, Murphy AG, Maloy KJ. Epithelial Cell Inflammasomes in Intestinal Immunity and Inflammation. Front Immunol. 2017;8:1168.

553. Perregaux D, Gabel CA. Interleukin-1 beta maturation and release in response to ATP and nigericin. Evidence that potassium depletion mediated by these agents is a necessary and common feature of their activity. J Biol Chem. 1994;269(21):15195–203.
554. Rozario P, Pinilla M, Gorse L, Vind AC, Robinson KS, Toh GA, et al. Mechanistic basis for potassium efflux–driven activation of the human NLRP1 inflammasome. Proceedings of the National Academy of Sciences. 2024;121(2):e2309579121.
555. Cao J, Li L, Yao Y, Xing Y, Ma H. Dehydroepiandrosterone exacerbates nigericin-induced abnormal autophagy and pyroptosis via GPER activation in LPS-primed macrophages. Cell Death & Disease. 2022;13(4):372.
556. He WT, Wan H, Hu L, Chen P, Wang X, Huang Z, et al. Gasdermin D is an executor of pyroptosis and required for interleukin-1β secretion. Cell Res. 2015;25(12):1285–98.
557. Wu L, Bai S, Huang J, Cui G, Li Q, Wang J, et al. Nigericin Boosts Anti-Tumor Immune Response via Inducing Pyroptosis in Triple-Negative Breast Cancer. Cancers (Basel). 2023;15(12).
558. Furrie E, Macfarlane S, Thomson G, Macfarlane GT. Toll-like receptors-2, -3 and -4 expression patterns on human colon and their regulation by mucosal-associated bacteria. Immunology. 2005;115(4):565–74.
559. Sharif O, Bolshakov VN, Raines S, Newham P, Perkins ND. Transcriptional profiling of the LPS induced NF-kappaB response in macrophages. BMC Immunol. 2007;8:1.
560. Guo Y, Wang B, Wang T, Gao L, Yang ZJ, Wang FF, et al. Biological characteristics of IL-6 and related intestinal diseases. Int J Biol Sci. 2021;17(1):204–19.
561. Li CK, Seth R, Gray T, Bayston R, Mahida YR, Wakelin D. Production of proinflammatory cytokines and inflammatory mediators in human intestinal epithelial cells after invasion by Trichinella spiralis. Infect Immun. 1998;66(5):2200–6.
562. Leppkes M, Roulis M, Neurath MF, Kollias G, Becker C. Pleiotropic functions of TNF-α in the regulation of the intestinal epithelial response to inflammation. Int Immunol. 2014;26(9):509–15.
563. Yu S, Gao N. Compartmentalizing intestinal epithelial cell toll-like receptors for immune surveillance. Cell Mol Life Sci. 2015;72(17):3343–53.
564. Bruning EE, Coller JK, Wardill HR, Bowen JM. Site-specific contribution of Toll-like receptor 4 to intestinal homeostasis and inflammatory disease. J Cell Physiol. 2021;236(2):877–88.
565. Wang L, Jiang Z, Huang D, Duan J, Huang C, Sullivan S, et al. JAK/STAT3 regulated global gene expression dynamics during late-stage reprogramming process. BMC Genomics. 2018;19(1):183.
566. Cerneckis J, Cai H, Shi Y. Induced pluripotent stem cells (iPSCs): molecular mechanisms of induction and applications. Signal Transduction and Targeted Therapy. 2024;9(1):112.
567. Galli G, Saleh M. Immunometabolism of Macrophages in Bacterial Infections. Front Cell Infect Microbiol. 2020;10:607650.
568. Stagg AJ, Hart AL, Knight SC, Kamm MA. The dendritic cell: its role in intestinal inflammation and relationship with gut bacteria. Gut. 2003;52(10):1522–9.
569. Cao X, van den Hil FE, Mummery CL, Orlova VV. Generation and Functional Characterization of Monocytes and Macrophages Derived from Human Induced Pluripotent Stem Cells. Curr Protoc Stem Cell Biol. 2020;52(1):e108.
570. Pang PD, Ahmed SM, Nishiga M, Stockbridge NL, Wu JC. Tackling the challenges of new approach methods for predicting drug effects from model systems. Nat Rev Drug Discov. 2024;23(8):565–6.

571. Burnett SD, Blanchette AD, Chiu WA, Rusyn I. Cardiotoxicity Hazard and Risk Characterization of ToxCast Chemicals Using Human Induced Pluripotent Stem Cell-Derived Cardiomyocytes from Multiple Donors. Chem Res Toxicol. 2021;34(9):2110–24.
572. Ford LC, Lin H-C, Zhou Y-H, Wright FA, Gombar VK, Sedykh A, et al. Characterizing PFAS hazards and risks: a human population-based in vitro cardiotoxicity assessment strategy. Human Genomics. 2024;18(1):92.
573. Maloy KJ, Powrie F. Intestinal homeostasis and its breakdown in inflammatory bowel disease. Nature. 2011;474(7351):298–306.
574. Castro-Viñuelas R, Sanjurjo-Rodríguez C, Piñeiro-Ramil M, Hermida-Gómez T, Rodríguez-Fernández S, Oreiro N, et al. Generation and characterization of human induced pluripotent stem cells (iPSCs) from hand osteoarthritis patient-derived fibroblasts. Scientific reports. 2020;10(1):4272.
575. Ching JC, Lobanova L, Loewen ME. Secreted hCLCA1 is a signaling molecule that activates airway macrophages. PloS one. 2013;8(12):e83130.
576. Teodorowicz M, Perdijk O, Verhoek I, Govers C, Savelkoul HFJ, Tang Y, et al. Optimized Triton X-114 assisted lipopolysaccharide (LPS) removal method reveals the immunomodulatory effect of food proteins. PloS one. 2017;12(3):e0173778.
577. OECD. Global Plastics Outlook2022.
578. Landrigan PJ, Raps H, Cropper M, Bald C, Brunner M, Canonizado EM, et al. The Minderoo-Monaco Commission on Plastics and Human Health. Ann Glob Health. 2023;89(1):23.
579. Hernandez LM, Xu EG, Larsson HCE, Tahara R, Maisuria VB, Tufenkji N. Plastic Teabags Release Billions of Microparticles and Nanoparticles into Tea. Environmental science & technology. 2019;53(21):12300–10.
580. Geneva; World Health Organization. Dietary and inhalation exposure to nano- and microplastic particles and potential implications for human health. 2022.
581. Joris F, Manshian BB, Peynshaert K, De Smedt SC, Braeckmans K, Soenen SJ. Assessing nanoparticle toxicity in cell-based assays: influence of cell culture parameters and optimized models for bridging the in vitro–in vivo gap. Chem Soc Rev. 2013;42(21):8339–59.
582. Stone V, Gottardo S, Bleeker EAJ, Braakhuis H, Dekkers S, Fernandes T, et al. A framework for grouping and read-across of nanomaterials- supporting innovation and risk assessment. Nano Today. 2020;35:100941.
583. Koelmans AA, Redondo-Hasselerharm PE, Nor NHM, de Ruijter VN, Mintenig SM, Kooi M. Risk assessment of microplastic particles. Nature Reviews Materials. 2022;7(2):138–52.
584. Vethaak AD, Legler J. Microplastics and human health. Science. 2021;371(6530):672–4.
585. Busch M, Brouwer H, Aalderink G, Bredeck G, Kämpfer AAM, Schins RPF, et al. Investigating nanoplastics toxicity using advanced stem cell-based intestinal and lung in vitro models. Frontiers in Toxicology. 2023;5.
586. Domenech J, Villacorta A, Ferrer JF, Llorens-Chiralt R, Marcos R, Hernández A, et al. In vitro cell-transforming potential of secondary polyethylene terephthalate and polylactic acid nanoplastics. J Hazard Mater. 2024;469:134030.
587. Villacorta A, Vela L, Morataya-Reyes M, Llorens-Chiralt R, Rubio L, Alaraby M, et al. Titanium-doped PET nanoplastics of environmental origin as a true-to-life model of nanoplastic. Science of The Total Environment. 2023;880:163151.
588. Parker LA, Höppener EM, van Amelrooij EF, Henke S, Kooter IM, Grigoriadi K, et al. Protocol for the production of micro- and nanoplastic test materials. Microplastics and Nanoplastics. 2023;3(1):10.

589. Lundqvist M, Stigler J, Elia G, Lynch I, Cedervall T, Dawson KA. Nanoparticle size and surface properties determine the protein corona with possible implications for biological impacts. Proceedings of the National Academy of Sciences of the United States of America. 2008;105(38):14265–70.
590. Cai R, Ren J, Guo M, Wei T, Liu Y, Xie C, et al. Dynamic intracellular exchange of nanomaterials' protein corona perturbs proteostasis and remodels cell metabolism. Proceedings of the National Academy of Sciences. 2022;119(23):e2200363119.
591. Saptarshi SR, Duschl A, Lopata AL. Interaction of nanoparticles with proteins: relation to bioreactivity of the nanoparticle. Journal of nanobiotechnology. 2013;11(1):26.
592. Hu M, Palić D. Micro- and nano-plastics activation of oxidative and inflammatory adverse outcome pathways. Redox Biology. 2020;37:101620.
593. Germaine Aalderink HB, Jingxuan Wang, Aafke Janssen, Meike van der Zande, Coen Govers, Tamara Hoppenbrouwers, Hans Bouwmeester, Mathias Busch. Induced pluripotent stem cell-derived intestinal epithelial cell and Caco-2 cell model to emulate LPS and nigericin-induced inflammatory responses. Manuscript in preparation.
594. Blucher C, Zilberfain C, Venus T, Spindler N, Dietrich A, Burkhardt R, et al. Single cell study of adipose tissue mediated lipid droplet formation and biochemical alterations in breast cancer cells. Analyst. 2019;144(18):5558–70.
595. Wendrich JR, Boeren S, Möller BK, Weijers D, De Rybel B. In Vivo Identification of Plant Protein Complexes Using IP-MS/MS. Methods Mol Biol. 2017;1497:147–58.
596. Brouwer H, Porbahaie M, Boeren S, Busch M, Bouwmeester H. The in vitro gastrointestinal digestion-associated protein corona of polystyrene nano- and microplastics increases their uptake by human THP-1-derived macrophages. Part Fibre Toxicol. 2024;21(1):4.
597. Zheng L, Boeren S, Liu C, Bakker W, Wang H, Rietjens IMCM, et al. Proteomics-based identification of biomarkers reflecting endogenous and exogenous exposure to the advanced glycation end product precursor methylglyoxal in SH-SY5Y human neuroblastoma cells. International Journal of Biological Macromolecules. 2024;272:132859.
598. Cox J, Mann M. MaxQuant enables high peptide identification rates, individualized p.p.b.-range mass accuracies and proteome-wide protein quantification. Nat Biotechnol. 2008;26(12):1367–72.
599. Ritchie ME, Phipson B, Wu D, Hu Y, Law CW, Shi W, et al. limma powers differential expression analyses for RNA-sequencing and microarray studies. Nucleic Acids Research. 2015;43(7):e47–e.
600. Aleksander SA, Balhoff J, Carbon S, Cherry JM, Drabkin HJ, Ebert D, et al. The Gene Ontology knowledgebase in 2023. Genetics. 2023;224(1).
601. Consortium TU. UniProt: the Universal Protein Knowledgebase in 2023. Nucleic Acids Research. 2022;51(D1):D523–D31.
602. Pascovici D, Handler DCL, Wu JX, Haynes PA. Multiple testing corrections in quantitative proteomics: A useful but blunt tool. PROTEOMICS. 2016;16(18):2448–53.
603. Vela L, Villacorta A, Venus T, Estrela-Lopis I, Pastor S, Garcia-Rodriguez A, et al. The potential effects of in vitro digestion on the physicochemical and biological characteristics of polystyrene nanoplastics. Environ Pollut. 2023;329:121656.
604. Venus T, Meyer T, Zilberfain C, Böttner J, Lampen A, Creutzenberg O, et al. Chapter 15 Dosimetry and Imaging of Micro and Nanoparticles by Means of High Resolution Techniques. Environmental Nanopollutants: Sources, Occurrence, Analysis and Fate: The Royal Society of Chemistry; 2023. p. 363–88.

605. Hou Z, Meng R, Chen G, Lai T, Qing R, Hao S, et al. Distinct accumulation of nanoplastics in human intestinal organoids. Science of The Total Environment. 2022;838:155811.
606. Akhmetova DR, Rogova A, Tishchenko YA, Mitusova KA, Postovalova AS, Dovbysh OV, et al. An investigation of nano- and micron-sized carriers based on calcium carbonate and polylactic acid for oral administration of siRNA. Expert Opinion on Drug Delivery. 2024;21(8):1279–95.
607. Peng M, Vercauteren M, Grootaert C, Catarino AI, Everaert G, Rajkovic A, et al. Bioenergetic effects of pristine and ultraviolet-weathered polydisperse polyethylene terephthalate and polystyrene nanoplastics on human intestinal Caco-2 cells. Science of The Total Environment. 2024;908:168267.
608. Domenech J, de Britto M, Velázquez A, Pastor S, Hernández A, Marcos R, et al. Long-Term Effects of Polystyrene Nanoplastics in Human Intestinal Caco-2 Cells. Biomolecules. 2021;11(10):1442.
609. Hesler M, Aengenheister L, Ellinger B, Drexel R, Straskraba S, Jost C, et al. Multi-endpoint toxicological assessment of polystyrene nano- and microparticles in different biological models in vitro. Toxicology in Vitro. 2019.
610. Chen Y, Williams AM, Gordon EB, Rudolph SE, Longo BN, Li G, et al. Biological effects of polystyrene micro- and nano-plastics on human intestinal organoid-derived epithelial tissue models without and with M cells. Nanomedicine: Nanotechnology, Biology and Medicine. 2023;50:102680.
611. Domenech J, Hernández A, Rubio L, Marcos R, Cortés C. Interactions of polystyrene nanoplastics with in vitro models of the human intestinal barrier. Archives of toxicology. 2020.
612. Zhuang J, Chen Q, Xu L, Chen X. Combined exposure to polyvinyl chloride and polystyrene microplastics induces liver injury and perturbs gut microbial and serum metabolic homeostasis in mice. Ecotox Environ Safe. 2023;267:115637.
613. Jia R, Han J, Liu X, Li K, Lai W, Bian L, et al. Exposure to Polypropylene Microplastics via Oral Ingestion Induces Colonic Apoptosis and Intestinal Barrier Damage through Oxidative Stress and Inflammation in Mice. Toxics. 2023;11(2):127.
614. Espinosa K, Castillo LA, Barbosa SE. 18 - Polypropylene/talc nanocomposites films as low-cost barrier materials for food packaging. In: Grumezescu AM, editor. Food Packaging: Academic Press; 2017. p. 603–36.
615. Carlos KS, de Jager LS, Begley TH. Investigation of the primary plasticisers present in polyvinyl chloride (PVC) products currently authorised as food contact materials. Food additives & contaminants Part A, Chemistry, analysis, control, exposure & risk assessment. 2018;35(6):1214–22.
616. Bruinink A, Wang J, Wick P. Effect of particle agglomeration in nanotoxicology. Archives of toxicology. 2015;89(5):659–75.
617. Xu Z, Shen J, Lin L, Chen J, Wang L, Deng X, et al. Exposure to irregular microplastic shed from baby bottles activates the ROS/NLRP3/Caspase-1 signaling pathway, causing intestinal inflammation. Environ Int. 2023;181:108296.
618. Lynch HN, Lauer DJ, Leleck OM, Freid RD, Collins J, Chen K, et al. Systematic review of the association between talc and female reproductive tract cancers. Front Toxicol. 2023;5:1157761.
619. Tavakolpournegari A, Villacorta A, Morataya-Reyes M, Arribas Arranz J, Banaei G, Pastor S, et al. Harmful effects of true-to-life nanoplastics derived from PET water bottles in human alveolar macrophages. Environmental pollution. 2024;348:123823.
620. Alzaben M, Burve R, Loeschner K, Møller P, Roursgaard M. Nanoplastics from ground polyethylene terephthalate food containers: Genotoxicity in human lung epithelial A549 cells. Mutation Research/Genetic Toxicology and Environmental Mutagenesis. 2023;892:503705.

621. Arribas Arranz J, Villacorta A, Rubio L, García-Rodríguez A, Sánchez G, Llorca M, et al. Kinetics and toxicity of nanoplastics in ex vivo exposed human whole blood as a model to understand their impact on human health. Science of The Total Environment. 2024;948:174725.
622. Proquin H, Rodríguez-Ibarra C, Moonen CGJ, Urrutia Ortega IM, Briedé JJ, de Kok TM, et al. Titanium dioxide food additive (E171) induces ROS formation and genotoxicity: contribution of micro and nano-sized fractions. Mutagenesis. 2016;32(1):139–49.
623. Kumar A, Bicer EM, Morgan AB, Pfeffer PE, Monopoli M, Dawson KA, et al. Enrichment of immunoregulatory proteins in the biomolecular corona of nanoparticles within human respiratory tract lining fluid. Nanomedicine: Nanotechnology, Biology and Medicine. 2016;12(4):1033–43.
624. Singh S, Brocker C, Koppaka V, Chen Y, Jackson BC, Matsumoto A, et al. Aldehyde dehydrogenases in cellular responses to oxidative/electrophilicstress. Free Radical Biology and Medicine. 2013;56:89–101.
625. Liu Y, Hong H, Lu X, Wang W, Liu F, Yang H. L-Ascorbic Acid Protected Against Extrinsic and Intrinsic Apoptosis Induced by Cobalt Nanoparticles Through ROS Attenuation. Biol Trace Elem Res. 2017;175(2):428–39.
626. Pavlin M, Lojk J, Strojan K, Hafner-Bratkovič I, Jerala R, Leonardi A, et al. The Relevance of Physico-Chemical Properties and Protein Corona for Evaluation of Nanoparticles Immunotoxicity-In Vitro Correlation Analysis on THP-1 Macrophages. Int J Mol Sci. 2022;23(11).
627. Kessler A, Hedberg J, Blomberg E, Odnevall I. Reactive Oxygen Species Formed by Metal and Metal Oxide Nanoparticles in Physiological Media-A Review of Reactions of Importance to Nanotoxicity and Proposal for Categorization. Nanomaterials (Basel). 2022;12(11).
628. Wang B, Yang A, Zhao Z, He C, Liu Y, Colman RW, et al. The Plasma Kallikrein–Kininogen Pathway Is Critical in the Pathogenesis of Colitis in Mice. Frontiers in Immunology. 2018;9.
629. Sahu A, Lambris JD. Structure and biology of complement protein C3, a connecting link between innate and acquired immunity. Immunol Rev. 2001;180:35–48.
630. Lohr K, Sardana H, Lee S, Wu F, Huso DL, Hamad AR, et al. Extracellular matrix protein lumican regulates inflammation in a mouse model of colitis. Inflamm Bowel Dis. 2012;18(1):143–51.
631. Papini E, Tavano R, Mancin F. Opsonins and Dysopsonins of Nanoparticles: Facts, Concepts, and Methodological Guidelines. Front Immunol. 2020;11:567365.
632. Dalal PJ, Muller WA, Sullivan DP. Endothelial Cell Calcium Signaling during Barrier Function and Inflammation. Am J Pathol. 2020;190(3):535–42.
633. Huang AL, Vita JA. Effects of Systemic Inflammation on Endothelium-Dependent Vasodilation. Trends in Cardiovascular Medicine. 2006;16(1):15–20.
634. Bhagat K, Vallance P. Inflammatory cytokines impair endothelium-dependent dilatation in human veins in vivo. Circulation. 1997;96(9):3042–7.
635. Shaw CA, Mortimer GM, Deng ZJ, Carter ES, Connell SP, Miller MR, et al. Protein corona formation in bronchoalveolar fluid enhances diesel exhaust nanoparticle uptake and pro-inflammatory responses in macrophages. Nanotoxicology. 2016;10(7):981–91.
636. Borgognoni CF, Mormann M, Qu Y, Schäfer M, Langer K, Öztürk C, et al. Reaction of human macrophages on protein corona covered TiO_2 nanoparticles. Nanomedicine. 2015;11(2):275–82.
637. Brodkorb A, Egger L, Alminger M, Alvito P, Assunção R, Ballance S, et al. INFOGEST static in vitro simulation of gastrointestinal food digestion. Nature Protocols. 2019;14(4):991–1014.
638. Gruber MM, Hirschmugl B, Berger N, Holter M, Radulović S, Leitinger G, et al. Plasma proteins facilitates placental transfer of polystyrene particles. Journal of nanobiotechnology. 2020.

639. Ritz S, Schöttler S, Kotman N, Baier G, Musyanovych A, Kuharev J, et al. Protein Corona of Nanoparticles: Distinct Proteins Regulate the Cellular Uptake. Biomacromolecules. 2015;16(4):1311–21.
640. Boerio FJ, Bahl SK, Mcgraw GE. Vibrational Analysis of Polyethylene Terephthalate and Its Deuterated Derivatives. J Polym Sci Pol Phys. 1976;14(6):1029–46.
641. Itoh N, Hanari N. Development of a Polystyrene Reference Material for Raman Spectrometer (NMIJ RM 8158-a). Anal Sci. 2021;37(11):1533–+.
642. Ludwig V, Ludwig ZMD, Rodrigues MM, Anjos V, Costa CB, das Dores DRS, et al. Analysis by Raman and infrared spectroscopy combined with theoretical studies on the identification of plasticizer in PVC films. Vib Spectrosc. 2018;98:134–8.
643. Yang Y, Huang ZL, Wang JD, Jiang BB, Yang YR, Song WB. Measurement of Properties of Polypropylene Copolymers by Raman Spectrum. Spectrosc Spect Anal. 2012;32(12):3262–6.
644. Nobrega MM, Olivato JB, Müller CMO, Yamashita F. Biodegradable Starch-Based Films Containing Saturated Fatty Acids: Thermal, Infrared And Raman Spectroscopic Characterization. Polimeros. 2012;22(5):475–80.
645. Miller JV, Bartick EG. Forensic analysis of single fibers by Raman spectroscopy. Appl Spectrosc. 2001;55(12):1729–32.
646. Sample Passports MOMENTUM Test Materials. [Internet]. Zenodo. . 2024.
647. Micro- And nanoplastics-current state of knowledge with the focus on oral uptake and toxicity, (2020).
648. Zangmeister CD, Radney JG, Benkstein KD, Kalanyan B. Common Single-Use Consumer Plastic Products Release Trillions of Sub-100 nm Nanoparticles per Liter into Water during Normal Use. Environmental Science & Technology. 2022;56(9):5448–55.
649. Gigault J, Halle At, Baudrimont M, Pascal P-Y, Gauffre F, Phi T-L, et al. Current opinion: What is a nanoplastic? Environmental Pollution. 2018;235:1030–4.
650. Zhang Q, Zhao Y, Du F, Cai H, Wang G, Shi H. Microplastic Fallout in Different Indoor Environments. Environmental Science & Technology. 2020;54(11):6530–9.
651. Schwabl P, Köppel S, Königshofer P, Bucsics T, Trauner M, Reiberger T, et al. Detection of Various Microplastics in Human Stool: A Prospective Case Series. Ann Intern Med. 2019;171(7):453–7.
652. Zarus GM, Muianga C, Hunter CM, Pappas RS. A review of data for quantifying human exposures to micro and nanoplastics and potential health risks. Sci Total Environ. 2021;756:144010.
653. Brodkorb A, Egger L, Alminger M, Alvito P, Assunção R, Ballance S, et al. INFOGEST static in vitro simulation of gastrointestinal food digestion. Nat Protoc. 2019;14(4):991–1014.
654. Jani PU, McCarthy DE, Florence AT. Nanosphere and microsphere uptake via Peyer's patches: observation of the rate of uptake in the rat after a single oral dose. International Journal of Pharmaceutics. 1992;86(2):239–46.
655. Klisuric A, Thierry B, Delon L, Prestidge CA, Gibson RJ. Identifying human and murine M cells in vitro. Experimental Biology and Medicine. 2019;244(7):554–64.
656. Delon L, Gibson RJ, Prestidge CA, Thierry B. Mechanisms of uptake and transport of particulate formulations in the small intestine. J Control Release. 2022;343:584–99.
657. Lunov O, Syrovets T, Loos C, Beil J, Delacher M, Tron K, et al. Differential uptake of functionalized polystyrene nanoparticles by human macrophages and a monocytic cell line. ACS nano. 2011.
658. Kuhn DA, Vanhecke D, Michen B, Blank F, Gehr P, Petri-Fink A, et al. Different endocytotic uptake mechanisms for nanoparticles in epithelial cells and macrophages. Beilstein Journal of Nanotechnology. 2014;5:1625–36.

659. Ruder B, Becker C. At the Forefront of the Mucosal Barrier: The Role of Macrophages in the Intestine. Cells. 2020;9(10).
660. Mowat AM. Anatomical basis of tolerance and immunity to intestinal antigens. Nature Reviews Immunology. 2003;3(4):331–41.
661. Turnbull EL, Yrlid U, Jenkins CD, Macpherson GG. Intestinal dendritic cell subsets: differential effects of systemic TLR4 stimulation on migratory fate and activation in vivo. J Immunol. 2005;174(3):1374–84.
662. Viola MF, Boeckxstaens G. Intestinal resident macrophages: Multitaskers of the gut. Neurogastroenterol Motil. 2020;32(8):e13843.
663. Hussain N, Jaitley V, Florence AT. Recent advances in the understanding of uptake of microparticulates across the gastrointestinal lymphatics. Adv Drug Deliv Rev. 2001;50(1-2):107–42.
664. Zhang Z, Lu Y, Qi J, Wu W. An update on oral drug delivery via intestinal lymphatic transport. Acta Pharm Sin B. 2021;11(8):2449–68.
665. Zolnik BS, González-Fernández Af, Sadrieh N, Dobrovolskaia MA. Minireview: Nanoparticles and the Immune System. Endocrinology. 2010;151(2):458–65.
666. Micro- and nano-plastics activation of oxidative and inflammatory adverse outcome pathways, (2020).
667. Yang Y, Fan S, Chen Q, Lu Y, Zhu Y, Chen X, et al. Acute exposure to gold nanoparticles aggravates lipopolysaccharide-induced liver injury by amplifying apoptosis via ROS-mediated macrophage-hepatocyte crosstalk. Journal of nanobiotechnology. 2022;20(1):37.
668. Starr T, Bauler TJ, Malik-Kale P, Steele-Mortimer O. The phorbol 12-myristate-13-acetate differentiation protocol is critical to the interaction of THP-1 macrophages with Salmonella Typhimurium. Plos One. 2018;13(3):e0193601.
669. Schindelin J, Arganda-Carreras I, Frise E, Kaynig V, Longair M, Pietzsch T, et al. Fiji: an open-source platform for biological-image analysis. Nature Methods. 2012;9(7):676–82.
670. Kulak NA, Pichler G, Paron I, Nagaraj N, Mann M. Minimal, encapsulated proteomic-sample processing applied to copy-number estimation in eukaryotic cells. Nature Methods. 2014;11(3):319–24.
671. Tyanova S, Temu T, Sinitcyn P, Carlson A, Hein MY, Geiger T, et al. The Perseus computational platform for comprehensive analysis of (prote)omics data. Nature Methods. 2016;13(9):731–40.
672. Yan H. The R Graph Gallery 2018 [Available from: https://r-graph-gallery.com/about.html.
673. Conway JR, Lex A, Gehlenborg N. UpSetR: an R package for the visualization of intersecting sets and their properties. Bioinformatics. 2017;33(18):2938–40.
674. Arezki Y, Delalande F, Schaeffer-Reiss C, Cianférani S, Rapp M, Lebeau L, et al. Surface charge influences protein corona, cell uptake and biological effects of carbon dots. Nanoscale. 2022;14(39):14695–710.
675. Nazarenus M, Zhang Q, Soliman MG, del Pino P, Pelaz B, Carregal-Romero S, et al. In vitro interaction of colloidal nanoparticles with mammalian cells: What have we learned thus far? Beilstein Journal of Nanotechnology. 2014;5:1477–90.
676. Gessner A, Lieske A, Paulke B, Müller R. Influence of surface charge density on protein adsorption on polymeric nanoparticles: analysis by two-dimensional electrophoresis. Eur J Pharm Biopharm. 2002;54(2):165–70.
677. Oh JY, Kim HS, Palanikumar L, Go EM, Jana B, Park SA, et al. Cloaking nanoparticles with protein corona shield for targeted drug delivery. Nature Communications. 2018;9(1):4548.

678. Yan Y, Gause KT, Kamphuis MMJ, Ang C-S, O'Brien-Simpson NM, Lenzo JC, et al. Differential Roles of the Protein Corona in the Cellular Uptake of Nanoporous Polymer Particles by Monocyte and Macrophage Cell Lines. ACS Nano. 2013;7(12):10960–70.
679. Lesniak A, Campbell A, Monopoli MP, Lynch I, Salvati A, Dawson KA. Serum heat inactivation affects protein corona composition and nanoparticle uptake. Biomaterials. 2010;31(36):9511–8.
680. Fleischer CC, Payne CK. Secondary Structure of Corona Proteins Determines the Cell Surface Receptors Used by Nanoparticles. The Journal of Physical Chemistry B. 2014;118(49):14017–26.
681. Deng ZJ, Liang M, Monteiro M, Toth I, Minchin RF. Nanoparticle-induced unfolding of fibrinogen promotes Mac-1 receptor activation and inflammation. Nature nanotechnology. 2011.
682. Gopinath PM, Saranya V, Vijayakumar S, Mythili Meera M, Ruprekha S, Kunal R, et al. Assessment on interactive prospectives of nanoplastics with plasma proteins and the toxicological impacts of virgin, coronated and environmentally released-nanoplastics. Scientific reports. 2019;9(1):8860.
683. Moghimi SM, Haroon HB, Yaghmur A, Hunter AC, Papini E, Farhangrazi ZS, et al. Perspectives on complement and phagocytic cell responses to nanoparticles: From fundamentals to adverse reactions. J Control Release. 2023;356:115–29.
684. Gavin C, Meinke S, Heldring N, Heck KA, Achour A, Iacobaeus E, et al. The Complement System Is Essential for the Phagocytosis of Mesenchymal Stromal Cells by Monocytes. Front Immunol. 2019;10:2249.
685. Das R, Ganapathy S, Settle M, Plow EF. Plasminogen promotes macrophage phagocytosis in mice. Blood. 2014;124(5):679–88.
686. Heissig B, Salama Y, Takahashi S, Osada T, Hattori K. The multifaceted role of plasminogen in inflammation. Cellular Signalling. 2020;75:109761.
687. Ichinose A. Factor XIII is a key molecule at the intersection of coagulation and fibrinolysis as well as inflammation and infection control. International Journal of Hematology. 2012;95(4):362–70.
688. Aliyandi A, Reker-Smit C, Bron R, Zuhorn IS, Salvati A. Correlating Corona Composition and Cell Uptake to Identify Proteins Affecting Nanoparticle Entry into Endothelial Cells. ACS Biomater Sci Eng. 2021;7(12):5573–84.
689. Drakeford C, Aguila S, Roche F, Hokamp K, Fazavana J, Cervantes MP, et al. von Willebrand factor links primary hemostasis to innate immunity. Nat Commun. 2022;13(1):6320.
690. Yan X, Kuipers F, Havekes LM, Havinga R, Dontje B, Poelstra K, et al. The role of apolipoprotein E in the elimination of liposomes from blood by hepatocytes in the mouse. Biochemical and Biophysical Research Communications. 2005;328(1):57–62.
691. Nich C, Takakubo Y, Pajarinen J, Ainola M, Salem A, Sillat T, et al. Macrophages-Key cells in the response to wear debris from joint replacements. J Biomed Mater Res A. 2013;101(10):3033–45.
692. Pozzi D, Caracciolo G, Digiacomo L, Colapicchioni V, Palchetti S, Capriotti AL, et al. The biomolecular corona of nanoparticles in circulating biological media. Nanoscale. 2015;7(33):13958–66.
693. Sharma P, Sen D, Neelakantan V, Shankar V, Jhunjhunwala S. Disparate effects of PEG or albumin based surface modification on the uptake of nano- and micro-particles. Biomaterials Science. 2019;7(4):1411–21.
694. Champion JA, Walker A, Mitragotri S. Role of particle size in phagocytosis of polymeric microspheres. Pharm Res. 2008;25(8):1815–21.

695. Wang L, Wu W-M, Bolan NS, Tsang DCW, Li Y, Qin M, et al. Environmental fate, toxicity and risk management strategies of nanoplastics in the environment: Current status and future perspectives. J Hazard Mater. 2021;401:123415.
696. Koelmans AA, Besseling E, Shim WJ. Nanoplastics in the aquatic environment. Critical review. Marine Anthropogenic Litter2015. p. 325–40.
697. Alimi OS, Claveau-Mallet D, Kurusu RS, Lapointe M, Bayen S, Tufenkji N. Weathering pathways and protocols for environmentally relevant microplastics and nanoplastics: What are we missing? J Hazard Mater. 2022;423:126955.
698. Dusza Hanna M, Katrukha Eugene A, Nijmeijer Sandra M, Akhmanova A, Vethaak AD, Walker Douglas I, et al. Uptake, Transport, and Toxicity of Pristine and Weathered Micro- and Nanoplastics in Human Placenta Cells. Environmental Health Perspectives.130(9):097006.
699. Du T, Yu X, Shao S, Li T, Xu S, Wu L. Aging of Nanoplastics Significantly Affects Protein Corona Composition Thus Enhancing Macrophage Uptake. Environmental Science & Technology. 2023;57(8):3206–17.
700. Ramsperger AFRM, Narayana VKB, Gross W, Mohanraj J, Thelakkat M, Greiner A, et al. Environmental exposure enhances the internalization of microplastic particles into cells. Sci Adv. 2020;6(50):eabd1211.
701. Di Silvio D, Rigby N, Bajka B, MacKie A, Baldelli Bombelli F. Effect of protein corona magnetite nanoparticles derived from bread in vitro digestion on Caco-2 cells morphology and uptake. International Journal of Biochemistry and Cell Biology. 2016.
702. Coreas R, Cao X, DeLoid GM, Demokritou P, Zhong W. Lipid and protein corona of food-grade TiO2 nanoparticles in simulated gastrointestinal digestion. NanoImpact. 2020;20:100272.
703. Collin-Faure V, Vitipon M, Torres A, Tanyeres O, Dalzon B, Rabilloud T. The internal dose makes the poison: higher internalization of polystyrene particles induce increased perturbation of macrophages. Front Immunol. 2023;14:1092743.
704. Miclăuş T, Beer C, Chevallier J, Scavenius C, Bochenkov VE, Enghild JJ, et al. Dynamic protein coronas revealed as a modulator of silver nanoparticle sulphidation in vitro. Nature Communications. 2016;7(1):11770.
705. Jiang P, Zhu Y, Kang K, Luo B, He J, Wu Y. Protein corona of magnetic PEI/siRNA complex under the influence of a magnetic field improves transfection efficiency via complement and coagulation cascades. Journal of Materials Chemistry B. 2019;7(26):4207–16.
706. Shannahan JH, Lai X, Ke PC, Podila R, Brown JM, Witzmann FA. Silver nanoparticle protein corona composition in cell culture media. Plos One. 2013;8(9):e74001.
707. Galmarini S, Hanusch U, Giraud M, Cayla N, Chiappe D, von Moos N, et al. Correction to Beyond Unpredictability: The Importance of Reproducibility in Understanding the Protein Corona of Nanoparticles. Bioconjugate Chemistry. 2019;30(6):1832–.
708. Pisani C, Gaillard J-C, Odorico M, Nyalosaso JL, Charnay C, Guari Y, et al. The timeline of corona formation around silica nanocarriers highlights the role of the protein interactome. Nanoscale. 2017;9(5):1840–51.
709. Qin M, Zhang J, Li M, Yang D, Liu D, Song S, et al. Proteomic analysis of intracellular protein corona of nanoparticles elucidates nano-trafficking network and nano-bio interactions. Theranostics. 2020;10(3):1213–29.
710. Liebezeit G, Liebezeit E. Non-pollen particulates in honey and sugar. Food additives & contaminants Part A, Chemistry, analysis, control, exposure & risk assessment. 2013;30(12):2136–40.
711. ten Hietbrink S, Materić D, Holzinger R, Groeskamp S, Niemann H. Nanoplastic concentrations across the North Atlantic. Nature. 2025;643(8071):412–6.

712. V. L. Leonard S, Liddle CR, Atherall CA, Chapman E, Watkins M, D. J. Calaminus S, et al. Microplastics in human blood: Polymer types, concentrations and characterisation using μFTIR. Environ Int. 2024;188:108751.
713. Physiologically based mathematical models of nanomaterials for regulatory toxicology: A review, (2019).
714. Lu B, Wang J, Hendriks AJ, Nolte TM. Clearance of nanoparticles from blood: effects of hydrodynamic size and surface coatings. Environmental Science: Nano. 2024;11(1):406–17.
715. Dogra P, Butner JD, Ruiz Ramírez J, Chuang Y-l, Noureddine A, Jeffrey Brinker C, et al. A mathematical model to predict nanomedicine pharmacokinetics and tumor delivery. Computational and Structural Biotechnology Journal. 2020;18:518–31.
716. Price E, Gesquiere AJ. Animal simulations facilitate smart drug design through prediction of nanomaterial transport to individual tissue cells. Sci Adv. 2020;6(4):eaax2642.
717. Im C, Kim H, Zaheer J, Kim JY, Lee Y-J, Kang CM, et al. PET Tracing of Biodistribution for Orally Administered ⁶⁴Cu-Labeled Polystyrene in Mice. Journal of Nuclear Medicine. 2022;63(3):461–7.
718. Choi YJ, Woo PJ, Yong L, Sungbaek S, and Hwang DY. In vivo impact assessment of orally administered polystyrene nanoplastics: biodistribution, toxicity, and inflammatory response in mice. Nanotoxicology. 2021;15(9):1180–98.
719. Liang B, Zhong Y, Huang Y, Lin X, Liu J, Lin L, et al. Underestimated health risks: polystyrene micro- and nanoplastics jointly induce intestinal barrier dysfunction by ROS-mediated epithelial cell apoptosis. Particle and Fibre Toxicology. 2021;18(1):20.
720. Liu Z, Zhuan Q, Zhang L, Meng L, Fu X, Hou Y. Polystyrene microplastics induced female reproductive toxicity in mice. J Hazard Mater. 2022;424(Pt C):127629.
721. Ma S, Wang L, Li S, Zhao S, Li F, Li X. Transcriptome and proteome analyses reveal the mechanisms involved in polystyrene nanoplastics disrupt spermatogenesis in mice. Environmental pollution. 2024;342:123086.
722. Liang B, Deng Y, Zhong Y, Chen X, Huang Y, Li Z, et al. Gastrointestinal Incomplete Degradation Exacerbates Neurotoxic Effects of PLA Microplastics via Oligomer Nanoplastics Formation. Adv Sci (Weinh). 2024;11(28):e2401009.
723. Rohatgi A. Webplotdigitizer: Version 4.5. URL https://automeris io/WebPlotDigitizer. 2020;411:860.
724. Brown RP, Delp MD, Lindstedt SL, Rhomberg LR, Beliles RP. Physiological parameter values for physiologically based pharmacokinetic models. Toxicol Ind Health. 1997;13(4):407–84.
725. Faxén H. About T. Bohlin's paper: On the drag on rigid spheres, moving in a viscous liquid inside cylindrical tubes. Kolloid-Zeitschrift. 1959;167(2):146–.
726. Kellen MR, Bassingthwaighte JB. An integrative model of coupled water and solute exchange in the heart. Am J Physiol Heart Circ Physiol. 2003;285(3):H1303–16.
727. Bean CP. The physics of porous membranes--neutral pores. Membranes. 1972;1:1–54.
728. BASSINGTHWAIGHTE JB. A Practical Extension of Hydrodynamic Theory of Porous Transport for Hydrophilic Solutes. Microcirculation. 2006;13(2):111–8.
729. Boyer JL. Bile Formation and Secretion. Comprehensive Physiology2013. p. 1035–78.
730. Baron. KT. mrgsolve: Simulate from ODE-Based Models. R package version 1.5.2, 2024 [Available from: https://github.com/metrumresearchgroup/mrgsolve.
731. Davies B, Morris T. Physiological parameters in laboratory animals and humans. Pharmaceutical research. 1993;10(7):1093–5.
732. Hugenholtz F, de Vos WM. Mouse models for human intestinal microbiota research: a critical evaluation. Cellular and Molecular Life Sciences. 2018;75(1):149–60.

733. Satchell SC, Braet F. Glomerular endothelial cell fenestrations: an integral component of the glomerular filtration barrier. Am J Physiol Renal Physiol. 2009;296(5):F947–56.
734. ICRP. IBasic Anatomical and Physiological Data for Use in Radiological Protection Reference Values. ICRP Publication 89. . Ann ICRP 32 (3-4). 2002.
735. Soetaert K, Petzoldt T. Inverse Modelling, Sensitivity and Monte Carlo Analysis in R Using Package FME. Journal of Statistical Software. 2010;33(3):1 – 28.
736. Price WL. A controlled random search procedure for global optimisation. The Computer Journal. 1977;20(4):367–70.
737. Nelder JA, Mead R. A Simplex Method for Function Minimization. The Computer Journal. 1965;7(4):308–13.
738. Fragki S, Piersma AH, Westerhout J, Kienhuis A, Kramer NI, Zeilmaker MJ. Applicability of generic PBK modelling in chemical hazard assessment: A case study with IndusChemFate. Regul Toxicol Pharm. 2022;136:105267.
739. Punt A, Louisse J, Pinckaers N, Fabian E, van Ravenzwaay B. Predictive Performance of Next Generation Physiologically Based Kinetic (PBK) Model Predictions in Rats Based on In Vitro and In Silico Input Data. Toxicol Sci. 2022;186(1):18–28.
740. Moerenhout TMJA, Chen J, Bouwmeester H, Rietjens IMCM, Kramer NI. Development of a Generic Physiologically Based Kinetic Model for the Prediction of Internal Exposure to Organophosphate Pesticides. Environmental science & technology. 2024;58(42):18834–45.
741. Müller K, Fedosov DA, Gompper G. Margination of micro- and nano-particles in blood flow and its effect on drug delivery. Scientific reports. 2014;4(1):4871.
742. Decuzzi P, Lee S, Bhushan B, Ferrari M. A theoretical model for the margination of particles within blood vessels. Ann Biomed Eng. 2005;33(2):179–90.
743. Cooley M, Sarode A, Hoore M, Fedosov DA, Mitragotri S, Sen Gupta A. Influence of particle size and shape on their margination and wall-adhesion: implications in drug delivery vehicle design across nano-to-micro scale. Nanoscale. 2018;10(32):15350–64.
744. Curry F. Handbook of Physiology. The Cardiovascular System. Microcirculation. Bethesda, MD: American Physiological Society. 1984:309–74.
745. Mescam M, Eliat PA, Fauvel C, Certaines JD, Bézy-Wendling J. A physiologically based pharmacokinetic model of vascular-extravascular exchanges during liver carcinogenesis: application to MRI contrast agents. Contrast Media Mol Imaging. 2007;2(5):215–28.
746. Barboriak DP, MacFall JR, Viglianti BL, Dewhirst Dvm MW. Comparison of three physiologically-based pharmacokinetic models for the prediction of contrast agent distribution measured by dynamic MR imaging. J Magn Reson Imaging. 2008;27(6):1388–98.
747. Mescam M, Kretowski M, Bezy-Wendling J. Multiscale model of liver DCE-MRI towards a better understanding of tumor complexity. IEEE Trans Med Imaging. 2010;29(3):699–707.
748. Ilium L, Davis SS, Wilson CG, Thomas NW, Frier M, Hardy JG. Blood clearance and organ deposition of intravenously administered colloidal particles. The effects of particle size, nature and shape. Int J Pharm. 1982;12(2):135–46.
749. Lin P, Chen JW, Chang LW, Wu JP, Redding L, Chang H, et al. Computational and ultrastructural toxicology of a nanoparticle, Quantum Dot 705, in mice. Environmental Science and Technology. 2008.
750. Li D, Johanson G, Emond C, Carlander U, Philbert M, Jolliet O. Physiologically based pharmacokinetic modeling of polyethylene glycol-coated polyacrylamide nanoparticles in rats. Nanotoxicology. 2014.

751. Dogra P, Adolphi NL, Wang Z, Lin Y-S, Butler KS, Durfee PN, et al. Establishing the effects of mesoporous silica nanoparticle properties on in vivo disposition using imaging-based pharmacokinetics. Nature Communications. 2018;9(1):4551.
752. The road to nowhere: Equilibrium partition coefficients for nanoparticles, (2014).
753. Tao J, Deng P, Lin M, Chen C, Ma Q, Yang L, et al. Long-term exposure to polystyrene microplastics induces hepatotoxicity by altering lipid signatures in C57BL/6J mice. Chemosphere. 2024;347:140716.
754. Wyss PP, Lamichhane SP, Abed A, Vonwil D, Kretz O, Huber TB, et al. Renal clearance of polymeric nanoparticles by mimicry of glycan surface of viruses. Biomaterials. 2020;230:119643.
755. Henry C, Hartsock RJ, Kirk Z, Behrer R. Detection of Viruria in Cytomegalovirus-infected Infants by Electron Microscopy. American Journal of Clinical Pathology. 1978;69(4):435–9.
756. Laine RF, Albecka A, Van De Linde S, Rees EJ, Crump CM, Kaminski CF. Structural analysis of herpes simplex virus by optical super-resolution imaging. Nature Communications. 2015;6.
757. Dalpiaz A, Fogagnolo M, Ferraro L, Beggiato S, Hanuskova M, Maretti E, et al. Bile salt-coating modulates the macrophage uptake of nanocores constituted by a zidovudine prodrug and enhances its nose-to-brain delivery. European Journal of Pharmaceutics and Biopharmaceutics. 2019;144:91–100.
758. Jiang P, Yuan Gh, Jiang Br, Zhang Jy, Wang Yq, Lv Hj, et al. Effects of microplastics (MPs) and tributyltin (TBT) alone and in combination on bile acids and gut microbiota crosstalk in mice. Ecotox Environ Safe. 2021.
759. Yadav H, Khan MRH, Quadir M, Rusch KA, Mondal PP, Orr M, et al. Cutting Boards: An Overlooked Source of Microplastics in Human Food? Environmental science & technology. 2023;57(22):8225–35.
760. Witzig CS, Földi C, Wörle K, Habermehl P, Pittroff M, Müller YK, et al. When Good Intentions Go Bad-False Positive Microplastic Detection Caused by Disposable Gloves. Environmental science & technology. 2020;54(19):12164–72.
761. Rauert C, Pan Y, Okoffo ED, O'Brien JW, Thomas KV. Extraction and Pyrolysis-GC-MS analysis of polyethylene in samples with medium to high lipid content. Journal of Environmental Exposure Assessment. 2022;1(2):13.
762. Liang G, Zhang Y. Genetic and epigenetic variations in iPSCs: potential causes and implications for application. Cell Stem Cell. 2013;13(2):149–59.
763. Saari J, Siddique F, Korpela S, Mäntylä E, Ihalainen TO, Kaukinen K, et al. Toward Xeno-Free Differentiation of Human Induced Pluripotent Stem Cell-Derived Small Intestinal Epithelial Cells. Int J Mol Sci. 2022;23(3).
764. Deplancke B, Gaskins HR. Microbial modulation of innate defense: goblet cells and the intestinal mucus layer123. The American Journal of Clinical Nutrition. 2001;73(6):1131S–41S.
765. Chen C-Y, Lin Z. Exploring the potential and challenges of developing physiologically-based toxicokinetic models to support human health risk assessment of microplastic and nanoplastic particles. Environ Int. 2024;186:108617.
766. Takayama K, Negoro R, Yamashita T, Kawai K, Ichikawa M, Mori T, et al. Generation of Human iPSC-Derived Intestinal Epithelial Cell Monolayers by CDX2 Transduction. Cell Mol Gastroenterol Hepatol. 2019;8(3):513–26.
767. Takenaka T, Harada N, Kuze J, Chiba M, Iwao T, Matsunaga T. Application of a Human Intestinal Epithelial Cell Monolayer to the Prediction of Oral Drug Absorption in Humans as a Superior Alternative to the Caco-2 Cell Monolayer. J Pharm Sci. 2016;105(2):915–24.
768. Bevins CL. The Paneth cell and the innate immune response. Curr Opin Gastroenterol. 2004;20(6):572–80.

769. Boonekamp KE, Dayton TL, Clevers H. Intestinal organoids as tools for enriching and studying specific and rare cell types: advances and future directions. Journal of Molecular Cell Biology. 2020;12(8):562–8.
770. Fujii M, Matano M, Toshimitsu K, Takano A, Mikami Y, Nishikori S, et al. Human Intestinal Organoids Maintain Self-Renewal Capacity and Cellular Diversity in Niche-Inspired Culture Condition. Cell Stem Cell. 2018;23(6):787–93.e6.
771. Grouls M, Janssen AWF, Duivenvoorde LPM, Hooiveld GJEJ, Bouwmeester H, van der Zande M. Differential gene expression in iPSC-derived human intestinal epithelial cell layers following exposure to two concentrations of butyrate, propionate and acetate. Scientific reports. 2022;12(1):13988.
772. De Smedt K, Vos E. The Application of the Precautionary Principle in the EU. In: Mieg HA, editor. The Responsibility of Science. Cham: Springer International Publishing; 2022. p. 163–86.
773. Basson MD, Turowski G, Emenaker NJ. Regulation of human (Caco-2) intestinal epithelial cell differentiation by extracellular matrix proteins. Experimental cell research. 1996;225(2):301–5.
774. Schwarzbauer J. Basement membranes: Putting up the barriers. Current biology : CB. 1999;9(7):R242–4.
775. Stylianopoulos T, Poh MZ, Insin N, Bawendi MG, Fukumura D, Munn LL, et al. Diffusion of particles in the extracellular matrix: the effect of repulsive electrostatic interactions. Biophys J. 2010;99(5):1342–9.
776. Rezakhani S, Gjorevski N, Lutolf MP. Extracellular matrix requirements for gastrointestinal organoid cultures. Biomaterials. 2021;276:121020.
777. Zhang Y, Lukacova V, Reindl K, Balaz S. Quantitative characterization of binding of small molecules to extracellular matrix. J Biochem Biophys Methods. 2006;67(2-3):107–22.
778. Takahashi Y, Sato S, Kurashima Y, Yamamoto T, Kurokawa S, Yuki Y, et al. A Refined Culture System for Human Induced Pluripotent Stem Cell-Derived Intestinal Epithelial Organoids. Stem Cell Reports. 2018.
779. Totaro S, Cotogno G, Rasmussen K, Pianella F, Roncaglia M, Olsson H, et al. The JRC Nanomaterials Repository: A unique facility providing representative test materials for nanoEHS research. Regul Toxicol Pharm. 2016;81:334–40.
780. Linsinger TP, Birgersson-Liebich A, Lamberty A, Pellizzato F, Venelinov T, Voorspoels S. Development of the first certified reference materials for several brominated flame retardants in polymers. Anal Chem. 2009;81(10):3792–800.
781. Hsissou R, Seghiri R, Benzekri Z, Hilali M, Rafik M, Elharfi A. Polymer composite materials: A comprehensive review. Composite Structures. 2021;262:113640.
782. Coleman EA. Plastics additives. Applied Plastics Engineering Handbook: Elsevier; 2017. p. 489–500.
783. McColley CJ, Nason JA, Harper BJ, Harper SL. An assessment of methods used for the generation and characterization of cryomilled polystyrene micro- and nanoplastic particles. Microplastics and Nanoplastics. 2023;3(1):20.
784. Manju Sudheer M, Fazli A, Sganga S, Tirelli N, Carzino R, Veronesi M, et al. Poly(lactic acid) nanoplastics through laser ablation: establishing a reference model for mimicking biobased nanoplastics in aquatic environments. Environmental Science: Nano. 2025;12(4):2395–406.
785. Cole M. A novel method for preparing microplastic fibers. Scientific reports. 2016;6(1):34519.
786. Schmiedgruber M, Hufenus R, Mitrano DM. Mechanistic understanding of microplastic fiber fate and sampling strategies: Synthesis and utility of metal doped polyester fibers. Water Res. 2019;155:423–30.

787. Hernandez E, Nowack B, Mitrano DM. Polyester Textiles as a Source of Microplastics from Households: A Mechanistic Study to Understand Microfiber Release During Washing. Environmental science & technology. 2017;51(12):7036–46.
788. Abdelkhaliq A, van der Zande M, Punt A, Helsdingen R, Boeren S, Vervoort JJM, et al. Impact of nanoparticle surface functionalization on the protein corona and cellular adhesion, uptake and transport. Journal of nanobiotechnology. 2018.
789. Ashkarran AA. Early Stage Soft Protein Corona Identification on Nanoparticles via Extended Size Exclusion Chromatography. Anal Chem. 2025;97(30):16449–55.
790. Weber C, Simon J, Mailänder V, Morsbach S, Landfester K. Preservation of the soft protein corona in distinct flow allows identification of weakly bound proteins. Acta Biomaterialia. 2018;76:217–24.
791. Mohammad-Beigi H, Hayashi Y, Zeuthen CM, Eskandari H, Scavenius C, Juul-Madsen K, et al. Mapping and identification of soft corona proteins at nanoparticles and their impact on cellular association. Nature Communications. 2020;11(1):4535.
792. Epanchintseva AV, Poletaeva JE, Bakhno IA, Belov VV, Grigor'eva AE, Baranova SV, et al. Fixation and Visualization of Full Protein Corona on Lipid Surface of Composite Nanoconstruction. Nanomaterials. 2023;13(24):3094.
793. Nienhaus K, Nienhaus GU. Mechanistic Understanding of Protein Corona Formation around Nanoparticles: Old Puzzles and New Insights. Small. 2023;19(28):2301663.
794. Chang M, Alsaigh T, Kistler EB, Schmid-Schönbein GW. Breakdown of mucin as barrier to digestive enzymes in the ischemic rat small intestine. PloS one. 2012;7(6):e40087.
795. Chang M, Kistler EB, Schmid-Schönbein GW. Disruption of the mucosal barrier during gut ischemia allows entry of digestive enzymes into the intestinal wall. Shock. 2012;37(3):297–305.
796. Johansson MEV, Sjövall H, Hansson GC. The gastrointestinal mucus system in health and disease. Nature Reviews Gastroenterology & Hepatology. 2013;10(6):352–61.
797. Marchbank T, Freeman TC, Playford RJ. Human pancreatic secretory trypsin inhibitor. Distribution, actions and possible role in mucosal integrity and repair. Digestion. 1998;59(3):167–74.
798. Choki K, Li S, Ye A, Jameson GB, Singh H. Fate of hydroxyapatite nanoparticles during dynamic in vitro gastrointestinal digestion: the impact of milk as a matrix. Food Funct. 2021;12(6):2760–71.
799. Öz Elrai H, Mısırlı NS, Bayan Karakadılar E, Yildirim-Elikoğlu S, Dudak FC. Impact of Milk on the Behavior and Toxicity of Nanosized SiO(2) Particles during In Vitro Digestion Simulation. ACS Omega. 2025;10(24):26148–63.
800. Lima T, Bernfur K, Vilanova M, Cedervall T. Understanding the Lipid and Protein Corona Formation on Different Sized Polymeric Nanoparticles. Scientific reports. 2020;10(1):1129.
801. Olenick LL, Troiano JM, Vartanian A, Melby ES, Mensch AC, Zhang L, et al. Lipid Corona Formation from Nanoparticle Interactions with Bilayers. Chem. 2018;4(11):2709–23.
802. Andersen CJ. Lipid Metabolism in Inflammation and Immune Function. Nutrients. 2022;14(7).
803. Sharon N. Carbohydrates as recognition determinants in phagocytosis and in lectin-mediated killing of target cells. Biol Cell. 1984;51(2):239–45.
804. Kim SH, Lee C, Jang GJ, Yoo S, Lee S, Han SY. Understanding the Biomolecular Coronas of High-Density Lipoproteins on PEGylated Au Nanoparticles: Implication for Lipid Corona Formation in the Blood. ACS Applied Nano Materials. 2022;5(2):2018–28.
805. Grintzalis K, Lawson TN, Nasser F, Lynch I, Viant MR. Metabolomic method to detect a metabolite corona on amino-functionalized polystyrene nanoparticles. Nanotoxicology. 2019;13(6):783–94.

806. Maity A, De SK, Chakraborty A. Interaction of Aromatic Amino Acid-Functionalized Gold Nanoparticles with Lipid Bilayers: Insight into the Emergence of Novel Lipid Corona Formation. Journal of Physical Chemistry B. 2021;125(8):2113–23.
807. Maity A, Nath P, Bagchi D, Debnath S, Tabassum H, Sinha S, et al. Formation of lipid corona on Ag nanoparticles and its impact on Ag+ ion dissolution and aggregation of Ag nanoparticles against external stimuli. Chemical Physics Impact. 2024;8.
808. Palchetti S, Digiacomo L, Pozzi D, Zenezini Chiozzi R, Capriotti AL, Laganà A, et al. Effect of Glucose on Liposome–Plasma Protein Interactions: Relevance for the Physiological Response of Clinically Approved Liposomal Formulations. Advanced Biosystems. 2019;3(2).
809. Doherty BT, Hammel SC, Daniels JL, Stapleton HM, Hoffman K. Organophosphate Esters: Are These Flame Retardants and Plasticizers Affecting Children's Health? Curr Environ Health Rep. 2019;6(4):201–13.
810. Zlatnik MG. Endocrine-Disrupting Chemicals and Reproductive Health. J Midwifery Womens Health. 2016;61(4):442–55.
811. Salawu OA, Olivares CI, Adeleye AS. Adsorption of PFAS onto secondary microplastics: A mechanistic study. J Hazard Mater. 2024;470:134185.
812. Kaur K, Reddy S, Barathe P, Oak U, Shriram V, Kharat SS, et al. Microplastic-associated pathogens and antimicrobial resistance in environment. Chemosphere. 2022;291:133005.
813. Groh KJ, Backhaus T, Carney-Almroth B, Geueke B, Inostroza PA, Lennquist A, et al. Overview of known plastic packaging-associated chemicals and their hazards. The Science of the total environment. 2019;651(Pt 2):3253–68.
814. Naasz S, Altenburger R, Kühnel D. Environmental mixtures of nanomaterials and chemicals: The Trojan-horse phenomenon and its relevance for ecotoxicity. Science of the Total Environment. 2018;635:1170–81.
815. Koch HM, Calafat AM. Human body burdens of chemicals used in plastic manufacture. Philosophical transactions of the Royal Society of London Series B, Biological sciences. 2009;364(1526):2063–78.
816. Casas M, Chevrier C, Hond ED, Fernandez MF, Pierik F, Philippat C, et al. Exposure to brominated flame retardants, perfluorinated compounds, phthalates and phenols in European birth cohorts: ENRIECO evaluation, first human biomonitoring results, and recommendations. International Journal of Hygiene and Environmental Health. 2013;216(3):230–42.
817. Zheng G, Eick SM, Salamova A. Elevated Levels of Ultrashort- and Short-Chain Perfluoroalkyl Acids in US Homes and People. Environmental Science and Technology. 2023;57(42):15782–93.
818. Pletz M. Ingested microplastics: Do humans eat one credit card per week? Journal of Hazardous Materials Letters. 2022;3:100071.
819. Pikuda O, Xu EG, Berk D, Tufenkji N. Toxicity Assessments of Micro- and Nanoplastics Can Be Confounded by Preservatives in Commercial Formulations. Environmental Science & Technology Letters. 2019;6(1):21–5.
820. Malafaia G, Luz TMd, Ahmed MAI, Karthi S, Araújo APdC. When toxicity of plastic particles comes from their fluorescent dye: a preliminary study involving neotropical Physalaemus cuvieri tadpoles and polyethylene microplastics. Journal of Hazardous Materials Advances. 2022;6:100054.
821. Catarino AI, Frutos A, Henry TB. Use of fluorescent-labelled nanoplastics (NPs) to demonstrate NP absorption is inconclusive without adequate controls. Science of The Total Environment. 2019;670:915–20.

822. Nizzero S, Li F, Zhang G, Venuta A, Borsoi C, Mai J, et al. Systematic comparison of methods for determining the in vivo biodistribution of porous nanostructured injectable inorganic particles. Acta Biomater. 2019;97:501–12.
823. Backhouse CM, Ball PR, Booth S, Kelshaw MA, Potter SR, Mccollum CN. Particulate contaminants of intravenous medications and infusions. Journal of Pharmacy and Pharmacology. 1987;39(4):241–5.
824. Kuramoto K, Shoji T, Nakagawa Y. Usefulness of the Final Filter of the IV Infusion Set in Intravenous Administration of Drugs
 —Contamination of Injection Preparations by Insoluble Microparticles and Its Causes&mdash. YAKUGAKU ZASSHI. 2006;126(4):289–95.
825. Garvan JM, Gunner BW. THE HARMFUL EFFECTS OF PARTICLES IN INTRAVENOUS FLUIDS. Med J Aust. 1964;2:1–6.
826. Perez M, Maiguy-Foinard A, Barthélémy C, Décaudin B, Odou P. Particulate Matter in Injectable Drugs: Evaluation of Risks to Patients. Pharmaceutical Technology in Hospital Pharmacy. 2016;1(2):91–103.
827. Kanke M, Simmons GH, Weiss DL, Bivins BA, DeLuca PP. Clearance of ¹⁴¹Ce-labeled microspheres from blood and distribution in specific organs following intravenous and intraarterial administration in beagle dogs. Journal of Pharmaceutical Sciences. 1980;69(7):755–62.
828. Short A, Montoya ML, Gebb SA, Presson Jr RG, Wagner Jr WW, Capen RL. Pulmonary capillary diameters and recruitment characteristics in subpleural and interior networks. Journal of Applied Physiology. 1996;80(5):1568–73.
829. Toropov AA, Toropova AP, Benfenati E, Leszczynska D, Leszczynski J. SMILES-based optimal descriptors: QSAR analysis of fullerene-based HIV-1 PR inhibitors by means of balance of correlations. Journal of Computational Chemistry. 2010;31(2):381–92.
830. Fourches D, Pu D, Tassa C, Weissleder R, Shaw SY, Mumper RJ, et al. Quantitative Nanostructure−Activity Relationship Modeling. ACS nano. 2010;4(10):5703–12.
831. Fourches D, Pu D, Tropsha A. Exploring Quantitative Nanostructure-Activity Relationships (QNAR) Modeling as a Tool for Predicting Biological Effects of Manufactured Nanoparticles. Combinatorial Chemistry & High Throughput Screening. 2011;14(3):217–25.
832. Puzyn T, Rasulev B, Gajewicz A, Hu X, Dasari TP, Michalkova A, et al. Using nano-QSAR to predict the cytotoxicity of metal oxide nanoparticles. Nature nanotechnology. 2011;6(3):175–8.
833. Sizochenko N, Syzochenko M, Fjodorova N, Rasulev B, Leszczynski J. Evaluating genotoxicity of metal oxide nanoparticles: Application of advanced supervised and unsupervised machine learning techniques. Ecotox Environ Safe. 2019;185:109733.
834. Chou WC, Chen Q, Yuan L, Cheng YH, He C, Monteiro-Riviere NA, et al. An artificial intelligence-assisted physiologically-based pharmacokinetic model to predict nanoparticle delivery to tumors in mice. J Control Release. 2023;361:53–63.
835. Ozbek O, Genc DE, O. Ulgen K. Advances in Physiologically Based Pharmacokinetic (PBPK) Modeling of Nanomaterials. ACS Pharmacology & Translational Science. 2024;7(8):2251–79.
836. Chen P, Dong B, Yao W. Numerical simulation study of nanoparticle diffusion in gray matter. Computational and Structural Biotechnology Journal. 2024;25:95–104.
837. He X, Yang Y, Han Y, Cao C, Zhang Z, Li L, et al. Extracellular matrix physical properties govern the diffusion of nanoparticles in tumor microenvironment. Proceedings of the National Academy of Sciences of the United States of America. 2023;120(1):e2209260120.
838. Islam MA, Rahman SMM, Mim JJ, Khan S, Khan F, Patwary MAI, et al. Applications of molecular dynamics in nanomaterial design and characterization - A review. Chemical Engineering Journal Advances. 2025;22:100731.
839. Haase A, Klaessig F, Nymark P, Paul K, Greco D. EU US Roadmap Nanoinformatics 20302018.

Summary

The invention of plastic has revolutionized our world by providing a readily available, moldable material which is light, strong and durable. However, excessive use of plastics has led to universal pollution of our planet. Over time plastic waste and products can degrade, leading to release of microscopic particles called microplastics and nanoplastics(MNPs). MNPs are abundant in our food, the water we drink and the air we breathe and in turn human exposure is unavoidable. Oral ingestion is the biggest source of MNP exposure for humans and amidst all human organs the intestine faces the largest MNP exposure which potentially affects intestinal health. In animals, MNP exposure can cause inflammatory effects and barrier disruption in the intestine, however it is unknown if these effects occur in humans. Given the diversity of MNPs found in nature, exhaustive safety testing through animal studies is undesirable and instead *In vitro* and *in silico* methods (collectively called New Approach Methodologies (NAMs)) can aid MNP toxicity assessment. Current MNP research with NAMs has limited ability to predict toxicity in humans due to lack of assessment of true-to-life secondary MNPs, aberrant phenotype of *in vitro* cell lines and a lack of understanding of mechanisms like protein-corona formation and biokinetic processes.

The aim of this thesis was to improve in vitro and in silico NAMs for MNP toxicity assessment and to improve understanding of the formation and effects of the protein corona on MNPs.

Chapter 1 introduces the aim of the thesis and outlined key aspects of MNPs including their formation, properties, human exposure, biokinetics and potential toxicity.

Chapter 2 provides a review on current use of *in vitro* NAMs for intestinal toxicity, considerations when assessing MNPs with *in vitro* models and the potential of stem-cell derived models for MNP toxicity testing. The chapter describes that cancer-cell lines like Caco-2 and Caco-2 coculture with other cells are the most frequently used models for MNP testing, however phenotypic alterations due to the cancerous origin of Caco-2 may affect the observed toxicity. Instead, stem-cell derived models have fewer phenotypic alteration compared to cell lines and can give rise to a diversity of relevant cell types. In this chapter it was concluded that while the use of stem-cell derived models is still infrequent, their advantages over cell lines makes them well-suited for MNP toxicity testing.

In **Chapter 3** a two-dimensional induced pluripotent stem-cell (iPSC) derived intestinal model was characterized and compared to Caco-2 cells in their responsiveness to inflammatory stimulants. The iPSC derived intestinal epithelial model was differentiated on an insert separating the apical and basolateral compartments, allowing the assessment of

barrier disruption permeability using TEER. The iPSC derived model showed the presence of enterocytes, goblet cells and Paneth cells as indicated by expression of Villin, Mucin-2 and Chromogranin-A. Next, both the iPSC-derived intestinal epithelia and differentiated Caco-2 cells were exposed to LPS and nigericin, which act as stimulatory agents for TLR-4 induced inflammation. Co-treatment of LPS and nigericin resulted in significant cytotoxicity and barrier disruption for the iPSC-derived epithelium. Furthermore, the co-treatment increased the gene-expression and secretion of the pro-inflammatory cytokines IL-6, IL-8 and TNF-α. On the contrary, LPS and nigericin co-treatment caused no significant toxic effects in the Caco-2 model. It was concluded that the iPSC-derived intestinal epithelia shows improved sensitivity over Caco-2 models for barrier disruption, cytotoxicity and cytokine secretion.

Until now, MNP research was mostly conducted with primary polystyrene (PS) MNPs which only reflect a small part of human exposure. Therefore in **Chapter 4** we utilized the iPSC derived intestinal model from **Chapter 3** to assess and compare the toxicity of primary PS MNPs and secondary polylactic acid (PLA), polypropylene-Talc (PP-Talc), Polyethylene terephthalate-TiO_2 (PET-TiO_2), polyvinyl chloride (PVC) and polyamide (PA) MNPs. iPSC exposure to PET-TiO_2 and PVC caused a significant drop in TEER, indicating potential effects on barrier integrity. Exposure to PET-TiO_2, PP-Talc or PA caused accumulation of intracellular reactive oxygen species (ROS), while exposure to PP-Talc, PVC or PA could induce pro-inflammatory cytokine secretion. In contrast no effects were observed with PS or PLA particles highlighting MNP specific toxicity. To investigate whether the protein corona influenced cellular toxicity the protein corona of all MNPs was isolated and measured using LC-MS-MS. The secondary MNPs inducing ROS showed a significant increase in binding of ROS scavenging proteins compared to PS while secondary NPs inducing cytokine secretion showed a significant increase in pro-inflammatory opsonin binding compared to PS. Based on this observation we concluded that sequestering of proteins protective against ROS and presentation of pro-inflammatory on the MNP surface are plausible mechanisms of protein-corona induced toxicity. After confirming significant correlation between the protein corona composition and effects it was concluded that the protein corona plausibly affects in vitro toxicity outcomes.

In **chapter 5** the role of in vitro digestion on the protein corona of MNPs was investigated and linked to MNP properties using a panel of PS MNPs of varied size and charge. First, the dynamic change of the protein corona was assessed by performing in vitro digestion with MNPs and assessing whether the protein corona changes after exposure to cell culture medium with fetal bovine serum (representative of blood proteins). The digestion associated protein corona was sparse compared to previous observations in blood and could be retained and affect subsequent corona formation when exposed to cell-culture medium. This indicates that the history of the matrices in which the MNP resided can

affect protein corona and that the protein corona in blood may be different for inhaled and ingested MNPs. Afterwards, the effect of the digestion associated protein corona on phagocytosis by THP-1 derived macrophages was assessed and compared to MNPs which were not in vitro digested. In vitro digestion significantly affected the uptake of uncharged MNPs ≤200nm but had no significant effect on MNPs ≥ 500nm or charged MNPs. After confirming that the protein corona composition was correlated to the altered uptake of MNPs it was concluded that digestion should be considered when assessing uncharged MNPs ≤ 200nm but is less relevant for larger or strongly charged MNPs.

At the moment there is a lack of PBK models which allow translation of *in vitro* results to *in vivo* exposure (QIVIVE) for MNPs. In **chapter 6** we implement and adapt a mechanistic colloid-PBK model for the prediction of MNP tissue distribution in humans and mice after oral exposure. The PBK model used hydrodynamic formulas to predict MNP transport through capillary vessels and predicted oral absorption of MNPs based on the bioavailability reported in rodents. The mechanistic mouse model accurately predicted observed tissue concentrations within a 10-fold difference for blood (94%), lung (88%), kidney (75%), heart (75%) and gut (75%) when used to predict tissue concentrations after single oral administration of radiolabelled PS. When considering both acute and chronic exposure, the mechanistic PBK model predicted mouse tissue concentrations within 10-folds in approximately 50% for blood and around 30-40% for remaining tissues. When compared to an empirically fit model, the mechanistic PBK model showed improved prediction of mouse validation data. To predict tissue concentrations in humans, lifelong (75 years) oral exposure to 5 µg/week (80) of MNPs was simulated. The model indicated three separate biokinetic patterns of MNPs and suggests that nanoplastics may not be able to accumulate efficiently in the body and that a tempered risk perception of nanoplastics may be warranted. Regardless of particle size, a similar concentration between blood and organs was observed which indicates that the blood concentration may potentially be used as a proxy for MNP tissue concentrations. The predicted MNP concentrations in human internal tissues ranged from 0.23 pg/g to 15 ng/g. While the lack of high-quality validation data prevents estimation of model accuracy, the predicted tissue concentrations in humans are considerably lower tissue concentrations than previously thought.

Finally **Chapter 7** presents the general discussion, the main conclusions of the thesis and future perspectives on the use of NAMs for MNP toxicity testing. The main conclusions highlighted are: 1. That stem-cell derived models are suitable for MNP testing and show improved sensitivity over cell-line models 2. That the protein corona affects both transport and toxicity of MNPs and that in vitro digestion should be included when assessing uncharged MNPs ≤ 200nm 3. That the toxicity of secondary MNPs is different from primary PS MNPs, warranting their inclusion in MNP safety assessment 4. That the MNP

concentrations in human non-barrier organs is unlikely to elicit toxic effects given the current estimates of MNP exposure.

Overall the studies described in this thesis indicate that the gut is one of the target organs of environmental microplastics which may be harmful to the human intestine, and that a realistic protein corona composition needs to be considered for both toxicokinetic and toxicodynamic assessment of microplastics.

Acknowledgements

Well, the day has finally come. After four and a bit years of experiments, literature study and social activities I have finalized my thesis. Throughout these four years I have met many wonderful people who have influenced me both personally and professionally. While a thesis attests to ones personal capacity as a scientist, it is also the culmination of a PhD which could never be finalized by ones lonesome. Therefore, I want to spent the next few pages express gratitude to the people without whom my PhD would not be the same.

First, I want to thank my direct promotor Hans and ex-promotor Ivonne for giving me the opportunity to do my PhD at tox.

Ivonne, we have not worked together very intensely, but your guidance during my first year of PhD and our occasional discussions always forced me to keenly think about my plans and what I actually intend to achieve, a skill which will undoubtedly be needed in the future. I fondly look back on all the coffee breaks, meetings for social gatherings, and overall great personal commitment you have shown throughout my PhD. We all know that you are going through hard times right now, and while we cannot do anything concretely to help you, know our hearts go out to you.

Hans, we have closely worked together from the start of my PhD all the way till the end. Our many discussions and involvement in the international consortia have greatly enabled me to deepen my knowledge on nanoparticles and toxicology in general. You were always proactive in stimulating my growth through the suggestion of literature or useful meetings and by discussing whether novel developments in the field could be adopted in our lab. Our discussions forced me to consider potential ambiguity in sentences and harmonization of documents, a useful skill that did not come natural to me. Besides the professional aspect, your suggestions for me to be proactive in organizing fun events at toxicology after covid and your general openness on issues and developments at the department helped me develop as a person. Thank you for all the time and effort you have put in my supervision, all the opportunities to grow as a scientist and for the many fun memories at the department.

In addition to my promotors, I also want to thank my co-promotor **Mathias**. Mathias you were always a great sparring partner for ideas and a role model for how early-career particle toxicologists should be. You applied at toxicology for a postdoc position at the momentum project right after my first year at tox. At the time I had already formed a mental image of a stern knowledgeable German researcher based on your papers and resume, so you can imagine my surprise when you turned out to be a very jolly knowledgeable

German researcher. Back then, there were many aspects of particle toxicology I was still uncertain about, which made your knowledge invaluable to (in)-validate my ideas and to learn some of the ins and outs of particle toxicology. Throughout my PhD I have known you as a post-doc, Herr labormanager and full-blown Toxikologischer Wissenschaftler. While you initially felt hesitant to accept the position of permanent staff, I feel proud to have had a tiny hand in pushing you towards the researcher position you have today. We have intensely worked together on all of my papers and on other ideas at the department, and I was happy that you were always there to help with my project and that you fairly considered many of my ideas and helped shape their implementation at tox. Additionally, thanks for getting me into sports, piano and guitar and for the killer birthday parties. Mathias, thanks for your involvement in my PhD and for overall being a great friend.

I also want to thank and my opponents for taking the time to read and evaluate my thesis, without which it would not be possible to warrant the academic standard of our degree.

Then I want to thank my co-authors and the PlasticHeal consortia/CUSP cluster. **Sjef** and **Mojtaba**, thank you for supporting my proteomics and initial flow-cytometry experiments. To the members of the plasticHeal consortium, thank you for all the opportunities to discuss my work, for the social events, the funding and most of all the work you have put in our papers.

To my paranymphs **Gijs and Thijs**.
Gijs, you have an unmatched talent for "slap geouwehoer". Especially in a professional environment where you have to set your own goals and timelines, I think your talent for taking a step back yet somehow maintaining progress is praiseworthy. Talking about timelines, you somehow always seemed to be more up to date on my deadlines and goals than me, which at the same time was infuriating, hilarious and motivating. This always stimulated me to give it my all, and while I was not able to beat you at the Veluweloop last year, at least I consistently beat you at karaoke. Additionally, your uncompromising humour was in equal parts funny and a great mirror for the many flaws we have as people. In general people avoid these topics, but I always enjoyed our 11 o'clock "onder de bus gooien" moment as it always helped me "keep it real". Just be sure not to get yourself in trouble by being too frank.

Thijs, I think you are one of the most unintentionally funny people I know. You exude dryness from all your actions and gestures, and regardless of subject matter our conversations sooner or later I was smiling ear-to-ear. Additionally, you were always enthusiastic about collaborations and while our integrated microparticle-chylomicron PBK shiny app has not yet taken roots, I have good hopes for the future. Your goofy demeanour allowed for many jokes and running gags which will not quickly be forgotten (looking at you

travel-Thijs and Jäger-Thijster). Thank you for being part of the many events at tox, the game nights with the PhDtrip organization committee, Hot-ones spicytox events and the Canada trip. I really enjoyed the meaningless chit-chat You, Gijs and I had throughout the days and thanks to you guys for agreeing to be my paranymphs.

To the staff and other PIs which support our endeavours at Tox.

Nico, I mostly interacted with you at the coffee table, and at social events like the neonicotinoid pizza event and the many barbeques at your place which remain among my most cherished memories at tox. It was always a joy to talk to you and I think your soberness, openness and kindness will greatly help you in your new role as chair of the department. **Nynke**, your endless enthusiasm for science is very contagious, and while I was initially sceptical of the idea of PBK models, throughout our many conversations you have thoroughly convinced me in their value. I think I speak for everyone when I say that your enthusiasm for science spurs us on to do our best. **Gerda** and **Carla**, thanks for all the administrative help you have given throughout my PhD and for all the chitchat we had throughout the days and the coffee breaks. **Naomi**, I still remember the time when PhD students had to do all the supporting work in the lab and let me tell you, we are very happy that you help lighten our workload. Alex, Sebas, Wouter, David, Nacho, Bert and Laura I have not worked with you guys intensely on a professional level, but greatly appreciated your presence at the department. **Alex**, thank you for all the movie and music suggestions, I am a closet cinephile and loved hearing your in-depth explanations about the cultural relevance of buster Keaton, equilibrium and the many spaghetti westerns we talked about. **Sebas**, thank you for being an overall jolly person with an inexhaustible source of dad-jokes. While sometimes hectic, I fondly look back on our practical courses together. **Wouter**, thank you for being down to earth and easy-going even when we forced you to participate in events like the Veluweloop. I have personally never heard you complain and will forever associate a peanut butter sandwich with you and Thijs. **David**, thanks for the discussions on statistics we had and for re-immersing me in magic the gathering, bouldering and other sports events. I repeat to you the words that your predecessor **Nacho** once imparted to me "you are the social pillars that support the joy of working in the toxicology department". Please continue this to keep tox a happy and accepting place for all. Nacho, sorry for forcing you to participate in the Veluweloop and thank you for not complaining that day despite your ankles. The words you said to me and Katharina gave me a lot of strength. All the best in your current endeavours. **Bert**, I have never directly worked together with you but thanks for being super kind and telling me stories about my dad when he still worked at Tox. Let's both do our best at the 4-daagse from now on. **Laura**, thank you for your early involvement in my project and teaching me the ropes in the toxicology department. Your laid-back attitude was a source of relaxation for us all and I know you played a large role in maintaining the mental health

of many of us PhDs. It is terrible that disease struck you so soon after retirement. I hope you are able to make a clean recovery and enjoy the slow life on the farm you described to us when you left tox.

Next, I would like to thank the many PhDs and postdocs who were my colleagues and friends throughout my PhD. Thanks to the PhDtrip organizing committee for helping us reimplement the PhDtrips in tox, I had a great time during the whole process and enjoy that we are still able to have gamenights afterwards. **Katharina**, where I was the hype-man for organizing social events, you were the brains. Thank you for always hosting us during gamenights and for stimulating me to be as outgoing as possible. Also thank you for arranging so much of the Canada trip, it was unforgettable. **Veronique** and **Jingxuan**, together with Katharina you were the seniors (unfortunately we don't have a good word for senpai or xuechang in western languages) who helped keep us juniors in check. I feel your guys' presence and reality checks on plans helped give me confidence to proceed with many of the social events at tox. Thank you for being a reassuring presence and best luck in your current endeavours. **Liang** and **Wisse**, thank you guys for being my friends also outside of tox and for the many types of good food I got to try at your guys' places. Lets continue to hang out and hopefully do a China trip in 2026. **Germaine**, we worked intensely on my chapter 2, and without your involvement in this chapter there is no way the stem-cell work would've been a success. You are a very enthusiastic person and despite my occasional whining, your vocal reenactment of Disney songs, K-pop and trashy television series grew on me. I feel like we got to be good friends over the course of my PhD and want to thank you for getting me interested in bouldering.

Shivani, we have been friends for some close to 4 years now, thanks for joining on the Croatia vacation and inviting me over for dinner games and stuff it was great. Good luck with the finalization of your own thesis also a shoutout to **Vedran** for teaching me a lot about music theory and bass. **Frances**, You were one of the few PhDs who had equal or more hobbies than me, thank you for joining me and Wisse for diving, for motivating me to do the 4-daagse and for hosting the many spicytox events. You are a fun enthusiastic person to be around and thank you and **Robert** for always being welcoming. **Yasser**, in my whole life I have not met a kinder person than you. Whenever I needed any favour you were always there and you always had time for a chat with fresh made coffee and snacks. Now, when I think of Saudi-Arabia I instantly associate it with your kindness. **Tom**, your presence always livened up the coffee breaks and events with your out-of-the-blue remarks and humour. You too had to deal with a lot of the start-up issues on stem-cell models and I was happy to have another person that shares these issues. Additionally, I am super happy you and Donovan motivated me to get into guitar and am looking forwards to the next upgrade. **Kiri**, I don't know how you do it but you have a talent for rapid comebacks and great self-deprecating humour. Your rapidly formulated rebukes to many

of the stupid stuff said at the coffee table reminds me of "tsukkomi" a type of Japanese humour were a smart (wo)man points out flaws in outlandish statements. I think this type of humour is very welcome at tox and really helps maintain an enjoyable atmosphere.
Donovan, thank you for all the discussions at CBI on how best to do flow cytometry and for bringing so many good vibes to social events like the Veluweloop and pull-up club. Also thanks for getting me back into magic, looking forwards to playing more games with you Nick and David. All the best during your work in Switzerland. **Tanne**, **Haomiao** and **Elise**, thanks for the tips on piano playing and for suggesting good repertoire. Also, Tanne, your quote booklet is pure comedy gold and should be used more often at defences. **Jiaqi** and **Chrysa** thanks for the fruitful discussion on PBK modelling, through talking to you guys I got to realise how much more there is to learn about the field. **Ghaliya**, thank you for helping organize the first part of PhDtrip and for always donating your food whenever you had leftovers. Your energy together with Yasser's kindness completely altered my worldview on the middle-east. **Mirena**, thank you for all your guidance on micro- and nanoparticle analytics. Your compliments and greetings always brought a smile to my face.
Aafke, around the start of my PhD you were dealing with serious medical issues, but I am happy that I got to know you better after you made a full recovery. I fondly remember all the coffee breaks with you, Laura and Merel as well as the joy you showed when talking about birds, or football. To my officemates **Xiyu**, **Merel**, **Wei-jia**, **Quihui**, **Thijs** and **Gijs**.
Thank you for making Tox a comfortable place to work in. I can confidently say we were by far the most cozy office in tox. To my later officemates **Katharina**, **Xuan**, **Xukun**, **Sylvia** and **Matteo**. Thank you for welcoming me in the office in the later part of my PhD after my first office got a little bit too cozy. The go-to humour of the office was always centred around pitch black depression jokes which were especially appreciated near the end of my PhD.
Undoubtedly I have forgotten to include many of the other events that occurred throughout my PhD, but want to thank the remaining PhDs and Postdocs; **Nick**, **Yiming**, **Thoriq**, **Ling**, **Rebeka**, E**dith**, **Sussannah**, **Thitirat**, **Feihan**, **Barbara**, **Danlei**, **Menno, Shuo, Marta**, B**iyao**, **Jing**, A**nnelies**, **Nina**, **Samantha** and **Qianrui** for their time at tox and our fun interactions. Additionally I want to thank my students **Yipeng**, **Kirsten**, **Janne, Lotte, Soraya**, A**nika,** W**enke** and **Vaiva** for their help throughout my projects and our social interactions.

Last but definitely not least I want to thank my friends and family who have supported me over the years.

Victor, we have been friends since the first day of highschool. I am super glad we share so many interests in fighting games, Asia and Japanese culture. I really enjoy how much our conversations teach me about politics and economics as well as more frivolous topics like

option-selects, okizeme and set play. Thanks for being a cool dude for all these years and for putting up with my scatterbrained self.

To my friends from Genki Japanese language school Nicholas, John, Felix and Thiago. When I left Japan, I never imagined we would still be having frequent contact, thanks for being active in maintaining contact. **Nicholas**, I still found it crazy how we randomly met at Fukuoka through our joint acquaintance Jesse. I am super happy you moved to the Netherlands from Lichtenstein and that you have really found your role doing a PhD at Rotterdam. I always enjoyed learning Japanese phrases from you (Nandeyanen!?) and completely going mental at Karaoke with rocket man, donten and shura. **Thiago**, thanks for the Luxembourg trip the Amsterdam exploration and all the cool music suggestions. I am super happy things are going well at amazon and lets hang out again in the near future.
John, thanks for hanging out in Japan and for the in depth look at what it is like to live in Japan. I am super happy you found a girlfriend and are looking for a house together now. **Felix**, thanks for being super jolly and being an uncompromising weeb. It is always fun hanging out in Munchen, the Netherlands or in Japan and feel like I can really embrace Japanese culture again whenever we hang out. I find it super cool that you get to travel the world nowadays, just make sure to return to Germany once in a while to hang out.

To the friends who have joined my Japan trip this year; **Peter**, **Mike**, **Robin** and **Baris**. It was super fun travelling Japan, drinking good liquor and eating good food. We definitely have to go again in the upcoming years to really taste izakaya food in the countryside. Particular shoutout to Peter for introducing me to many new aspects of Japanese pop-culture and for being super knowledgeable on Japanese food and liquor in general.

To my **grandma**, all my **nephews**, **nieces**, **cousins**, **uncles** and **aunts.** It is wonderful that we all live in the same village and get to have family get-togethers so often. You always make my return to Wassenaar welcoming and worthwhile. Thanks for organizing all these family events, it may sometimes feel like a chore, but I think it is why we have such a tight-knit familial bond.

Then finally, to my parents Astrid and Bram, my sister **Anouk** and her husband Timo. Anouk, thanks for the many hour-long calls and random chit-chat. This always cheered me up throughout my PhD. I am so happy that you are finally enjoying work now that you have started at our company. I think it is going to be interesting and fun, but maybe also sometimes frustrating to have to work closely together every day but lets both do our best. **Timo**, thanks for overall being a chill dude and for all the concert, food, game, anime and drink suggestions. I am very happy with your addition to our family, so make sure you don't blow yourself up once your teaching duties at the EOD end.

Astrid and Bram, Thanks for always being there for me and for all the love and support you have given me over the many years. I never thought I would end up in the same field as you **Bram**, but I do guess the apple doesn't fall far from the proverbial tree. Thank you for always pushing me to do my best in academics and other fields. Since my employment at BDS we are going to be working closely together for a while which will give both of us a chance to see the professional side of one-another.

Astrid, thank you for always supporting me and Anouk emotionally. Thanks to you our family home still feels very cozy to return to. Many of the things you do for us we sometimes take for granted and we don't say thank you enough, but know we really appreciate it. Bram and Astrid, You are some of the few people I know that are too kind for their own good, so you would put me at ease if you take the opportunity to be a bit more selfish in the years to come. Hopefully, Me and Anouk grow enough in the company that we can finally actually force you guys to retire (😉) and actually go on all the holidays you deserve.

Biography

Hugo Brouwer was born in Wageningen on October 24th 1994. After his secondary education in Wassenaar, Hugo attended the joint undergraduate life science and technology program of the Leiden university and Delft technical university. After obtaining his Bachelors degree in 2013, Hugo proceeded with the graduate study life science and technology at the Leiden University. During this period Hugo conducted a thesis on neocannabinoid medicines at the leiden chemical institute and a thesis on hematopoietic stem cell differentiation at the Karolinska institute in Sweden and Hugo obtained his masters degree in 2019. During the period of 2019-2021 Hugo was employed as a researcher at MicroLife solutions where he researched ways to produce recombinant cellulosome proteins for lignocellulose degradation. Afterwards Hugo was employed as a PhD candidate at the department of toxicology at the Wageningen university. During his PhD Hugo followed several courses of the post-graduate education in toxicology for registration as an European registered toxicologist. Hugo is currently employed at Biodetection Systems where he researches reporter gene assays for food-borne and environmental pollutants.

List of publications

This Thesis

Busch M, **Brouwer H**, Aalderink G, Bredeck G, Kämpfer AAM, Schins RPF, Bouwmeester H. (2023) Investigating nanoplastics toxicity using advanced stem cell-based intestinal and lung in vitro models. *Front Toxicol. doi: 10.3389/ftox.2023.1112212.*

Aalderink G*, **Brouwer H***, Wang J, Janssen AWF, van der Zande M, Govers C, Hoppenbrouwers T, Bouwmeester H, Busch M. (2025) Pro-inflammatory response of human iPSC-derived intestinal epithelial monolayers towards microbial toxins LPS and nigericin. *Arch Toxicol. doi: 10.1007/s00204-025-04215-9.* * These authors contributed equally

Brouwer H, Busch M, Yang S, Venus T, Aalderink G, Crespo JFF, Villacorta A, Hernández A, Estrela-Lopis I, Boeren S, Bouwmeester H. (2025) Toxicity of true-to-life microplastics to human iPSC-derived intestinal epithelia correlates to their protein corona composition. *J Hazard Mater. doi: 10.1016/j.jhazmat.2025.138908.*

Brouwer H, Porbahaie M, Boeren S, Busch M, Bouwmeester H. (2024) The in vitro gastrointestinal digestion-associated protein corona of polystyrene nano- and microplastics increases their uptake by human THP-1-derived macrophages. *Part Fibre Toxicol. doi: 10.1186/s12989-024-00563-z.*

Brouwer H, Busch M, Kramer N, Bouwmeester H. (in preparation) Mechanistic PBK Modelling for Biodistribution Prediction of Ingested Micro- and Nanoplastics.

Other Publications

Brouwer H, Van Oijen F. L.N., Bouwmeester H. (2023) Chapter 40 - Potential human health effects following exposure to nano- and microplastics, lessons learned from nanomaterials, *Present Knowledge in Food Safety,Academic Press, ISBN 9780128194706, https://doi.org/10.1016/B978-0-12-819470-6.00014-7.*

de Boer, T.E, **Brouwer H,** Nguyen K. T, Ha H, Ha D.T.C, Ha, C.H, Brouwer, A. (2022) Hot Spring Metagenome Characterization for Industrially Relevant Bio-Based Enzymes. *Available at Social Science Research Network (SSRN) http://dx.doi.org/10.2139/ssrn.4192376*

Overview of completed training activities

Discipline specific activities	
General toxicology, WUR	2021
Molecular Toxicology, PET	2021
Cellular Toxicology, PET	2022
Epidemiology, PET	2022
Organ Toxicology, PET	2022
Pathobiology, PET	2022
Risk Assessment, PET	2022
Regulatory Toxicology, PET	2022
Neurotoxicology, PET	2022
Food toxicology, WUR	2023
Environmental toxicology, WUR	2023
General courses	
PhD week, VLAG	2022
Applied statistics, VLAG	2023
Efficient writing strategies, VLAG	2023
Life science data integration challenge, VLAG	2021
Preparing research proposal, VLAG	2021
Teaching and supervision	
Teaching assistant Food Toxicology	2022-2024
Teaching assistant Advanced Biochemical Analysis of Foods	2024
Supervision of graduate students	2021-2024
Conferences and meetings	
Chair PhD trip organization committee,	2023
Participated in PhD trip to the United Kingdom	2023
Poster presentation at 64th Society of Toxicology conference, The USA	2025
Annual poster presentations Plasticheal conference	2021-2025
Speaker at Dosimetry workshop Momentum 1.0 project	2024

Funding

The research in this thesis was financially supported by the division of Toxicology at Wageningen University, as well as the the LymphChip project (number NWA-ORC 2019 1292.19.019)(NWO), the Plasticheal project under the European Union's Horizon 2020 research and innovation program (grant no. 965196) and the Netherlands Organization for Health Research and Development the MOMENTUM project (grant no. 458001101).

Financial support by Wageningen university for the printing and design of this thesis is gratefully acknowledged